

Effect of Plasticity and Pre-ageing on Precipitation in Al-Zn-Mg-Cu Alloy AA7075

*A thesis submitted to The University of Manchester for the degree of
Doctor of Philosophy in the Faculty of Science and Engineering.*

2023

Ziyu Ma

School of Natural Sciences
Department of Materials

Contents

List of Figures	6
List of Tables	13
Abstract	14
Declaration	15
Copyright Statement	16
Acknowledgements	17
1 Introduction	18
1.1 Structure and Objectives	22
Bibliography	23
2 Literature Review	28
2.1 Aluminium Alloys in Automotive Industry	28
2.2 7xxx Aluminium Alloys	29
2.2.1 Role of Elements	30
2.2.2 Decomposition Processes	31
2.2.3 Guinier-Preston (GP) Zones	31
2.2.4 η' Phase	33
2.2.5 Other Metastable Phases	35
2.2.6 Equilibrium Phases	36
2.3 Ageing Strategy	37
2.3.1 One Step Ageing	37
2.3.2 Two Steps Ageing	38
2.3.3 Retrogression and Re-ageing	39

2.4	Precipitation Strengthening	40
2.4.1	Strengthening Mechanism	41
2.4.2	Strengthening Model	43
2.5	Deformation-Precipitation Interaction	45
2.5.1	Pre-deformation Effects on Precipitation	46
2.5.2	Dynamic Strain Ageing	47
2.5.3	Excess Vacancy Assisted Dynamic Precipitation	49
	Bibliography	52
3	Experimental Methods	64
3.1	Materials	64
3.2	Heat Treatments	64
3.3	Micro-hardness	65
3.4	Mechanical Testing	67
3.4.1	Room temperature testing	67
3.4.2	Warm temperature testing - Dilatometer	67
3.4.3	Warm temperature testing - ETMT	68
3.5	Transmission Electron Microscopy	70
3.6	Small Angle X-ray Scattering	73
3.6.1	Theory	74
3.6.2	Instruments	76
3.6.3	Data analysis	79
3.7	Differential Scanning Calorimetry	85
3.7.1	Identification of precipitation	86
3.7.2	Investigation of precipitation evolution	86
3.8	X-ray Diffraction - Line broadening	89
	Bibliography	92
4	Dynamic Precipitation in Supersaturated Al-Zn-Mg-Cu during Warm Stretching	96
4.1	Introduction	98
4.2	Methodology	99
4.3	Results	103

4.4	Discussion	110
4.5	Conclusions	115
	Bibliography	116
5	Microstructural Stability and Paint Bake Response of Pre-aged AA7075	119
5.1	Introduction	121
5.2	Methodology	123
5.3	Results	126
5.3.1	Isothermal/Isochronal pre-ageing	126
5.3.2	Optimised pre-ageing process	128
5.3.3	Paint bake response of samples preaged 8 hours at 80 °C . . .	129
5.4	Discussion	135
5.5	Conclusions	139
	Bibliography	141
6	Understanding the Effect of Deformation Combined with Heat Treatment on Age Hardening of Al-Zn-Mg-Cu Alloy AA7075	147
6.1	Introduction	149
6.2	Methodology	150
6.3	Results	153
6.4	Discussion	162
6.5	Conclusions	168
	Bibliography	169
7	In-situ Investigation of Dynamic Precipitation in Pre-aged Al-Zn-Mg-Cu Alloy AA7075	173
7.1	Introduction	175
7.2	Methodology	176
7.3	Results	179
7.3.1	Effect of plastic strain and strain rate	179
7.3.2	Effect of temperature	182
7.4	Discussion	184
7.5	Conclusions	191

Bibliography	192
------------------------	-----

8 Conclusions	195
----------------------	------------

8.1 Future work	197
---------------------------	-----

Word Count: 37,797

List of Figures

1.1	The average aluminium content (kg) per vehicle in 2019 and 2025 (predicted). A-Basic, B-Sub-compact, C-compact, D-Midsize and E-Large.	18
1.2	The electric vehicle production (units) in Europe from 2016. Data between 2019 to 2025 were predicted values	19
1.3	Weight difference between electric vehicles and their petrol equivalent	20
2.1	The timeline of the application of Magnesium and Aluminium in automobile industry	28
2.2	Predicted aluminium gains and losses (kg) by component group . . .	29
2.3	HRTEM micrograph of GPII zones in a Al-Zn-Mg alloy	32
2.4	The schematic of four η' variants and their crystal orientation relationship to the aluminium matrix	34
2.5	TEM micrograph shows precipitates in a AA7050 sample	37
2.6	A schematic of RRA treatments for AA7075	40
2.7	Schematic of the intersection of two screw dislocations produces edge-jogs, and the movement of these edge-jogs by climbing produces vacancies	49
3.1	Schematic of Vickers hardness test	66
3.2	TA instrument DIL805 A/D/T dilatometer	68
3.3	Instron electro-thermo-mechanical testing machine (ETMT)	68
3.4	Schematic of basic operations of TEM in (a) diffraction mode and (b) imaging mode	72
3.5	Schematic of the relationship between incident wave, scattered wave and scattering vector q	74

3.6	TEM micrograph ($\langle 1\ 1\ 0 \rangle$ zone axis) and SAXS images of θ and T_1 phases in a Al-Cu-Li-Mg system.	80
3.7	Bright field STEM micrograph ($\langle 1\ 1\ 0 \rangle$ zone axis) and SAXS image of η' phase in a Al-Zn-Mg-Cu system.	80
3.8	Estimating relative volume fraction of precipitates using DSC	87
3.9	Measuring the evolution of relative volume fraction of precipitates using isothermal calorimetry	88
4.1	Test sample geometry used for dilatometer experiments. All dimensions are in mm.	100
4.2	The temperature profile of sample solution heat treated at 480°C followed by the deformation at 180°C. Online version in color.	101
4.3	(a) true stress-strain curves of samples deformed at 180°C with different strains and strain rates. (b) work hardening rate calculated from samples deformed with 6×10^{-3} and $7 \times 10^{-4} \text{ s}^{-1}$ strain rate to 5% strain. Online version in color.	103
4.4	Bright field TEM images taken along $\langle 110 \rangle$ zone axis. (a)-(b) from the sample deformed at 180°C with $7 \times 10^{-4} \text{ s}^{-1}$ strain rate to 12% strain. (c)-(d) from the sample having identical heat treatments as (a) and (b) but without deformation.	104
4.5	Kratky plots of SAXS results. (a) samples deformed with $7 \times 10^{-4} \text{ s}^{-1}$ strain rate. (b) samples deformed with $6 \times 10^{-3} \text{ s}^{-1}$ strain rate. (c) samples deformed to approximately 9% strain. (d) sample deformed at $6 \times 10^{-3} \text{ s}^{-1}$ for 13s (longest time) and $7 \times 10^{-4} \text{ s}^{-1}$ for 29s (shortest time) (e) sample deformed to 12% strain at $7 \times 10^{-4} \text{ s}^{-1}$ strain rate, compared to equivalent non-deformed material. (f) sample deformed to 8% strain at $6 \times 10^{-3} \text{ s}^{-1}$ strain rate, compared to equivalent non-deformed condition. Online version in color.	105
4.6	(a) Evolution of Guiner radius for the slower ($7 \times 10^{-4} \text{ s}^{-1}$) and faster ($6 \times 10^{-3} \text{ s}^{-1}$) strain rates compared with the non-deformed case with (a) time, (b) strain. Calculated growth rate for faster and slower strain rates compared with the non-deformed case plotted as a function of (c) time, (d) strain. Online version in color.	107

4.7	(a) Evolution of integrated intensity (assumed proportional to volume fraction) for the slower ($7 \times 10^{-4} \text{ s}^{-1}$) and faster ($6 \times 10^{-3} \text{ s}^{-1}$) strain rates compared with the non-deformed case with (a) time, (b) strain. Derived evolution of relative precipitate number density for faster and slower strain rates compared with the non-deformed case plotted as a function of (c) time, (d) strain. Online version in color.	109
4.8	Calculated evolution of dislocation density and excess vacancy concentration at 180°C for (a) slower strain rate $7 \times 10^{-4} \text{ s}^{-1}$, (b) higher strain rate, $6 \times 10^{-3} \text{ s}^{-1}$. Online version in color.	113
4.9	Measured growth rate and predicted excess vacancy concentration for (a) slower strain rate $7 \times 10^{-4} \text{ s}^{-1}$, (b) higher strain rate, $6 \times 10^{-3} \text{ s}^{-1}$. Online version in color.	114
5.1	(a) Microhardness evolution of samples pre-aged at 80°C and after pre-ageing plus simulated paint-bake for 20 minutes at 185°C (b) Guinier radius, integrated intensity and number density as a function of pre-ageing time at 80°C Integrated intensity and number density are normalised to their maximum value to bring the data in to the range $[0, 1]$. Error bars correspond to one standard deviation.	126
5.2	Microhardness of samples pre-aged 8 hours at 40, 60, 80 and 100°C and after pre-ageing plus simulated paint-bake for 20 minutes at 185°C . Error bars correspond to the standard deviation.	127
5.3	(a) Kratky plot of SAXS results of samples pre-aged 8 hours at 40, 60, 80 and 100°C . (b) Guinier radius, integrated intensity and number density correspond to samples in (a). Integrated intensity and number density are normalised to their maximum value to bring the data in to the range $[0, 1]$. Error bars correspond to one standard deviation.	127
5.4	True stress - strain curve of pre-aged (8 hr at 80°C) and T6 (24 hr at 120°C) samples.	129

5.5	(a) Microhardness evolution, (b) Guinier radius, integrated intensity and number density evolution of the preaged sample (80 °C 8 hours) during the following 7 months natural ageing. Integrated intensity and number density are normalised to their maximum value to bring the data in to the range [0, 1]. Error bars correspond to one standard deviation.	129
5.6	(a) Bright field TEM and (b) HRTEM images taken from the sample pre-aged at 80 °C 8 hours in $\langle 1\ 1\ 0 \rangle$ zone axis showing the existence of small GP zones.	130
5.7	Microhardness evolution of pre-aged samples baking at 185 °C 0-25 minutes with fast and slow heating rates, compared to the original pre-aged microhardness.	130
5.8	Kratky plots of SAXS results of pre-aged samples baking at 185 °C with fast (black) and slow (red) heating rates. (a) 0 minute, (b) 5 minutes, (c) 10 minutes, (d) 15 minutes, (e) 20 minutes, (f) 25 minutes.	131
5.9	(a) Guinier radius and (b) integrated intensity (c) normalised number density of pre-aged samples baking at 185 °C 0-25 minutes with fast and slow heating rates, compared to the original pre-aged condition. .	132
5.10	Bright field TEM images with (a) low magnification and (b) high magnification, taken along the $\langle 1\ 1\ 0 \rangle$ zone axis from the sample pre-aged at 80 °C 8 hours followed by baking at 185 °C 20 minutes. .	133
5.11	(a) Heat flow and temperature profile of the isothermal calorimetry tests of the sample pre-aged 8 hours at 80 °C baking at 185 °C in the calorimetry. (b) the normalised integrated peak area calculated from the isothermal calorimetry and the beamline SAXS results.	134
5.12	(a) Hardening fraction as a function of pre-ageing temperature. (b) Time-Temperature-Transformation (TTT) diagram calculated by using JMatPro, superimposed with the experimental conditions. . . .	137
6.1	Hardness evolution at 120 °C of samples with or without deformation, compared to the hardness of samples in the T6 condition (peak-aged).	154

6.2	(a) True stress-strain curves of selected samples. (b) Repeated tests of deforming pre-deformed (10% strain) samples to failure. PA denotes pre-ageing 8 h at 80 °C.	154
6.3	Summary of the 0.2% proof stress and strain to failure of deformed samples after the second ageing treatment at 120 °C	155
6.4	Bright field TEM images taken in $\langle 110 \rangle$ zone-axis from deformed samples (a) without any second ageing treatment, (b) after 2 h at 120 °C, (c) and (d) after 6 h at 120 °C.	156
6.5	Kratky plots of SAXS results. (a) pre-aged samples before and after deformation (10% strain). (b~f) after 2~10 h ageing at 120 °C from samples with or without deformation.	157
6.6	Evolution of (a) Guinier radius, (b) normalised integrated intensity and (c) normalised number density during the second ageing at 120 °C for samples with or without 10% strain.	159
6.7	(a) Heat flow and temperature profile of the isothermal calorimetry test for the deformed sample (b) normalised integrated heat flow from isothermal calorimetry results and normalised integrated scattering intensity from SAXS results.	160
6.8	X-ray line broadening results (a) Modified Williamson-Hall plot. (b) evolution of dislocation density as a function of time at 120 °C.	161
6.9	(a) The growth rate of precipitates and (b) the enhancement effect of the deformation as a function of the ageing time at 120 °C.	163
6.10	(a) Evolution of strengthening components for deformed samples at 120 °C. (b) Predicted yield strength of deformed and undeformed samples as a function of time at 120 °C.	166
7.1	Temperature profile of samples deformed at 120 °C and 150 °C with the slow strain rate $1 \times 10^{-4} \text{ s}^{-1}$. Upon reaching the target strain, load was immediately reduced to 0 N. The sample was maintained at the target temperature for additional 400 seconds.	177
7.2	True stress-strain curves of samples deformed at 150 °C with different strain rates.	179

7.3	Bright field TEM images taken along $\langle 110 \rangle$ zone axis (a) from the sample deformed at 150°C with $2 \times 10^{-4} \text{ s}^{-1}$ strain rate to 8% strain. (b) from the sample having identical heat treatments but without deformation.	180
7.4	Examples of the smoothing process of the raw Guinier radius collected from samples deformed at 150°C with (a) the slow strain rate ($1 \times 10^{-4} \text{ s}^{-1}$) and (b) the intermediate strain rate ($2 \times 10^{-4} \text{ s}^{-1}$). Raw data are marked by the scattering points. Solid lines represent the smoothed data. Dash lines, which are calculated as $\pm 2\%$ of the smoothed data, capture the upper and lower bounds of the raw data,	181
7.5	The evolution of Guinier radius during deformation at 150°C with different strain rates, compared to the reference sample that only being heated at 150°C without any deformation	182
7.6	The evolution of the precipitate growth rate at 150°C (a) as a function of time and (b) as a function of plastic strain.	182
7.7	True stress-strain curves of samples deformed at 150°C and 120°C with the slow strain rate ($1 \times 10^{-4} \text{ s}^{-1}$).	183
7.8	The evolution of (a) Guinier radius as a function of time (b) growth rate as a function of strain during deformation at 150°C and 120°C with the slow strain rate ($1 \times 10^{-4} \text{ s}^{-1}$), compared to reference samples that only being heated at 150°C and 120°C without any deformation	183
7.9	The growth rate of precipitates during additional holding at (a) 150°C and (b) 120°C after the deformation, compared to the reference samples without any deformation.	184
7.10	The evolution of vacancy concentration and dislocation density as a function of the plastic strain during deformation. κ is the arrangement factor in the range of 1 (homogeneous) to 10 (cellular).	187

7.11	The evolution of deformation enhanced growth rate and excess vacancy concentration (a, c and e) as a function of plastic strain during deformation, (b, d and f) as a function of time during the additional 400 seconds holding at 150 °C after the deformation. (a and b) were collected from the slow strain rate test. (c and d) were collected from the intermediate strain rate test. (e and f) were collected from the fast strain rate.	188
7.12	The evolution of deformation enhanced growth rate and excess vacancy concentration (a) as a function of plastic strain during deformation at 150 °C and 120 °C with the slow strain rate ($1 \times 10^{-4} \text{ s}^{-1}$), (b) as a function of time during the additional 400 seconds holding at 150 °C and 120 °C after the deformation.	189

List of Tables

2.1	Weight reduction potentials by material substitution	28
2.2	Crystallographic orientations of η in Al-Zn-Mg-(Cu) systems	36
2.3	Conventional ageing conditions for AA7075	38
3.1	Heat treatments in this study	65
3.2	Common laboratory metal anode used to generate X-ray	76
3.3	Form factors for common geometries	81
3.4	Elastic constants of aluminium at room temperature	91
3.5	The parameters a,b,c and d for equation 3.31	91
3.6	Calculated diffraction peaks of aluminium	92
4.1	Nominal composition of AA7075 in wt.%	99
4.2	Guinier radius of deformed samples determined from SAXS	106
6.1	Nominal composition of AA7075 in wt.%	150
6.2	Parameters for the modified Williamson-Hall plot	161
6.3	Parameters for the strengthening model	165
7.1	Nominal composition of AA7075 in wt.%	176
7.2	Parameters for excess vacancy model	186

Abstract

High-strength Al-Zn-Mg-Cu alloys are widely applied in the aerospace and automotive industries due to their significant strength-to-weight benefits. These alloys achieve their exceptional strength primarily through precipitation, and the development of these strengthening precipitates can be impacted significantly by deformation. In this study, the dynamic interaction between deformation and precipitation was investigated in a commercial AA7075 under various conditions.

To study the deformation effect in a supersaturated microstructure, a dilatometer was used to perform directly quenching from the solution treatment temperature at 480°C to a warm temperature at 180°C, immediately followed by uni-axial deformation. Small angle X-ray scattering revealed the presence of clusters only 5 s after quenching, and the subsequent evolution of the microstructure involved the growth and coarsening of these clusters. Transmission electron microscopy demonstrated the precipitates were homogeneously distributed in the matrix with and without deformation. Deformation was found to strongly enhance the growth rate of these clusters/precipitates, which increased linearly with increasing strain, and was faster at higher strain rates for the same strain level. Neither SAXS nor TEM evidenced an enhancement effect of warm deformation on precipitate nucleation.

To design a pre-aged microstructure that could be potentially applied to the automotive industry, the evolution of precipitates during the pre-ageing, natural ageing, and paint bake process was investigated using SAXS, TEM and isothermal calorimetry. The results showed that 8 hours of pre-ageing at 80°C can produce a stable microstructure, which further allows 94% of the T6 hardness after a short paint bake process. This pre-ageing strategy was found to be capable of retaining sufficient work hardening response at room temperature. Therefore, it is of interest to explore the possibility of coupling deformation and precipitation to achieve enhanced strength. The results showed that uni-axial deformation to 10% strain enabled significant work hardening and resulted in strengths greater than those obtained with a T6 heat treatment but with a sacrifice in further strain to failure. Post-ageing at 120°C was found to be effective in partially recovering dislocations and promoting precipitation strengthening.

Finally, for this pre-aged microstructure, the effect of warm deformation on precipitation was in-situ investigated using high energy synchrotron small angle X-ray scattering. The results showed that the precipitate growth rate increased linearly with the applied strain at low plastic strains, but at high plastic strains, the relation deviated slightly from linearity. Temperature and strain rate were also found to have an impact on the enhancement effect of deformation on precipitate growth rate, with a stronger effect at low temperatures and high strain rates for a given strain. After plastic straining, the deformation enhancement effect quickly diminishes within 400 s for the studied conditions.

For all investigations in this study, when deformation was applied concurrently with deformation at warm temperature, the deformation enhancement effect is consistent with the idea of plastic strain induced excess vacancy enhancing the solute diffusion rate. The acceleration effect of prior deformation on the growth of precipitation during post-ageing is consistent with the effect of dislocations acting as the fast diffusion paths.

Declaration

No portion of the work referred to in the thesis has been submitted in support of an application for another degree or qualification of this or any other university or other institute of learning.

Copyright Statement

The author of this thesis (including any appendices and/or schedules to this thesis) owns certain copyright or related rights in it (the “Copyright”) and s/he has given The University of Manchester certain rights to use such Copyright, including for administrative purposes.

Copies of this thesis, either in full or in extracts and whether in hard or electronic copy, may be made only in accordance with the Copyright, Designs and Patents Act 1988 (as amended) and regulations issued under it or, where appropriate, in accordance with licensing agreements which the University has from time to time. This page must form part of any such copies made.

The ownership of certain Copyright, patents, designs, trademarks and other intellectual property (the “Intellectual Property”) and any reproductions of copyright works in the thesis, for example graphs and tables (“Reproductions”), which may be described in this thesis, may not be owned by the author and may be owned by third parties. Such Intellectual Property and Reproductions cannot and must not be made available for use without the prior written permission of the owner(s) of the relevant Intellectual Property and/or Reproductions.

Further information on the conditions under which disclosure, publication and commercialisation of this thesis, the Copyright and any Intellectual Property and/or Reproductions described in it may take place is available in the University IP Policy (see <http://documents.manchester.ac.uk/DocuInfo.aspx?DocID=24420>), in any relevant Thesis restriction declarations deposited in the University Library, The University Library’s regulations (see <http://www.library.manchester.ac.uk/about/regulations/>) and in The University’s policy on Presentation of Theses.

Acknowledgements

I would like to express my sincere gratitude to my supervisor, Professor Joe Robson, for his endless guidance, support, and encouragement throughout my PhD program. I am grateful for the opportunity to work with him. His expertise and insights have been invaluable to me.

I also want to thank the academic and technical staff at the University of Manchester who provided training and support for the equipment used in this project. Their expertise and assistance were critical to the success of this research.

I would like to extend my thanks to my colleagues and friends who have been a constant source of inspiration, motivation, and camaraderie throughout my PhD journey.

I am also grateful to the industry sponsor, Constellium, for their financial support and collaboration throughout this project. Their partnership and guidance have helped to ensure that this research is relevant and meaningful in the real world.

Lastly, I would like to express my heartfelt thanks to my family for their unwavering love and support. Their encouragement and sacrifices have made it possible for me to pursue my dreams.

Chapter 1

Introduction

Aluminium, as the most abundant metal on the Earth comprising over 8% of the crust, has a long and successful history since the 18th century [1, 2, 3]. Successful attempts of alloying aluminium with other elements to increase its strength were reported in the early 20th century [4]. The discovery of precipitation strengthening in Al-Cu alloys by Alfred Wilm marked the beginning of exploring high-strength aluminium alloys, particularly for aerospace industry [4, 5]. Other precipitation-hardenable aluminium alloys, such as Al-Zn-Mg (7xxx) and Al-Mg-Si (6xxx), were then developed successively.

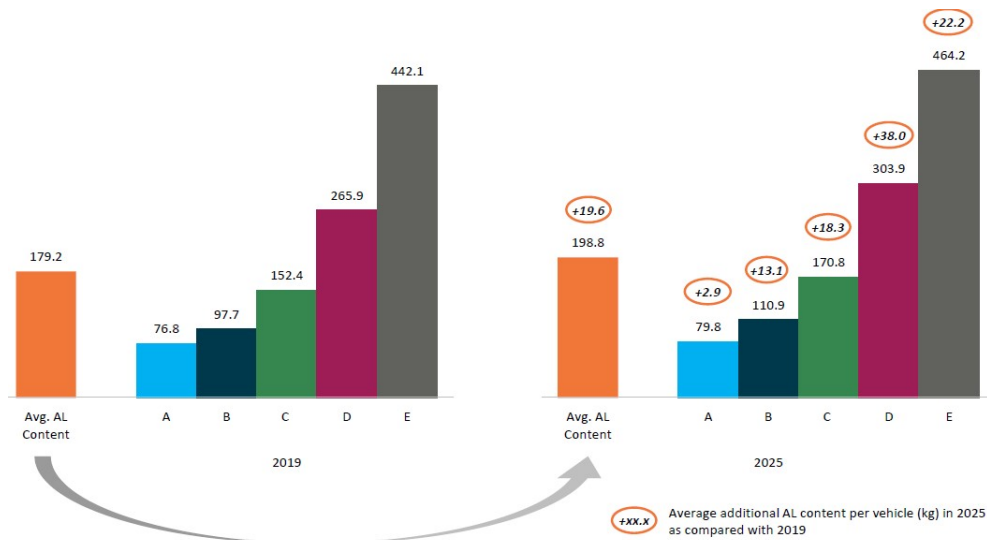


Figure 1.1: The average aluminium content (kg) per vehicle in 2019 and 2025 (predicted). A-Basic, B-Sub-compact, C-compact, D-Midsized and E-Large. [6]

The application of aluminium alloys in the automotive industry has grown significantly in the past decade, which is mainly driven by the goal of reducing the

greenhouse gas (CO₂) emission [7]. The fuel consumption during driving is found to be the primary part of the energy consumption during the life-cycle of an automobile [8, 9]. Weight reduction is seen as one of the strategies to tackle this problem. Studies found an estimated weight reduction of 40 to 60% can be expected by replacing mild steels with aluminium alloys [9, 10, 11, 12]. Many automobile manufacturers have started this transformation. According to the survey from DuckerFrontier, until 2019, the average aluminium content in a European car has increased to 179kg from 62kg in 1990. It is further forecasted a continuous growth to 198kg by 2025, as shown in figure 1.1 [6]. Currently, 6xxx and 5xxx are the main aluminium alloys in the automotive industry primarily due to the combination of medium strength, sufficient formability and good corrosion resistance [9, 10, 11]. For example, 6016 and 6014 sheet with thickness in 1~1.2mm is preferred on outer panel production [10, 13]. High magnesium 5xxx aluminium alloys sheets (eg.5182) are used on body inner panels[10, 13, 14].

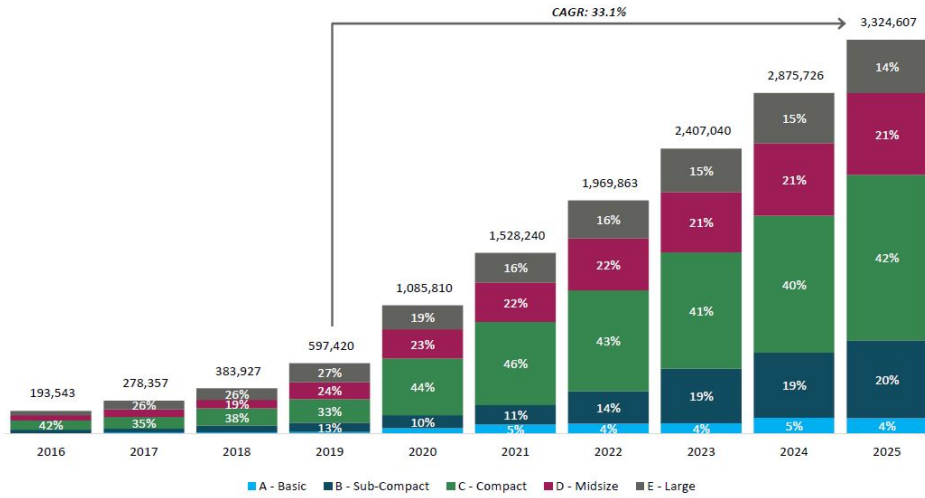


Figure 1.2: The electric vehicle production (units) in Europe from 2016. Data between 2019 to 2025 were predicted values [6]

Although replacing steels with aluminium alloys can theoretically reduce the weight of vehicles, the reality is that the mass of newly built vehicles in the US has risen since 1990 with 12% on cars and 7% on SUVs [15], mainly due to the constantly increased demands of high safety, performance and comfort from customers. In addition to this, electric vehicles have gained significant attention in recent years as being an essential strategy to decarbonize transport. As shown in figure 1.2,

the compound annual growth rate of electric vehicle production in Europe has been predicted as 33% between 2019 to 2025 [6]. Ultimately using sustainable electric energy to replace fossil fuel is on many countries' schedules. Even though battery electric vehicles (BEVs) generally have significantly higher aluminium content than the internal combustion engine vehicles (ICEs) [6], more weights are yet added on electric vehicles to support the batteries, as shown in figure 1.3. Therefore, developing and utilising ultra-high strength aluminium alloys is invigorated.

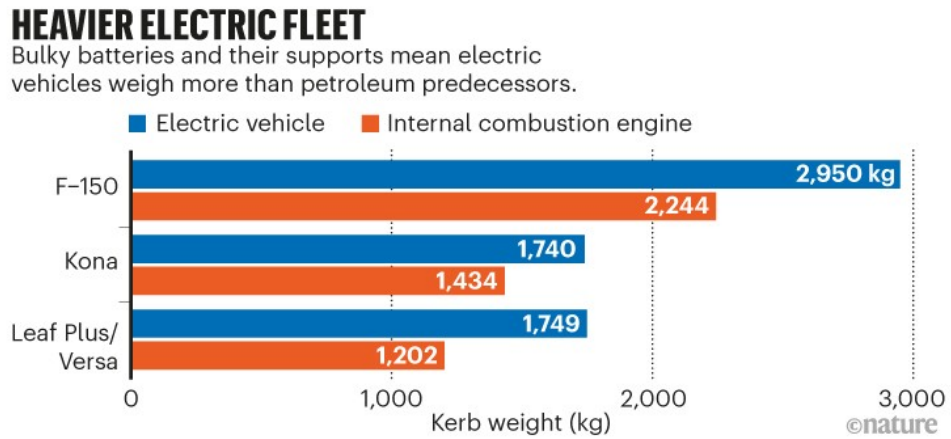


Figure 1.3: Weight difference between electric vehicles and their petrol equivalent [15] (Copyright obtained from Springer Nature)

Recently, attention is brought to 7xxx aluminium alloys which possess the highest strength among the aluminium family. It is, therefore, expected an optimised weight reduction while maintaining the structural integrity. Despite the attractive benefits of adopting 7xxx aluminium alloys into the automotive industry, the popularization and application are limited by their low room temperature formability and poor resistance to stress corrosion cracking (SCC) [9, 13]. Until now, the application of 7xxx aluminium alloys in automobiles is limited to safety-critical components such as the bumper, pillars and beams where ultra-high strength and crush worthiness are the major concerns [16, 17, 18].

Numerous studies reported the formability may be improved by tailoring the initial temper condition further coupled with a specially designed forming process. For example, the formability of peak aged (T6) AA7075 can be significantly enhanced by forming at elevated temperatures [19, 20], however, with the consequence of destroying the carefully designed precipitate distribution and sacrificing the strength. Furthermore, a long post-form heat treatment may be required to

recover the strength or even produce overaged T7 tempers to attenuate the SCC susceptibility [21, 22, 23, 24, 25]. Distinctive to the peak aged condition, underaged tempers may possess better formability at ambient temperature. With a carefully designed pre-ageing heat treatment, the drawback of the unstable microstructure can be improved, which is also helpful in extending the shelf life of the raw materials in the automotive manufacturing [26, 27, 28, 29, 30]. To maximise the light-weighting benefit, it is desired to utilise 7xxx aluminium alloys in their peak aged condition. However, precipitation in 7xxx aluminium alloys at ambient/warm temperature is a slow process [31]. Deformation is found to be effective on accelerating the precipitation kinetics [32, 33]. The dynamic effect and the underlying mechanism of deformation-precipitation interaction is of interest to the present study.

The existing research on the interaction between deformation and precipitation dynamics in aluminium alloys, particularly 7xxx series, has identified the significance of strain-induced excess vacancies in enhancing precipitate growth [34, 35, 36, 37]. However, several key knowledge gaps remain. Firstly, while previous studies have shown how deformation influences the growth of existing precipitates, there is a lack of clarity regarding the nucleation of new particles during warm deformation, especially in highly supersaturated initial states. Additionally, the impact of various deformation parameters, such as strains, strain rates, and temperatures, on vacancy production and annihilation needs further investigation. Previous research on pre-aged microstructures during uniaxial tensile strains has shown strain-dependent enhanced growth rates [34, 35, 36], where vacancy production dominates with little effect from vacancy annihilation at vacancy sinks. However, the impact of vacancy annihilation can become significant when dislocation spacing is smaller than vacancy diffusion distance [38, 39]. Furthermore, most experimental investigations have focused on a single deformation temperature for a given microstructure [34, 35, 36, 38], limiting the understanding of how temperature variations affect the overall vacancy evolution and dynamic precipitation behaviour. Given that vacancy annihilation is diffusion-controlled, temperature is anticipated to be crucial in governing overall vacancy behaviour. Addressing these gaps would provide a more comprehensive understanding of the complex interplay between deformation and precipitation in these alloys.

1.1 Structure and Objectives

This thesis seeks to fill the knowledge gaps in understanding the interaction between deformation and precipitation in 7xxx aluminium alloys during various industrial forming processes. Each result chapter presents results from exploring a distinct condition relevant to an industrial operation to gain valuable insights. By investigating the deformation-precipitation interactions under these diverse conditions, it is possible to unlock the full potential of 7xxx aluminium alloys for broader industrial applications.

This thesis begins with an overview of the potential opportunities and challenges of 7xxx aluminium alloys. In Chapter 2, Section 2.1 provides a review of the application of aluminium alloys in the automotive industry. Section 2.2 covers a review of 7xxx aluminium alloys and the possible second-phase particles in this system. Section 2.3 briefly reviews the ageing strategy of 7xxx aluminium alloys. Section 2.4 contains a review of the fundamental strengthening theories, with an emphasis on precipitation strengthening. Section 2.5 provides a review of theories explaining the possible interactions between deformation and precipitation.

Chapters 4 to 7 are presented in an alternative journal format, with the necessary experimental details to repeat this work given in each chapter. To complement these sections, Chapter 3 gives a brief description of the theory underlying each experimental technique used in this study.

Chapter 4 focuses on investigating the immediate impact of warm stretching on precipitation in supersaturated AA7075 (Al-Zn-Mg-Cu) alloys. This study is particularly relevant to scenarios where warm forming follows directly after solution heat treatment. One key objective of this study was to determine whether the initial supersaturated state would result in a significant influence of deformation on precipitate nucleation during warm deformation conditions.

Chapter 5 delves into developing a pre-ageing strategy that can stabilise the natural ageing and promote a rapid precipitation response during a simulated paint bake process. Unlike previous pre-ageing studies that primarily focused on optimizing the final product strength, this study emphasizes establishing relationships between pre-aged microstructure and final precipitate distribution in AA7075. This

was achieved through an extensive characterization of precipitate evolution under various pre-ageing conditions, coupled with a comprehensive examination of microstructural changes during a simulated paint bake cycle.

Chapter 6 is dedicated to exploring a novel strategy to achieve ultra-high strength in the pre-aged AA7075 by synergistically combining working hardening and precipitation strengthening. Through the characterization of precipitate evolution and changes in dislocation density, the study seeks to comprehensively understand the individual contributions of each mechanism to the final strength and explain how specific property combinations can be tailored to achieve desired strength levels. This research has relevance to industrial forming operations, where pre-ageing and post-ageing are commonly used before and after deformation to optimize material properties.

Chapter 7 is devoted to investigating the instantaneous effect of warm deformation on precipitation in a pre-aged AA7075, which is highly relevant to industrial warm forming operations. This chapter is seen as an increment to previous studies that explored the influence of deformation-induced excess vacancies on solute diffusion in Al-Zn-Mg-Cu alloys, by providing detailed examination of the annihilation of vacancies and its specific influence on the growth rate of precipitates during and after deformation at various temperatures.

The final chapter, Chapter 8, presents the main conclusions that can be drawn from this thesis and provides possible directions for future work.

Bibliography

- [1] J. Ashby, The aluminium legacy: the history of the metal and its role in architecture, *Construction History* 15 (1999) 79.
- [2] J. W. Richards, Aluminium: its history, occurrence, properties, metallurgy and applications, including its alloys, HC Baird & Company, 1890.
- [3] G. Favero, P. Jobstraibizer, The distribution of aluminium in the earth: from cosmogenesis to sial evolution, *Coordination chemistry reviews* 149 (1996) 367–400.

- [4] J. Staley, History of wrought–aluminium–alloy development, *Aluminium Alloys: Contemporary Research and Applications*, *Treaties on Materials Science and Technology* 31 (2012) 3–31.
- [5] E. Hornbogen, Hundred years of precipitation hardening, *Journal of light metals* 1 (2) (2001) 127–132.
- [6] DuckerFrontier, Aluminium content in european passenger cars, https://www.european-aluminium.eu/media/2802/aluminum-content-in-european-cars_european-aluminium_public-summary_101019-1.pdf, accessed: 2021–11–14 (2019).
- [7] C. Springer, A. Hasanbeigi, Emerging energy efficiency and carbon dioxide emissions-reduction technologies for industrial production of aluminum (2016).
- [8] A. Jambor, M. Beyer, New cars—new materials, *Materials & design* 18 (4-6) (1997) 203–209.
- [9] R. A. Nolan, Microstructure Formability Relationships in New Generation High Strength Aluminium Automotive Alloys, The University of Manchester (United Kingdom), 2015.
- [10] I. Fridlyander, V. Sister, O. Grushko, V. Berstenev, L. Sheveleva, L. Ivanova, Aluminum alloys: promising materials in the automotive industry, *Metal science and heat treatment* 44 (9) (2002) 365–370.
- [11] J. Gould, Joining aluminum sheet in the automotive industry—a 30 year history, *Welding Journal* 91 (1) (2012) 23–34.
- [12] A. Luo, Recent advances in light metals and manufacturing for automotive applications, *CIM Journal* (2021) 1–9.
- [13] J. Hirsch, Recent development in aluminium for automotive applications, *Transactions of Nonferrous Metals Society of China* 24 (7) (2014) 1995–2002.
- [14] H. Sun, J. Wang, G. Shen, P. Hu, Application of warm forming aluminum alloy parts for automotive body based on impact, *International Journal of Automotive Technology* 14 (4) (2013) 605–610.

- [15] B. Shaffer, M. Auffhammer, C. Samaras, Make electric vehicles lighter to maximize climate and safety benefits, *Nature* 598 (7880) (2021) 254–256.
- [16] R. Long, E. Boettcher, D. Crawford, Current and future uses of aluminum in the automotive industry, *JOM* 69 (12) (2017) 2635–2639.
- [17] T. Grohmann, Forming of amag 7xxx series aluminium sheet alloys, *Proceedings of the New Developments in Sheet Metal Forming and New Developments in Hydroforming*, Fellbach, Germany (2016) 10–11.
- [18] E. Sáenz de Argandoña, L. Galdos, R. Ortubay, J. Mendiguren, X. Agirretxe, Room temperature forming of aa7075 aluminum alloys: W-temper process, in: *Key Engineering Materials*, Vol. 651, Trans Tech Publ, 2015, pp. 199–204.
- [19] W. Huo, L. Hou, Y. Zhang, J. Zhang, Warm formability and post-forming microstructure/property of high-strength AA 7075-T6 Al alloy, *Materials Science and Engineering: A* 675 (2016) 44–54.
- [20] W. Hui, Y.-b. LUO, P. Friedman, M.-h. CHEN, G. Lin, Warm forming behavior of high strength aluminum alloy AA7075, *Transactions of Nonferrous Metals Society of China* 22 (1) (2012) 1–7.
- [21] K. Zheng, Y. Dong, J.-H. Zheng, A. Foster, J. Lin, H. Dong, T. A. Dean, The effect of hot form quench (HFQ[®]) conditions on precipitation and mechanical properties of aluminium alloys, *Materials Science and Engineering: A* 761 (2019) 138017.
- [22] K. Zheng, Y. Dong, D. Zheng, J. Lin, T. A. Dean, An experimental investigation on the deformation and post-formed strength of heat-treatable aluminium alloys using different elevated temperature forming processes, *Journal of Materials Processing Technology* 268 (2019) 87–96.
- [23] S. Knight, N. Birbilis, B. Muddle, A. Trueman, S. Lynch, Correlations between intergranular stress corrosion cracking, grain-boundary microchemistry, and grain-boundary electrochemistry for Al–Zn–Mg–Cu alloys, *Corrosion Science* 52 (12) (2010) 4073–4080.

- [24] X. Sun, B. Zhang, H. Lin, Y. Zhou, L. Sun, J. Wang, E.-H. Han, W. Ke, Correlations between stress corrosion cracking susceptibility and grain boundary microstructures for an Al–Zn–Mg alloy, *Corrosion science* 77 (2013) 103–112.
- [25] A. Azarniya, A. K. Taheri, K. K. Taheri, Recent advances in ageing of 7xxx series aluminum alloys: a physical metallurgy perspective, *Journal of Alloys and Compounds* 781 (2019) 945–983.
- [26] J. A. Österreicher, G. Kirov, S. S. Gerstl, E. Mukeli, F. Grabner, M. Kumar, Stabilization of 7xxx aluminium alloys, *Journal of alloys and compounds* 740 (2018) 167–173.
- [27] J. A. Österreicher, M. A. Tunes, F. Grabner, A. Arnoldt, T. Kremmer, S. Pogatscher, C. M. Schlögl, Warm-forming of pre-aged Al–Zn–Mg–Cu alloy sheet, *Materials & Design* 193 (2020) 108837.
- [28] P. A. Schuster, J. A. Österreicher, G. Kirov, C. Sommitsch, O. Kessler, E. Mukeli, Characterisation and comparison of process chains for producing automotive structural parts from 7xxx aluminium sheets, *Metals* 9 (3) (2019) 305.
- [29] M. Kumar, N. Ross, Influence of temper on the performance of a high-strength Al–Zn–Mg alloy sheet in the warm forming processing chain, *Journal of materials processing technology* 231 (2016) 189–198.
- [30] Y.-S. Lee, D.-H. Koh, H.-W. Kim, Y.-S. Ahn, Improved bake-hardening response of Al–Zn–Mg–Cu alloy through pre-aging treatment, *Scripta Materialia* 147 (2018) 45–49.
- [31] J. Nie, Physical Metallurgy of Light Alloys, in: D. E. Laughlin, K. Hono (Eds.), *Physical Metallurgy*, 5th Edition, Elsevier, Oxford, 2014, pp. 2009–2156.
- [32] A. Deschamps, Y. Brechet, P. Guyot, E. Livet, On the influence of dislocations on precipitation in an al-zn-mg alloy, *Stal* 1 (1) (1997) 1–1.
- [33] A. Deschamps, F. Livet, Y. Brechet, Influence of predeformation on ageing in an al-zn-mg alloy—i. microstructure evolution and mechanical properties, *Acta materialia* 47 (1) (1998) 281–292.

- [34] A. Deschamps, G. Fribourg, Y. Brechet, J. L. Chemin, C. Hutchinson, In situ evaluation of dynamic precipitation during plastic straining of an al–zn–mg–cu alloy, *Acta materialia* 60 (5) (2012) 1905–1916.
- [35] L. Couturier, A. Deschamps, F. De Geuser, F. Fazeli, W. Poole, An investigation of the strain dependence of dynamic precipitation in an al–zn–mg–cu alloy, *Scripta Materialia* 136 (2017) 120–123.
- [36] W. Mirihanage, J. Robson, S. Mishra, P. Hidalgo-Manrique, J. Q. da Fonseca, C. Daniel, P. Prangnell, S. Michalik, O. Magdysyuk, T. Connolley, et al., Direct observation of the dynamic evolution of precipitates in aluminium alloy 7021 at high strain rates via high energy synchrotron x-rays, *Acta Materialia* 205 (2021) 116532.
- [37] J. Robson, P. Jessner, M. Taylor, Z. Ma, Dynamic precipitation in supersaturated al–zn–mg–cu alloy during warm stretching, *Metallurgical and Materials Transactions* (2023) 1–11.
- [38] C. Hutchinson, F. De Geuser, Y. Chen, A. Deschamps, Quantitative measurements of dynamic precipitation during fatigue of an al–zn–mg–(cu) alloy using small-angle x-ray scattering, *Acta materialia* 74 (2014) 96–109.
- [39] W. Sun, Y. Zhu, R. Marceau, L. Wang, Q. Zhang, X. Gao, C. Hutchinson, Precipitation strengthening of aluminum alloys by room-temperature cyclic plasticity, *Science* 363 (6430) (2019) 972–975.

Chapter 2

Literature Review

2.1 Aluminium Alloys in Automotive Industry

The use of aluminium in the automotive industry, as shown in Figure 2.1, dates back to the early 20th century [1, 2, 3]. Since then, driven by the increasing demands for weight reduction, aluminium, along with other lightweight materials, has been designed and developed to replace traditional steel and cast iron, as shown in Table 2.1 [1, 4].

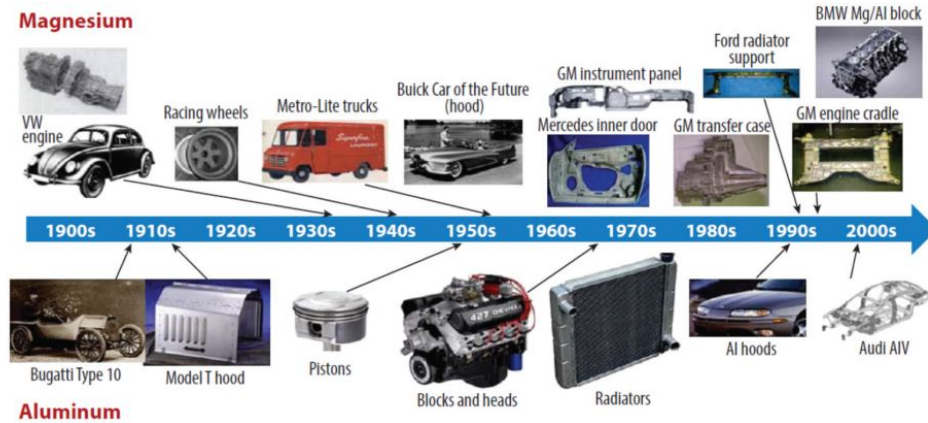


Figure 2.1: The timeline of the application of Magnesium and Aluminium in automobile industry [3, 1]

Table 2.1: Weight reduction potentials by material substitution [1, 4]

Lightweight material	Material replaced	Mass reduction (%)	Relative cost per part
Magnesium	Steel, cast iron	60~70	1.5~2.5
Aluminium	Steel, cast iron	40~60	1.3~2
Titanium	Steel	40~55	1.5~10+
Aluminium metal composites	Steel, cast iron	40~60	1.5~3+
Carbon fibre composites	Steel	50~60	2~10+
Glass fibre composites	Steel	25~35	1~1.5
Advanced high strength steel	Mild steel	15~25	1~1.5

Traditionally, components with complex shapes, such as engine blocks and chassis parts, have been made by casting, which is still the predominant forming process, contributing to more than 50% of the aluminium content in European vehicles [5]. However, extrusions and sheets are expected to gain market share from the casting process. As shown in Figure 2.2, with the increasing popularity of electric vehicles, battery boxes and body closures are expected to account for most of the growth in aluminium content [5]. It should be noted that in this thesis, studies were conducted only on sheets made from aluminium alloys.

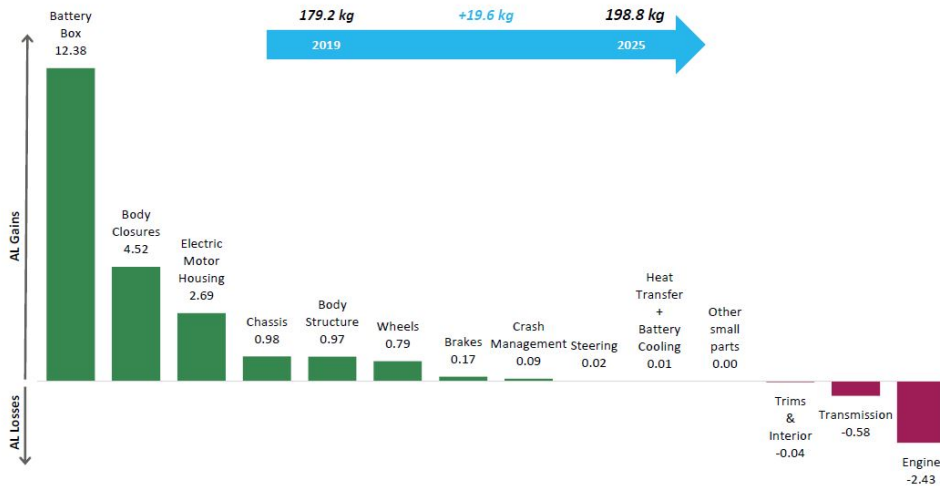


Figure 2.2: Predicted aluminium gains and losses (kg) by component group [5]

The first application of aluminium sheets in automotive panels was the 2xxx series (Al-Cu) in the EU and USA [6]. Due to their poor corrosion resistance and paint bake response [7], they were soon replaced by the 6xxx (Al-Mg-Si) and 5xxx (Al-Mg) series, which exhibit a good compromise between formability, strength, and corrosion resistance [6]. However, higher strengths are becoming increasingly important to facilitate the need for weight reduction. The implementation of 7xxx (Al-Zn-Mg) aluminium alloys is not only attractive but imperative.

2.2 7xxx Aluminium Alloys

Soon after the discovery of precipitation strengthening in an Al-Cu system, Zn and Mg were also found to have a high solubility in the aluminium matrix, which could potentially provide the highest strength among all aluminium alloys [8]. Although

early studies were conducted on the Al-Zn-Mg ternary system, the first well-known 7xxx aluminium alloy was based on the Al-Zn-Mg-Cu system. X74S (5.2% Zn, 2.1% Mg, 1.5% Cu, and 0.4% Mn) originally made for the aerospace application showed very high susceptibility to stress corrosion cracking (SCC)[8, 9]. This problem was then attenuated by a small addition of Cr (0.2–0.35%). With a further modification of the Zn, Mg and Cu content, 7075 was developed in 1943 and soon applied on the B-29 Super Fortress bomber [8, 9]. In the 1960s, Cu-free 7xxx aluminium alloys (Al-Zn-Mg) were developed and showed improved weldability and SCC resistance but with a modest sacrifice on the strength [8, 9].

2.2.1 Role of Elements

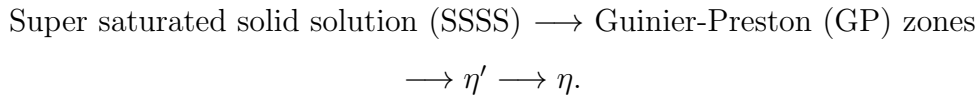
- Zn and Mg are the main elements to form precipitates during ageing to provide high strength. A high Zn content and Zn/Mg ratio were used in designing ultra-high strength 7xxx aluminium alloys but may suffer from high quench sensitivity (e.g.7055). By reducing the Mg content while maintaining a high Zn/Mg ratio, high strength and low quench sensitivity can be achieved (e.g.7085)[10, 11].
- Early research found Cu elements improved the final strength. With the help of modern technologies such as atom probe tomography and transmission electron microscopy, it has been revealed Cu has an effect on joining the early-stage precipitation of GP zones [12]. In the peak-aged condition, Cu atoms tend to dissolve into the η' phase by substituting Zn, Mg and Al atoms [13, 14]. Cu enrichment on the broad face of η' and η precipitates has also been reported in an over-aged condition [15]. High content of Cu may lead to high quenching sensitivity in Al-Zn-Mg-Cu systems [16].
- Apart from Zn, Mg and Cu, there are also other minor alloying elements in 7xxx alloys affecting the microstructure. A small amount of Ti or TiB₂ was added as the grain refiner during casting [17]. Mn, Zr and Sc may have effects on controlling the grain structure and recrystallisation behaviour by forming dispersoids (Al₃Zr, Al₃Sc and Al₂₀Cu₂Mn₃) pinning the grain boundaries [18, 19, 20]. Cr may also be useful in improving the corrosion resistance but could

result in high quench sensitivity [21]. In some cases, Ag is added in 7xxx alloys. It is reported a small amount of Ag can stimulate the formation of fine η' , which may be related to the high affinity of Ag to vacancies in aluminium alloys [22, 23, 24].

- Si and Fe are considered impurities. Due to their low solubility, insoluble constituents can be formed by consuming other elements. In 7xxx alloys, Al_3Fe , $\text{Al}_7\text{Cu}_2\text{Fe}$, Mg_2Si , $\text{Al}_6\text{Fe}_x\text{Mn}_{1-x}$, $\text{Al}_{12}\text{Fe}_x\text{Mn}_{1-x}$ Si can be commonly found in the microstructure [25, 26]. Since they could result in poor mechanical properties and corrosion resistance, it is expected to minimise their content in designing 7xxx alloys.

2.2.2 Decomposition Processes

7xxx aluminium alloys obtain their high strength mainly by forming nano-size precipitates in the matrix during heat treatments. In the absence of deformation, a simple precipitation path can be summarised as [27] :



It is also worthy of being mentioned that in real cases multiple metastable phases could be found at a given time evolving towards their stable state [28]. Consequently, the precipitation sequence can be more complicated than the one shown above.

2.2.3 Guinier-Preston (GP) Zones

Near room temperature, the formation of metastable precipitates is favoured kinetically. In 7xxx aluminium alloys, the formation of GP zones facilitates the decomposition of supersaturated solid solution. It is generally discussed two types of GP zone can be found in 7xxx aluminium alloys. GP I zone has coherent layers of Zn and Mg/Al atoms on $\{1\ 0\ 0\}$ planes with spherical structures [29, 30]. They can form from room temperature to around 140°C [31]. Unlike GP I zone, GP II zones are observed after quenching from 450°C and then ageing above 70°C [31]. Using HRTEM, the crystal structure of GP II zones is observed to be a thin disc of a few

atomic layers on $\{1\ 1\ 1\}$ planes [31]. Figure 2.3 shows an HRTEM micrograph of GPII zones in an Al-Zn-Mg alloy [31].

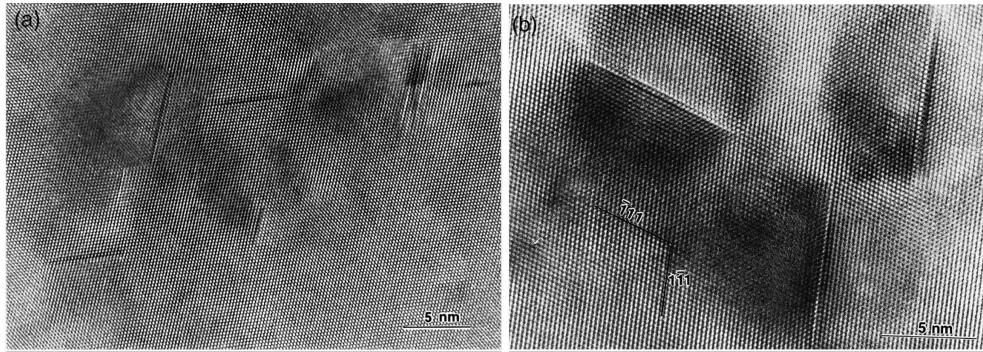


Figure 2.3: HRTEM micrograph of GPII zones in a Al-Zn-Mg alloy [31] (Copyright obtained from Elsevier)

Early studies in Al-Zn-Mg systems show the formation of GP zones is related to the interaction between solutes and vacancies (quenched-in vacancies and solute-vacancy pairs) [27]. It is discussed quenched-in free vacancies are less important to the formation of GP zones at room temperature since most of them are bounded with Mg atoms [27]. Furthermore, it is still subject to debate whether the nuclei of GP zones are Zn-rich or Mg-rich clusters. Recent studies using APT indicate Mg-rich clusters were quickly formed during or after the quenching [12, 32]. The formation kinetics is controlled by the motion of Mg atoms[27]. This agrees with previous studies showing the activation energy of the formation of GP zones is close to the magnesium migration energy (0.6eV) [33, 34].

Likely due to their extremely small size, it is difficult to accurately measure the composition of GP zones. In the early studies of GP zones in Al-Zn-Mg systems, Schmalzried and Gerold proposed a Zn/Mg ratio of 1:1 [35]. Later experimental studies found the ratio may vary from 0.5 to 1.9, depending on the Zn/Mg ratio of the alloy and also the temperature that GP zones formed at [30, 36]. In cases where the Zn/Mg ratio of the alloys is between 0.5 to 2, Groma et al. using small angle X-ray scattering (SAXS) show the Zn content in GP zones is around 40 at% at room temperature [37]. However, large uncertainties remain. Firstly, SAXS is only sensitive to Zn atoms due to their high electron density contrast to the Al matrix. Secondly, an accurate calculation from SAXS data requires reliable atomic volumes of GP zones, which is not readily available. Studies using ATP investigating the

composition of GP zones have found Zn/Mg ratio lower than 1 at the early clustering stage (Mg-rich clusters). With the growth of them, the clusters gradually become Zn-rich (Zn/Mg >1), which is likely due to the faster diffusion rate of Zn than Mg [32, 38].

2.2.4 η' Phase

Another important metastable phase in 7xxx alloys is η' , which is generally accepted to be responsible for the high strength. Although numerous studies have been reported on studying this metastable phase, until now, the crystal structure and chemical stoichiometry are still controversial. It is generally agreed η' precipitates are plate-shape on $\{1\ 1\ 1\}$ plane. The first discovery of η' can be tract back to 1956 by Graf et al. who also subsequently proposed the hexagonal structure with $a=0.496$ nm and $c=1.403$ nm. This has been supported by later studies [39, 40, 41, 42]. Auld and Cousland in 1974 found the crystal orientation of η' as following [43]:

$$(0001)_{\eta'_1} || (1\bar{1}1)_{Al}; [10\bar{1}0]_{\eta'_1} || [110]_{Al}$$

Wolverton in 2001 using the first principle total energy calculation elucidated the feasibility of this crystal orientation having the lowest energy among different models [44].

TEM observation of η' further reveals additional three variants. A schematic of four η' variants and their crystal orientation relationships to the aluminium matrix are shown in figure 2.4 [45].

$$(0001)_{\eta'_2} || (1\bar{1}\bar{1})_{Al}; [10\bar{1}0]_{\eta'_2} || [110]_{Al}$$

$$(0001)_{\eta'_3} || (111)_{Al}; [10\bar{1}0]_{\eta'_3} || [\bar{1}10]_{Al}$$

$$(0001)_{\eta'_4} || (11\bar{1})_{Al}; [10\bar{1}0]_{\eta'_4} || [\bar{1}10]_{Al}$$

Many attempts were made towards finding the chemical stoichiometry of η' . In the early stage of the study, Auld and Cousland (1974) proposed $Mg_4Zn_{11}Al$ [43]. This was opposed by Li et al. (1999) [42] using HRTEM suggesting the structure model of $Mg_2Zn_{5-x}Al_{2+x}$. This was further supported by the atom probe analysis

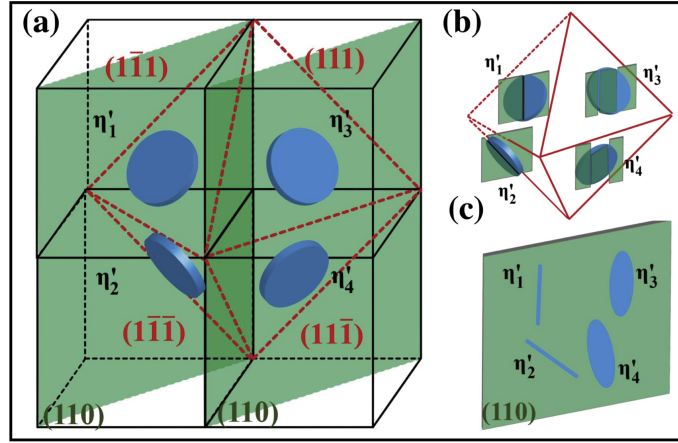


Figure 2.4: The schematic of four η' variants and their crystal orientation relationship to the aluminium matrix [45] (Copyright obtained from Elsevier)

from Engdahl et al (2002) [46]. Nevertheless, these studies were based on the Al-Zn-Mg system with the consideration of aluminium atoms substituting zinc atoms. Indeed, Cu atoms can also substitute Zn. In Al-Zn-Mg-Cu systems, Brenner et al. (1992) [13] successfully found Cu contained η' precipitates using atom probe analysis. Hence, they proposed the formula of $\text{Mg}(\text{AlZnCu})_2$. The segregation of Cu atoms on the broad faces of η' was also found by Cassell et al. (2020) using HAADF-STEM [15]. In terms of the Zn/Mg ratio, the majority of studies reported a value between 0.7 to 1.5 [13, 47, 48, 49]. The largest theoretical value of 2.5 proposed by Li et al. (1999) [42] was based on their structure model, which was opposed by Wolverton (2001) [44].

The formation of η' is also subject to further investigation. Different mechanisms may be applied depending on the composition and the thermomechanical process. In general, the discussion can be classified as either direct nucleation from the matrix or transformation from the pre-existing metastable precipitates (such as GP zones).

- Small GP zones formed during the pre-ageing process can be expected to act as the nuclei of η' . One advantage of this mechanism is the absence of new nucleation of the η' phase. Therefore, the kinetics of this transformation is mainly considered towards the change of composition facilitated by the diffusion of solutes. In 7xxx aluminium alloys, GP II zone is most likely to follow this mechanism due to its similar crystal orientation to η' . Experiments supporting this mechanism include the design of two-steps ageing when the reversion of GP zones, consequently strength, was not observed in the second

step of ageing. Instead, a much faster hardening response in the following ageing process supports the theory of direct transformation of GP zones to η' [50, 51, 52].

- η' precipitates directly nucleate from the matrix is kinetically unfavoured at room temperature [27]. The formation of GP zones has been found quickly during or soon after the quenching [53]. In this mechanism, any pre-existing metastable precipitates reduce the solute content in the matrix, which could result in the nucleation of η' being more difficult. Therefore, experiments support this mechanism showing the reduction of mechanical strength at the early stage of ageing, which indicates the reversion of GP zones releasing the solutes back into the matrix [27, 54, 55, 56].

2.2.5 Other Metastable Phases

Depending on the composition and the precipitation temperature, other metastable phases may exist in the system.

At ageing temperatures similar to η' , Liu et al. (2010) observed another metastable strengthening phase denoted as η^p [57]. Using HRTEM, the crystal structure was identified to be hexagonal with the lattice parameter $a=0.496$ nm and $c=0.935$ nm [57]. Accordingly, they proposed the precipitation sequence of $\text{SSSS} \rightarrow \text{GP}_{\eta^p} \rightarrow \eta^p \rightarrow \eta$, coexisting with the sequence of $\text{SSSS} \rightarrow \text{GP}_{\eta'} \rightarrow \eta' \rightarrow \eta$ [58, 59]. To date, η^p was only found in alloys with a high (Zn+Cu)/Mg ratio such as 7010, 7150 and 7055 [57, 58, 59].

Metastable semi-coherent S' phase is the precursor of the equilibrium incoherent S phase. They are predominately found as the strengthening phases in 2xxx aluminium alloys (Al-Cu-Mg) [60, 61]. In some studies, the difference between S' and S phases are not distinguished, since it is argued the difference is only about the coherency of the interface and the orientation with the aluminium matrix [62, 63, 64]. In Al-Zn-Mg-Cu systems with relatively high Cu content (7010, 7050 and 7175), it is reported lath-shaped S' phase (Al_2CuMg) with an orthorhombic structure can form within grains during cooling from homogenization and/or solution heat treatment temperatures [65, 66, 67, 68]. Since they are not the main hardening phases in 7xxx aluminium alloys, forming relatively large precipitates during cooling consumes the

available solutes, which is detrimental to the subsequent age-hardening response.

In some Al-Zn-Mg-Cu systems, T' phase may be formed during ageing treatments, which can subsequently transform to the equilibrium T phase. It is reported that T' has a body-centred cubic structure with $a=1.435$ nm [69]. The crystal orientation is given by $(100)_{T'} || (111)_{Al}; (010)_{T'} || (11\bar{2})_{Al}$ [70]. The strengthening effect of T' is found to be less than η' phases [69]. Only in alloys with low Zn/Mg ratio, T' and T may be considered as the strengthening phases [71].

2.2.6 Equilibrium Phases

In 7xxx aluminium alloys, depending on the composition and temperature, η , T and S phases can often be found in the microstructure, which all have an incoherent interface with the aluminium matrix [27, 72]. Since the high strength is considered to be provided by the metastable η' , the presence of equilibrium phases coincides with the over-ageing stage when the strength is lower than the maximum achievable.

Table 2.2: Crystallographic orientations of η in Al-Zn-Mg-(Cu) systems [27, 73, 74]

Variants	Orientation relationships
η_1	$(0001)_\eta (110)_{Al}; [\bar{1}0\bar{1}0]_\eta [001]_{Al}$
η_2	$(0001)_\eta (1\bar{1}\bar{1})_{Al}; [\bar{1}0\bar{1}0]_\eta [110]_{Al}$
η_3	$(0001)_\eta (1\bar{1}\bar{1})_{Al}; [11\bar{2}0]_\eta [110]_{Al}$
η_4	$(0001)_\eta (110)_{Al}; [\bar{1}2\bar{1}0]_\eta [1\bar{1}\bar{1}]_{Al}$
η_5	$(30\bar{3}2)_\eta (110)_{Al}; [\bar{1}2\bar{1}0]_\eta [1\bar{1}\bar{1}]_{Al}$
η_6	$(20\bar{2}1)_\eta (1\bar{1}2)_{Al}; [\bar{1}2\bar{1}0]_\eta [1\bar{1}\bar{1}]_{Al}$
η_7	$(10\bar{1}4)_\eta (110)_{Al}; [\bar{1}2\bar{1}0]_\eta [1\bar{1}\bar{1}]_{Al}$
η_8	$(0001)_\eta (31\bar{1})_{Al}; [\bar{1}2\bar{1}0]_\eta [1\bar{1}2]_{Al}$
η_9	$(0001)_\eta (110)_{Al}; [\bar{1}2\bar{1}0]_\eta [001]_{Al}$
η_{10}	$(0001)_\eta (1\bar{1}\bar{1})_{Al}; [11\bar{2}0]_\eta [1\bar{3}4]_{Al}$
η_{11}	$(0001)_\eta (110)_{Al}; [\bar{1}0\bar{1}0]_\eta [1\bar{1}\bar{1}]_{Al}$

η phase is seen in most 7xxx alloys, which is well studied having the theoretical chemical composition of $MgZn_2$ and a hexagonal crystal structure ($a=0.523$ nm $c=0.857$ nm) [73]. Since practically Al and Cu can substitute Zn, $Mg(ZnAlCu)_2$ is recognised as the more accurate formula. Up to date, there are 11 different crystallographic orientations observed for η phases, which are summarised in the table 2.2. The shape of the η phase depends on its crystallographic orientation. In general, they are observed as plates, rods or laths [27, 74]. Figure 2.5 shows a TEM micrograph of η phases in an AA7050 sample [45].

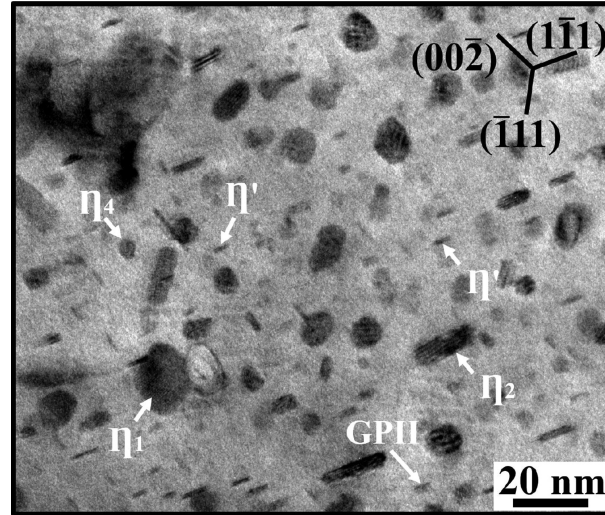


Figure 2.5: TEM micrograph shows precipitates in a AA7050 sample [45] (Copyright obtained from Elsevier)

2.3 Ageing Strategy

The decomposition process in Al-Zn-Mg-Cu systems is facilitated by multi-step heat treatments. The first step is the solution heat treatment during which pre-existing precipitates are dissolved and solute atoms are redistributed. This process is typically performed at temperatures between 450°C to 510°C followed by rapid quenching to suppress solute diffusion and precipitation [75]. A successful solute heat treatment should maintain the alloy in the state of the super-saturated solid solution. The final stage is the ageing process during which 7xxx aluminium alloys obtain most of the strength by forming strengthening phase precipitates in the matrix. Depending on the temperature, an ageing practice can be classified into either natural ageing which occurs at room temperature or artificial ageing which is performed in a heating environment.

Designing proper ageing practices is important in controlling the microstructure and material's properties. This review is only focused on artificial ageing treatments.

2.3.1 One Step Ageing

Single-step ageing is the practice of performing the ageing treatment isothermally at a constant temperature. The whole decomposition process is expected to take place at this temperature. The most widely adopted single-step ageing is the peak ageing

treatment (T6). For AA7075, this is performed at 120°C for 24 hours. During this process, the formation of GP zones, the transformation and growth of η' from GP zones and the direct nucleation and growth of η' can all simultaneously occur in the matrix. The final microstructure is usually observed with uniform distributed precipitates dominated by the η' phase [76]. Although single-step T6 treatment enables high strength of 7xxx aluminium alloys, studies have demonstrated T6 alloys are susceptible to the stress corrosion cracking (SCC). The mechanism of SCC in the Al-Zn-Mg-Cu system is a complex topic which is beyond the scope of this review. In general, the SCC behaviour is affected by both chemical composition (Cu content, Zn/Mg ratio) and temper condition (precipitation distribution) [77].

2.3.2 Two Steps Ageing

Conventional T7X practices are designed in two steps for Cu contained 7xxx aluminium alloys, aiming at attenuating the susceptibility to stress corrosion cracking in saline environments. Typical ageing conditions for the AA7075 sheet (or plate) are summarised in table 2.3.

Table 2.3: Conventional ageing conditions for AA7075 [26, 78]

Designation	Ageing practice
T6	120°C 24 hours
T76	107°C 4 hours + 163°C 16 hours
T73	107°C 7 hours + 163°C 27 hours

In the microstructure of T7X treated samples, small continuous precipitates on the grain boundaries are replaced by coarsened discontinuous precipitates. The small strengthening η' precipitates in the matrix are also transformed into coarsened η precipitates. Therefore, although T7X treatments increase the corrosion resistance by suppressing the anodic dissolution channels and reducing the potential difference between grain boundaries and the matrix, such benefits are at the expense of 10% \sim 15% of the T6 strength. [26, 79].

Another research direction of designing two-step ageing is to save the total ageing time. From table 2.3, it is clear that precipitation in the Al-Zn-Mg-Cu system is a slow process, which is due to the slow diffusion of solute atoms. Although the diffusion rate can be significantly accelerated by increasing the temperature, the

direct formation of η phase and the coarsening effect of η' phase coincide with the over-ageing regime. The sacrifice of strength is undesirable. Two-step ageing treatments are designed based on the idea of using low temperatures to promote the nucleation of GP zones and fine η' precipitates followed by using relatively high temperatures to promote the growth of them [80]. Li et al. (2008) reported $\sim 500\text{MPa}$ 0.2% proof stress after ageing 7 hours at 115°C and 3 hours at 160°C in a Al-Zn-Mg-Cu alloy [51]. Osterreicher et al. (2018) reported $\sim 510\text{MPa}$ 0.2% proof stress after ageing 2 hours at 120°C and 20 minutes at 185°C for AA7075[51]. Similar strategies have also been studied in Al-Zn-Mg-Zr systems [80, 81].

2.3.3 Retrogression and Re-ageing

Most of the two-steps ageing treatments can not provide simultaneously high strength and sufficient resistance to the stress corrosion cracking. Retrogression and re-ageing (RRA) is designed for Al-Zn-Mg-Cu alloys to tackle this problem. Typically, RRA consists of three stages. Alloys are first pre-aged at a low temperature for hours, which promotes the precipitation of fine GP zones and η' precipitates. Alloys are then subjected to a retrogression treatment at a high temperature for minutes, during which pre-existing GP zones and η' precipitates are partially dissolved releasing solutes back to the matrix. A low temperature re-ageing treatment is then applied for hours to form new small GP zones and η' precipitates. Those precipitates not dissolved during the retrogression treatment can keep growing to larger size or even transform to coarsened η precipitates. A schematic of RRA treatments for AA7075 is shown in figure 2.6[82].

A considerable amount of work has been done on tailoring the RRA practice and investigating its effect on the final microstructure [83, 84, 85, 86, 87]. In terms of the mechanical properties, adopting appropriate RRA time, temperature and heating rate can enable T6 strength. TEM studies of the microstructure of RRA-treated Al-Zn-Mg-Cu alloys suggest that the strengthening precipitates in the matrix have size and distribution similar to the T6 temper [84]. Marlaud et al. (2010) studied the precipitates in peak-aged and RRA-treated Al-Zn-Mg-Cu alloys using SAXS and APT [85]. They found in the RRA-treated sample precipitates are richer in Cu. Apart from the strengthening precipitates with the size smaller than 3nm, they

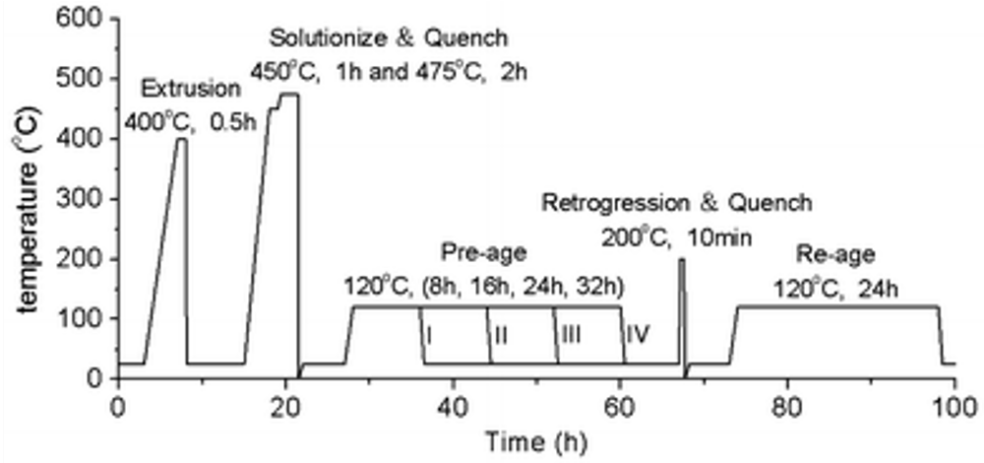


Figure 2.6: A schematic of RRA treatments for AA7075 [82] (Copyright obtained from Springer Nature)

also observed a dense distribution of small clusters in RRA samples. In terms of the SCC resistance, it has been reported RRA treatments can result in T7X behaviour [84, 86]. This is mainly rationalised by the discontinuous distribution of coarsened η precipitates with higher Cu content on the grain boundaries, which suppress the galvanic reaction and reduce the potential difference between the grain boundaries and the matrix [88]. Despite the attractive properties of RRA-treated alloys, the industrial application of this practice on alloys with large dimensions is still limited by the short time of retrogression treatment [89].

2.4 Precipitation Strengthening

An uniform distribution of nano-sized precipitates in the aluminium matrix restricts the movement of dislocations during plastic deformation, which consequently strengthen the material. In Al-Zn-Mg-Cu alloys, it has been well-studied that the ultra-high strength is mainly provided by η' precipitates with size less than 5nm and number density in the range of 10^{24} m^{-3} [90]. The strengthening mechanism depends on the nature of the precipitate and how it interacts with the dislocation. In this section, we will first review the concept of two basic mechanisms (precipitate shearing and bypassing), then the strengthening models commonly used for spherical precipitates.

2.4.1 Strengthening Mechanism

When a moving dislocation is stopped by precipitates, it will bow out under the applied stress until the pinning precipitate can not sustain the stress. The maximum force that a precipitate can sustain (F_m), which is estimated from the dislocation line tension (Γ), is used to calculate the critical shear stress (τ_{css}). In a polycrystalline system, the macroscopic stress increment due to the precipitation strengthening can be calculated using equation 2.1 where M is the orientation factor (3.06 for f.c.c) and L is the effective precipitate spacing.

$$\sigma_p = M\tau_{css} = \frac{MF_m}{bL} \quad (2.1)$$

L and F_m have different expressions depending on the strengthening mechanism, which yields different equations to estimate the precipitation strengthening.

Shearing Small and weak precipitates can be sheared by moving dislocations. In this mechanism, the precipitate strength (F_m) is mainly controlled by creating atomic mismatches within the precipitate, an extra particle-matrix interface and an elastic modulus mismatch.

Studies have found the elastic strain field around small coherent precipitates has a stronger strengthening effect than the precipitates themselves [91]. This term is referred as coherency strain hardening. In 7xxx aluminium alloys, equation 2.2 has been used to calculate the coherency strain hardening effect, where α_ϵ is a constant taken as 2.6 for f.c.c, b is the Burgers vector, ϵ_c is the constrained misfit strain, G is the shear modulus of aluminium, R and V_f are the mean radius and volume fraction of precipitates [92, 93].

$$\sigma_{cs} = M\alpha_\epsilon G\epsilon_c^{3/2} \left(\frac{RV_f}{0.5b} \right)^{1/2} \quad (2.2)$$

The modulus mismatch between the precipitate and the matrix will also strengthen the material. Equation 2.3 has been used in aluminium alloys to calculate this contribution where ΔG is the modulus difference between precipitate and matrix, m is a characteristic constant close to 0.85 [92, 93, 94].

$$\sigma_{ms} = M0.0055(\Delta G)^{3/2} \left(\frac{2V_f}{G}\right)^{1/2} \left(\frac{r}{b}\right)^{\frac{3m}{2}-1} \quad (2.3)$$

Once dislocations pass through precipitates, atomic mismatches may be created in the form of antiphase boundaries opposing the movement of the next dislocation. This is usually referred to as chemical hardening or order hardening. Ardell derives the following equation to estimate the strength increment, where γ_{APB} is the antiphase boundary energy [95].

$$\sigma_{os} = M0.81 \frac{\gamma_{APB}}{2b} \left(\frac{3\pi V_f}{G}\right)^{1/2} \quad (2.4)$$

For a given situation of mean radius R and volume fraction V_f , the highest of $\sigma_{cs} + \sigma_{ms}$ or σ_{os} is taken as the effective strengthening component from the shearing mechanism.

Bypassing Once a dislocation line is stopped by large and strong precipitates that are not shearable, the dislocation line continues to bow out until it encloses itself again. A dislocation ring is left around the bypassed precipitate. Many equations can be found in the literature to estimate the strength of Orowan bypassing. They usually follow the general form:

$$\tau_{orowan} \propto \frac{Gb}{\lambda} \quad (2.5)$$

Under the assumption of finite precipitate size, the inter-particle spacing in the slip plane (λ) can be calculated from the number of precipitates per unit area ($\frac{V_f}{2/3\pi R^2}$).

$$\lambda = \frac{1}{\sqrt{N_s}} = \left(\frac{2\pi}{3V_f}\right)^{1/2} R \quad (2.6)$$

Combining equation 2.5 and 2.6 yields the Orowan stress being proportional to $\frac{V_f^{1/2}}{R}$. Bacon et al. further developed this by considering the effect of dislocation self-interaction, which gives the Orowan stress in the basic form as equation 2.7, where A is $1/2\pi$ for edge dislocations or $1/2\pi(1 - \nu)$ for screw dislocations, B is a constant, D is the precipitate diameter [96]. As an example, equation 2.9 may be used to estimate the stress increment from the bypassing mechanism in 7xxx

aluminium alloys [92, 93]. The inter-precipitate spacing λ_p is slightly modified from equation 2.6, which reflects that the assumption of finite precipitate size may be invalid in the late stage of precipitation (with a relatively high volume fraction).

$$\tau_{orowan} = \frac{GbA}{\lambda} [\ln(D) + B] \quad (2.7)$$

$$\sigma_{orowan} = M \frac{0.4}{\pi} \frac{Gb}{\sqrt{1-\nu}} \frac{\ln(\frac{\sqrt{2/3}R}{b})}{\lambda_p} \quad (2.8)$$

$$\lambda_p = \left(\left(\frac{2\pi}{3V_f} \right)^{1/2} - \sqrt{\frac{8}{3}} \right) R \quad (2.9)$$

2.4.2 Strengthening Model

There are many precipitation strengthening models available in the literature. A complete review of them is beyond the scope of this thesis. We will only provide a basic review of a few influential models based on Friedel statistics and Kocks statistics [97].

Friedel statistics, which has been proved to be suitable for shearable precipitate, gives equation 2.10 describing the relation between L and λ [95, 98].

$$\lambda = L \left(\frac{F_m}{2\Gamma} \right)^{1/2} \quad (2.10)$$

Combining equation 2.10 and 2.6, the effective precipitate spacing under Friedel statistics is given by 2.12.

$$L \left(\frac{F_m}{2\Gamma} \right)^{1/2} = \left(\frac{2\pi}{3V_f} \right)^{1/2} R \quad (2.11)$$

$$L = \left(\frac{4\pi\Gamma R^2}{3V_f F_m} \right)^{1/2} \quad (2.12)$$

The maximum force that a precipitate can sustain (F_m) depends on the precipitate radius [98]. Considering a size distribution function $f(R)$, the average precipitate strength can be estimated using equation 2.13.

$$\overline{F_m} = \int_0^\infty F_m(R)f(R)dR \quad (2.13)$$

Finally, substituting equation 2.12 and 2.13 into the general precipitation strengthening equation 2.1, the precipitation strengthening under Friedel statistics can be obtained (equation 2.14) [98].

$$\sigma_p^F = \frac{M}{Rb} \sqrt{\frac{3V_f}{4\pi\Gamma}} \left[\int_0^\infty F_m(R)f(R)dR \right]^{3/2} \quad (2.14)$$

As introduced in the previous section, different mechanism yields different expression to calculate the precipitate strength F . Indeed, all equations in the previous section of the shearing mechanism are based on the Friedel statistic[95]. However, it is clear that using those equations (2.2, 2.3 and 2.4) requires a good understanding of physical parameters such as misfit strain ϵ , modulus difference between precipitates and matrix ΔG and antiphase boundary energy γ_{APB} . These parameters are not readily available for complex alloy systems. Particularly, in 7xxx aluminium alloys, many precipitate phases can co-exist in the matrix, which adds extra difficulties to use these parameters to estimate the stress increment from the shearing mechanism.

$$F(R) = kGbR \quad (2.15)$$

Gerold proposed a general expression (equation 2.15) using an adjustable parameter k to estimate F without going deep into the mechanisms involved [99]. The applicability of this simple formula in 7xxx aluminium alloys has been demonstrated by Deschamps and Brechet [98]. Under the circumstance that all precipitates are shearable and the assumption that dislocation line tension is constant as βGb^2 ($\beta \sim 0.5$), combining equation 2.14 and 2.15 yields equation 2.16 to estimate the precipitation contribution to the macroscopic stress [98].

$$\sigma_p^F = \sqrt{\frac{3}{4\pi\beta}} \frac{k^{3/2}MG}{\sqrt{b}} (V_f R)^{1/2} \quad (2.16)$$

For non-shearable precipitates, Kocks statistics which is based on the numerical simulation of dislocation gliding through a set of precipitates is the alternative approach to model the precipitation strengthening [95, 98, 97]. Deschamps and Brechet

proposed equation 2.17 to estimate the effective precipitate spacing [98]. Further assuming the average precipitate strength is equal to 2Γ , the strength contribution can be calculated using equation 2.18 [98]. It is clear this model underlines that the effective precipitate spacing (L) is 15% larger than the inter-particle spacing (λ) derived under the finite precipitate size assumption. Although this 15% adjustment is valid in their case, the applicability under other ageing conditions requires further evaluation.

$$L_{bp} = 1.15 \sqrt{\frac{2\pi}{3V_f}} R \quad (2.17)$$

$$\sigma_p^K = \frac{M}{1.15bR} \sqrt{\frac{3V_f}{2\pi}} \int_0^\infty F_m(R) f(R) dR \quad (2.18)$$

$$\sigma_p^{KV} = 0.9MGb\sqrt{N_s} \cos\left(\frac{\phi}{2}\right)^{3/2} \left(1 - \frac{1}{6} \cos\left(\frac{\phi}{2}\right)^5\right) \quad (2.19)$$

Another recent attempt of using Kocks statistics to model the strength contribution from non-shearable precipitates was made by Vaucorbeil et al [100]. They proposed equation 2.19, which is purely empirical, using the breaking angle ϕ . Although this equation has been successfully applied in some 6xxx systems [100, 97], the applicability in 7xxx systems requires further investigation.

2.5 Deformation-Precipitation Interaction

The interactions between deformation and precipitation can affect the precipitation behaviour in different ways [98, 101, 102, 103], depending on the sequence of ageing and deformation. In the simple situation of precipitation without any deformation, relatively homogeneous precipitation of GP zones may be observed in the matrix. Consequently, the common proposed precipitation sequence from GP zones to η' phase and then η phase, may be fulfilled [104, 105]. However, when the ageing process is applied on alloys with pre-deformation, or when the ageing process is coupled with deformation, the precipitation behaviour may not be the same as usual.

2.5.1 Pre-deformation Effects on Precipitation

The effect of pre-deformation on the subsequent precipitation behaviour is mainly considered as the competition between homogeneous precipitation in the matrix and heterogeneous precipitation on dislocations. Energetically, the high elastic energy of dislocations decreases the energy barrier of nucleation. Kinetically, on the one hand, dislocations may modify the distribution of surrounding solutes. On the other hand, they also provide fast diffusion paths for solutes. In 7xxx aluminium alloys, the combination of both effects may lead to the following concepts depending on the initial temper and the heating rate of the subsequent ageing [28, 98]

- Dislocations act as the vacancy sink, which can reduce the formation of GP zones. Thus the η' phase amount is also limited.
- Dislocations are the preferred heterogeneous nucleation sites, which can reduce the formation energy of more stable phases such as η . Studies further proved under such circumstances the growth of η phase favours a small misorientation between the growth direction of precipitates and the initial dislocation line direction[106].
- The high diffusion rate along dislocation limits the solute for the bulk diffusion to form the GP zones. But it can accelerate the coarsening of precipitates on dislocations during the over-ageing process.

The influence of pre-deformation is particularly interesting in the condition when a small amount of strain is applied between the solution heat treatment and ageing process to relieve the internal stress induced by the quenching step [107, 80, 108, 109].

In 7xxx aluminium alloys where the high strength is usually achieved by a uniform distribution of the fine precipitates, introducing dislocations in the early stage of ageing may have negative effects on the hardening response [107, 80]. On the one hand, large and stable precipitates on dislocations limit the solutes for small homogeneous precipitates in the matrix. On the other hand, a large precipitate may result in a local solute concentration gradient, which favours the dissolution of small precipitates and the growth of large precipitates. Therefore, a carefully designed

balance between precipitation in bulk and on dislocations is important to optimise the final mechanical properties.

Deschamps et al.(1997) studied the pre-deformation effect on subsequent ageing using an Al-Zn-Mg alloy in the supersaturated condition [107]. They have reported the heating rate of the following artificial ageing affects the final peak strength. For a fast heating rate, such as the isothermal heat treatment, the difficulty of forming GP zones around dislocations results in a spread of the size of precipitates between dislocations and the matrix. Consequently, the non-uniform distribution of the main hardening phases (GP zone and η') limits the peak strength. If the heating rate of the subsequent artificial ageing is slow (30°C/hr), GP zones will have more chance to form in the matrix during the heating ramp. Therefore, after the artificial ageing, the negative effect of the dislocations on the final peak strength is not as strong as samples undergoing the artificial ageing with a fast heating rate.

2.5.2 Dynamic Strain Ageing

Precipitation behaves differently during deformation. Positive effects are mainly observed as an accelerated nucleation rate and/or growth rate of precipitates. Dynamic strain ageing is the mechanism describing the interactions between the obstacles and the dislocations. Even though the commonly discussed obstacles are the solutes, the precipitates in the matrix may affect the macroscopic behaviour of the dynamic strain ageing [110, 111]. In some conditions, when the serrated yield curve appears, the Portevin-Le Chatelier (PLC) phenomenon reflects the appearance of the dynamic strain ageing [112]. Traditionally, the theory explaining the dynamic strain ageing effect is proposed by Cottrell. In this theory, the strengthening is attributed to the decreased dislocation movement by the pinning points. The serrations on the stress-strain curve are explained by the pinning and unpinning of the mobile dislocations by the solutes. The occurrence of the PLC effect commonly depends on the solute concentration, temperature and strain rate. It is also reported that a critical strain has to be reached for the occurrence of the serrations.

In 7xxx aluminium alloys, the dynamic strain ageing effect may not be characterised by the serrated yield curve. It is often used to explain the high work hardening rate and negative strain rate sensitivity observed during deforming the

samples with high solute concentrations [112, 113]. When dislocations are arrested on the obstacles, solutes can diffuse to and build up at the dislocations. After de-pinning, the solute-rich clusters left behind can nucleate and grow into precipitates. The non-saturated Cottrell-Bilby law can be used to estimate the solute concentration at the dislocations [113]. Consequently, the nucleation rate contributed by the dynamic strain ageing can be estimated as shown in equation 5.1, where r is the precipitate radius, b is the Burgers vector, ρ is the forest dislocation density, ρ_m is the mobile dislocation density, k' is the proportional constant, $\dot{\epsilon}$ is the strain rate [113, 114].

$$\frac{dN}{d\epsilon} = \frac{3}{4\pi} \frac{1}{r^3} \frac{k' \rho_m^{2/3} \rho^{1/6}}{b^{1/3} \dot{\epsilon}^{2/3}} \quad (2.20)$$

In the early works of studying the concurrent effect of precipitation and deformation [112, 113], the dynamic strain ageing mechanism has been used to explain the inverse PLC effect during deforming the supersaturated aluminium alloys at room temperature. Small-angle X-ray scattering was performed in-situ and ex-situ to study the high strain hardening rate and the negative strain rate sensitivity. It is reported that fast precipitation kinetics was observed compared to simple thermal ageing without deformation.

Although the dynamic strain ageing model may explain the precipitation behaviour at a slow strain rate with the negative strain rate sensitivity, it mainly considers the heterogeneous precipitation on the dislocations with limited contribution from the bulk diffusion [113, 115]. For the fast strain rate and the low-temperature deformation, it is argued that dislocation-induced atomic movement may also contribute to the dynamic precipitation [113]. In the early time of studying dynamic precipitation, the discussions were mainly focused on the dislocation effect such as the pipe diffusion and the solute collector. It should be addressed that multiple effects could happen simultaneously, especially at the early stage of precipitation, such as shearing small coherent clusters [112, 116].

2.5.3 Excess Vacancy Assisted Dynamic Precipitation

Vacancies play critical roles in the precipitation process. One of the most important aspect is to assist the diffusion of substitutional solutes. Conventionally, vacancies exist naturally in crystals. The equilibrium concentration at a temperature below the melting point is defined by the minimum free energy. This can be theoretically calculated by using equation 2.21, where Q_f is the formation energy and k_B is the Boltzmann's constant.

$$\exp\left(\frac{-Q_f}{k_B T}\right) \quad (2.21)$$

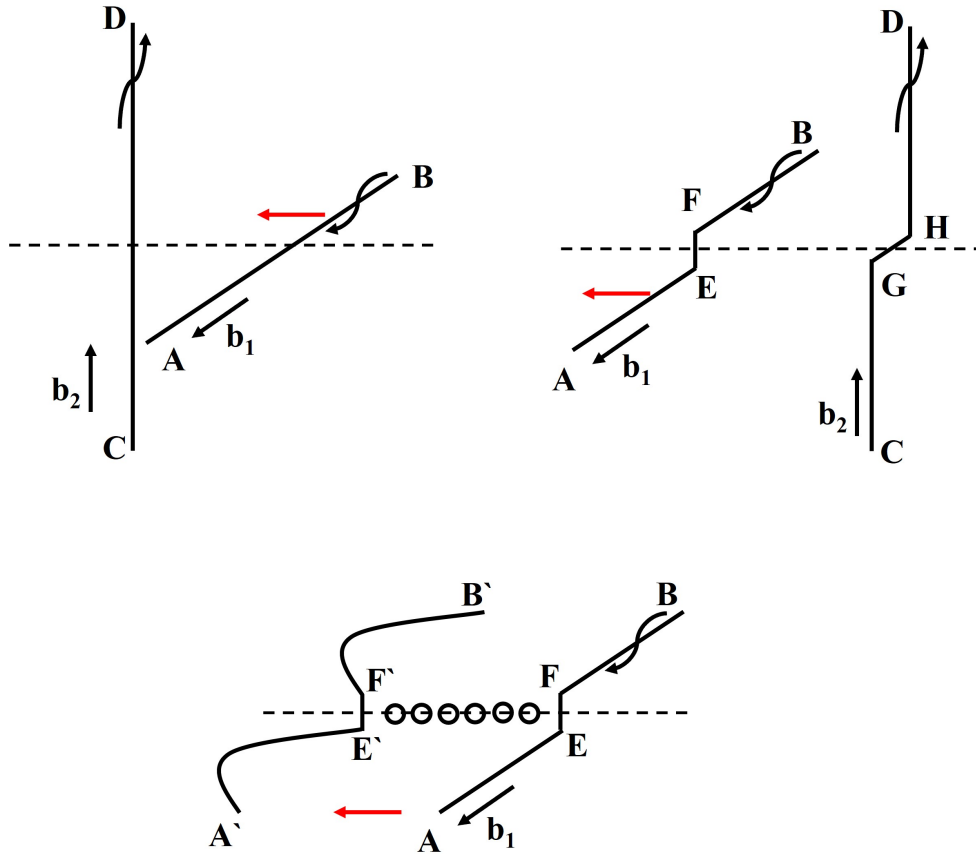


Figure 2.7: Schematic of the intersection of two screw dislocations produces edge-jogs, and the movement of these edge-jogs by climbing produces vacancies

Vacancies can also be mechanically produced by moving dislocation jogs [117]. As shown in figure 2.7, when two screw dislocations (AB and CD) intersect each other, edge-type jogs (EF and GH) will be formed with Burgers vectors the same as their parent dislocations and line vectors same as the Burgers vectors of cutting

dislocations. For example, EF edge jog has a Burgers vector b_1 and a line vector b_2 . Since the line vector b_2 is out of the plane, EF edge jog can not glide to $E'F'$. Therefore, the only way for AB screw dislocation to slip to $A'B'$ is by taking EF with it through a non-conservative motion such as climb which is a thermally activated process. Under this circumstance, jogs will act as pinning points resulting in the dislocation to bow out. Once the shear stress applied overcomes the stress for EF to climb, EF can leave the plane and climb to $E'F'$ leaving vacancies behind.

Compared to the thermal vacancies, deformation-induced vacancies can achieve a higher concentration depending on the temperature, strain and strain rate [103]. Since the diffusivity of substitutional solutes is proportional to the concentration of vacancies, deformation-induced vacancies could have a strong influence on precipitation behaviour. Unlike the pre-deformation effect and the dynamic strain ageing effect which predominately focus on dislocations favouring the heterogeneous precipitation, the excess vacancy mechanism has been found to accelerate homogeneous precipitation [101, 102].

In aluminium alloys, the evolution of excess vacancies can be quantitatively estimated using equation 2.22 [101, 102, 103, 118], where ρ is dislocation density, Q_f is the formation energy of the vacancy, D_v is the diffusivity of vacancies to the dislocation, χ and Ω are a constant number and the atomic volume. Most importantly, equation 2.22 indicates the production rate is proportional to the strain rate and the plastic stress. The annihilation rate of excess vacancies is proportional to the dislocation density and the concentration of excess vacancies.

$$\frac{dC_v}{dt} = \frac{dC_v^+}{dt} - \frac{dC_v^-}{dt} = \chi \frac{\sigma\Omega}{Q_f} \dot{\epsilon} - D_v \rho C_v \quad (2.22)$$

For the purpose of simplification, two extreme conditions may be fulfilled depending on the experimental conditions. Deschamps et al. (2012) reported an experimental condition of non-steady-state evolution of excess vacancies. When pre-aged samples made of 7xxx aluminium alloys were monotonically deformed at 160 °C with slow strain rates ($\sim 10^{-5} \text{ s}^{-1}$), the annihilation rate was smaller enough to be negligible compared to the production rate [101]. Overall, the growth rate of precipitates showed a linear relation to the applied plastic strain indicating the accumulation of vacancies with increasing strain.

A steady-state condition of excess vacancy evolution was reported by Hutchinson et al (2014). When under-aged samples made of AA7050 were cyclically deformed at room temperature, they found the nucleation rate of precipitates ($dN/d\varepsilon$) was independent of the strain rates [102]. In the classical nucleation theory, the nucleation rate of precipitates with respect to strain should be inversely proportional to the plastic strain rate [102]. In their study, this strain rate effect is balanced by the steady-state excess vacancy concentration which is proportional to the plastic strain rate. They further rationalised the steady-state condition by arguing cyclic loading resulted in a short distance between dislocations promoting a fast annihilation of vacancies.

Under what circumstance the evolution of excess vacancy reaches the steady or non-steady state is critical to the understanding of this mechanism. In more complex situations, the evolution of excess vacancies could be in somewhere between the two extreme conditions mentioned above. For example, the annihilation rate is neither small enough to be fully ignored nor large enough to balance the production rate to reach the steady-state condition. In addition, to accurately calculate the net production rate of excess vacancies and predict the precipitation behaviour, other parameters, such as the formation energy of vacancies and the diffusivity of vacancies to the dislocation, are also critical. Unfortunately, to this day, they are far from being well studied [103].

$$\frac{dN}{d\varepsilon} = C_1 \left(\frac{dN}{d\varepsilon} \right)_{\text{vacancies}} + C_2 \left(\frac{dN}{d\varepsilon} \right)_{\text{dislocations}} \quad (2.23)$$

The situation may be even more complicated if dynamic precipitation happens in the under-aged 7xxx aluminium alloys when dynamic strain ageing could also play an important role. There is an attempt made by Moghanaki and Kazeminezhad (2016) to try to explain the dynamically enhanced nucleation in a supersaturated condition [114]. In addition to producing excess vacancies, the dislocation effect on nucleation was also considered using the dynamic strain ageing theory. Solutes can segregate to dislocations during the waiting time of dislocations arrested on obstacles [113]. For the purpose of simplification, in their attempt, a proportional relationship was assumed between the nucleation rate and the solute concentration on dislocations [114]. As shown in equation 2.23, C_1 and C_2 are used to represent the portion of

each mechanism. Although this method successfully fits the data from Deschamps et al (2003) [113], the physical meaning of the portion factors (C_1 and C_2) still needs to be further investigated. Furthermore, when they considered the excess vacancy evolution, they simply followed the steady-state assumption from Hutchinson et al (2014)[102] without providing convincing explanations of the applicability of such an assumption. Indeed, different experimental conditions may lead to the invalidation of the steady-state assumption.

Bibliography

- [1] A. Luo, Recent advances in light metals and manufacturing for automotive applications, *CIM Journal* (2021) 1–9.
- [2] N. Hashimoto, Application of aluminum extrusions to automotive parts, *Kobelco Technology Review* 35 (2017) 69–75.
- [3] P. Krajewski, A. Sachdev, A. Luo, J. Carsley, J. Schroth, Automotive aluminum and magnesium: innovation and opportunities, *Light Metal Age* 67 (5) (2009) 6.
- [4] W. Joost, Energy, materials, and vehicle weight reduction, US Department of Energy, Washington, DC (2015).
- [5] DuckerFrontier, Aluminium content in european passenger cars, https://www.european-aluminium.eu/media/2802/aluminum-content-in-european-cars_european-aluminium_public-summary_101019-1.pdf, accessed: 2021-11-14 (2019).
- [6] T. Sakurai, The latest trends in aluminum alloy sheets for automotive body panels, *Kobelco technology review* (28) (2008) 22–28.
- [7] G. Burger, A. Gupta, P. Jeffrey, D. Lloyd, Microstructural control of aluminum sheet used in automotive applications, *Materials Characterization* 35 (1) (1995) 23–39.
- [8] J. M. Runge, A brief history of aluminum and its alloys, in: *The Metallurgy of Anodizing Aluminum*, Springer, 2018, pp. 1–63.

- [9] J. Ashby, The aluminium legacy: the history of the metal and its role in architecture, *Construction History* 15 (1999) 79.
- [10] D. Chakrabarti, J. Liu, R. Sawtell, G. Venema, New generation high strength high damage tolerance 7085 thick alloy product with low quench sensitivity, in: *Materials Forum*, Vol. 28, 2004, pp. 969–974.
- [11] S. Lim, S. Yun, S. W. Nam, Improved quench sensitivity in modified aluminum alloy 7175 for thick forging applications, *Materials Science and Engineering: A* 371 (1-2) (2004) 82–90.
- [12] G. Sha, A. Cerezo, Early-stage precipitation in al–zn–mg–cu alloy (7050), *Acta Materialia* 52 (15) (2004) 4503–4516.
- [13] S. Brenner, J. Kowalik, H. Ming-Jian, Fim/atom probe analysis of a heat treated 7150 aluminum alloy, *Surface science* 246 (1-3) (1991) 210–217.
- [14] F. Cao, J. Zheng, Y. Jiang, B. Chen, Y. Wang, T. Hu, Experimental and dft characterization of η nano-phase and its interfaces in alznmgcu alloys, *Acta Materialia* 164 (2019) 207–219.
- [15] A. Cassell, J. Robson, X. Zhou, T. Hashimoto, M. Besel, The direct observation of copper segregation at the broad faces of η and η precipitates in aa7010 aluminium alloy, *Materials Characterization* 163 (2020) 110232.
- [16] J.-S. Chen, X.-W. Li, B.-Q. Xiong, Y.-A. Zhang, Z.-H. Li, H.-W. Yan, H.-W. Liu, S.-H. Huang, Quench sensitivity of novel al–zn–mg–cu alloys containing different cu contents, *Rare Metals* 39 (12) (2020) 1395–1401.
- [17] G. K. Sigworth, T. A. Kuhn, Grain refinement of aluminum casting alloys, *International Journal of Metalcasting* 1 (1) (2007) 31–40.
- [18] J. Robson, P. Prangnell, Dispersoid precipitation and process modelling in zirconium containing commercial aluminium alloys, *Acta Materialia* 49 (4) (2001) 599–613.
- [19] J. Robson, Optimizing the homogenization of zirconium containing commercial aluminium alloys using a novel process model, *Materials Science and Engineering: A* 338 (1-2) (2002) 219–229.

- [20] D.-W. Suh, S.-Y. Lee, K.-H. Lee, S.-K. Lim, K. H. Oh, Microstructural evolution of al–zn–mg–cu–(sc) alloy during hot extrusion and heat treatments, *Journal of Materials Processing Technology* 155 (2004) 1330–1336.
- [21] S. Liu, Q. Zhong, Y. Zhang, W. Liu, X. Zhang, Y. Deng, Investigation of quench sensitivity of high strength al–zn–mg–cu alloys by time–temperature–properties diagrams, *Materials & Design* 31 (6) (2010) 3116–3120.
- [22] S. Maloney, K. Hono, I. Polmear, S. Ringer, The effects of a trace addition of silver upon elevated temperature ageing of an al–zn–mg alloy, *Micron* 32 (8) (2001) 741–747.
- [23] R. Ferragut, A. Dupasquier, M. Iglesias, C. E. Macchi, A. Somoza, I. J. Polmear, Vacancy-solute aggregates in al-zn-mg-(cu, ag), in: *Materials science forum*, Vol. 519, Trans Tech Publ, 2006, pp. 309–314.
- [24] Q. Zhu, L. Cao, X. Wu, Y. Zou, M. J. Couper, Effect of ag on age-hardening response of al-zn-mg-cu alloys, *Materials Science and Engineering: A* 754 (2019) 265–268.
- [25] R. A. Nolan, *Microstructure Formability Relationships in New Generation High Strength Aluminium Automotive Alloys*, The University of Manchester (United Kingdom), 2015.
- [26] P. A. Rometsch, Y. Zhang, S. Knight, Heat treatment of 7xxx series aluminium alloys—some recent developments, *Transactions of Nonferrous Metals Society of China* 24 (7) (2014) 2003–2017.
- [27] H. Löffler, I. Kovács, J. Lendvai, Decomposition processes in al-zn-mg alloys, *Journal of Materials Science* 18 (8) (1983) 2215–2240.
- [28] A. Deschamps, C. Hutchinson, Precipitation kinetics in metallic alloys: Experiments and modeling, *Acta Materialia* 220 (2021) 117338.
- [29] A. Mukhopadhyay, Guinier-preston zones in a high-purity al-zn-mg alloy, *Philosophical magazine letters* 70 (3) (1994) 135–140.

- [30] K. Stiller, P. Warren, V. Hansen, J. Angenete, J. Gjønnnes, Investigation of precipitation in an al–zn–mg alloy after two-step ageing treatment at 100 and 150 c, *Materials Science and Engineering: A* 270 (1) (1999) 55–63.
- [31] L. Berg, J. Gjønnnes, V. x. Hansen, X. Li, M. Knutson-Wedel, D. Schryvers, L. Wallenberg, Gp-zones in al–zn–mg alloys and their role in artificial aging, *Acta materialia* 49 (17) (2001) 3443–3451.
- [32] G. Sha, A. Cerezo, Kinetic monte carlo simulation of clustering in an al–zn–mg–cu alloy (7050), *Acta materialia* 53 (4) (2005) 907–917.
- [33] C. Panseri, T. Federighi, Evidence for the interaction between mg atoms and vacancies in al–zn 10%–mg 0.1% alloy, *Acta Metallurgica* 11 (6) (1963) 575–584.
- [34] A. Melander, P. Å. Persson, The strength of a precipitation hardened alznmg alloy, *Acta Metallurgica* 26 (2) (1978) 267–278.
- [35] H. Schmalzried, V. Gerold, Age-hardening in an al—mg—zn alloy, *Z. Metallkd* 49 (1958) 291–301.
- [36] G. Groma, E. Kovacs-Csetenyi, I. Kovács, J. Lendvai, T. Ungár, The composition of guinier–preston zones in al–zn–mg alloys, *Philosophical Magazine A* 40 (5) (1979) 653–665.
- [37] T. Grohmann, Forming of amag 7xxx series aluminium sheet alloys, *Proceedings of the New Developments in Sheet Metal Forming and New Developments in Hydroforming*, Fellbach, Germany (2016) 10–11.
- [38] A. Lervik, E. Thronsen, J. Friis, C. D. Marioara, S. Wenner, A. Bendo, K. Matsuda, R. Holmestad, S. J. Andersen, Atomic structure of solute clusters in al–zn–mg alloys, *Acta Materialia* 205 (2021) 116574.
- [39] J. Auld, S. M. Cousland, The transition phase η in al zn mg alloys, *Scripta Metallurgica* 5 (9) (1971) 765–769.
- [40] C. Régnier, J. Bouvaist, J. Simon, Etude cristallographique de la phase de transition m” dans al–8% zn–1% mg, *Journal of Applied Crystallography* 15 (6) (1982) 590–593.

- [41] J. Auld, S. Cousland, On the structure of the m'phase in al-zn-mg alloys, *Journal of applied crystallography* 18 (1) (1985) 47–48.
- [42] X. Li, V. Hansen, J. Gjønnes, L. Wallenberg, Hrem study and structure modeling of the η phase, the hardening precipitates in commercial al-zn-mg alloys, *Acta materialia* 47 (9) (1999) 2651–2659.
- [43] J. Auld, S. Coulsland, The structure of the metastable η phase in aluminium-zinc-magnesium alloys, *Journal of the Australian Institute of Metals* 19 (3) (1974) 194–199.
- [44] C. Wolverton, Crystal structure and stability of complex precipitate phases in al-cu-mg-(si) and al-zn-mg alloys, *Acta Materialia* 49 (16) (2001) 3129–3142.
- [45] T.-F. Chung, Y.-L. Yang, B.-M. Huang, Z. Shi, J. Lin, T. Ohmura, J.-R. Yang, Transmission electron microscopy investigation of separated nucleation and in-situ nucleation in aa7050 aluminium alloy, *Acta Materialia* 149 (2018) 377–387.
- [46] T. Engdahl, V. Hansen, P. Warren, K. Stiller, Investigation of fine scale precipitates in al-zn-mg alloys after various heat treatments, *Materials Science and Engineering: A* 327 (1) (2002) 59–64.
- [47] P. Warren, C. Grovenor, J. Crompton, Field-ion microscope/atom-probe analysis of the effect of rra heat treatment on the matrix strengthening precipitates in alloy al-7150, *Surface science* 266 (1-3) (1992) 342–349.
- [48] S. Maloney, K. Hono, I. Polmear, S. P. Ringer, The chemistry of precipitates in an aged al-2.1 zn-1.7 mg at.% alloy, *Scripta Materialia* 41 (10) (1999).
- [49] A. Deschamps, A. Bigot, F. Livet, P. Auger, Y. Brechet, D. Blavette, A comparative study of precipitate composition and volume fraction in an al-zn-mg alloy using tomographic atom probe and small-angle x-ray scattering, *Philosophical Magazine A* 81 (10) (2001) 2391–2414.
- [50] Y.-S. Lee, D.-H. Koh, H.-W. Kim, Y.-S. Ahn, Improved bake-hardening response of Al-Zn-Mg-Cu alloy through pre-aging treatment, *Scripta Materialia* 147 (2018) 45–49.

- [51] Z. Li, B. Xiong, Y. Zhang, B. Zhu, F. Wang, H. Liu, Investigation of microstructural evolution and mechanical properties during two-step ageing treatment at 115 and 160° c in an al–zn–mg–cu alloy pre-stretched thick plate, *Materials Characterization* 59 (3) (2008) 278–282.
- [52] J. A. Österreicher, M. A. Tunes, F. Grabner, A. Arnoldt, T. Kremmer, S. Pogatscher, C. M. Schlögl, Warm-forming of pre-aged Al-Zn-Mg-Cu alloy sheet, *Materials & Design* 193 (2020) 108837.
- [53] P. Schloth, J. Wagner, J. Fife, A. Menzel, J.-M. Drezet, H. Van Swygenhoven, Early precipitation during cooling of an al-zn-mg-cu alloy revealed by in situ small angle x-ray scattering, *Applied Physics Letters* 105 (10) (2014) 101908.
- [54] G. Groma, E. Kovacs-Csetenyi, Reversion and re-ageing in an alznmg alloy, *Philosophical Magazine* 32 (4) (1975) 869–872.
- [55] G. Groma, E. Kovács-Csetényi, I. Kovács, J. Lendvai, T. Ungár, Investigation of the reversion phenomena in an al-3, 2% zn-2, 2% mg alloy, *International Journal of Materials Research* 67 (6) (1976) 404–409.
- [56] I. Kovács, J. Lendvai, T. Ungar, K. Banizs, J. Lakner, Effect of two and three step ageing on the eta prime phase formation in al-4. 8 wt per cent zn-1. 2 wt per cent mg, *Aluminium* 53 (8) (1977) 497–503.
- [57] J. Liu, J. Chen, X. Yang, S. Ren, C. Wu, H. Xu, J. Zou, Revisiting the precipitation sequence in al–zn–mg-based alloys by high-resolution transmission electron microscopy, *Scripta Materialia* 63 (11) (2010) 1061–1064.
- [58] J. Liu, J. Chen, D. Yuan, C. Wu, J. Zhu, Z. Cheng, Fine precipitation scenarios of alznmg (cu) alloys revealed by advanced atomic-resolution electron microscopy study part i: structure determination of the precipitates in alznmg (cu) alloys, *Materials Characterization* 99 (2015) 277–286.
- [59] J. Liu, J. Chen, Z. Liu, C. Wu, Fine precipitation scenarios of alznmg(cu) alloys revealed by advanced atomic-resolution electron microscopy study part ii: Fine precipitation scenarios in alznmg(cu) alloys, *Materials Characterization* 99 (2015) 142–149.

- [60] A. Gupta, P. Gaunt, M. Chaturvedi, The crystallography and morphology of the s'-phase precipitate in an al (cumg) alloy, *Philosophical Magazine A* 55 (3) (1987) 375–387.
- [61] J. Majimel, G. Molenat, F. Danoix, O. Thuillier, D. Blavette, G. Lapasset, Casanove, High-resolution transmission electron microscopy and tomographic atom probe studies of the hardening precipitation in an al–cu–mg alloy.
- [62] M. J. Styles, C. Hutchinson, Y. Chen, A. Deschamps, T. J. Bastow, The coexistence of two s (al2cumg) phases in al–cu–mg alloys, *Acta Materialia* 60 (20) (2012) 6940–6951.
- [63] M. J. Styles, R. K. W. Marceau, T. J. Bastow, H. E. Brand, M. A. Gibson, C. R. Hutchinson, The competition between metastable and equilibrium s (al2cumg) phase during the decomposition of alcumg alloys, *Acta materialia* 98 (2015) 64–80.
- [64] D. Petschke, F. Lotter, T. E. Staab, Revisiting the crystal structure of the equilibrium s (al2cumg) phase in al–cu–mg alloys using x-ray absorption spectroscopy (xafs), *Materialia* 6 (2019) 100341.
- [65] D. Godard, P. Archambault, E. Aeby-Gautier, G. Lapasset, Precipitation sequences during quenching of the aa 7010 alloy, *Acta Materialia* 50 (9) (2002) 2319–2329.
- [66] S. T. Lim, I. S. Eun, S. W. Nam, Control of equilibrium phases (m, t, s) in the modified aluminum alloy 7175 for thick forging applications, *Materials Transactions* 44 (1) (2003) 181–187.
- [67] J. Robson, Microstructural evolution in aluminium alloy 7050 during processing, *Materials Science and Engineering: A* 382 (1-2) (2004) 112–121.
- [68] P. Priya, D. R. Johnson, M. J. Krane, Precipitation during cooling of 7xxx aluminum alloys, *Computational Materials Science* 139 (2017) 273–284.
- [69] Y. Zou, X. Wu, S. Tang, Q. Zhu, H. Song, L. Cao, Co-precipitation of t and η phase in al–zn–mg–cu alloys, *Materials Characterization* 169 (2020) 110610.

- [70] A. Bigot, P. Auger, S. Chambreland, D. Blavette, A. Reeves, Atomic scale imaging and analysis of θ' precipitates in Al-Mg-Zn alloys, *Microscopy Microanalysis Microstructures* 8 (2) (1997) 103–113.
- [71] G. Sha, A. Cerezo, Characterization of precipitates in an aged 7xxx series Al alloy, *Surface and Interface Analysis* 36 (56) (2004) 564–568.
- [72] C. Mondal, A. Mukhopadhyay, On the nature of θ ($\text{Al}_2\text{Mg}_3\text{Zn}_3$) and θ (Al_2CuMg) phases present in as-cast and annealed 7055 aluminum alloy, *Materials Science and Engineering: A* 391 (1-2) (2005) 367–376.
- [73] M. Nicolas, A. Deschamps, Characterisation and modelling of precipitate evolution in an Al-Zn-Mg alloy during non-isothermal heat treatments, *Acta Materialia* 51 (20) (2003) 6077–6094.
- [74] H. P. Degischer, W. Lacom, A. Zahra, C. Y. Zahra, Decomposition processes in an Al-5% Zn-1% Mg alloy, *International Journal of Materials Research* 71 (4) (1980) 231–238.
- [75] C. Moon, S. Thuillier, J. Lee, M.-G. Lee, Mechanical properties of solution heat treated Al-Zn-Mg-Cu (7075) alloy under different cooling conditions: Analysis with full field measurement and finite element modeling, *Journal of Alloys and Compounds* 856 (2021) 158180.
- [76] H. Zhao, B. Gault, D. Ponge, D. Raabe, F. De Geuser, Parameter free quantitative analysis of atom probe data by correlation functions: Application to the precipitation in Al-Zn-Mg-Cu, *Scripta Materialia* 154 (2018) 106–110.
- [77] N. Holroyd, G. Scamans, Stress corrosion cracking in Al-Zn-Mg-Cu aluminum alloys in saline environments, *Metallurgical and Materials Transactions A* 44 (3) (2013) 1230–1253.
- [78] G. Silva, B. Rivolta, R. Gerosa, U. Derudi, Study of the SCC behavior of 7075 aluminum alloy after one-step aging at 163 °C, *Journal of materials engineering and performance* 22 (1) (2013) 210–214.
- [79] P. Xie, S. Chen, K. Chen, H. Jiao, L. Huang, Z. Zhang, Z. Yang, Enhancing the stress corrosion cracking resistance of a low-Cu containing Al-Zn-Mg-Cu

- aluminum alloy by step-quench and aging heat treatment, *Corrosion Science* 161 (2019) 108184.
- [80] V. Hansen, J. Gjønnnes, S. Skjervold, Effect of predeformation and preaging at room temperature in al–zn–mg–(cu, zr) alloys, *Materials Science and Engineering: A* 303 (1-2) (2001) 226–233.
- [81] I. Westermann, O. S. Hopperstad, K. Marthinsen, B. Holmedal, Ageing and work-hardening behaviour of a commercial aa7108 aluminium alloy, *Materials Science and Engineering: A* 524 (1-2) (2009) 151–157.
- [82] R.-m. Su, Y.-d. Qu, J.-h. You, R. de Li, Effect of pre-aging on stress corrosion cracking of spray-formed 7075 alloy in retrogression and re-aging, *Journal of Materials Engineering and Performance* 24 (11) (2015) 4328–4332.
- [83] F. Chun, Z.-y. LIU, A.-l. NING, Y.-b. LIU, S.-m. ZENG, Retrogression and re-aging treatment of al-9.99% zn-1.72% cu-2.5% mg-0.13% zr aluminum alloy, *Transactions of Nonferrous Metals Society of China* 16 (5) (2006) 1163–1170.
- [84] J. Li, N. Birbilis, C. Li, Z. Jia, B. Cai, Z. Zheng, Influence of retrogression temperature and time on the mechanical properties and exfoliation corrosion behavior of aluminium alloy aa7150, *Materials Characterization* 60 (11) (2009) 1334–1341.
- [85] T. Marlaud, A. Deschamps, F. Bley, W. Lefebvre, B. Baroux, Influence of alloy composition and heat treatment on precipitate composition in al–zn–mg–cu alloys, *Acta Materialia* 58 (1) (2010) 248–260.
- [86] Y.-P. Xiao, Q.-L. Pan, W.-B. Li, X.-Y. Liu, Y.-B. He, Influence of retrogression and re-aging treatment on corrosion behaviour of an al–zn–mg–cu alloy, *Materials & Design* 32 (4) (2011) 2149–2156.
- [87] L. Liu, Q. Pan, X. Wang, S. Xiong, The effects of aging treatments on mechanical property and corrosion behavior of spray formed 7055 aluminium alloy, *Journal of Alloys and Compounds* 735 (2018) 261–276.

- [88] A. Azarniya, A. K. Taheri, K. K. Taheri, Recent advances in ageing of 7xxx series aluminum alloys: a physical metallurgy perspective, *Journal of Alloys and Compounds* 781 (2019) 945–983.
- [89] J.-C. Lin, H.-L. Liao, W.-D. Jehng, C.-H. Chang, S.-L. Lee, Effect of heat treatments on the tensile strength and scc-resistance of aa7050 in an alkaline saline solution, *Corrosion Science* 48 (10) (2006) 3139–3156.
- [90] H. Zhao, Y. Chen, B. Gault, S. K. Makineni, D. Ponge, D. Raabe, (al, zn) 3zr dispersoids assisted η precipitation in al-zn-mg-cu-zr alloy, *Materialia* 10 (2020) 100641.
- [91] T. Gladman, Precipitation hardening in metals, *Materials science and technology* 15 (1) (1999) 30–36.
- [92] S.-H. Lee, J.-G. Jung, S.-I. Baik, D. N. Seidman, M.-S. Kim, Y.-K. Lee, K. Euh, Precipitation strengthening in naturally aged al–zn–mg–cu alloy, *Materials Science and Engineering: A* 803 (2021) 140719.
- [93] K. Ma, H. Wen, T. Hu, T. D. Topping, D. Isheim, D. N. Seidman, E. J. Lavernia, J. M. Schoenung, Mechanical behavior and strengthening mechanisms in ultrafine grain precipitation-strengthened aluminum alloy, *Acta Materialia* 62 (2014) 141–155.
- [94] H. Wen, T. D. Topping, D. Isheim, D. N. Seidman, E. J. Lavernia, Strengthening mechanisms in a high-strength bulk nanostructured cu–zn–al alloy processed via cryomilling and spark plasma sintering, *Acta Materialia* 61 (8) (2013) 2769–2782.
- [95] A. J. Ardell, Precipitation hardening, *Metallurgical Transactions A* 16 (12) (1985) 2131–2165.
- [96] D. Bacon, U. Kocks, R. Scattergood, The effect of dislocation self-interaction on the orowan stress, *Philosophical Magazine* 28 (6) (1973) 1241–1263.
- [97] B. Holmedal, Strength contributions from precipitates, *Philosophical Magazine Letters* 95 (12) (2015) 594–601.

- [98] A. Deschamps, F. Livet, Y. Brechet, Influence of predeformation on ageing in an al–zn–mg alloy—i. microstructure evolution and mechanical properties, *Acta materialia* 47 (1) (1998) 281–292.
- [99] V. Gerold, Precipitation hardening, in: J. P. Hirth, L. Kubin (Eds.), *Dislocations in solids*, Vol. 4, Elsevier, 2009, p. 219.
- [100] A. De Vaucorbeil, W. Poole, C. Sinclair, The superposition of strengthening contributions in engineering alloys, *Materials Science and Engineering: A* 582 (2013) 147–154.
- [101] A. Deschamps, G. Fribourg, Y. Brechet, J. L. Chemin, C. Hutchinson, In situ evaluation of dynamic precipitation during plastic straining of an al–zn–mg–cu alloy, *Acta materialia* 60 (5) (2012) 1905–1916.
- [102] C. Hutchinson, F. De Geuser, Y. Chen, A. Deschamps, Quantitative measurements of dynamic precipitation during fatigue of an al–zn–mg–(cu) alloy using small-angle x-ray scattering, *Acta materialia* 74 (2014) 96–109.
- [103] J. Robson, Deformation enhanced diffusion in aluminium alloys, *Metallurgical and Materials Transactions A* 51 (10) (2020) 5401–5413.
- [104] J. Nie, Physical Metallurgy of Light Alloys, in: D. E. Laughlin, K. Hono (Eds.), *Physical Metallurgy*, 5th Edition, Elsevier, Oxford, 2014, pp. 2009–2156.
- [105] M. Starink, S. Wang, A model for the yield strength of overaged Al–Zn–Mg–Cu alloys, *Acta Materialia* 51 (17) (2003) 5131–5150.
- [106] R. M. Allen, J. B. Vander Sande, The oriented growth of precipitates on dislocations in al–zn–mg—part i. experimental observations, *Acta Metallurgica* 28 (9) (1980) 1185–1195.
- [107] A. Deschamps, Y. Brechet, P. Guyot, E. Livet, On the influence of dislocations on precipitation in an al–zn–mg alloy, *Stal* 1 (1) (1997) 1–1.
- [108] D. Wang, D. Ni, Z. Ma, Effect of pre-strain and two-step aging on microstructure and stress corrosion cracking of 7050 alloy, *Materials Science and Engineering: A* 494 (1-2) (2008) 360–366.

- [109] N. Han, X. Zhang, S. Liu, B. Ke, X. Xin, Effects of pre-stretching and ageing on the strength and fracture toughness of aluminum alloy 7050, *Materials Science and Engineering: A* 528 (10-11) (2011) 3714–3721.
- [110] E. Pink, W. Webernig, Precipitation during serrated flow in alzn5mg1, *Acta Metallurgica* 35 (1) (1987) 127–132.
- [111] E. Pink, The effect of precipitates on characteristics of serrated flow in alzn5mg1, *Acta Metallurgica* 37 (7) (1989) 1773–1781.
- [112] A. Deschamps, M. Niewczas, F. Bley, Y. Brechet, J. Embury, L. L. Sinq, F. Livet, J. Simon, Low-temperature dynamic precipitation in a supersaturated ai-zn-mg alloy and related strain hardening, *Philosophical Magazine A* 79 (10) (1999) 2485–2504.
- [113] A. Deschamps, F. Bley, F. Livet, D. Fabregue, L. David, In-situ small-angle x-ray scattering study of dynamic precipitation in an al-zn-mg-cu alloy, *Philosophical Magazine* 83 (6) (2003) 677–692.
- [114] S. K. Moghanaki, M. Kazeminezhad, Modeling of the mutual effect of dynamic precipitation and dislocation density in age hardenable aluminum alloys, *Journal of Alloys and Compounds* 683 (2016) 527–532.
- [115] Y. Brechet, Y. Estrin, On the influence of precipitation on the portevin-le chatelier effect, *Acta metallurgica et materialia* 43 (3) (1995) 955–963.
- [116] C. Hutchinson, P. T. Loo, T. J. Bastow, A. Hill, J. da Costa Teixeira, Quantifying the strain-induced dissolution of precipitates in al alloy microstructures using nuclear magnetic resonance, *Acta materialia* 57 (19) (2009) 5645–5653.
- [117] D. Hull, D. J. Bacon, *Introduction to dislocations*, Vol. 37, Elsevier, 2011.
- [118] M. Militzer, W. Sun, J. Jonas, Modelling the effect of deformation-induced vacancies on segregation and precipitation, *Acta metallurgica et materialia* 42 (1) (1994) 133–141.

Chapter 3

Experimental Methods

This chapter summaries the basic principles behind the experimental techniques which were used in this study. The detailed experimental procedures which are necessary to repeat the results in this thesis are presented in relevant chapters.

3.1 Materials

The research in this thesis was conducted on 7075 aluminium alloys, which is a typical high strength 7xxx aluminium alloys widely used in the automotive and aerospace industry. The materials were industrially manufactured by direct chill casting and homogenisation followed by hot rolling to 90% thickness reduction and cold rolling to 65% thickness reduction. The sheets were then supplied by Constellium in the as fabricated condition (F-temper) with a final thickness of 1.5mm. The nominal composition and the dimension of samples for each experiment are reported in relevant chapters.

3.2 Heat Treatments

Heat treatments in the present study are classified into either high temperature solution heat treatment or intermediate temperature ageing. The solution heat treatments were performed in an air circulated furnace which has a maximum limit of 600 °C. All the ageing processes were performed in an air circulated furnace which has a maximum limit of 300 °C. The purpose of this practice is to make the best

usage of each furnace's heating range to obtain better signal to noise ratio and ensure high repeatability of experiments.

After the solution heat treatment, samples were water quenched to room temperature producing a status of supersaturated solid solution. To avoid natural ageing, samples were immediately transferred to the ageing furnace with pre-set temperature. Afterwards, materials were stored in the freezer at -29°C waiting to be further processed or characterised.

The temperature and time for each heat treatment in this thesis are summarised in table3.1.

Table 3.1: Heat treatments in this thesis		
Heat treatments	Temperature	Time
Solution heat treatments	480°C	1 hour
Peak ageing (T6)	120°C	24 hour
Paint bake process	185°C	20 minutes
Pre-ageing	40 to 100°C	2 to 8 hours
Second-ageing	120°C	2 to 12 hours

3.3 Micro-hardness

Hardness testing is a non-destructive method to characterise material's resistance to the plastic deformation. It is a simple and efficient method that can provide an initial indication of a wide range of material's mechanical properties such as strength, wear resistance and toughness. In this study, Vickers hardness method is used to characterise material's strength. The schematic is illustrated in figure 3.1.

Tests were performed using a pyramid-shaped diamond indenter. A constant load was applied for a set amount of time to create a pyramid-shaped deformed zone. The diagonal lengths of the indentation was then measured using the optical microscope equipped on the hardness testing machine. Equation 3.1 is used to obtain the hardness value, where F is the applied load and d is the average diagonal length. Since the average diagonal length was substitute in the equation, the best practice is to have a symmetrical pyramid indentation which relies on the surface flatness and the homogeneity of material's property.

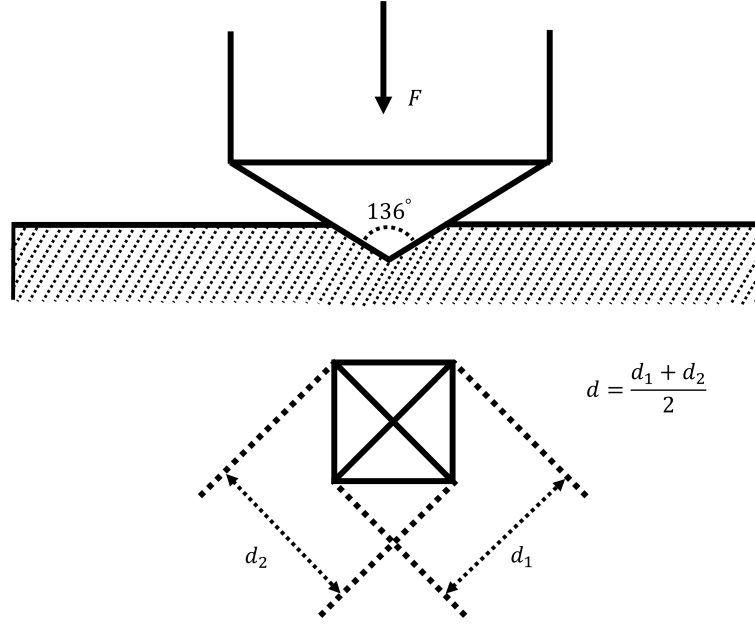


Figure 3.1: Schematic of Vickers hardness test

$$HV = \frac{2F \sin \frac{136^\circ}{2}}{d^2} \approx 1.854 \frac{F}{d^2} \quad (3.1)$$

Depending on the applied load (size of the indentation), Vickers hardness testing can be conducted on macro-scale and micro scale-scale. Generally, for an applied load below 1kgf, it is classified as micro-hardness. In this study, 0.5kgf load was used on all hardness measurements with 10 seconds dwelling time. Since micro-hardness usually produce a smaller indentation than macro-hardness, local heterogeneity of the material may scatter the results. Practically, an average hardness value and standard deviation were calculated from at least 10 indentations.

Before any hardness measurements, samples were progressively ground using silicon-carbide grinding papers from 300 grit to 4000 grit. When materials were ground using grinding paper with a grit number below 1200, water was used as the coolant and lubricant. When materials were ground using 1200, 2500 and 4000 grit grinding paper, water was replaced by methanol to provide high quality surface condition.

3.4 Mechanical Testing

Mechanical tests are designed to examine materials' mechanical properties. In this thesis, this is limited to uni-axial tensile test which provides information such as yield stress, ultimate tensile strength, elongation to failure and work hardening behaviour. Three machines were used in this study depending on the size of the sample and the purpose of the experiment.

3.4.1 Room temperature testing

An Instron 5569H1549 machine with a 30kN load cell was used to perform uni-axial tensile tests at room temperature. An extensometer with 25mm gauge length was attached on the sample to measure the plastic strain throughout the test with the plastic strain rate of 10^{-4}s^{-1} . The sample dimensions follow the ASTM E8-04 standard. Details are presented in the relevant result chapter.

3.4.2 Warm temperature testing - Dilatometer

TA instrument DIL805 A/D/T dilatometer was used to study material's behaviour at warm temperature between 120°C to 180°C . This instrument can perform tensile tests at strain rates between $7 \times 10^{-4} \text{ s}^{-1}$ to 1 s^{-1} with rapid heating and cooling (up to $100^{\circ}\text{C s}^{-1}$) and accurate temperature control (to within 0.1°C).

To achieve high temperature, the instrument is equipped with an electromagnet. By passing a high-frequency alternating current (AC), induced current is generated inside the sample. The resistance of the material to the induced currents generates Joule heat raising the temperature. To accurately measure and control the temperature, R-type thermocouple was spot welded onto the center of the parallel gauge area. During deformation, two push-rods were attached on the ends of gauge area to measure the elongation thus the plastic strain. After deformation, gas flow of nitrogen was used to achieve cooling in a controlled manner. An image of the dilatometer chamber is shown in figure 3.2 [1].

Taking the advantage of this cooling unit, solution heat treatment followed by gas quenching can also be simulated using this dilatometer. Compared to performing solution heat treatment in the furnace and then transferring samples onto

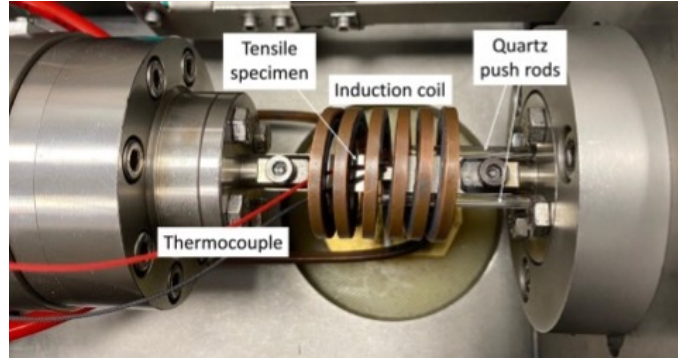


Figure 3.2: TA instrument DIL805 A/D/T dilatometer[1] (Copyright obtained from Elsevier)

the tensile machine, this method avoids natural ageing during sample transportation and artificial ageing during the reheating from room temperature to the target warm temperature. Sample dimensions and relevant experimental configuration are presented in chapter 4.

3.4.3 Warm temperature testing - ETMT

Instron electro-thermo-mechanical testing machine (ETMT) equipped with a 3kN load cell was used to perform uni-axial tensile deformation at warm temperature between 120 °C and 150 °C. An image of the ETMT instrument is shown in figure 3.3 [2].

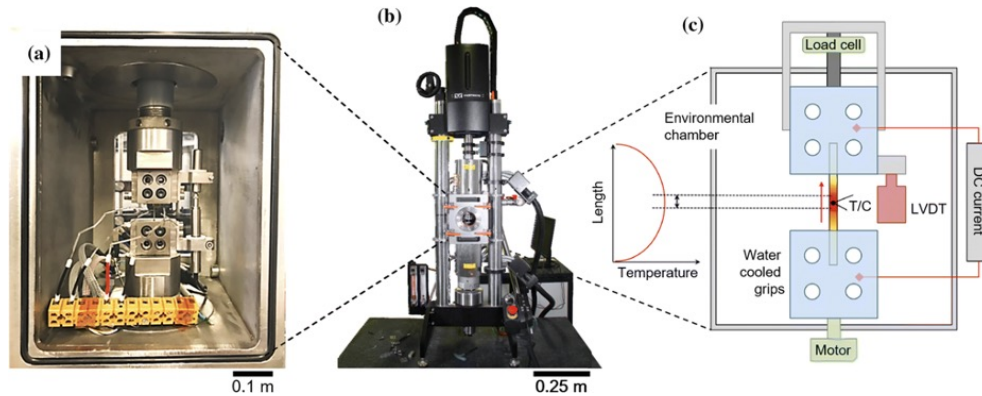


Figure 3.3: Instron electro-thermo-mechanical testing machine (ETMT). (a) an image of the environmental chamber, (b) an image of the overall ETMT instrument and (c) a schematic of the environmental chamber.[2] (Copyright obtained from Springer Nature)

Unlike the dilatometer, Joule heat is generated by passing direct current (DC) through the sample. R-type thermocouple was replaced by K-type thermocouple to

measure and control the temperature. Cooling was achieved by running cold water through the clamping grips.

The effect of this configuration on the temperature profile of the gauge area is illustrated in figure 3.3, revealing a parabolic temperature distribution with the highest temperature point aligned with the thermocouple's welding spot. Further measurements were conducted using additional thermocouples to assess temperature variations in this area. Notably, the present study detected a $\pm 1^\circ\text{C}$ difference when spot welding the additional thermocouples 2mm above and below the central thermocouple. Consequently, to minimize experimental error, it is imperative to conduct further characterizations within this effective gauge area. For example, TEM samples of 3mm diameter discs were sectioned from this region to study the distribution of precipitates. To ensure precise in-situ small angle X-rays scattering measurements, efforts were also made to control the beam size, thus effectively exposing the X-rays to this critical hot zone.

To analyse the effective plastic strain in this hot region, we utilized the commercial digital image correlation software, LaVision Davis 10. In this study, the gauge area (hot region) exhibited a generally uniform strain distribution, reflecting consistent material response to an external load. However, despite efforts to remove high-frequency noise by capturing a set of static condition images prior to deformation, subtle localized variations were still observed within this uniformity during deformation (e.g. $\pm 0.5\%$ at 9% strain). These variations, while minor, could be attributed to factors such as local microstructural heterogeneities, surface irregularities and experimental configurations (e.g. speckle pattern quality and subset size). Unfortunately, our study could not directly compare DIC-derived strains with external measurements from a high-temperature extensometer due to the unavailability of a suitable extensometer gauge length.

Limited by the capacity of the load cell and the power of the heating unit, samples to be tested using the ETMT usually have small dimensions which is not ideal to provide mechanical properties. However, ETMT has its own incomparable advantages. Without the requirement of using electromagnet, ETMT has an open experimental environment. Together with the synchrotron X-ray, in-situ experiments can be carried out to characterise the sample and collect material's properties in a

time-resolved manner. Detailed experimental condition and beamline configuration are presented in chapter 7.

3.5 Transmission Electron Microscopy

The ability of a perfect imaging system to resolve details is defined by the De Broglie wavelength of the ‘light’. Rayleigh criterion describes that the minimum resolvable distance of a perfect imaging system is proportional to the wavelength of the ‘light’ [3]. Based on the De Broglie hypothesis of wave–particle duality, high energy electrons can be used as ‘light’ to resolve details in the unit of angstrom or even sub-angstrom. As a complex system, TEM operates under the cooperation of multiple units. Modern TEM instruments are usually equipped with other advanced characterisation tools providing the ability to quantify the chemical and physical properties of the investigated material.

A typical TEM consists at least three units. First, the emission source is commonly referred as the electron gun. By connecting the gun to the high voltage, high energy electrons are emitted. There are mainly two types of electron gun. For a thermionic electron source, filament made of tungsten or LaB₆ is progressively heated. Electrons with enough energy to free from the solid surface are attract by the anode and directed into the column. In this study, TEM instruments are equipped with field emission gun (FEG) which uses electrostatic field to induce electron emission from a sharp tungsten wire. Although FEG is generally more expensive than thermionic gun, FEG provides high brightness and stability which are essential for atomic imaging.

Lenses, apertures and the sample stage compose the second unit. Lenses are made of coils. By passing electric currents, an electromagnetic field is created tailoring the path and trajectory of electrons. As lenses are not physically movable in the TEM system, focusing or spreading the beam are therefore archived by adjusting the current in the coil. Apertures are holes with specific sizes on a physical strip, which are used to select electrons. As illustrated in figure 3.4, in a typical TEM system there are condenser lenses and apertures, objective lenses and apertures, selected area apertures, intermediate lenses and projector lenses. Condenser lenses

and apertures control the incident (convergence) angle and size (diameter) of the beam on the sample. Below the sample stage, objective lenses are used to generate the first intermediate image. Intermediate lenses decide if the image or diffraction pattern of the sample is being passed down to the projector lenses which provide most of the magnification in a TEM system. Objective apertures and selected area apertures may be used depending on the operation mode of the TEM. In the imaging mode, objective apertures can be used to enhance certain contrast. Objective apertures are placed at the back focal plan of the objective lenses (as illustrated in figure 3.4 (b)), where diffraction patterns are formed. Unscattered beam can be selected to generate bright field image. Scattered beam can be selected to generate dark field image. In the diffraction mode when recording the diffraction pattern is the primary concern, selected area apertures located at the image plane of the objective lenses (as illustrated in figure 3.4 (a)) are used to select interested area of the sample.

The final part is the imaging unit. Conventional digital imaging on TEM instruments uses charge-couple device (CCD) camera, which is a two-dimensional sensor system with an array of pixels made of metal-oxide-semiconductor (MOS) capacitors. CCD cameras are sensitive to incident radiation such as electrons and photons. Directly exposing high energy electrons onto a sensor will damage the detector. Traditional CCD cameras have a layer of scintillating film converting the electrons into photons which are consequently passed to MOS capacitors to generate electrons. After the exposure event, these photo-generated electrons will be passed pixel by pixel to the read-out unit where they will be converted to voltage and create the final image. Complementary metal-oxide-semiconductor (CMOS) camera also referred as active-pixel camera is made of MOSFET amplifiers per pixel. For CMOS camera, rather than passing photo-generated electrons through neighbours to reach the final read-out unit, charge to voltage conversion happens in each pixel. This enables fast image read-out, which means images can be collected with fast frame rate. CMOS detectors are replacing CCD in modern TEM instruments.

Precipitates of interests in the present study are extremely small with size in the scale of nanometers. Transmission electron microscopy was, therefore, required to provide direct observation with spatial resolution. However, interpreting TEM

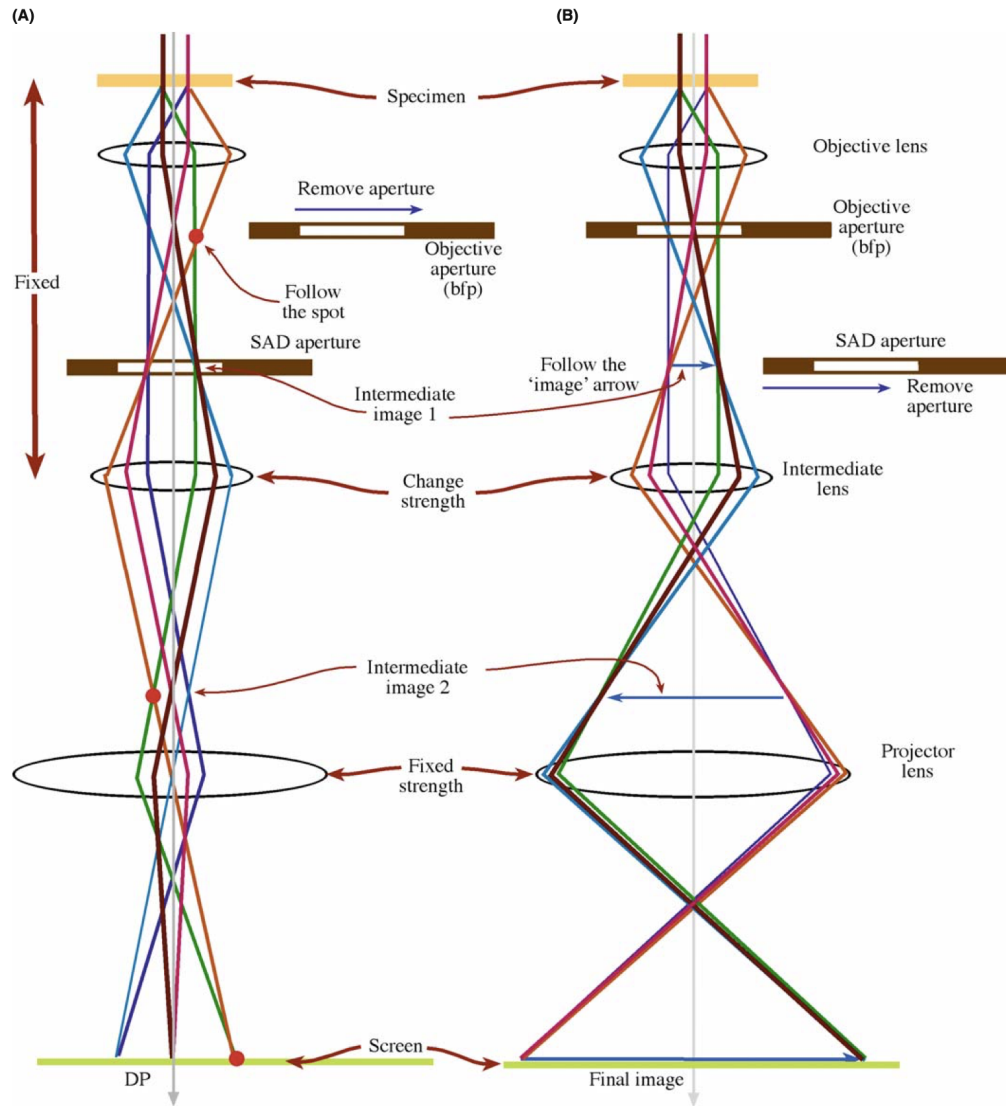


Figure 3.4: Schematic of basic operations of TEM in (a) diffraction mode and (b) imaging mode [3] (Copyright obtained from Springer Nature)

micrographs can be a challenging task since contrast may arise from different sources.

Mass-thickness contrast arises from the incoherent scattering of electrons. Thicker sample will scatter more electrons than a thinner sample. Similarly, heavy atoms with large atomic number Z will also scatter more electrons than light atoms. Consequently, in a bright field image, areas scattering more electrons will appear darker than area scattering less electrons. In materials without crystallinity such as amorphous polymer and biological tissues, mass-thickness contrast is the main source of contrast.

In crystalline materials, diffraction contrast aroused from the coherent elastic scattering of electrons can be used to study lattice defects such as dislocations. To

obtain a micrograph with diffraction contrast, sample needs to be carefully tilted to meet the two-beam condition when only one diffraction spot has intensity as strong as the unscattered beam [3].

Both mass-thickness contrast and diffraction contrast involve in changing the amplitude of electron waves. Therefore, they are classified as amplitude contrast. If the objective aperture is used to selected more than one beam, the micrograph will also contain phase contrast. In high resolution TEM (HRTEM), phase contrast is appeared as lattice fringes which are directly related to the periodicity of the real lattice. However, these lattice fringes are not direct images of the atomic structure. Extra caution is required when interpreting HRTEM images.

TEM images presented in this thesis were collected from two instruments. Micrographs in chapter 5 were collected using a FEI Tecnai G2 instrument equipped with a field emission gun operating at 300keV and a CCD camera to collect images. TEM images in other chapters were collected using a FEI Talos instrument equipped with a field emission gun operating at 200keV and a Ceta-M camera (CMOS sensor) to collect images. Twin-jet electropolishing method was used to make electron transparent area on samples with 3mm diameter and 80 microns thickness. Detailed experimental procedures are described in relevant chapters.

3.6 Small Angle X-ray Scattering

Scattering describes the process when an incident wave is forced to change from its original path by local heterogeneity. Visible light can be scattered by molecular particles in the atmosphere. As an example, Rayleigh scattering which is more effective at short wavelength result in the sky away from the sun showing blue colour. X-rays are scattered strongly by electrons. Compared to the visible light which has wavelength between $400 \sim 700\text{nm}$, X-ray which usually has a wavelength in the unit of angstrom (10^{-10}m) is the better choice of the incident light to investigate microstructure in the nanoscale.

Small angle scattering techniques collect the elastically scattered waves in the range of small angle, which contain the structural information of the scattering object. Unlike transmission electron microscopy which is mainly used to provide

local information with spatial resolution, small angle scattering is not an imaging technique. However, SAS can be applied on materials with large volume to provide statistical information of the investigated structure.

Particularly, small angle X-ray scattering has been proved as a promising technique to investigate precipitates in 7xxx and 2xxx aluminium alloys where an adequate electron density contrast exists between precipitates and the aluminium matrix [4]. The size, volume fraction and number density of precipitates can be efficiently obtained. Recent developments on the anomalous SAXS with variable X-ray wavelength may provide information related to the chemical composition of precipitates [5, 6, 7]. These quantitative data are invaluable to the understanding of materials' behaviour and the development of numerical models simulating materials' properties.

3.6.1 Theory

The wave factor of the incident radiation and scattered radiation are defined as k_i and k_s . The magnitude of them is defined by equation 3.2 where λ is the wavelength. Scattering vector q describes the difference between the incident and scattered wave vectors as shown in figure 3.5. The magnitude of q can be simply derived using equation 3.3.

$$|k_i| = |k_s| = \frac{2\pi}{\lambda} \quad (3.2)$$

$$|q| = \frac{4\pi \sin(\theta)}{\lambda} \quad (3.3)$$

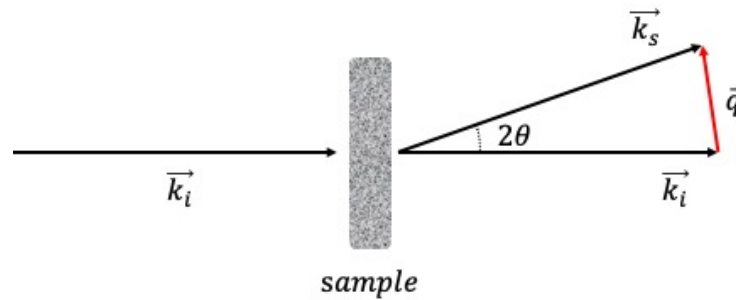


Figure 3.5: Schematic of the relationship between incident wave, scattered wave and scattering vector q .

For small angle scattering techniques, the scattering vector q is used to represent the scattering angle. The theoretical range of it is usually defined by the inter-atomic spacing of the investigated structure using equation 3.4 [8]. For pure aluminium with f.c.c structure, the inter-atomic spacing can be calculated using equation 3.5 where a is the lattice parameter (0.40478nm) and r is the atomic radius of the aluminium (143pm). This yields the scattering vector q in the range of $[0, 1.1] \text{ \AA}^{-1}$. Experimentally, the scattering range that can be practically collected is defined by the energy of the incident radiation and the camera configuration.

$$0 \leq q \leq \frac{\pi}{d_a} \quad (3.4)$$

$$d_a = 2r = \frac{a\sqrt{2}}{2} \quad (3.5)$$

The scattering amplitude (form factor) in a given direction is defined by equation 3.6, where $\rho(r)$ is electron density, V is the scattering volume and r is the position vector. In the isotropic scattering condition, scattering intensity written in equation 3.7 is defined as the square of the amplitude [6].

$$F(q) = \iiint_V f(r)\rho(r)\exp(-iqr)dV \quad (3.6)$$

$$I(q) = |F(q)|^2 = \left| \iiint_V f(r)\rho(r)\exp(-iqr)dV \right|^2 \quad (3.7)$$

Considering all orientations, the exponential term in equation 3.6 can be replaced by $\frac{\sin(qr)}{qr}$. Re-writing the intensity function with the auto-correlation of the electron density and replacing V with the equivalent radius, equation 3.8 can be obtained.

$$I(q) = V \int_V 4\pi r^2 \gamma(r) \frac{\sin(qr)}{qr} \quad (3.8)$$

For a spherical precipitate of radius R with a electron density contrast ($\rho_p - \rho_m$) from the matrix, the scattering intensity is given by equation 3.9. If multiple precipitates exist with a mean radius R and size distribution function $f(R)$, the total scattering intensity can be written as equation 3.10

$$I(q, R) = (\rho_p - \rho_m)^2 \left(\frac{4\pi R^3}{3} \right)^2 \left(3 \frac{\sin(qR) - qR \cos(qR)}{(qR)^3} \right)^2 \quad (3.9)$$

$$I(q, R) = (\rho_p - \rho_m)^2 \int_0^\infty f(R) \left(\frac{4\pi R^3}{3} \right)^2 \left(3 \frac{\sin(qR) - qR \cos(qR)}{(qR)^3} \right)^2 dR \quad (3.10)$$

3.6.2 Instruments

Small angle X-ray scattering experiments can be carried out using either laboratory based instruments or synchrotron facilities. The main difference between them is the X-ray source. For laboratory instruments, X-ray are usually generated by using a metal anode. Tungsten filament is used to generate high energy electrons which are then direct to the metal anode. If an accelerated electron has an energy above the excitation potential of the target metal atom, it will knock out an electron from the inner shell of the target atom [9]. An electron from the outer shell of the target atom will then jump down to fill the hole. Characteristic X-ray is emitted with energy equal to the difference between two orbits. Table 3.2 lists metals which are commonly used in laboratory to generate X-ray.

Table 3.2: Common laboratory metal anode used to generate X-ray [10]

Metal	$K_{\alpha 1}$ wavelength (Å)	$K_{\alpha 1}$ energy (keV)
Cu	1.5406	8.0478
Mo	0.7093	17.4799
Cr	2.2897	5.4147
Fe	1.9360	6.4038
Co	1.7890	6.9303
Ga	1.3401	9.2517

Using traditional metal anode to generate X-ray is usually inefficient. Only a small portion of the incident energy generates characteristic X-rays. The majority of the energy is converted to heat during the collision between accelerated electrons and the target metal anode [11]. To avoid melting of the metal anode, heat needs to be dissipated. For a fixed anode, the ability of the cooling system determines the flux of the X-ray. To improve the heat dissipation, it is ideal that the accelerated electrons not just bombard the same region of the metal anode. A rotating anode

(invented around 1930s) can generate X-rays with flux about one magnitude higher than a fixed anode [12].

Most recent development of the laboratory X-ray source (around 2000s) is liquid-metal-jet anode. Different to traditional metal anodes which have high melting temperatures, metals with low melting points (Gallium at 29.76 °C) are used for this type of X-ray source. Since the anode is working in the liquid state, accelerated electrons with much higher energy can be used to bombard the anode resulting in significantly improved X-ray flux ($\sim 100\times$ than rotating anode) [12].

When a moving electron is forced to bend from its original trajectory path, energy is emitted. If the speed of this moving electron is fast enough, energy will be emitted as X-rays. For a synchrotron facility, electrons are first generated and accelerated to millions of electron voltage using a linear particle accelerator (linac). These electrons are then ejected into the booster synchrotron where they are further accelerated to billions of electron voltage. Afterwards, these high energy electrons are sent to the storage ring which is made of straight sections angled together. Between adjacent straight sections, electromagnets are used to force the high speed electrons to travel though the storage ring under vacuum. Synchrotron X-rays generated in the storage ring will be channelled into each beamline where the X-ray beam will be filtered and focused in the optic hutch then passed down to the experimental hutch.

Regardless of whether the instrument is laboratory or synchrotron, once X-rays are generated, they will be direct to the monochromators which are used to narrow the energy of the beam to the selected value. Before exposing on the sample, slits are used to shape the beam size. A 2-dimensional detector is placed behind the sample to collect the transmitted scattered X-rays. For a dedicated SAXS beamline or a laboratory SAXS instrument, vacuum chamber is usually introduced between sample and detector to avoid signals from air scatterings.

In this thesis, laboratory SAXS experiments were performed on the following instruments:

1. A Bruker Nanostar instrument at the University of Sheffield is equipped with a Genix 3D microfocus $\text{CuK}\alpha$ source by Xenocs.
2. A Bruker Nanostar instrument at the University of Liverpool is equipped with a liquid gallium metal jet sourced by Excillum.

3. A Xeuss 3.0 instrument at Diamond Light Source (Diamond-Leeds facility) is equipped with a liquid gallium metal jet sourced by Excillum.

Synchrotron experiments were carried out at the Diamond Light Source UK using the following beamlines:

1. I12 is a high-energy beamline for imaging, diffraction and scattering. The incident X-rays are available with energy from 53 to 150keV. There are two primary advantages of this beamline. First, X-rays with high energy can penetrate thick samples. As an example, using laboratory SAXS instrument with Cu source to study precipitates in 7xxx aluminium alloys, samples thickness needs to be around 80 microns. Whereas at I12 beamline, scattering signals can be successfully collected from 1.5mm thickness using X-rays of 55keV energy. The second advantage is I12 can facilitate complex sample environments. In this thesis, an Instron electro-thermo-mechanical testing machine (ETMT) is used to perform tensile tests at warm temperature. However, I12 is not a dedicated SAXS beamline. One limitation is that no vacuum chamber is available to avoid air scatterings. Another limitation is that the camera length for SAXS experiment is fixed at 4.5m in the experimental hutch 1. This yields the minimum scattering vector of 0.055\AA^{-1} at 55keV X-rays.
2. I22 is a dedicated SAXS beamline operating at 7 to 20keV. I22 offers a flexible camera length from 1.9 to 9.9m with the increment of 0.25m under vacuum chamber [13]. This means I22 can access much lower scattering vector. As an example, when I22 is operated at 12.4keV energy with 3m camera length, the minimum scattering vector is 0.004\AA^{-1} . Furthermore, at I22, full range scattering profile can be obtained using two detectors placed with different camera lengths (SAXS and WAXS). Although X-rays at I22 with relatively low energy may potentially provide higher photon flux than I12, low energy X-rays also restrict the penetrable thickness. Another limitation of I22 is that only small sample environment can be facilitated. Large instruments such as ETMT can not be integrated onto the I22 beamline.

Detailed instrument configurations for each experiment are introduced in the related result chapter.

3.6.3 Data analysis

The scattering pattern of precipitates depends on their crystallographic structure. For precipitates with a strong crystallographic preference and aspect ratio, scattering spikes can be observed. An example of this is θ' and T_1 phases in Al-Cu-Li-Mg system (figure 3.6). For precipitates without a strong aspect ratio but having a crystallographic preference, spikes may be observed when SAXS is performed on a single crystal. If scattering signals are collected from multi-grains with different orientations, an isotropic scattering ring is usually observed. An example of this is η' phase in Al-Zn-Mg-Cu system (figure 3.7).

For anisotropic scattering pattern, data analysis usually involves studying the shape, angle and intensity of each spike [14]. In the present study, only isotropic scattering pattern is of interest. One-dimensional data can be calculated by circular averaging the scattering intensity at each scattering vector q .

$$I_{raw}q^4 = K_p + I_{Laue}q^4 \quad (3.11)$$

Air scattering (due to the lack of vacuum), isotropic scattering of disordered solid solution and fluorescence of secondary elements are considered as background noise ($I_{air} + I_{Laue}$) in SAXS measurements [6]. To eliminate the negative effect on the data, pure aluminium with the same thickness as the investigated sample was used as the reference sample. Under the same experimental configuration, the scattering intensity of the pure aluminium is subtracted from the scattering intensity of the investigated sample. When air scattering is not a concern (under sufficient vacuum environment), the background noise (I_{Laue}) can be determined by plotting Iq^4 as a function of q (equation 3.11, where the intercept K_p is referred as the Porod constant) [6].

In practice, the overall scattered intensity can frequently be accurately represented using equation 3.12, which indicates that the scattered intensity is directly proportional to several key factors. These factors include the number of scattering particles present (N_p), the volume of these particles (V_p), the electron density contrast ($\rho_p - \rho_m$) between the particles and the surrounding matrix (or solvent), as well as the form factor ($F(q)$) and structure factor ($S(q)$).

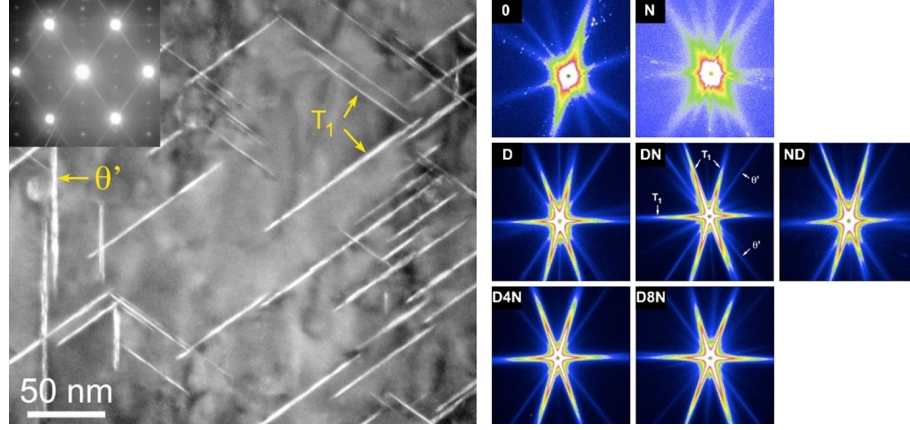


Figure 3.6: TEM micrograph and SAXS images of θ' and T_1 phases in a Al-Cu-Li-Mg system [15] (Copyright obtained from John Wiley and Sons).

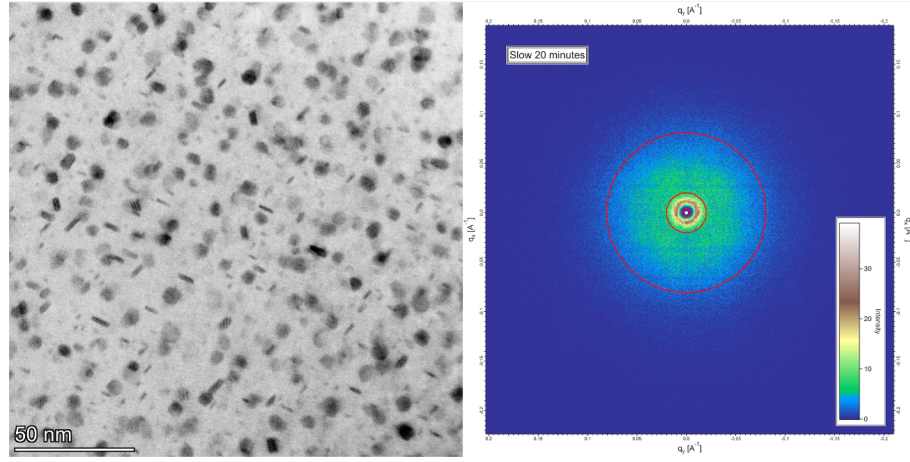


Figure 3.7: Bright field STEM micrograph ($\langle 110 \rangle$ zone axis) and SAXS image of η' phase in a Al-Zn-Mg-Cu system.

$$I(q) = N_p V_p^2 (\rho_p - \rho_m)^2 F(q) S(q) \quad (3.12)$$

The form factor is responsible for describing the shape of the scattering particles, providing crucial information about their geometric arrangement and dimensions. On the other hand, the structure factor, also known as structure interference, accounts for the effects of inter-particle interactions. In an ideal dilute solution, where particles are mono-dispersed and exhibit no significant interactions, the structure factor $S(q)$ is equal to unity. Consequently, in such ideal conditions, the overall scattered intensity $I(q)$ solely arises from the form factor $F(q)$, simplifying the analysis and interpretation of scattering data. By plotting the data as intensity versus scattering vector q in a logarithm scale, the presence of structural interference can

be directly identified as a peak. In 7xxx aluminium alloys, this interference is often observed in early-stage precipitation when precipitates are relatively small. As the precipitates grow larger in peak aged or over-aged conditions, the interference effect becomes less pronounced.

Even in cases where structural interference is negligible, fitting the experimental scattering profile using equation 3.12 to obtain detailed information about the investigated system can still be a challenging task. The form factor, which is a crucial component of equation 3.12, depends on the shape of the scattering particles. Different particle shapes have different form factor expressions, as summarized in Table 3.3 for common geometries.

Table 3.3: Form factors for common geometries [16]

Geometry	Form factor $F(q)$
Spheres (radius: R)	$(3 \frac{\sin(qR) - qR \cos(qR)}{(qR)^3})^2$
Cylinders (radius: R , length: L)	$4 \int_0^1 \frac{J_1^2(qR\sqrt{1-x^2})}{(qR\sqrt{1-x^2})^2} \frac{\sin^2(qLx/2)}{(qLx/2)^2} dx$
Thin disk (radius: R , length: 0)	$\frac{2 - J_1(2qR)/qR}{q^2 R^2}$

$J_1(x)$ is the first kind Bessel function of order 1

When dealing with poly-disperse spherical particles with radius R and a size distribution function $f(R)$, a simplified expression such as equation 3.10 can be used to fit the overall scattering intensity. However, in more complex systems with non-spherical or irregularly shaped particles, obtaining a precise fit using equation 3.12 can be considerably more challenging.

Overall, while the analysis of scattering data using equation 3.12 can provide valuable insights into the microstructure of materials, it is essential to be aware of the potential challenges and limitations, especially in cases involving non-spherical particles or complex systems with apparent structural interference. Moreover, in many situations, especially with in-situ experiments or high-throughput data col-

lection, the amount of scattering data to be analysed can be vast. Using equation 3.12 to analyse large datasets will require significant computing power to process the information in a reasonable time frame.

Therefore, in the present study, we employed the Guinier approximation as an alternative method to efficiently evaluate the size of precipitates. However, it is important to note that this method does not account for the geometry and size distribution of the investigated particles. Specifically, when using the Guinier radius to study the evolution of precipitates, errors may arise if the aspect ratio and size distribution of precipitates undergo significant changes during the investigated process.

Guinier radius

Signals of SAXS are resulted from the electron density contrast between precipitates and the aluminium matrix. Guinier approximation (equation 3.13) describes that signals at low scattering vector q can be used to characterise the overall size of the particles. R_g is referred as gyration radius or Guinier radius describing the average electron density weighted size of the particles. Converting equation 3.13 from its exponential form to the logarithmic form (equation 3.14) and plotting $\ln(I)$ as a function of q^2 , the Guinier radius can be calculated using the slope $(-\frac{1}{3}R_g^2)$. Theoretically, Guinier approximation is only valid in the range of $q R_g < 1$. Although studies have found the valid range may be extended to $1.7 < q R_g < 2.6$ [17], defining the straight regime to perform fitting of equation 3.14 is not practically simple.

$$I = I_0 \exp\left(-\frac{1}{3}R_g^2 q^2\right) \quad (3.13)$$

$$\ln(I) = \ln(I_0) - \frac{1}{3}R_g^2 q^2 \quad (3.14)$$

Another convenient way to evaluate Guinier radius is using the Kratky plot (Iq^2 as a function of q). The maximum value of Iq^2 can be indexed. The corresponded scattering vector q is used to calculate the Guinier radius (equation 3.15). It has been proved this method can provide reliable Guinier radius in 7xxx aluminium alloys [6, 17, 18].

$$R_g = \frac{\sqrt{3}}{q_{max}} \quad (3.15)$$

Guinier radius does not provide information about the shape of the precipitates being investigated. For spherical precipitates, equation 3.16 can be used to calculate the real radius [6]. For plate shape precipitates, real radius is calculated using equation 3.17 where t is the thickness [4]. For an ellipsoid with radius of a , b and c on the three semi-axis, equation 3.18 is used. Although these equations are theoretically restricted to condition of mono-dispersed precipitates, numerical and experimental studies have found the Guinier radius in a poly-dispersed system is very close to the mean radius [19, 20].

$$R_g = \sqrt{\frac{3}{5}} R_{real} \quad (3.16)$$

$$R_g = \sqrt{\frac{2 + (t/R_{real})^2}{5}} R_{real} \quad (3.17)$$

$$R_g = \sqrt{\frac{a^2 + b^2 + c^2}{5}} \quad (3.18)$$

Volume fraction

To accurately calculate the precipitate volume fraction (V_f), it requires the knowledge of the electron density contrast ($\Delta\rho$) between precipitates and the aluminium matrix. Due to the extremely small size of GP zones and η' , their chemical compositions are difficult to be determined. The exact stoichiometry is still under investigation. For the benefit of simplicity, the precipitate composition is assumed to be near constant [6, 17, 18, 21, 22], the integrated intensity of the Kratky plot (equation 3.19) is proportional to the precipitate volume fraction as shown in equation 3.20.

$$Q = \int_0^\infty I q^2 dq \quad (3.19)$$

$$Q = 2\pi^2 \Delta\rho^2 V_f (1 - V_f) \quad (3.20)$$

It is clear that scattering vector is not experimental accessible from 0 to the

infinity. In fact, every SAXS instrument has its minimum accessible scattering vector q_{min} and maximum accessible scattering vector q_{max} . Mathematical integration of Iq^2dq can be performed within this range (equation 3.21).

$$Q_2 = \int_{q_{min}}^{q_{max}} Iq^2dq \quad (3.21)$$

The scattering intensity at q smaller q_{min} is overlapped by the beam-stop or the direct transmitted beam. An linear evolution of the scattering intensity is assumed from 0 to $I(q_{min})$. The integrated intensity in this small region can, therefore, be estimated as the area of an triangle (equation 3.22).

$$Q_1 = \frac{I_{q_{min}}q_{min}^3}{2} \quad (3.22)$$

The scattering intensity at scattering vector larger than q_{max} is assumed to follow the Porod law (equation 3.11) [6]. The integrated intensity in this region can be estimated using equation 3.23, where K_p is the intercept from the linear fitting of equation 3.11.

$$Q_3 = \int_{q_{max}}^{\infty} \frac{K_p}{q^2}dq = \frac{K_p}{q_{max}} \quad (3.23)$$

The total integrated intensity of the Kratky plot is given by the sum of these three terms as shown in equation 3.24.

$$Q = Q_1 + Q_2 + Q_3 = \frac{I_{q_{min}}q_{min}^3}{2} + \int_{q_{min}}^{q_{max}} Iq^2dq + \frac{K_p}{q_{max}} \quad (3.24)$$

Number density

Number density describes the number of precipitates per unit volume. This gives an indication of the precipitation status. When nucleation is dominant, the precipitation of new clusters leads to an increase of the number density. The growth of precipitates does not change the number density. An plateau is, therefore, expected when the growth of existing precipitates is in dominant. The coarsening process relies on the dissolution of precipitates with sizes smaller than the critical value. The released solutes are then contributed to the growth of precipitates with sizes larger than the critical value. In the regime of coarsening, an decrease of the number

density is expected.

The average number density can be estimated from the average radius and the volume fraction. For spherical precipitates with an average radius of R_{mean} and a volume fraction of V_f , the average number density is given by equation 3.25.

$$N = \frac{V_f}{\frac{4\pi R_{mean}^3}{3}} \quad (3.25)$$

3.7 Differential Scanning Calorimetry

Differential scanning calorimetry (DSC), which is classified as a thermal analysis technique, measures the heat evolution during a controlled temperature program [23]. The mechanism of DSC relies on monitoring the difference of heat that is required for tested and referenced sample to reach the same temperature.

DSC has been extensively used in studying the phase transformation of aluminium alloys, especially the precipitation hardened series. Although DSC has the capability to identify physical properties such as melting temperature, crystallisation temperature and activation energy of an Arrhenius type reaction [23], this section is mainly focused on the application of DSC on investigating precipitation in 7xxx aluminium alloys, when most of the DSC experiments can be classified into the following two purposes:

1. Identify the precipitation population in a pre-aged sample before entering a controlled DSC heating program.
2. Investigate the precipitation evolution in a supersaturated or pre-aged sample during a controlled DSC heating program.

In this thesis, all calorimetry experiments were conducted on a TA instrument Q1000 machine. This equipment has a temperature range from -180 to 725 °C (when cooling accessory is available) with an accurate temperature control of ± 0.1 °C and a fast heating rate up to 200 °C per minute. This machine also has a small furnace which is ideal for a quick acceleration of the heating rate to limit the initial transient period. For all calorimetry experiments presented in this thesis, pure aluminium was

taken as the reference sample to correct the baseline drift. Detailed heating rate, target temperature and isothermal holding time are provided in the relevant chapter.

3.7.1 Identification of precipitation

When DSC is used to identify the precipitation population in a pre-aged aluminium alloy, the temperature program is usually set with a relatively fast heating rate (e.g. 20 °C per minute) to avoid precipitation during the heating event in DSC. Dissolution of precipitates is an endothermic reaction requiring additional energy from the environment. For 7xxx aluminium alloys, a broadened endothermic peak at temperature below 160 °C is associated to the dissolution of GP zones [24]. A relatively narrowed endothermic peak at temperature around 180 ~ 250 °C is usually expected to be the dissolution of metastable η' phase [24, 25, 26]. A widely broadened endothermic peak above 300 °C corresponds to the dissolution of stable η phase [24, 25, 26].

Studying dissolution peaks is not a simple task. Firstly, precipitates in aluminium alloys do not have clearly separated dissolution and precipitation peaks. Particularly for GP zones, where there is a large overlap on the precipitation and dissolution temperature range, it is rare to observe both peaks in one sample. Secondly, even for the same phase, the onset temperature of dissolution can be affected by other factors. Large precipitates tend to have higher dissolution temperature than small precipitates [25]. Faster heating rate shifts the peak to the higher temperature [23]. These all add challenges to the interpretation of peaks. Thirdly, DSC does not identify the phase involved in the phase transformation reaction [23]. For a well-studied alloy system (such as 7xxx aluminium alloys), the temperature range of each potential reaction can be found in literature or thermodynamic database. For a new developed alloy system, other techniques, such as high resolution electron microscopy and 3D atom probe tomography, are required to further characterise the sample and provide conclusive information.

3.7.2 Investigation of precipitation evolution

When the main objective is to study the precipitation evolution during a thermal event, DSC can be used to simulate this heating profile. In this case, a relatively

slow heating rate (e.g. 5 °C per minute) is usually programmed to facilitate both precipitation and dissolution. If the sample is supersaturated (e.g. solution heat treated followed by water quenched), the whole precipitation sequence can be studied from the beginning. The first peak is, therefore, expected to be the exothermic precipitation peak of GP zones, which is usually at temperature below 120 °C. If the sample has been pre-aged before the DSC scanning, the purpose is then to study the evolution of these pre-existing precipitates.

DSC can also be applied to study the precipitation evolution during an isothermal heat treatment. A fast heating rate (e.g. 30 °C per minute) is usually used to quickly reach the target temperature. Afterwards, the sample is isothermally held at this temperature for a period of time during which the heat flow signal is recorded. Contradict to the traditional DSC plots where heat flow is shown as a function of temperature, heat flow is plotted against time to study the kinetics of reaction(s) at a specific temperature.

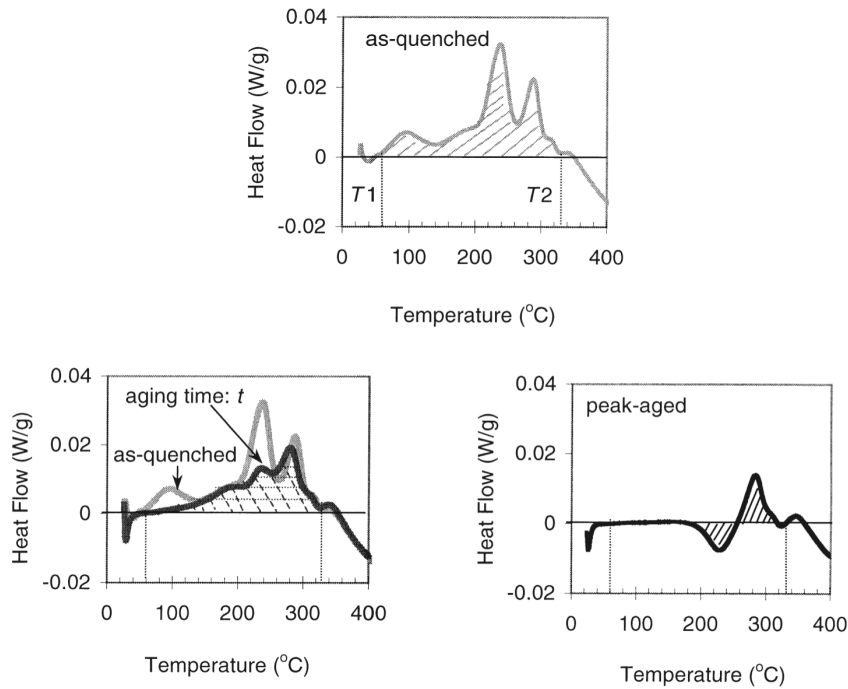


Figure 3.8: Estimating relative volume fraction of precipitates using DSC [27] (Copyright obtained from Springer Nature)

$$V_f = \frac{A_{SSSS} - A_{pre-aged}}{A_{SSSS} - A_{peak-aged}} \quad (3.26)$$

Both differential scanning calorimetry and isothermal calorimetry can be used to

quantitatively study precipitation. The integration of the heat flow curve provides information of the precipitate volume fraction. For differential scanning calorimetry, Esmacili et al. developed a simple method to calculate the relative volume fraction of a pre-aged sample, as shown in figure 3.8. The integrated area of heat flow curve between temperature T_1 and T_2 is assumed to represent the net heat evolution of the overall precipitation and dissolution [27]. The precipitation process is assumed to have been completed in the peak-aged sample. The as quenched sample is assumed to be fully supersaturated without any precipitation. Equation 3.26 is used to estimate the relative volume fraction of precipitation in a pre-aged sample [27]. A_{SSSS} , $A_{peak-aged}$ and $A_{pre-aged}$ are respectively the integrated area of as quenched, peak-aged and pre-aged sample.

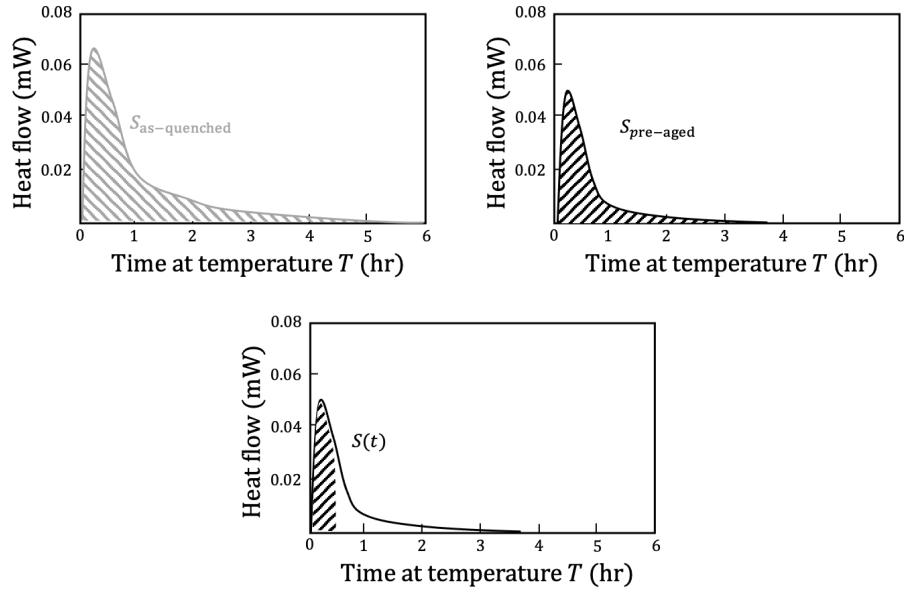


Figure 3.9: Measuring the evolution of relative volume fraction of precipitates using isothermal calorimetry

$$V_f = \frac{S_{as-quenched} - S_{pre-aged}}{S_{as-quenched}} + \frac{S(t)}{S_{as-quenched}} \quad (3.27)$$

Apart from estimating the relative volume fraction of precipitate in the pre-aged sample, it is also possible to identify precipitates pre-existed in the pre-aged sample, if the temperature range of each dissolution peak is well studied. However, it is difficult to obtain kinetics information from this method. For example, if the evolution of the relative volume fraction during an ageing process is of interest, multiple samples with different ageing time need to be prepared. In such case,

isothermal calorimetry is the alternative option [27, 28]. The integration of heat flow as a function of time represents the evolution of precipitate volume fraction. As shown in figure 3.9, the whole integrated area of the as quenched sample is assumed to be the measure of the maximum possible precipitation at temperature T . With sufficient holding time t , the whole integrated area of the pre-aged sample is assumed to be maximum remaining precipitation. The difference between them reflects the precipitation in the pre-aged sample before entering into the isothermal calorimetry. Equation 3.27 is used to estimate the evolution of the relative volume fraction during the isothermal holding at temperature T . The first term of equation 3.27 represents the initial relative volume fraction of precipitate before entering into the calorimetry. The second term considers the additional relative volume fraction gained from isothermally ageing at temperature T with time t in the calorimetry. It is clear in equation 3.27 $S(t)$ is a function of time. Therefore, isothermal calorimetry can provide a continuous measurement of the evolution of the relative precipitate volume fraction at temperature T from a single sample, which is considerably more efficient than using differential scanning calorimetry with multiple samples.

3.8 X-ray Diffraction - Line broadening

X-ray diffraction is a powerful technique in studying crystal symmetry where the periodicity of atoms gives lattice structure. The underpinning scattering theory is the same between SAXS and XRD, that X-rays can be elastically scattered by electrons. The difference is that in XRD only waves that were scattered by lattice planes and underwent constructive interference are of interest.

$$n\lambda = 2d\sin\theta \quad (3.28)$$

Bragg's Law (equation 3.28) defines the relationship between lattice spacing (d), diffraction angle (θ), X-ray wavelength (λ), and diffraction order (n). When measuring the scattering intensity as a function of scattering angle, diffraction peaks are only visible when the scattering angle satisfies the Bragg's condition. By analysing these diffraction peaks, the crystallographic structure can be obtained.

Although an infinite crystal should theoretically result in only diffraction lines

without widths at discrete diffraction angles, in reality, experimental diffraction peaks are always broadened by instrument and specimen effects. The effects of the instrument on peak broadening can usually be well-defined by using standard lanthanum hexaboride (such as LaB_6). The specimen effects can be further classified into the effect of crystallite size (finite crystals) and the effect of strain. In metals, there could be many sources of strain, such as dislocations, point defects, and chemical heterogeneities [29]. Therefore, apart from being extensively used for phase identification, XRD is also a powerful tool for defect analysis. In 7xxx aluminium alloys, the diffraction peaks of strengthening precipitates are extremely weak due to their small size and volume fraction. It is usually not an effective way to determine the existence of these strengthening phases in the microstructure. In this study, we are only interested in analyzing line defects using the strong diffraction peaks from the aluminium matrix.

When dislocations are the major source of strain causing the lattice distortion, the dislocation density may be estimated from analyzing the broadened diffraction peaks. The modified Williamson-Hall plot (equation 3.29) can be used to evaluate this effect on the full widths at half maximum (FWHM) [30]. By plotting ΔK as a function of $K\sqrt{C}$ and fitting a straight line, the slope is used to estimate the dislocation density.

$$\Delta K = \frac{0.9}{D} + \frac{\pi M^2 b^2}{2} \rho^{1/2} K^2 C + O(K^4 C^2) \quad (3.29)$$

K is equal to $2\sin\theta/\lambda$. D is referred as size parameter. C is the dislocation contrast factor. ρ is the dislocation density. b is Burgers vector. M is a parameter depending on the arrangement of dislocation. O is a higher-order term. C is the dislocation contrast factor for each hkl diffraction (equation 3.30 [31]).

$$C = C_{av} \left[1 - q \left(\frac{h^2 k^2 + h^2 l^2 + k^2 l^2}{h^2 + k^2 + l^2} \right) \right] \quad (3.30)$$

C_{av} is the average dislocation contrast factor depends on the portion of screw and edge dislocations. In most previous studies, it is assumed an equal amount of screw and edge dislocations [30, 31, 32, 33]. For pure screw and pure edge conditions, the dislocation contrast factor can be calculated using equation 3.31 [31].

$$\overline{C}_{h00} = a[1 - \exp(\frac{-A_i}{b})] + cA_i + d \quad (3.31)$$

A_i is the elastic anisotropy, as shown in equation 3.32 [31]. For aluminium at room temperature, c_{11} , c_{12} and c_{44} are summarised in table 3.4. In equation 3.31, the value of a, b, c and d depend on the ratio of c_{12} to c_{44} . In the case of aluminium at room temperature, they are summarised in table 3.5 [31].

$$A_i = \frac{2c_{44}}{c_{11} - c_{12}} \quad (3.32)$$

Table 3.4: Elastic constants of aluminium at room temperature [34]

c_{11}	c_{12}	c_{44}
107	60.9	28.3

Table 3.5: The parameters a,b,c and d for equation 3.31 [31]

	a	b	c	d
Screw	0.1740	1.9522	0.0293	0.0662
Edge	0.2438	2.4243	0.0172	0.0816

As shown in equation 3.29, the reliability of this method is affected by the number of data points. The best practice in a laboratory instrument with a $\text{CuK}\alpha$ radiation gives 9 diffraction peaks in the 2θ range from 20° to 140° . The miller indices of these lattice planes, the calculated lattice spacing d and the calculated diffraction angle 2θ are summarised in table 3.6.

Using modified Williamson-Hall plot to estimate dislocation density is limited by the the parameter M in equation 3.29, which is not experimentally obtainable. Most previous studies assume a constant value in the range from 1 to 2 for dislocation density in the range from 1×10^{14} to 5×10^{15} [33, 35]. In this thesis for the purpose of simplification,, M is assumed as 1. The interpretation of modified Williamson-Hall plot is qualitative rather than quantitative.

Table 3.6: Calculated diffraction peaks of aluminium ($\lambda = 0.15406\text{nm}$, $a = 0.40478\text{nm}$)

2θ ($^\circ$)	Miller indices	Lattice spacing $d(\text{\AA})$
38.490	(111)	2.3370
44.742	(200)	2.0239
65.130	(220)	1.4311
78.268	(311)	1.2205
82.481	(222)	1.1685
99.147	(400)	1.0119
112.100	(331)	0.9286
116.656	(420)	0.9051
137.570	(422)	0.8263

Bibliography

- [1] J. A. Österreicher, M. A. Tunes, F. Grabner, A. Arnoldt, T. Kremmer, S. Pogatscher, C. M. Schlögl, Warm-forming of pre-aged Al-Zn-Mg-Cu alloy sheet, *Materials & Design* 193 (2020) 108837.
- [2] A. K. Ackerman, A. J. Knowles, H. M. Gardner, A. A. Németh, I. Bantounas, A. Radecka, M. P. Moody, P. A. Bagot, R. C. Reed, D. Rugg, et al., The kinetics of primary alpha plate growth in titanium alloys, *Metallurgical and Materials Transactions A* 51 (1) (2020) 131–141.
- [3] D. B. Williams, C. B. Carter, The transmission electron microscope, in: *Transmission electron microscopy*, Springer, 1996, pp. 3–17.
- [4] G. Fribourg, Precipitation and plasticity couplings in a 7xxx aluminium alloy: application to thermomechanical treatments for distortion correction of aerospace component, Ph.D. thesis, Institut National Polytechnique de Grenoble-INPG (2009).
- [5] G. Goerigk, H.-G. Haubold, O. Lyon, J.-P. Simon, Anomalous small-angle x-ray scattering in materials science, *Journal of applied crystallography* 36 (3) (2003) 425–429.
- [6] F. De Geuser, A. Deschamps, Precipitate characterisation in metallic systems by small-angle x-ray or neutron scattering, *Comptes Rendus Physique* 13 (3) (2012) 246–256.

- [7] T. Marlaud, A. Deschamps, F. Bley, W. Lefebvre, B. Baroux, Influence of alloy composition and heat treatment on precipitate composition in al-zn-mg-cu alloys, *Acta Materialia* 58 (1) (2010) 248–260.
- [8] V. Gerold, G. Kostorz, Small-angle scattering applications to materials science, *Journal of Applied Crystallography* 11 (5) (1978) 376–404.
- [9] E. P. Bertin, *Introduction to X-ray spectrometric analysis*, Springer Science & Business Media, 2013.
- [10] J. A. Bearden, A. Burr, Reevaluation of x-ray atomic energy levels, *Reviews of Modern Physics* 39 (1) (1967) 125.
- [11] G. Michael, X-ray computed tomography, *Physics Education* 36 (6) (2001) 442.
- [12] O. Hemberg, M. Otendal, H. Hertz, Liquid-metal-jet anode electron-impact x-ray source, *Applied Physics Letters* 83 (7) (2003) 1483–1485.
- [13] A. Smith, S. Alcock, L. Davidson, J. Emmins, J. Hiller Bardsley, P. Holloway, M. Malfois, A. Marshall, C. Pizzey, S. Rogers, et al., I22: SAXS/WAXS beam-line at diamond light source—an overview of 10 years operation, *Journal of Synchrotron Radiation* 28 (3) (2021).
- [14] A. Deschamps, F. De Geuser, Quantitative characterization of precipitate microstructures in metallic alloys using small-angle scattering, *Metallurgical and Materials Transactions A* 44 (1) (2013) 77–86.
- [15] B. Decreus, A. Deschamps, F. de Geuser, C. Sigli, Influence of natural ageing and deformation on precipitation in an al-c u-l i alloy, *Advanced Engineering Materials* 15 (11) (2013) 1082–1085.
- [16] L. Feigin, D. I. Svergun, et al., *Structure analysis by small-angle X-ray and neutron scattering*, Vol. 1, Springer, 1987.
- [17] A. Deschamps, F. Bley, F. Livet, D. Fabregue, L. David, In-situ small-angle x-ray scattering study of dynamic precipitation in an al-zn-mg-cu alloy, *Philosophical Magazine* 83 (6) (2003) 677–692.

- [18] A. Deschamps, G. Fribourg, Y. Brechet, J. L. Chemin, C. Hutchinson, In situ evaluation of dynamic precipitation during plastic straining of an al–zn–mg–cu alloy, *Acta materialia* 60 (5) (2012) 1905–1916.
- [19] M. Dumont, A. Steuwer, A. Deschamps, M. Peel, P. Withers, Microstructure mapping in friction stir welds of 7449 aluminium alloy using saxs, *Acta materialia* 54 (18) (2006) 4793–4801.
- [20] A. Deschamps, F. De Geuser, On the validity of simple precipitate size measurements by small-angle scattering in metallic systems, *Journal of Applied Crystallography* 44 (2) (2011) 343–352.
- [21] A. Deschamps, Y. Brechet, P. Guyot, E. Livet, On the influence of dislocations on precipitation in an al–zn–mg alloy, *Stal* 1 (1) (1997) 1–1.
- [22] C. Hutchinson, F. De Geuser, Y. Chen, A. Deschamps, Quantitative measurements of dynamic precipitation during fatigue of an al–zn–mg–(cu) alloy using small-angle x-ray scattering, *Acta materialia* 74 (2014) 96–109.
- [23] M. Starink, Analysis of aluminium based alloys by calorimetry: quantitative analysis of reactions and reaction kinetics, *International Materials Reviews* 49 (3-4) (2004) 191–226.
- [24] R. A. Nolan, Microstructure Formability Relationships in New Generation High Strength Aluminium Automotive Alloys, The University of Manchester (United Kingdom), 2015.
- [25] X. Li, M. J. Starink, Analysis of precipitation and dissolution in overaged 7xxx aluminium alloys using dsc (2000).
- [26] P. Lang, T. Wojcik, E. Povoden-Karadeniz, A. Falahati, E. Kozeschnik, Thermo-kinetic prediction of metastable and stable phase precipitation in al–zn–mg series aluminium alloys during non-isothermal dsc analysis, *Journal of Alloys and Compounds* 609 (2014) 129–136.
- [27] S. Esmacili, X. Wang, D. Lloyd, W. Poole, On the precipitation-hardening behavior of the Al–Mg–Si–Cu alloy AA6111, *Metallurgical and Materials Transactions A* 34 (13) (2003) 751–763.

- [28] S. Esmaeili, D. J. Lloyd, Characterization of the evolution of the volume fraction of precipitates in aged AlMgSiCu alloys using DSC technique, *Materials characterization* 55 (4-5) (2005) 307–319.
- [29] Measurement methods — structural properties: X-ray and neutron diffraction, in: J. Garche (Ed.), *Encyclopedia of Electrochemical Power Sources*, Elsevier, Amsterdam, 2009, pp. 718–737.
- [30] T. Ungár, Dislocation densities, arrangements and character from x-ray diffraction experiments, *Materials Science and Engineering: A* 309 (2001) 14–22.
- [31] T. Ungár, I. Dragomir, Á. Révész, A. Borbély, The contrast factors of dislocations in cubic crystals: the dislocation model of strain anisotropy in practice, *Journal of applied crystallography* 32 (5) (1999) 992–1002.
- [32] T. Ungár, J. Gubicza, P. Hanák, I. Alexandrov, Densities and character of dislocations and size-distribution of subgrains in deformed metals by x-ray diffraction profile analysis, *Materials Science and Engineering: A* 319 (2001) 274–278.
- [33] R. Renzetti, H. Sandim, R. Bolmaro, P. Suzuki, A. Möslang, X-ray evaluation of dislocation density in ods-eurofer steel, *Materials Science and Engineering: A* 534 (2012) 142–146.
- [34] J. Bozek, J. Hochhalter, M. Veilleux, M. Liu, G. Heber, S. Sintay, A. Rollett, D. Littlewood, A. Maniatty, H. Weiland, et al., A geometric approach to modeling microstructurally small fatigue crack formation: I. probabilistic simulation of constituent particle cracking in aa 7075-t651, *Modelling and Simulation in Materials Science and Engineering* 16 (6) (2008) 065007.
- [35] G. Ribárik, T. Ungár, Characterization of the microstructure in random and textured polycrystals and single crystals by diffraction line profile analysis, *Materials Science and Engineering: A* 528 (1) (2010) 112–121.

Chapter 4

Dynamic Precipitation in Supersaturated Al-Zn-Mg-Cu during Warm Stretching

J. D. Robson¹, P. Jessner², M. Taylor¹, Z. Ma¹

1 – Department of Materials, University of Manchester, Manchester,
M13 9PL, UK

2 – Constellium Technology Center, 38341 Voreppe Cedex, France

Published at Metallurgical and Materials Transactions A, 2023, Page 1-11. Z.Ma: Conceptualization, Methodology, Investigation, Formal analysis, Writing - Original Draft, Writing - Review & Editing. M.Taylor: Investigation. P.Jessner: Writing - Review & Editing, Resources. J.D.Robson: Conceptualization, Methodology, Investigation, Formal analysis, Writing - Original Draft, Writing - Review & Editing and Supervision.

Abstract

High strength Al-Zn-Mg-Cu alloys such as AA7075 rely on precipitation to obtain their properties, and the evolution of these precipitates can be strongly influenced by deformation. In this study, the effect of warm stretching on precipitation in supersaturated AA7075 was investigated. A dilatometer was used to enable rapid quenching directly from the solution treatment temperature to the warm stretching temperature. The evolution of precipitates was monitored using small angle x-ray scattering (SAXS) and transmission electron microscopy (TEM). SAXS revealed the presence of clusters only 5 s after quenching, and the subsequent evolution of the microstructure involved the growth and coarsening of these clusters. Deformation strongly enhanced the cluster/precipitate growth rate, which increased linearly with increasing strain. A strain rate effect was also noted, with the growth rate being faster at the higher strain rate for the same strain level. However, the acceleration of growth with increasing strain rate was not sufficient to compensate for the reduced time, so that deformation at higher strain rate led to small precipitates (at iso-strain). TEM revealed the precipitates to be homogeneously dispersed in the matrix both with and without deformation. There was no evidence for enhanced nucleation due to deformation, indeed the opposite was the case, with fewer but larger precipitates observed in the deformed microstructure. The linear increase in growth rate with strain is consistent with a dominant effect of excess vacancies in enhancing diffusion rates.

4.1 Introduction

Strong aluminium alloys obtain their properties through the formation of a controlled distribution of nano-scale precipitates. It is now well established that deformation can profoundly influence the evolution of these precipitates [1, 2, 3, 4]. The coupled effect of deformation and temperature on the precipitates in aluminium alloys is particularly important in warm forming, creep age forming, high pressure torsion, and fatigue, where strong dynamic interactions can occur [1, 2, 3, 5, 6, 7].

It has previously been demonstrated that the growth of a pre-existing precipitate population can be greatly enhanced by warm deformation [2, 4]. In these studies, a dominant role for strain induced excess vacancies was identified in enhancing diffusivity [2, 3, 6, 8]. Excess vacancies are produced by the non-conservative movement of jogs on dislocations, consuming a small portion of the applied mechanical work [9, 10]. The excess vacancies influence diffusivity and other kinetic processes governing precipitation [3]. Further details of the excess vacancy effect are given elsewhere [11].

One important factor in determining which dynamic effects will be observed is the initial microstructural state of the material and in particular the level of supersaturation at the deformation temperature. Most previous studies have focussed on material deformed in a pre-tempered condition where there is an existing distribution of precipitates [2]. Even in cases where the initial starting condition of the material was solution treated and quenched, the natural ageing that occurs in aluminium alloys plus the rapid initial precipitate evolution during heating means that significant changes will occur before deformation is applied [4]. In such cases, it has been demonstrated that the main effect of deformation is to accelerate the growth and coarsening of the existing precipitates rather than nucleate new particles. On the other hand, at room temperature, it has been shown that cyclic deformation of an initially supersaturated matrix leads to accelerated decomposition through the nucleation of new GP zones [3, 6]. The significance of deformation on nucleation versus accelerated growth of precipitates is not yet established for the industrially important case of warm deformation, where the initial condition is strongly supersaturated.

A key aim of the present study was to investigate the effect of warm deformation on precipitate evolution in a case where the initial matrix is as supersaturated as possible. In an industrial context, this would be most relevant in a case where forming occurs directly after solution treatment. To achieve this, the final solution treatment and warm deformation must be performed in a combined process so that precipitation does not occur between steps by natural ageing or during pre-heat.

4.2 Methodology

The material used in this study was 7075 aluminium alloy sheet of 1.5 mm thickness produced from commercially direct-chill cast and rolled plate, supplied in the F temper (as fabricated) by Constellium Technology Center (France) with the nominal composition shown in Table 6.1.

Table 4.1: Nominal composition of AA7075 in wt.%

	Zn	Mg	Cu	Si	Fe	Mn	Cr	Al
AA7075	5.6	2.5	1.6	0.2	0.25	0.15	0.23	Bal

Deformation and heating were performed using a TA Instruments DIL 805 A/D/T dilatometer. This instrument allows accurate temperature control (to within 0.1°C), rapid specimen heating and cooling (up to $100^{\circ}\text{C s}^{-1}$ when working in the tension mode) and controlled strain rates of up to 1 s^{-1} . The sample geometry for testing in the dilatometer is shown in Figure 4.1.

Prior to loading in the dilatometer solution heat treatment was first performed at 480°C in an air recirculating furnace for 1.5 h, followed by water quenching to room temperature. This dissolves the large precipitates present in the F-temper condition and reduces the time necessary to achieve a fully solutionized condition in the dilatometer.

To reverse any undesired natural ageing during the transport and equipment setup, specimens were subject to a second short solution treatment of 10 minutes in the dilatometer itself at the same temperature of 480°C (using a heating rate of $10^{\circ}\text{C s}^{-1}$). Samples were subsequently gas quenched (using nitrogen) to 180°C followed by an additional 5 seconds holding to stabilise the temperature. The aim was to minimize the precipitation that occurs before applying deformation.

Two deformation strain rates were used, with an approximately order of magnitude difference. Average strain rates were calculated by fitting a linear function on the strain-time plot. Nominal average strain rates of $7 \times 10^{-4} \text{ s}^{-1}$ and $6 \times 10^{-3} \text{ s}^{-1}$ were measured for slow and fast deformation. The evolution of the specimen elongation was measured using push-rods, which was then converted into the true strain variation, monitored throughout deformation. Tests were interrupted at different values of plastic strain to study the dynamic precipitation evolution. Upon reaching the target final strain, unloading and gas quenching were performed simultaneously. The unloading was essential to prevent further plastic strain due to thermal contraction, and this was confirmed by monitoring the load on the specimen. Reference samples were also produced in the dilatometer. These underwent exactly the same thermal history, but without any deformation. To ensure no deformation due to thermal expansion or contraction, the dilatometer was operated in load control and the specimen was allowed to freely expand and contract as the temperature changed.

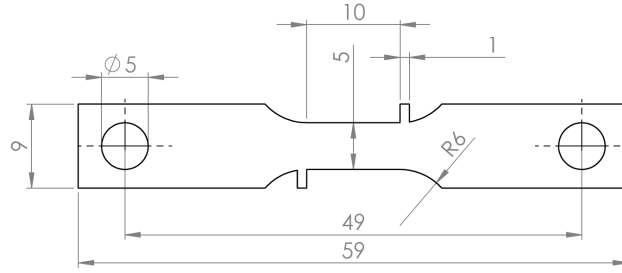


Figure 4.1: Test sample geometry used for dilatometer experiments. All dimensions are in mm.

Figure 4.2 demonstrates an example thermal history for a sample solution heat treated 10 minutes at 480°C followed by gas quenching to 180°C for tensile tests with 6×10^{-3} and $7 \times 10^{-4} \text{ s}^{-1}$ strain rate. The average quenching rates after solution heat treatment and deformation were measured as 149 and 68°C s^{-1} respectively. Stable temperature control was obtained with $\pm 0.9^\circ\text{C}$ standard deviation from the target temperature throughout the test.

After dilatometer testing, all samples were stored at -23°C in a freezer to prevent any further precipitate evolution prior to being prepared for the SAXS measurements.

Immediately before being dispatched for analysis, samples were taken from the

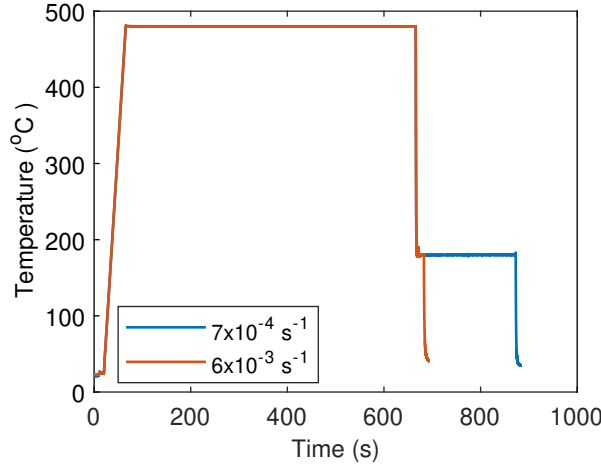


Figure 4.2: The temperature profile of sample solution heat treated at 480°C followed by the deformation at 180°C. Online version in color.

freezer. The grip area was removed using a Struers Accutom-5 precision cut-off machine with a feed speed of 0.05 mm s^{-1} , giving a total time of 4 minutes to remove both grip sections. The gauge area was mechanically ground to $70 \mu\text{m}$ thickness for small-angle x-ray scattering (SAXS) characterisation. The time at room temperature between removal from the freezer and SAXS measurement was approximately 7 days. SAXS experiments were performed at DL-SAXS Diamond Light Source on a Xeuss 3.0 instrument, which equipped an Excillum Gallium MetalJet x-ray source providing 9.2keV energy and an Eiger 2 R 1M silicon detector with a pixel size of 75 microns. The camera length was selected as 0.5 m to provide a useful scattering vector range $[0.009, 0.6] \text{ \AA}^{-1}$. The 2-dimensional scattering patterns of each sample were collected using a 600 s exposure time. Since the scattering patterns were isotropic, the average results and standard deviations were calculated by doing a circular average of scattering signals at each scattering vector q .

Analysis of the SAXS results was performed using procedures described in detail in [12]. Briefly, from the SAXS data, the Guinier radius can be calculated using the scattering vector q corresponded to the peak in the Kratky plot, as shown in equation 4.1 [12, 1].

$$R_g = \frac{\sqrt{3}}{q_{peak}} \quad (4.1)$$

The relation between the Guinier radius R_g and true radius depends on the

shape of the particles. With the hypothesis of spherical geometry at the early stage of precipitation, which is considered reasonable for the precipitates in 7xxx alloys [13], the true radius can be estimated as $\sqrt{5/3} \cdot R_g$. Further assuming the precipitate composition is near constant, the volume fraction of precipitates is proportional to the integrated intensity of the Kratky plot. The relative precipitate number density can then be estimated by dividing the integrated intensity (as a proxy for the volume fraction) by the average volume of individual precipitate. In the present study, the morphology of small precipitates is close to spherical, which will be demonstrated in TEM images later. Further considering Guinier radius as a good representation of the average precipitate radius, the average volume of each precipitate is, therefore, proportional to the cube of Guinier radius (R_g^3). The number density can then be estimated by dividing the area of the Kratky plot by R_g^3 .

Before producing the Kratky plot, Porod plots (Iq^4 vs q^4) were analysed to identify the background noise caused by the Laue scattering of the disordered solid solution and instrument noise [12]. This noise intensity was then subtracted from the total scattering intensity. Further details of the use of SAXS to analyse precipitates in aluminium alloys can be found elsewhere [12, 14, 15].

To complement SAXS and provide local and spatially resolved information about the precipitates, transmission electron microscopy (TEM) was performed on samples cut from the same ground specimens as for SAXS. Twin jet electropolishing was performed at 15V and -40 °C in nitric acid and methanol solution (1:3 vol%) to produce electron transparent areas. Afterwards, samples were further thinned by using a Gatan precision ion polishing system (PIPS II) with Ar ions under dual beam modulation with $\pm 4^\circ$ gun angles. The polishing sequence was set as 5 minutes at 1keV followed by 10 minutes at 0.5keV and finally 15 minutes at 0.1keV. TEM was performed on a FEI Talos machine equipped with a X-FEG field emission gun operating at an accelerating voltage of 200kV. All images were captured in bright field mode with the diffraction patterns taken along $\langle 110 \rangle$ zone-axis to identify the precipitate phase. On the bright field images, the precipitates were manually selected and their projected area measured using ImageJ. This was used to calculate the precipitate size as the radius of a circle of equal area. At least 100 precipitates were analysed in each condition.

4.3 Results

The stress-strain responses for specimens in all test conditions are shown in Figure 6.2(a). Slightly higher (< 20 MPa greater) yield and flow stresses were recorded for specimens deformed at the slower strain rate. Specimens deformed to different levels of strain but under otherwise identical conditions show overlapping curves as expected, demonstrating the high level of repeatability of the experiments. The work hardening rate was calculated from the stress-strain data and is shown in Figure 6.2(b). This demonstrates that there is no large difference between work hardening rate at the different strain rates.

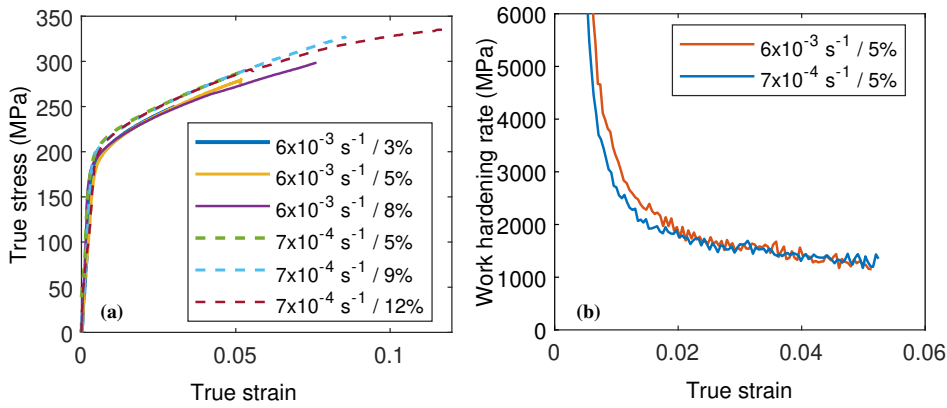


Figure 4.3: (a) true stress-strain curves of samples deformed at 180°C with different strains and strain rates. (b) work hardening rate calculated from samples deformed with 6×10^{-3} and $7 \times 10^{-4} \text{ s}^{-1}$ strain rate to 5% strain. Online version in color.

Figure 4.4 (a) and (b) show example bright field TEM images of the microstructure of the sample deformed to 12% strain with $7 \times 10^{-4} \text{ s}^{-1}$ strain rate at various magnifications. A fine and homogeneous distribution of nano-scale precipitates can be seen, which are identified as η' from the diffraction pattern (inset). In the low magnification image (Figure 4.4(a)) some much larger particles are also observed (10-100 nm in length) which are consistent with the size and morphology expected for the E-phase (Cr rich) dispersoids [16].

As a comparison for the deformed case, the microstructure of the non-deformed (but otherwise identically heat treated) material is shown in Figure 4.4 (c) and (d). A similar microstructure and spatial distribution of precipitates is observed as in the deformed sample (Figure 4.4 (a) and (b)). In the deformed sample the

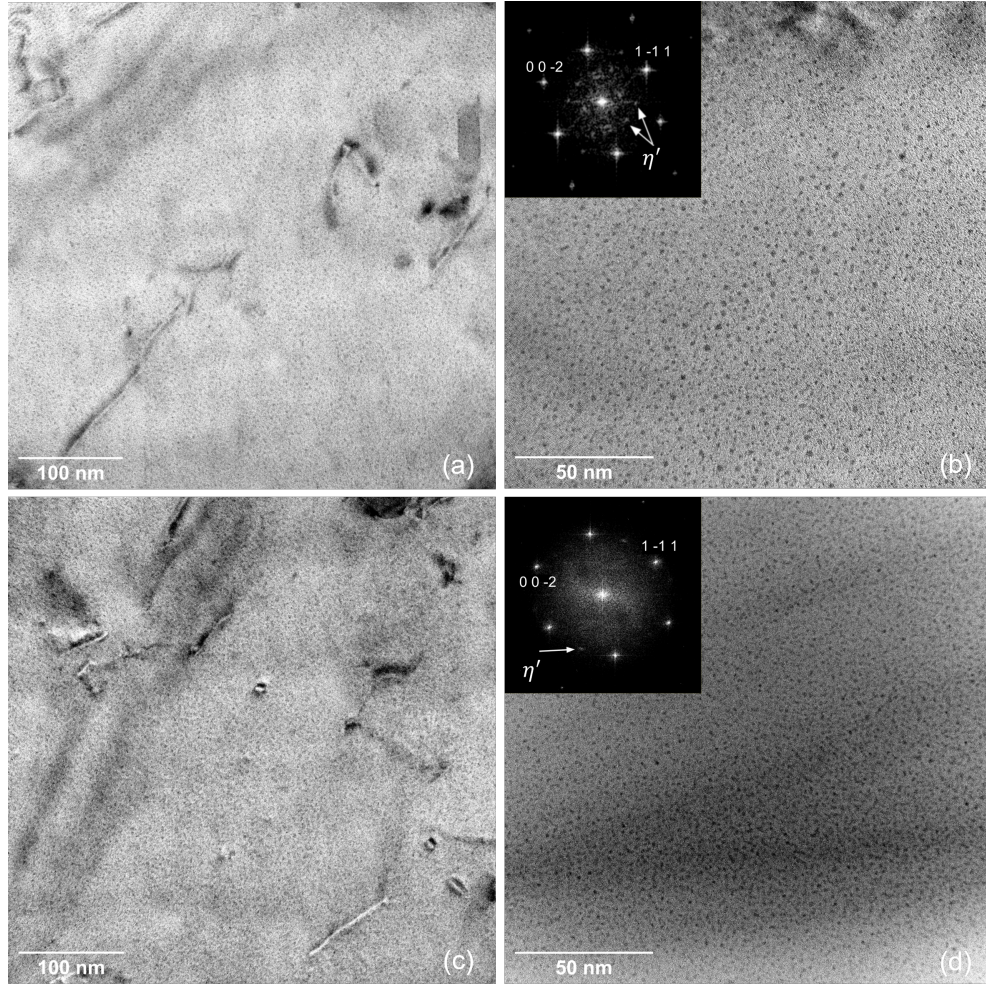


Figure 4.4: Bright field TEM images taken along $\langle 110 \rangle$ zone axis. (a)-(b) from the sample deformed at 180°C with $7 \times 10^{-4} \text{ s}^{-1}$ strain rate to 12% strain. (c)-(d) from the sample having identical heat treatments as (a) and (b) but without deformation.

precipitates are slightly larger and more widely spaced than in the non-deformed condition (compare (b) and (d)). From the TEM images, the morphology of small precipitates is close to spherical. The average radius is $0.8 \pm 0.2 \text{ nm}$ for the deformed case, which is larger than $0.5 \pm 0.2 \text{ nm}$ for the non-deformed sample.

To obtain a quantitative comparison of the precipitate parameters as a function of strain and strain rate, SAXS was used. This enables a larger and more statistically significant volume of material to be investigated in a more efficient way than is possible with the TEM. The results from the SAXS experiments are shown as Kratky plots in Figure 4.5.

The x -axis of these plots shows the scattering vector (q), which is inversely proportional to the precipitate size. A shift of the peak towards the left therefore represents a growth in the modal average size. The area under each curve scales

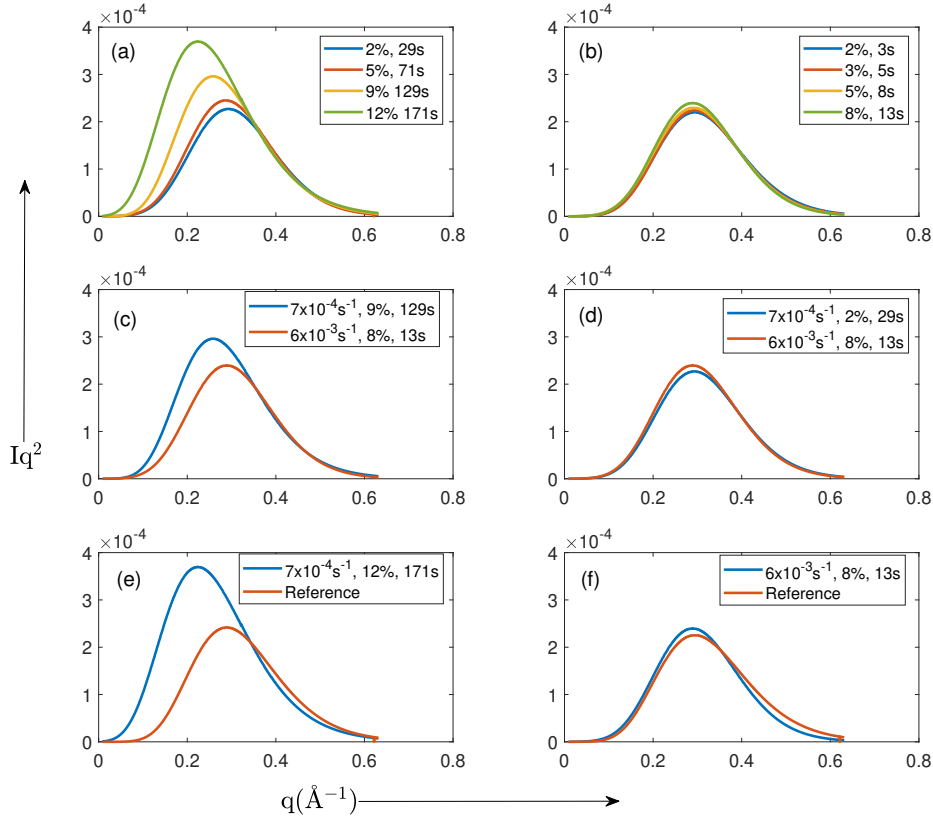


Figure 4.5: Kratky plots of SAXS results. (a) samples deformed with $7 \times 10^{-4} \text{ s}^{-1}$ strain rate. (b) samples deformed with $6 \times 10^{-3} \text{ s}^{-1}$ strain rate. (c) samples deformed to approximately 9% strain. (d) sample deformed at $6 \times 10^{-3} \text{ s}^{-1}$ for 13s (longest time) and $7 \times 10^{-4} \text{ s}^{-1}$ for 29s (shortest time) (e) sample deformed to 12% strain at $7 \times 10^{-4} \text{ s}^{-1}$ strain rate, compared to equivalent non-deformed material. (f) sample deformed to 8% strain at $6 \times 10^{-3} \text{ s}^{-1}$ strain rate, compared to equivalent non-deformed condition. Online version in color.

with the volume fraction, under the assumption that the precipitate composition is approximately invariant. Figure 4.5(a,b) show the evolution of the Kratky plot with increased strain (which also means increasing time) for (a) the lower and (b) the higher strain rate. As expected, increasing strain and time leads to a shift in the curves to the left and upwards, representing both an increase in the average precipitate size and volume fraction. The change is most pronounced at the lower strain rate, noting that the time to reach each strain level is approximately 10 times longer in this case. The changes over the much shorter duration of the higher strain rate deformation are smaller, but still significant.

Figure 4.5(c) compares the plots from the higher and lower strain rate for the case of a high level of strain (8-9%) and similar strain levels (near iso-strain). The

lower strain rate and longer time condition has lead to more precipitate growth and a greater volume fraction. Figure 4.5(d) compares the shortest time at the lower strain rate with the longest time at the higher strain rate. Although the time at the higher strain rate is slightly less than half that at the slower strain rate, the Kratky plots for both conditions are very similar. Indeed, the faster strain rate but shorter time has led to a slightly larger area under the curve and a shift in the peak towards slightly larger particle sizes. This indicates that the higher strain rate is able to partly compensate for the reduction in time, as will be explored in more detail later.

Figure 4.5(e) and (f) compare the Kratky plots at the highest strain (for lower and higher strain rates respectively) with those for the reference (non-deformed) condition heated for the same times. At the slower strain rate and hence longer time, it can be seen that the deformation has had a strong effect in shifting the peak upwards and towards larger particle size. At the faster strain rate, and hence shorter time, the same trend is observed but is less pronounced.

These plots demonstrate that deformation plays a significant role in controlling the precipitate evolution, but to understand this better it is necessary to decouple the effects of strain, strain rate and time (since a lower strain rate necessarily means a longer holding time at iso-strain).

Table 4.2: Guinier radius of deformed samples determined from SAXS

Strain rate (s^{-1})	Strain (%)	Guinier radius (pm)
6×10^{-3}	2	589 ± 1
	3	590 ± 1
	4	594 ± 2
	5	599 ± 2
	8	630 ± 3
7×10^{-4}	2	591 ± 2
	5	602 ± 3
	9	671 ± 3
	12	771 ± 6

Figure 4.6 shows the effect of increasing time and strain on the evolution of the Guinier radius and the growth rate (defined as the rate of change of Guinier radius with time). Firstly, the precipitate size determined from SAXS using Equation 4.1 is summarised in Table 4.2, which can be compared to the precipitate size determined from TEM. After deforming at a slow strain rate ($7 \times 10^{-4} \text{ s}^{-1}$) to 12% strain, the measured Guinier radius of the precipitates was $0.77 \pm 0.06 \text{ nm}$, which is equivalent

to a true radius of 1.0 ± 0.1 nm. This is in close agreement with the average radius measured from TEM images (0.8 ± 0.2 nm). Some discrepancy is expected due to the difference in how precipitates are detected in SAXS and TEM [15].

The effect of deformation on the evolution of average precipitate size can now be considered. Figure 4.6(a) shows clearly an effect of deformation on the change of Guinier radius with time. In both higher and lower strain rate cases, the difference between the deformed and non-deformed case becomes greater as the time (and hence strain) increases. By plotting the Guinier radius as a function of strain (Figure 4.6(b)) it can be seen that at low strains ($< 5\%$) both higher and lower strain rates show a similar trend, but at high strains ($> 5\%$) the Guinier radius for a slower strain rate exceeds that at a higher strain rate (at iso-strain).

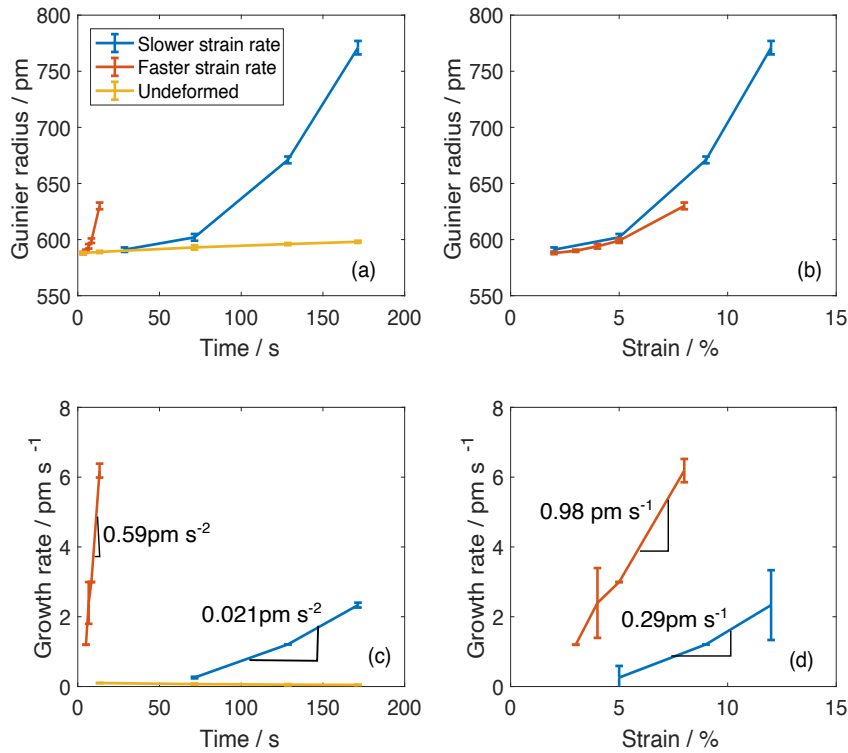


Figure 4.6: (a) Evolution of Guinier radius for the slower ($7 \times 10^{-4} \text{ s}^{-1}$) and faster ($6 \times 10^{-3} \text{ s}^{-1}$) strain rates compared with the non-deformed case with (a) time, (b) strain. Calculated growth rate for faster and slower strain rates compared with the non-deformed case plotted as a function of (c) time, (d) strain. Online version in color.

Plotting the growth rate (Figure 4.6(c,d)) more clearly highlights the differences between the cases. For the non-deformed condition, the growth rate is very low

across the whole time period and falls slightly with increasing time. For both higher and lower strain rate deformed cases, the growth rate increases with time and strain. The change in growth rate with time is approximately linear. The gradient of these lines gives growth acceleration, which can be seen to be approximately 30 times higher in the case of the higher strain rate compared with the lower strain rate. Although this difference is large, it is not sufficient to compensate for the reduction in time at higher strain rate. For example, for the Guinier radius to reach the same value at higher strain rate compared to lower strain rate (at iso-strain) the acceleration of the growth rate at the higher strain rate would have to be 73 times that at the slower strain rate ($\frac{\dot{\epsilon}_{fast}}{\dot{\epsilon}_{slow}}^2$). This is because the amount of growth is related to the acceleration of growth rate multiplied by the square of the time.

The change in growth rate with strain can also be plotted as a function of strain (Figure 4.6(d)). This demonstrates that the higher strain rate does lead to a greater increase in the growth rate for a given level of strain, and the increase is approximately linear (within error). The increase in growth rate with strain (the best-fit gradient of these lines) is shown, and in the higher strain rate case this is 3.4 times greater than in the slower strain rate case. As previously noted, this is insufficient to compensate for the reduction in time at the higher strain rate ($\frac{\dot{\epsilon}_{fast}}{\dot{\epsilon}_{slow}} = 8.6$).

Figure 4.7(a, b) shows the evolution of integrated intensity with time and strain respectively. This is taken as a proxy for the relative volume fraction of precipitates. These plots show similar behaviour to that already discussed for the evolution of Guinier radius, reflecting an accelerating effect of deformation on volume fraction increase, which is greater at the higher strain rate. Close inspection, particularly of Figure 4.7(b), shows that there is an important difference between the size and volume fraction evolution in the early stages of deformation (strains <3%), especially noticeable at the higher strain rate. Unlike the Guinier radius, which increases from the start of the test, the integrated intensity does not initially increase (indeed, it decreases slightly). This suggests that initially the volume fraction does not increase, even though the average precipitate size does. Possible explanations for this behaviour are discussed in detail later. The integrated intensity for the non-deformed case increases only very slightly over the full duration of the test.

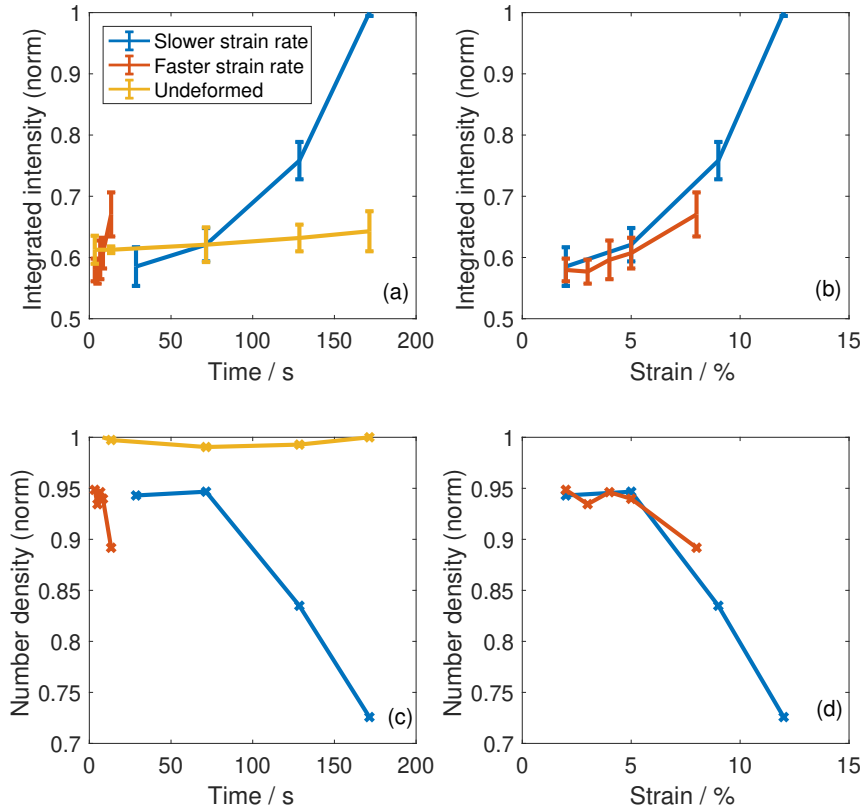


Figure 4.7: (a) Evolution of integrated intensity (assumed proportional to volume fraction) for the slower ($7 \times 10^{-4} \text{ s}^{-1}$) and faster ($6 \times 10^{-3} \text{ s}^{-1}$) strain rates compared with the non-deformed case with (a) time, (b) strain. Derived evolution of relative precipitate number density for faster and slower strain rates compared with the non-deformed case plotted as a function of (c) time, (d) strain. Online version in color.

Since precipitate size, volume fraction, and number density are all related it is possible to estimate the evolution in relative number density, assuming that the integrated intensity provides a good proxy for the relative precipitate volume fraction. The relative number density evolution calculated in this way is plotted in Figure 4.7(c,d) against time and strain respectively. These plots show that whilst the number density for the non-deformed case remains approximately constant, in the deformed case the number density decreases, and this decrease is most rapid after a strain of approximately 5% is exceeded (for both strain rates). This suggests that all of the precipitates or clusters that cause the scattering in SAXS are present at the start of the experiment (after quenching and a very short 5 s hold prior to deformation) and that new nucleation does not lead to a significant increase in the number density of these objects.

4.4 Discussion

The purpose of this study was to investigate the effect of warm deformation on precipitate evolution in an aluminium alloy starting from an initially supersaturated condition. This can be compared with previous work where the effect of deformation on a pre-existing precipitate distribution formed by pre-ageing has been studied [2]. One key objective was to determine whether a supersaturated starting condition would lead to a strong effect of deformation on precipitate nucleation under warm deformation conditions.

Considering first the non-deformed material, it was found that clusters were already detected after the quench and initial stabilisation hold (5 s at 180°C) and these clusters evolved only slightly during the subsequent hold (up to 200 s). The measured Guinier radius of approximately 0.56 nm is consistent with previous studies of cluster size during initial aging of similar alloys [17] and corresponds to a cluster containing around 40–70 atoms (assuming a 1:1 Zn to Mg ratio [17]). The initial clustering process is therefore very rapid, itself probably assisted by the high quenched in vacancy concentration, which at 180°C is expected to be 10 times higher than the equilibrium concentration [17, 18].

These initial clusters were also present in the deformed case before stretching was applied. Therefore, the subsequent evolution of the microstructure appears to be mainly determined by the effect of deformation on these pre-existing clusters rather than a significant effect in leading to nucleation of new clusters. This can be seen from the inferred number density plots, which show that deformation leads to a reduction rather than an increase in number density.

Deformation has been shown to strongly affect the size evolution of the clusters, and this is influenced by both strain and strain rate. The higher strain rate leads to an increase in the mean precipitate growth rate, but this is insufficient to compensate for the shorter time at higher strain rate. Therefore, for a given level of strain, the faster strain rate leads to a slightly smaller average precipitate size than the slower strain rate, and this difference increases with increasing strain. At the early stages of deformation, particularly in the highest strain rate case, the total volume fraction of clusters falls slightly, associated with a reduction in their number density. This

may be due to dislocation cutting, causing break up of some of the smaller clusters, with the solute eventually diffusing or being ballistically transported to grow the larger and more stable clusters.

Previous studies have demonstrated that the effect of deformation in similar aluminium alloys can be interpreted mainly by a consideration of the effect of the excess vacancies generated by non-conservative motion of jogs on gliding dislocations. For the temperature and strain rate regimes considered in this study, this effect is expected to be far more significant than direct precipitation on dislocations. TEM provides direct evidence that this is the case since it can be seen that precipitates are quite homogeneously distributed and most are not generally aligned along dislocations or associated directly with them. In addition, a direct effect of the dislocations should produce a negative strain rate sensitivity [1], which is not observed in this work.

Full details of the excess vacancy effect on deformation enhanced precipitate evolution, and the models to capture this, are considered in detail elsewhere [11]. In the present work, a model is used which is based on an adaption of a framework developed by Militzer et al. for steels [19], to understand if the excess vacancy effect can explain the observed results.

To summarise this model briefly, it is based on the idea that excess vacancies are created by jogs on gliding dislocations. These excess vacancies can enhance any vacancy mediated process such as substitutional diffusion. Since these vacancies are in excess of the equilibrium thermal vacancy concentration they seek to annihilate, which they will do at sinks such as dislocations and grain boundaries. The total excess vacancy concentration will therefore be controlled by the balance between creation and annihilation mechanisms.

The rate of excess vacancy production can be calculated from this balance. Neglecting the effect of thermal jogs and annihilation of excess vacancies at grain boundaries, which are insignificant for the conditions studies here [11], the excess vacancy production rate is given by:

$$\frac{dc_{ex}}{dt} = K_1 \sigma \dot{\epsilon} - K_2 \exp\left(-\frac{Q_m}{kT}\right) \rho_D c_{ex} \quad (4.2)$$

The first term is the excess vacancy generation rate, which is simply a proportion

of the applied plastic work (determined by the constant K_1). The second term is the excess vacancy annihilation rate, which is a function of temperature, the forest dislocation (sink) density ρ_D and the excess vacancy concentration itself c_{ex} , scaled by a constant K_2 . Other source and sink terms can be considered [19], but in the case of aluminium under the conditions studied here, they are of low significance. This equation was previously fitted to literature data from in-situ studies of precipitate growth evolution during deformation of a similar 7xxx alloy, and the constants K_1 and K_2 relevant to this case were determined [11]. A complicating factor is that not only are the excess vacancies evolving during deformation, but so is the sink dislocation density. This is included in the model through a simple and widely used empirical law in which the dislocation density increases from an initial to a saturation value [11].

Figure 4.8 shows the predictions of this model for (a) lower and (b) higher strain rate studied here. These plots show the total excess vacancies created (the integral of the first term in equation 4.2), the total excess vacancies annihilated (the integral of the second term in equation 4.2) and the resultant overall excess vacancy concentration. Also shown is the prediction of the evolving dislocation density. At both strain rates, it can be noted that steady-state has not been reached, either in the evolving dislocation density or in the excess vacancy concentration. Although this model is not expected to be accurate, the result is consistent with the experimentally measured stress-strain curves which show positive work hardening even at the end of the tests. In addition, the model suggests that at both strain rates, but particularly at the highest strain rate, the annihilation term is much smaller than the creation term across the whole strain range, so that the excess vacancies accumulate with increasing strain.

In both cases, the excess vacancy effect is far from reaching the steady-state that will eventually become established once the creation and annihilation rates reach a point of balance. This is consistent with previous in-situ work on the effect of deformation on the growth of pre-existing precipitates in aluminium alloys, where the results were explained assuming excess vacancy annihilation was negligible [2]. Note that this depends strongly on temperature and total applied strain; at higher temperature or higher cumulative strain the annihilation rate increases and eventu-

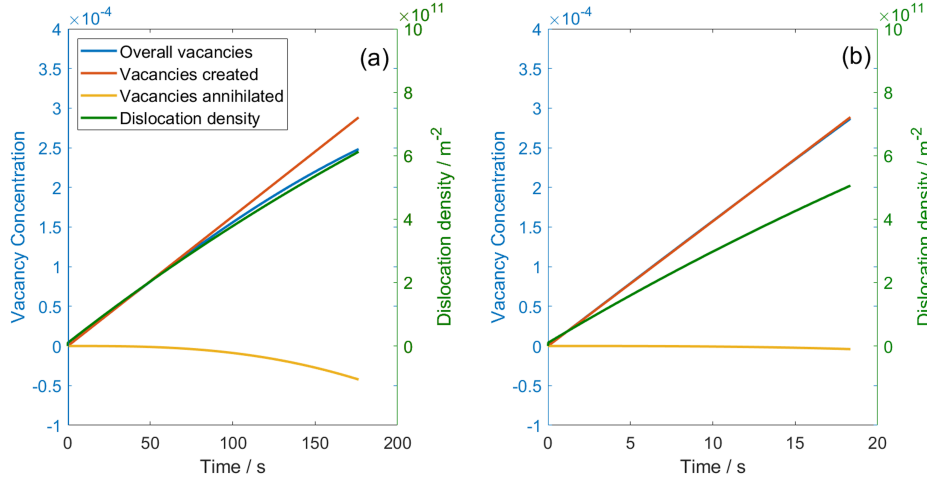


Figure 4.8: Calculated evolution of dislocation density and excess vacancy concentration at 180°C for (a) slower strain rate $7 \times 10^{-4} \text{ s}^{-1}$, (b) higher strain rate, $6 \times 10^{-3} \text{ s}^{-1}$. Online version in color.

ally a steady-state is established, which is a function of the temperature and strain rate [11].

To explore whether the excess vacancy concentration effect alone could explain the acceleration of growth rate seen with deformation, these two variables were plotted together, as shown in Figure 4.9 for both lower (a) and higher (b) strain rates. Although the number of experimental data-points is limited, it can be seen that in both cases the measured growth rate correlates well with the predicted excess vacancy concentration. At the higher strain rate, the correlation is less good, and there is a misfitting point, but there is significant uncertainty in the measurements. An important point to note is that this good correlation can only be obtained by re-scaling the growth rate axis from the lower to higher strain rate case. This is because application of equation 4.2 predicts that the excess vacancy concentration is relatively insensitive to strain rate in the regime of interest here (where annihilation is almost negligible) and depends only on the accumulated strain. Therefore, the expectation from the model is that the growth rate increase should be approximately independent of the strain rate. However, the experimental results clearly show there is a strain rate effect, with the growth rate increasing 3.4 times more for a given strain increment in the higher strain rate case compared to the lower strain rate case (Figure 4.6(d)).

The results from this study can be compared with those of Deschamps et al.[2]

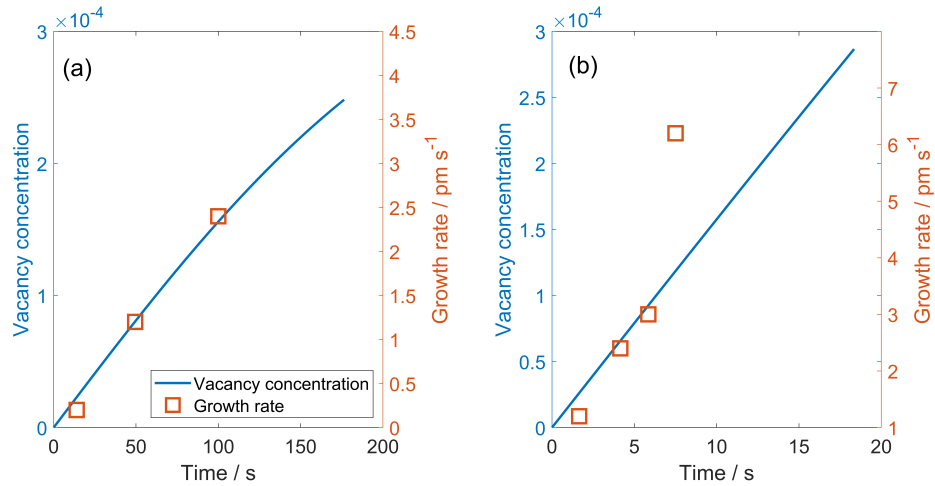


Figure 4.9: Measured growth rate and predicted excess vacancy concentration for (a) slower strain rate $7 \times 10^{-4} \text{ s}^{-1}$, (b) higher strain rate, $6 \times 10^{-3} \text{ s}^{-1}$. Online version in color.

who investigated a similar 7xxx alloy but in pre-aged conditions so that there was an initial precipitate population with mean radius of approximately 2 nm. In addition, the range of strain rates used in their study was approximately 10^{-5} to 10^{-4} s^{-1} and the deformation/ageing temperature was lower at 160°C . Consistent with the present work, they noted an enhancement in precipitate growth rate due to deformation. Growth rates of 6–7 times that in the non-deformed state were observed, which is similar to the growth rate enhancement observed at the higher strain rate and highest strain in the present study. Furthermore, they observed a linear increase in the growth rate with strain, as seen here. No simple monotonic effect of strain rate on the growth enhancement was found in [2] although there was observed to be a factor 3 difference between the greatest and least enhancement at different strain rates, which is similar to the difference obtained here. Deschamps et al. also demonstrated that their results were consistent with the excess vacancy effect and that dislocation pipe diffusion can only make a small contribution [2].

The excess vacancy model is therefore successful in explaining much of the behaviour observed in the present study and previous work. It correctly predicts the strong enhancement of growth rate with increasing strain, based on the direct relation between excess vacancies and solute diffusion rates. Even when the initial condition was achieved by rapid quenching from the solutionized state, the initial clustering is so rapid (at least at 180°C) that in all practical cases the effect of defor-

mation can be understood through its acceleration of growth and coarsening of the initial clusters, rather than an enhancement of nucleation. However, it is also clear that the excess vacancy model ignores some of the complexity of dynamic effects, hidden in the constants K_1 and K_2 , which for quantitative predictions require recalibrating for each temperature and strain rate. These limitations include neglecting the capture of excess vacancies by mobile dislocations, the effect of precipitates on dislocation motion, the dynamic recovery of the forest dislocations into cells, and the heterogeneous distribution of strain. Such effects would likely require a complex dislocation dynamics/precipitate interaction model to capture faithfully.

4.5 Conclusions

This study investigated the effect of deformation on precipitate evolution in AA7075 under warm conditions for the situation where the initial supersaturation of solute is at a maximum in the matrix. To achieve this, experiments were performed in a dilatometer that allowed rapid heating and cooling along with deformation under well controlled conditions. The following conclusions may be drawn from this work:

1. SAXS reveals that small solute clusters are present only 5 s after quenching from solution treatment to the test temperature (180°C).
2. The evolution of these clusters/precipitates is strongly affected by deformation. This is consistent with an effect on cluster growth rather than nucleation of new clusters or precipitates.
3. The precipitates formed during deformation are homogeneously distributed within the matrix. There is no evidence from either TEM or SAXS that deformation enhances the nucleation of new precipitates at the warm stretching temperature used in this study (180°C).
4. Deformation at a faster strain rate leads to a greater average cluster/precipitate growth rate at a given level of strain. However, the acceleration of growth rate with increasing strain rate is not sufficient to compensate for the reduction in time to reach a certain strain level. As a result, for a given strain, the final precipitate size is smaller after deformation at the higher strain rate.

5. A simple excess vacancy model can predict the observed linear increase in growth rate with strain. However, the model does not correctly predict the apparent strain rate effect observed in this study, suggesting it is an incomplete description of the complex interactions that occur between deformation and precipitation.

Acknowledgements

Constellium Technology Center is thanked for the provision of materials and financial support for this research. The EPSRC is thanked for financial support through the associated programme grant LightFORM (EP/R001715/1). This work was also supported by the Henry Royce Institute for Advanced Materials, funded through EPSRC grants (EP/R00661X/1, EP/S019367/1, EP/P025021/1 and EP/P025498/1). Dr S. Burholt is thanked for his assistance with the SAXS experiment on the Diamond-Leeds SAXS facility (EP/R042683/1). ZM appreciates the financial support from EPSRC grant Centre for Doctoral Training in Advanced Metallic Systems (EP/S022635/1). JDR acknowledges the support of the DSTL/RAEng Chair in Alloys for Extreme Environments.

The data required to reproduce these findings are available from the LightFORM Zenodo repository <https://zenodo.org/communities/lightform/>.

Bibliography

- [1] A. Deschamps, F. Bley, F. Livet, D. Fabregue, L. David, In-situ small-angle x-ray scattering study of dynamic precipitation in an al-zn-mg-cu alloy, *Philosophical Magazine* 83 (6) (2003) 677–692.
- [2] A. Deschamps, G. Fribourg, Y. Brechet, J. L. Chemin, C. Hutchinson, In situ evaluation of dynamic precipitation during plastic straining of an al-zn-mg-cu alloy, *Acta materialia* 60 (5) (2012) 1905–1916.
- [3] C. Hutchinson, F. De Geuser, Y. Chen, A. Deschamps, Quantitative measurements of dynamic precipitation during fatigue of an al-zn-mg-(cu) alloy using small-angle x-ray scattering, *Acta materialia* 74 (2014) 96–109.

- [4] W. Mirihanage, J. Robson, S. Mishra, P. Hidalgo-Manrique, J. Q. da Fonseca, C. Daniel, P. Prangnell, S. Michalik, O. Magdysyuk, T. Connolley, et al., Direct observation of the dynamic evolution of precipitates in aluminium alloy 7021 at high strain rates via high energy synchrotron x-rays, *Acta Materialia* 205 (2021) 116532.
- [5] M. Starink, N. Gao, N. Kamp, S. Wang, P. Pitcher, I. Sinclair, Relations between microstructure, precipitation, age-formability and damage tolerance of al-cu-mg-li (mn, zr, sc) alloys for age forming, *Materials Science and Engineering: A* 418 (1-2) (2006) 241–249.
- [6] W. Sun, Y. Zhu, R. Marceau, L. Wang, Q. Zhang, X. Gao, C. Hutchinson, Precipitation strengthening of aluminum alloys by room-temperature cyclic plasticity, *Science* 363 (6430) (2019) 972–975.
- [7] Y. Zhang, S. Jin, P. W. Trimby, X. Liao, M. Y. Murashkin, R. Z. Valiev, J. Liu, J. M. Cairney, S. P. Ringer, G. Sha, Dynamic precipitation, segregation and strengthening of an al-zn-mg-cu alloy (AA7075) processed by high-pressure torsion, *Acta Materialia* 162 (2019) 19–32.
- [8] L. Couturier, A. Deschamps, F. De Geuser, F. Fazeli, W. Poole, An investigation of the strain dependence of dynamic precipitation in an al-zn-mg-cu alloy, *Scripta Materialia* 136 (2017) 120–123.
- [9] G. Saada, Production de défauts ponctuels par écrouissage dans un métal cubique à faces centrées, *Physica* 27 (7) (1961) 657–660.
- [10] G. Saada, Interaction de dislocations écrouissage et production de défauts ponctuels dans les métaux cfc, *Acta Metallurgica* 9 (2) (1961) 166–168.
- [11] J. Robson, Deformation enhanced diffusion in aluminium alloys, *Metallurgical and Materials Transactions A* 51 (10) (2020) 5401–5413.
- [12] F. De Geuser, A. Deschamps, Precipitate characterisation in metallic systems by small-angle x-ray or neutron scattering, *Comptes Rendus Physique* 13 (3) (2012) 246–256.

- [13] G. Sha, A. Cerezo, Characterization of precipitates in an aged 7xxx series al alloy, *Surface and Interface Analysis* 36 (56) (2004) 564–568.
- [14] A. Deschamps, F. De Geuser, On the validity of simple precipitate size measurements by small-angle scattering in metallic systems, *Journal of Applied Crystallography* 44 (2) (2011) 343–352.
- [15] A. Deschamps, F. De Geuser, Quantitative characterization of precipitate microstructures in metallic alloys using small-angle scattering, *Metallurgical and Materials Transactions A* 44 (1) (2013) 77–86.
- [16] L. Ding, L. Zhao, Y. Weng, D. Schryvers, Q. Liu, H. Idrissi, Atomic-scale investigation of the heterogeneous precipitation in the e (al18mg3Cr2) dispersoid of 7075 aluminum alloy, *Journal of Alloys and Compounds* 851 (2021) 156890.
- [17] P. Schloth, J. Wagner, J. Fife, A. Menzel, J.-M. Drezet, H. Van Swygenhoven, Early precipitation during cooling of an al-zn-mg-cu alloy revealed by in situ small angle x-ray scattering, *Applied Physics Letters* 105 (10) (2014) 101908.
- [18] P. Schloth, A. Deschamps, C.-A. Gandin, J.-M. Drezet, Modeling of GP (i) zone formation during quench in an industrial AA7449 75 mm thick plate, *Materials and Design* 112 (2016) 46–57.
- [19] M. Militzer, W. Sun, J. Jonas, Modelling the effect of deformation-induced vacancies on segregation and precipitation, *Acta metallurgica et materialia* 42 (1) (1994) 133–141.

Chapter 5

Microstructural Stability and Paint Bake Response of Pre-aged AA7075

Z. Ma¹, E. Cooksey-Nash¹, D. Barbier², J. D. Robson¹

1 – Department of Materials, University of Manchester, Manchester,
M13 9PL, UK

2 – Constellium Technology Center, 38341 Voreppe Cedex, France

Published at Materials Characterization, 2023. Z.Ma: Conceptualization, Methodology, Investigation, Formal analysis, Writing - Original Draft, Writing - Review & Editing. E.Cooksey-Nash: Investigation. D.Barbier: Writing - Review & Editing, Resources. J.D.Robson: Conceptualization, Writing - Original Draft, Writing - Review & Editing and Supervision.

Abstract

High strength AA7xxx are attractive for use in the automotive industry, offering significant strength/weight benefits. These alloys are often used in tempers that require long ageing times of several hours. Pre-ageing has been proposed to be effective in suppressing natural ageing, and reducing the total ageing time by integrating the final ageing step into the paint bake cycle. However, the precipitate evolution during the pre-ageing and subsequent paint bake processes remains to be fully understood. In the present work, the pre-ageing process was studied for AA7075 over a wide range of temperatures and times. Small angle X-ray scattering (SAXS) was used as the main technique to investigate the precipitate evolution during the pre-ageing, natural ageing and paint bake, with the support from transmission electron microscopy (TEM) and isothermal calorimetry. For the first time, the results show that 8 hours pre-ageing at 80 °C can produce a microstructure consisting of GP zones with an average radius of approximately ~ 0.9 nm, which remains stable up to at least 7 months. After a short paint bake process, 94% of the T6 hardness can be obtained by uniformly distributed precipitates with an average radius of approximately ~ 2.6 nm. The final size and strengthening effect of the precipitates after 20 minutes baking is found to be insensitive to the heating rate, which has not been reported previously. The present results further suggest this process is robust for industrial application.

5.1 Introduction

High strength 7xxx alloys (Al-Zn-Mg-Cu) offer a greater specific strength than alloys from the 5xxx and 6xxx families and are thus of considerable interest to the automotive industry for the production of lightweight body structures. The high strength of these alloys is achieved by uniformly distributed nano-sized precipitates in the matrix. Ageing leads to a simplified precipitation sequence from GP zones to η' phase and finally to the equilibrium η phase [1, 2, 3]. Peak strength (the T6 condition) is achieved from a dispersion of small ($<5\text{nm}$ radius) η' precipitates, which is traditionally achieved by a long (24 hr) ageing treatment at moderately elevated temperature (120°C) [3, 4, 5, 6]. Commonly, these alloys are also slightly overaged by an additional heat treatment step to produce various T7 tempers, which results in improved resistance to environmentally assisted cracking, albeit at the expense of some strength [7, 8, 9]. In the aerospace industry where high strength 7xxx are most widely used, these heat treatment processes are performed at the material supplier, with the material provided in the final temper state. They are then manufactured into the final part, usually by machining, so that formability is not a prime consideration [10, 11].

In the automotive industry, sheets need to be formed into complex shapes to make car body panels and other components. The initial temper condition plays an important role in controlling formability. The material in the stable peak aged condition (T6) has severely limited room temperature formability [12, 13, 14]. To overcome this problem, elevated temperature forming of AA7075-T6 at around 200°C can be used [6, 12], but this leads to the partial dissolution and coarsening of the strengthening precipitates. Although the high strength can be preserved, it is partly relying on the dislocation strengthening [6]. Forming can also be performed above the precipitate solvus temperature, which combined with rapid quenching (e.g. the HFQ[®] process [15, 16]), can retain the solutes in the matrix for precipitation during a subsequent ageing heat treatment. In these cases, the carefully developed precipitate distribution created by the T6 temper is destroyed, and a long post-form heat treatment may be needed to restore T6 properties [17, 18].

On the other hand, material supplied in the W temper (after solution treatment

and quenching, but before any ageing) is also problematic since in this condition the alloy is unstable and will naturally age quickly over several months [19, 20]. The room-temperature formability will depend on the extent of the natural ageing process, as will the final properties achieved after post form ageing (necessary to reach the T6 condition). A promising strategy is to use a pre-ageing (underaged) treatment, applied at the material supplier, to stabilize the microstructure whilst retaining good formability. This strategy is used for 6xxx alloys, where natural ageing has a negative effect on subsequent artificial ageing response [21, 22, 23, 24]. A post-forming ageing treatment is then applied to bring the material to the T6 condition. In principle, this post-form ageing could be significantly reduced in duration since the initial precipitate distribution is established during the pre-ageing process [24, 25, 26, 27]. Ideally, the post-form ageing could be achieved by integrating into an existing process, such as the paint bake heat treatment, as is done for 6xxx alloys [27, 28, 29].

Recently, pre-ageing methods have been demonstrated to effectively improve the room temperature stability of underaged 7xxx aluminium alloys [14, 20, 30, 31, 32]. Generally, pre-ageing has been conducted at around 120 °C with times varying from 30 minutes to 12 hours. Pre-ageing effects have been studied for both low Cu, moderate strength 7xxx alloys (e.g. AA7021) and the higher strength, high Cu 7xxx alloys (e.g. AA7075). Kumar and Ross [30] reported that pre-ageing process of W temper AW-7021 sheet can stabilize the alloy at room temperature for two weeks. Österreicher et al. [31] reported that applying pre-ageing immediately after the solution heat treatment can inhibit the natural ageing of AA7021 and AA7075 for three weeks. They also found that after pre-ageing, the paint bake response of AA7075 was improved, with the yield strength close to the T6 peak-aged condition.

The development of pre- and post-form ageing practices to date has been mainly empirical in nature, based around optimising the final product strength [14, 20, 30, 31, 32, 33]. There remains a limited understanding of the interaction of the pre-ageing, forming process, and post ageing on the precipitate evolution and hence on the likely overall material performance. Furthermore, a better understanding of the fundamental microstructural changes occurring during each step is likely to inspire new strategies to both improve properties and reduce process times.

The present study aimed to establish relationships between the pre-aged microstructure and final precipitate distribution in a commercial 7075 aluminum alloy by performing a detailed characterization of precipitate evolution under a range of pre-ageing conditions and studying microstructural evolution during a simulated paint bake cycle. Although the quench sensitivity and corrosion resistance of 7075 may not be as remarkable as other 7xxx alloys like 7050 and 7085, exploring the microstructure and precipitation behaviour of this well-established commercial alloy system can serve as a benchmark for developing comparable pre-ageing approaches for other 7xxx series alloys. The study demonstrated that by optimizing the pre-ageing practice, the natural ageing of AA7075 can be effectively stabilized up to at least 7 months, while still achieving higher strain to failure than the traditional T6 temper. After a short paint bake process, 94% of the T6 strength can be obtained by uniformly distributed precipitates.

5.2 Methodology

7075 aluminium alloy sheets of 1.5 mm thickness with approximate composition (Zn-5.6wt% Mg-2.5wt% Cu-1.6wt% Al balance) were supplied by Constellium. These sheets were industrially manufactured by direct chill casting and homogenisation followed by hot and cold rolling reduction, and supplied in the as fabricated condition (F-temper). Samples were cut from these sheets into 1 cm² squares. Solution heat treatment was performed by placing samples in a pre-heated air circulating furnace at 480 °C for 1 hour followed by water quenching to room temperature.

To study the effect of pre-ageing time, the solution heat-treated samples were pre-aged isothermally at 80 °C for 1, 2, 5 or 8 hours followed by water quenching. Based on these results, 8 hours was chosen for the following isochronal pre-ageing study. To study the pre-ageing temperature effect, after solution heat treatment, the samples were immediately pre-aged at 40 °C, 60 °C, 80 °C and 100 °C for 8 hours followed by water quenching. The samples were kept in the freezer at -23 °C overnight for 16 hours before applying the bake hardening which was performed isothermally at 185 °C for 20 minutes followed by water quenching.

The paint bake response investigation was performed on samples pre-aged 8

hours at 80 °C. Two different heating rates were selected to study the effect of heating rate on the precipitation behaviour. The faster heating rate was achieved by putting the samples in the pre-heated furnace, which gave an average heating rate of 99 °C/minute recorded by a thermocouple on the specimen in the furnace. The slow heating rate was achieved by heating the furnace from room temperature to 185 °C, giving a measured heating rate of 6.9 °C/minute.

Vickers hardness was measured immediately after each step of the heat treatment, 10 measurements were taken in each case with 0.5 kgf force and a 10 s dwell, from which the mean and standard deviation were calculated.

Lab-based small-angle X-ray scattering was performed on a Bruker Nanostar modified with motorised scatterless slits and Genix 3D microfocus CuK α (1.54 Å, \sim 7.8 keV) source by Xenocs to study the samples in pre-aged conditions. A CCD camera was used to collect the scattering signals in the scattering vector range [0.01, 0.6] Å $^{-1}$. The exposure time was set as 300 seconds for all lab-based SAXS measurements. In order to compare results between different samples, the intensity was calibrated to correct for differences in the transmission coefficient, sample thickness and X-ray exposure time.

Synchrotron SAXS was performed at the beamline I22, at the Diamond Light Source to study the evolution of precipitates during the paint bake process. The benefits of using synchrotron SAXS are a highly monochromatic source, fast data acquisition time and the flexible camera length which can measure a much wider size range and also allows the direct comparison between pre-aged and paint baked samples. The experiment was conducted at 12.4 keV monochromatic X-ray energy with \pm 0.125 eV energy stability and 299×69 microns measured FWHM (full width at half maximum) focal size. The photon flux at this energy level was measured as 3.97×10^{12} photons per second [34]. Scattering patterns were collected as 100 frames of 100 milliseconds each, with a Pilatus P3-2M silicon hybrid pixel detector with 172 microns pixel size, which is located 3 meters away from the sample. The accessible scattering vector range was [0.004, 0.47] Å $^{-1}$. The average scattering results, after removing the background, are presented in this study.

From the SAXS results, the Guinier radius can be calculated by considering the scattering vector q related to the peak in the Kratky plot, as shown in equation 5.1.

The relation between the Guinier radius and true radius depends on the shape of the particles. For spherical geometry, the true radius can be calculated as $\sqrt{5/3} \cdot R_g$. Assuming the precipitate composition is near constant, the precipitate number density can be estimated by using the integrated peak area of the Kratky plot over $(R_g)^3$. The details of the data analysis method can be found elsewhere [35, 36, 37].

$$R_g = \frac{\sqrt{3}}{q_{peak}} \quad (5.1)$$

Differential scanning calorimetry was performed on a TA instrument DSC Q1000 machine using 30 °C/minutes heating rate followed by an isothermal hold, with pure aluminium as the reference. Isothermal calorimetry can be taken as a complementary method to study the volume fraction evolution of the precipitates [38, 39, 40]. The exothermal peak is related to the precipitation process. Thus, the evolution of heat flow can be used to study the precipitation kinetics. The relative volume fraction was calculated from the areas under the DSC curves as discussed later. To determine the relative precipitate volume fraction in the pre-aged condition, isothermal DSC was also performed on a specimen that had been resolutionized at a temperature of 480 °C for 1 hour, followed by water quenching. This sample was assumed to contain no precipitates, and so provides a benchmark for full precipitation at 185 °C, which was used to estimate the normalized precipitated volume fraction in the pre-aged condition as demonstrated later.

Transmission electron microscope (TEM) images were taken to support the precipitates size measurement from the SAXS results and provide detailed information on the microstructure. This was performed on a FEI Tecnai G2 F30 machine. The samples for TEM imaging were ground to 80 μm thickness followed by twin jet electropolishing at 15V and -40 °C in nitric acid and methanol solution (1:3 vol%). Afterwards, the samples were further thinned by using a Gatan precision ion polishing system (PIPS II).

Tensile specimens with 32 mm gauge length along the rolling direction and 6mm width were prepared with two initial temper conditions (pre-aged 8 hours 80 °C and peak-aged 24 hours 120 °C). Uniaxial deformation at room temperature was performed on an Instron 5569H1549 machine with a strain rate of 10^{-4} s^{-1} to failure. The plastic strain was mapped using commercial digital image correlation

(DIC) software LaVision DaVis 10 [41]. The strain hardening exponent (n) from Ludwik-Hollomon equation and plastic strain ratio (r) were calculated to compare the formability difference between pre-aged and peak-aged samples [42, 43].

5.3 Results

5.3.1 Isothermal/Isochronal pre-ageing

Figure 5.1 shows the effect of pre-ageing time for isothermal pre-ageing at 80 °C. This temperature was chosen since previous studies suggest it provides a good balance of formability after pre-ageing, but rapid hardening response during paint-baking. The validity of this assumption will be demonstrated later. As shown in figure 5.1(a), the hardness increased rapidly in the first two hours of pre-ageing. After 5 hours, the hardness becomes relatively stable. A similar increasing trend was observed in the SAXS results as shown in figure 5.1(b). The number density estimated from SAXS results further indicates the growth of precipitates dominates the increase in integrated intensity rather than nucleation of new particles.

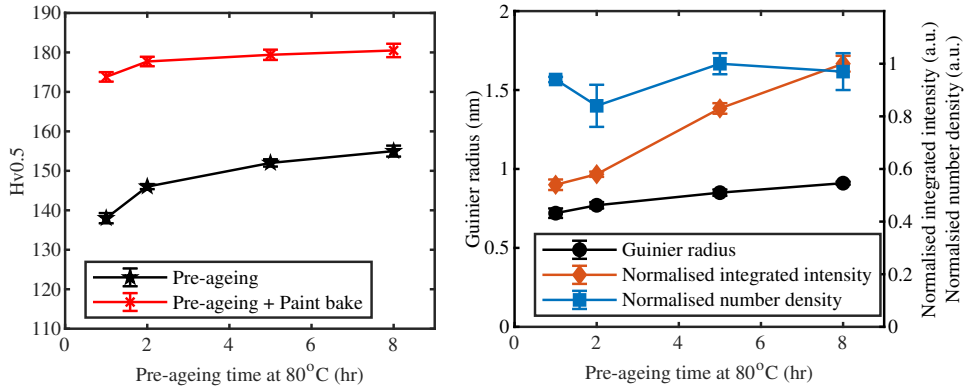


Figure 5.1: (a) Microhardness evolution of samples pre-aged at 80 °C and after pre-ageing plus simulated paint-bake for 20 minutes at 185 °C (b) Guinier radius, integrated intensity and number density as a function of pre-ageing time at 80 °C. Integrated intensity and number density are normalised to their maximum value to bring the data in to the range [0, 1]. Error bars correspond to one standard deviation.

The hardness measured both directly after pre-ageing for a range of temperatures and after subsequently simulated paint-baking is shown in figure 5.2. The SAXS

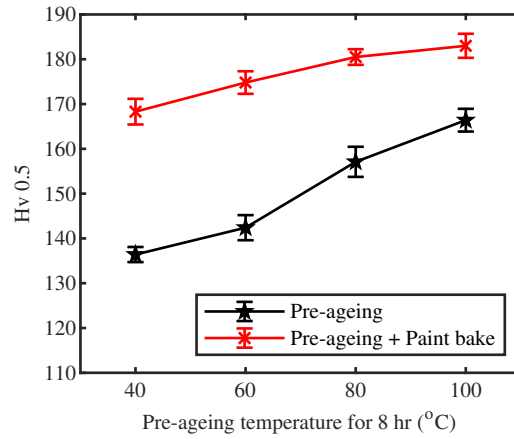


Figure 5.2: Microhardness of samples pre-aged 8 hours at 40, 60, 80 and 100 °C and after pre-ageing plus simulated paint-bake for 20 minutes at 185 °C. Error bars correspond to the standard deviation.

results of the pre-aged samples are presented and summarised in figure 5.3.

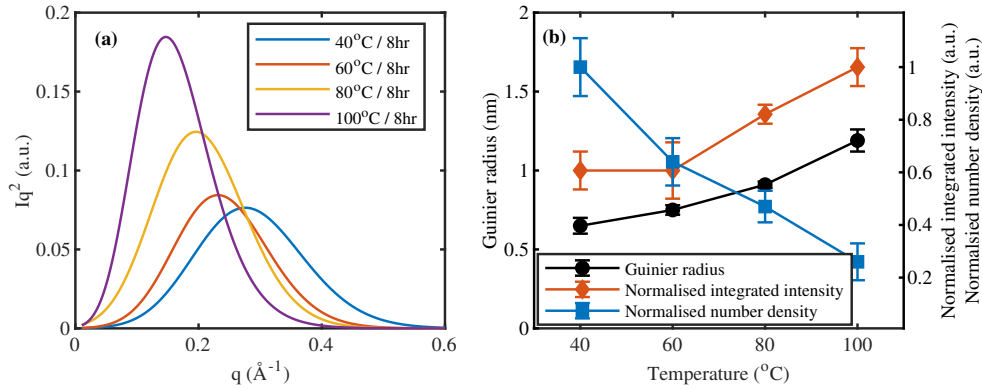


Figure 5.3: (a) Kratky plot of SAXS results of samples pre-aged 8 hours at 40, 60, 80 and 100 °C. (b) Guinier radius, integrated intensity and number density correspond to samples in (a). Integrated intensity and number density are normalised to their maximum value to bring the data in to the range [0, 1]. Error bars correspond to one standard deviation.

Figure 5.2 shows that as the pre-ageing temperature increases, the pre-aged hardness also increases, which is consistent with the increase in the extent of precipitation measured by SAXS as shown in figure 5.3. After paint baking, the hardness is further increased by additional precipitation. As expected, for a lower pre-ageing temperature, the hardness increases more during the paint baking step than at a higher pre-ageing temperature. This leads to a convergence of hardness values after

the simulated paint-bake. However, although the hardness values converge after the paint bake, they are not identical. A higher temperature pre-ageing treatment (80 °C or 100 °C) leads to a significantly greater final hardness, especially compared with pre-ageing at 40 °C. The measured hardness of the material in the standard T6 temper was 191 ± 2 HV. This means that the highest hardness observed for the pre-age and paint-bake treatments studied here achieved 94% of the T6 hardness.

The isochronal pre-ageing study confirmed that 80 °C provides a good compromise for the pre-ageing step, since the aim is to avoid too much hardening during pre-ageing which may negatively impact formability, whilst ensuring that sufficient hardening can be achieved during the paint bake so the alloy approaches its maximum T6 strength. An 8 hr pre-heat at 80 °C was therefore selected for the remainder of the study.

5.3.2 Optimised pre-ageing process

True stress-strain plots for pre-aged and T6 material are shown in figure 5.4. The proof strength, UTS, and true strain to failure of 394 MPa, 673 MPa, 0.18 respectively can be compared against those reported for the same sheet in the T6 temper (545 MPa, 689 MPa, 0.16). It can be seen that the pre-aged material has lower yield stress and greater elongation to failure. Larger strain hardening exponent and plastic strain ratio than the material in the T6 temper were also observed as summarized in figure 5.4. The higher work hardening rate and greater elongation to failure of the pre-aged material suggest it will have greater formability than the T6 material, as expected.

The stability of the pre-aged material was determined by long term natural ageing at ambient temperature. Figure 5.5 shows the hardness and Guinier radius remain stable up to at least one month and has only increased slightly from 155 Hv to 165 Hv and from 0.91 nm to 0.95 nm after 222 days (7 months). This confirms that the pre-ageing temper is effective in limiting natural ageing and stabilizing the alloy properties.

The microstructure after pre-ageing was revealed by the bright field TEM and HRTEM images in figure 5.6. The images were taken using a $\langle 110 \rangle$ zone axis. Spherical GP zones with their diameter around 2 nm were observed, which supports

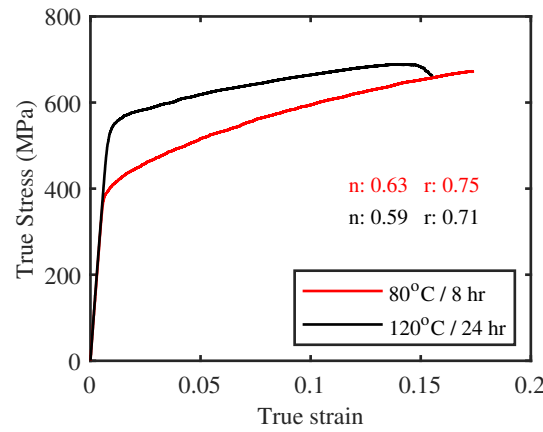


Figure 5.4: True stress - strain curve of pre-aged (8 hr at 80 °C) and T6 (24 hr at 120 °C) samples.

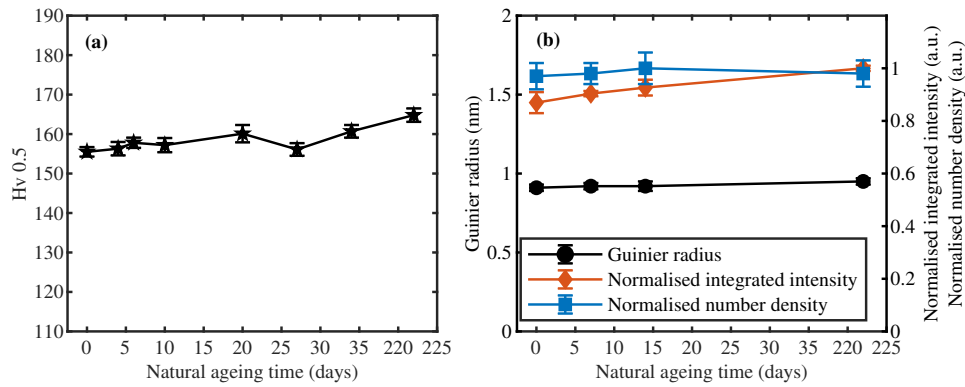


Figure 5.5: (a) Microhardness evolution, (b) Guinier radius, integrated intensity and number density evolution of the preaged sample (80 °C 8 hours) during the following 7 months natural ageing. Integrated intensity and number density are normalised to their maximum value to bring the data in to the range [0, 1]. Error bars correspond to one standard deviation.

the SAXS measurement of 0.9 nm Guinier radius (1.2 nm true radius).

5.3.3 Paint bake response of samples preaged 8 hours at 80 °C

An important consideration in understanding the paint bake response is the effect of heating rate. In an assembled vehicle going through the drying process of the cataphoretic coating, the heating rate could vary from position to position [44, 45,

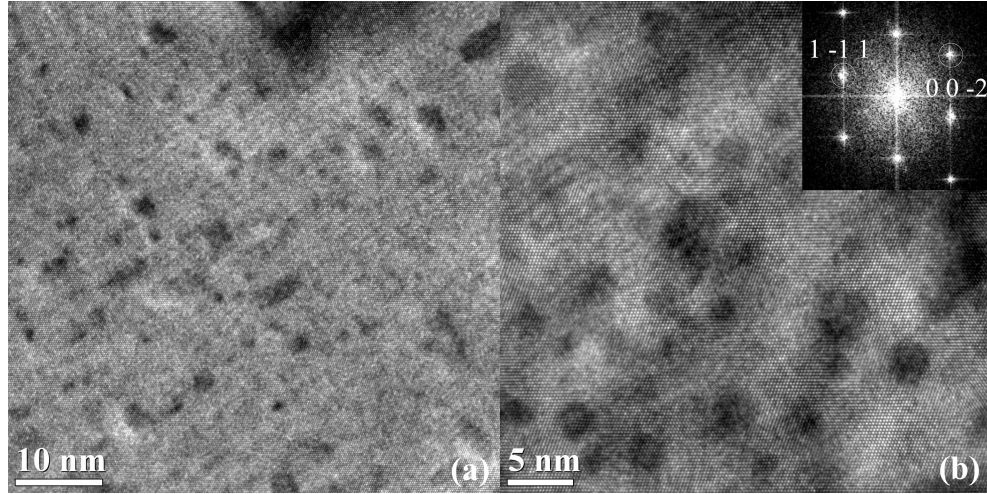


Figure 5.6: (a) Bright field TEM and (b) HRTEM images taken from the sample pre-aged at 80 °C 8 hours in $\langle 1\ 1\ 0 \rangle$ zone axis showing the existence of small GP zones.

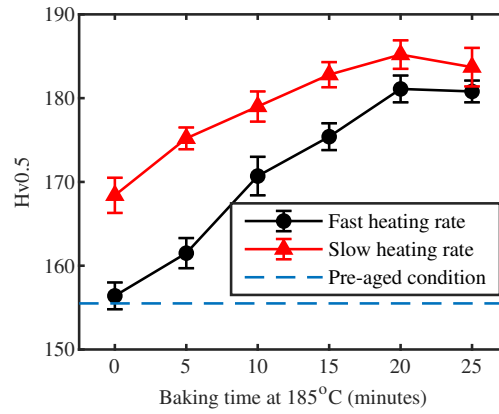


Figure 5.7: Microhardness evolution of pre-aged samples baking at 185 °C 0-25 minutes with fast and slow heating rates, compared to the original pre-aged microhardness.

46], and thus a strong degree of sensitivity to this parameter would be problematic. To study this, results from a fast (99 °C/minute) and slow (6.9 °C/minute) heating rate to paint-bake were compared. The evolution of microhardness with the duration of the paint-bake for both slow and fast heating is shown in figure 5.7. For samples heated at a slow rate, approximately half of the hardness increase associated with paint-baking occurred during the heating ramp to 185 °C. For this case, the highest hardness was obtained after 20 minutes of baking at 185 °C. For samples experiencing fast heating, almost no hardness increase occurred during the rapid (<2 minutes) heating ramp, and the subsequent hardness increase was more rapid during the

paint-bake. The hardness values for both heating rates converged after about 20 minutes, but there remained a small but persistent reduction in the hardness for the fast ramp compared with the slow one.

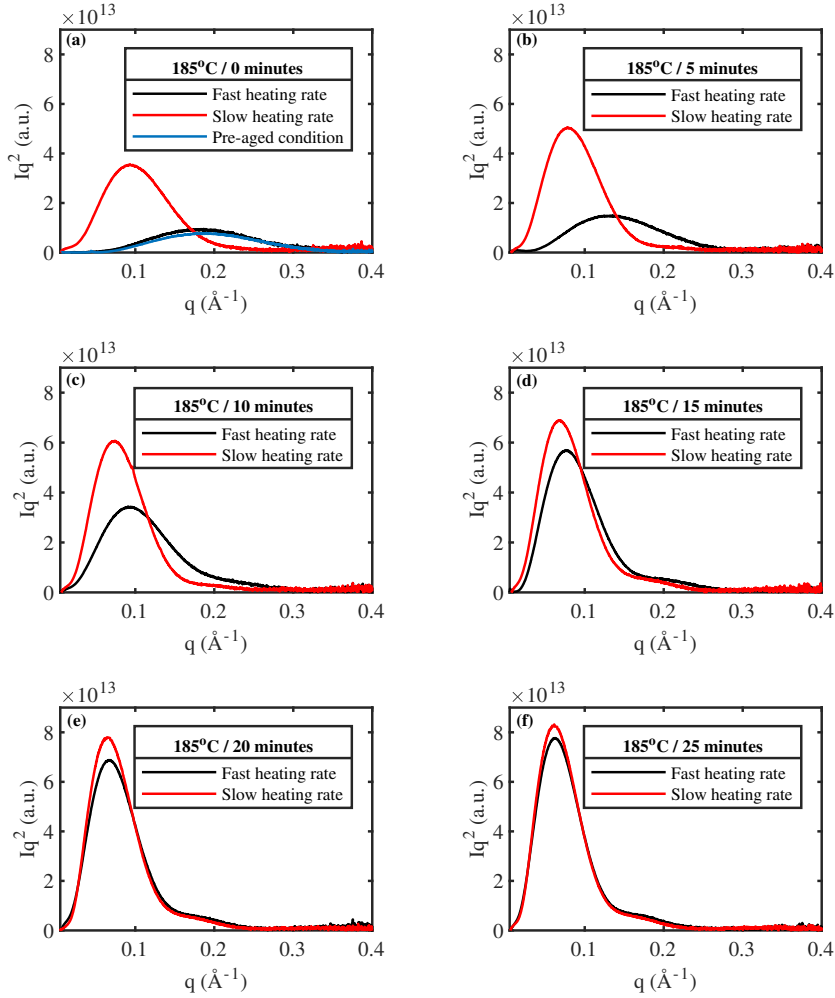


Figure 5.8: Kratky plots of SAXS results of pre-aged samples baking at 185 °C with fast (black) and slow (red) heating rates. (a) 0 minute, (b) 5 minutes, (c) 10 minutes, (d) 15 minutes, (e) 20 minutes, (f) 25 minutes.

The SAXS data corresponding to the microhardness measurements in figure 7 are shown as Kratky plots in figure 5.8. In this type of plot, assuming the composition of precipitates remains constant, a peak that shifts towards the left and has a higher integrated area represents larger precipitates with a higher volume fraction. The results in figure 5.8. (a) indicate, after the heating ramp, both the precipitates size and integrated peak area increased compared to the original pre-aged condition. This increment is more pronounced in samples with the slow heating rate. From

figure 5.8. (b) ~ (f), during the baking process at 185 °C, samples with slow heating rate shows larger peak and Guinier radius compared to samples with the fast heating rate. However, with extending the baking time at 185 °C, the peak difference between samples with fast and slow heating rate became small.

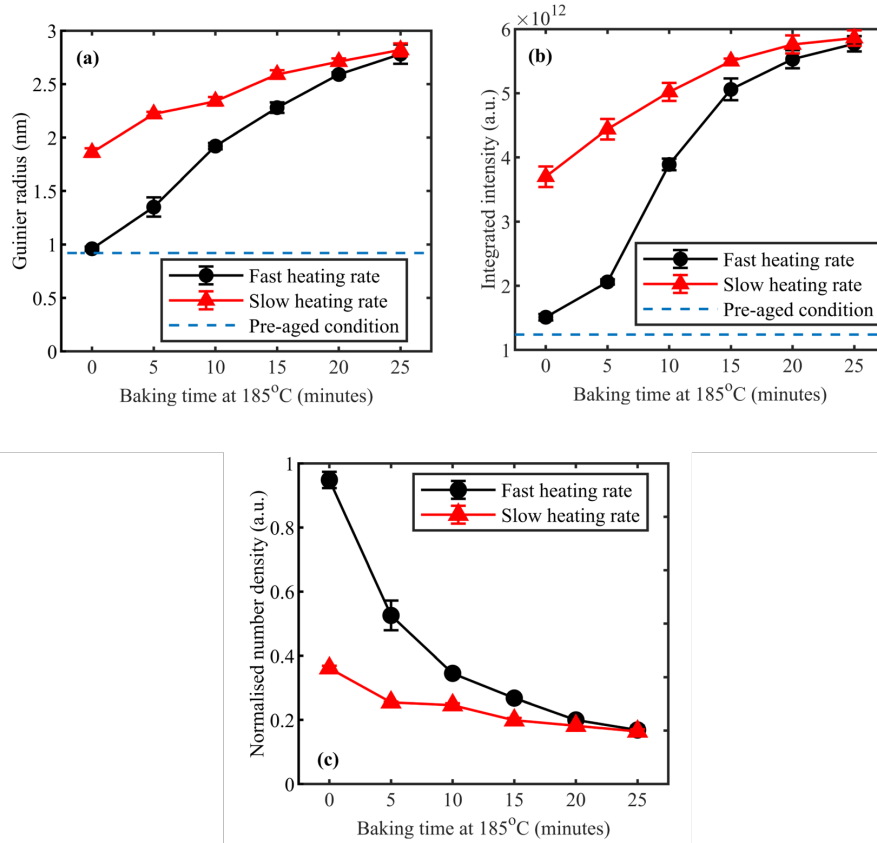


Figure 5.9: (a) Guinier radius and (b) integrated intensity (c) normalised number density of pre-aged samples baking at 185 °C 0-25 minutes with fast and slow heating rates, compared to the original pre-aged condition.

Quantitative measurements of the Guinier radius, integrated peak area derived from the SAXS data are summarised in figure 5.9 (a & b). These results are consistent with the microhardness measurements. They show that for the slow heating case, Guinier radius and integrated peak area increased by 104% and 198% after the heating ramp. The increment in 25 minutes baking at 185 °C was small (52% and 58% respectively). For the fast heating case, the growth of precipitates during heating ramp is almost negligible compared to the actual baking at 185 °C. The Guinier radius and integrated peak area only increased by 5% and 22% after the heating ramp, in comparison to the 190% and 282% increase during the 25 minutes at 185 °C.

Figure 5.9 (c) shows the evolution of the average number density normalised to the pre-aged condition. A continuous decrease of the normalised density was observed during baking at 185 °C, indicating the dissolution of small precipitates. The dissolution was significant during the heating ramp for samples subjected to the slow heating rate, while for samples subjected to the fast heating rate, the dissolution was more pronounced in the first 10 minutes of baking. From figure 5.9, it is shown that the Guinier radius, integrated peak area and normalised number density from samples under fast and slow heating rates also converged with extending the soaking time at 185 °C, which is consistent with the microhardness results shown in figure 5.7. It can be seen from figure 5.8 and 5.9, although convergence was observed in the SAXS results, there was still a small difference between fast and slow heating cases after 25 minutes at 185 °C, consistent with the microhardness results.

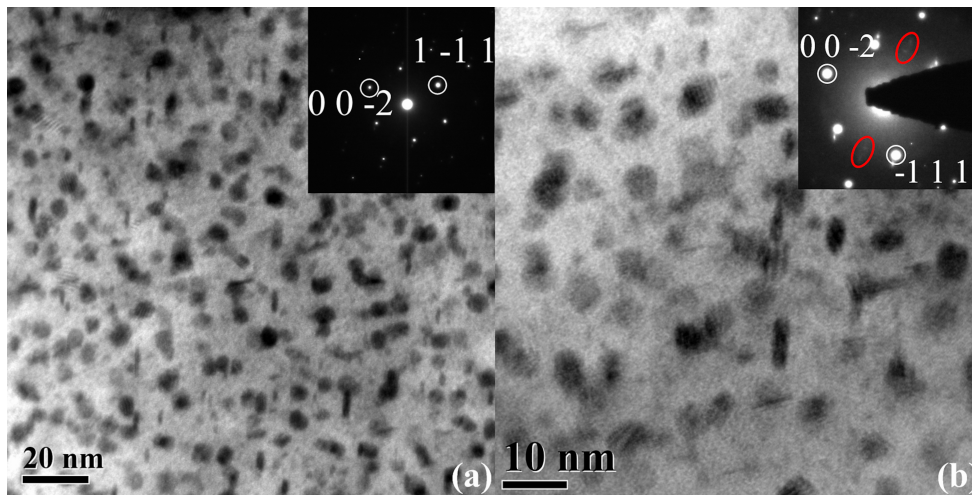


Figure 5.10: Bright field TEM images with (a) low magnification and (b) high magnification, taken along the $\langle 1\ 1\ 0 \rangle$ zone axis from the sample pre-aged at 80 °C 8 hours followed by baking at 185 °C 20 minutes.

To verify the precipitate size determined by SAXS, TEM images were taken from one condition as a comparison (fast heating rate and 20 minutes at 185 °C). Figure 5.10, shows examples of the microstructure viewed along the $\langle 1\ 1\ 0 \rangle$ zone axis. The TEM images demonstrate that larger precipitates are present than in the pre-aged condition, which are relatively spherical. Thin-plate shape precipitates resting on $\{111\}$ planes with their thickness less than 2nm were also exemplified in figure 5.10 (b). They are identified as the η' precipitates, with the evidence of the diffraction patterns located at $1/3\ [2\ \bar{2}\ 0]$ (marked by red ellipses) It has been demonstrated

by Yang et al. that these diffraction spots correspond to the variant 1 or variant 2 of the η' precipitates, which have the zone axis $[2 \bar{4} 2 3]$ or $[\bar{2} 4 \bar{2} 3]$ parallel to the $[1 1 0]$ aluminium matrix [47].

Figure 5.10 shows that the precipitates are uniformly distributed in the matrix. The particle radius is measured along the longest principle axis. The radius estimated from approximately 200 precipitates in the TEM images was 3.2 ± 0.6 nm. Small differences are to be expected, since the TEM measured particle radius along the principle axis is not an identical parameter to the Guinier radius measured from SAXS [35].

The Guinier radius from SAXS is measuring the electron density weighted root mean square distance from the gravity center [48]. If we consider ellipsoids shape in a mono-disperse condition, R_g is equal to $\sqrt{(a^2 + b^2 + c^2)/5}$, where a , b and c are the radius on the three semi-axes [49]. Assuming $a = b$ and the aspect ratio (c/a) is in range of 0.5 to 2 [35], it can be estimated that the ratio of true radius along the principle axis and Guinier radius (a/R_g) is in the range of 1.49 to 0.91. This is in good agreement with our results. The Guinier radius in the same sample determined by SAXS was 2.59 ± 0.02 nm. Together with the a radius from TEM images (3.2 ± 0.6 nm), this yields the a/R_g ratio to 1.2 ± 0.2 .

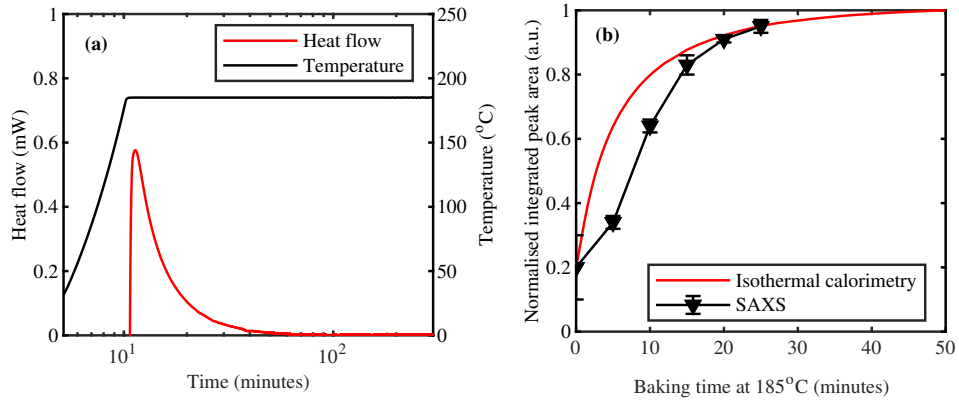


Figure 5.11: (a) Heat flow and temperature profile of the isothermal calorimetry tests of the sample pre-aged 8 hours at 80 °C baking at 185 °C in the calorimetry. (b) the normalised integrated peak area calculated from the isothermal calorimetry and the beamline SAXS results.

The isothermal calorimetry results are shown in figure 5.11. Figure 5.11(a) shows how the heat flow changes during a heat up (corresponding to a heating rate of

30 °C/minute) and hold at the paint-bake temperature. The peak corresponds to precipitate formation, which can be seen to be almost complete after 30 minutes (the standard paint-bake time) and fully complete after 50 minutes. For the isothermal calorimetry results, the relative volume fraction of the precipitates can be calculated by equation 2, where A_{SHT-PB} is the whole exothermal peak area of solution heat treated sample soaked in 185 °C, $A_{Preaged-PB}$ is the whole exothermal peak area of the pre-aged sample soaked at 185 °C, $A(t)$ is the integration of the heat flow curve of pre-aged sample soaked in 185 °C with time t in the range of 0 to 50 minutes.

$$V_{f_{relative}}(t) = \frac{A_{SHT-PB} - A_{Preaged-PB} + A(t)}{A_{SHT-PB}} \quad (5.2)$$

The evolution of the integrated heat flow from DSC data shown in figure 5.11(a) and the precipitation peak area measured by SAXS are compared in figure 5.11(b). Both of these measures are proxies for the precipitate volume fraction, but this can be complicated by changes in precipitate chemistry over time and other factors [36, 48]. It can be seen that while there is some difference in the shape of the evolution curve from both methods, the overall behaviour is the same. In particular, the time at which precipitation reaches completion is consistent using either method.

5.4 Discussion

To develop an optimised pre-ageing and paint-bake practice for industrial applications requires fulfilling several requirements that are often in competition with each other. For example, the pre-ageing step must lead to sufficient precipitation to stabilize the alloy against natural ageing and provide the necessary pre-cursors to enable full strengthening to be obtained during the paint-bake step. On the other hand, the pre-ageing step must limit precipitation to prevent a loss of formability and detrimental over-ageing during the paint-bake step. Ideally, the material will be in a state after pre-ageing that itself does not produce much hardening but produces a microstructure of pre-cursor precipitates that is able to harden strongly during the paint-bake cycle. Moreover, conducting the final ageing process at a slightly higher temperature could potentially enhance the resistance of the material to stress corrosion cracking (SCC) by encouraging the formation of large discontin-

uous η precipitates along grain boundaries. Nevertheless, a thorough investigation is necessary to examine the impact of pre-ageing and paint baking on the SCC behaviour. For industrial applications, the primary purpose of the paint-bake operation performed commercially is not to control precipitation; this heat treatment is usually fixed with little opportunity to change time and temperature. Therefore, the problem is reduced to optimise the pre-ageing practice to achieve the necessary balance in precipitation and properties.

Hardness measurements can be used to determine the fraction of the total hardening potential (hardening fraction) achieved during the pre-age and the fraction achieved during the paint-bake. This is calculated from:

$$f = \frac{HV - HV_i}{HV_{max} - HV_{min}} \quad (5.3)$$

Where HV is the hardness after the heat treatment step, HV_i is the initial hardness (before either the pre-ageing or paint-bake heat treatment), HV_{max} is the maximum (T6) hardness and HV_{min} is the minimum (W-temper) hardness. A plot of the calculated hardening fraction for pre-ageing at the different temperatures used in this study is shown in figure 5.12(a). This demonstrates the expected trend that as the fraction of hardening achieved during the pre-ageing process increases, the fraction obtained during paint-bake reduces. This has a compensatory effect, so that the final hardness obtained is relatively insensitive to the pre-ageing condition, providing a minimum level of pre-ageing is achieved. The pre-ageing temperature range 60-80 °C provides the best compromise for the paint-bake cycle studied here; at the low end of this range, the pre-aged material will be softer and the final hardness after paint bake slightly reduced compared to the high end. A pre-ageing temperature of 100 °C is too high; for this condition, over 70% of the hardening potential is exhausted after the pre-age, with less than 20% achieved during the paint bake. None of the conditions achieve the full T6 hardening potential, but 80 °C pre-ageing achieves 94% of this maximum value as demonstrated previously.

JMatPro is a powerful thermodynamic modelling software that can estimate the temperature-dependent precipitation kinetics in 7xxx aluminium alloys [50]. Based on the chemical composition and the investigated temperature and time, JMatPro is capable of predicting potential phases in the alloy system. In this study, to under-

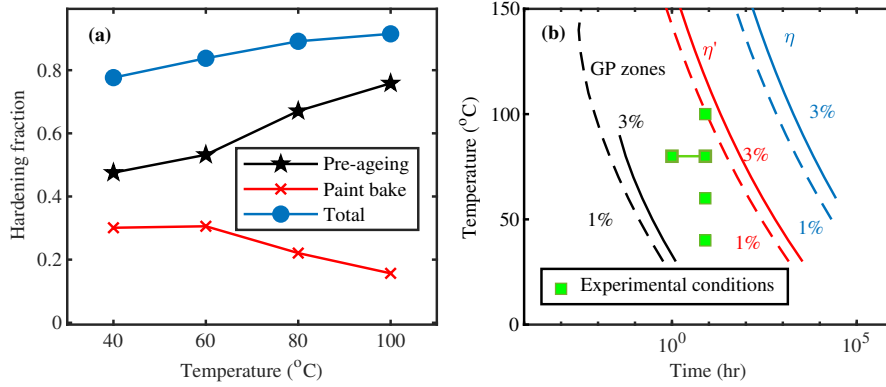


Figure 5.12: (a) Hardening fraction as a function of pre-ageing temperature. (b) Time-Temperature-Transformation (TTT) diagram calculated by using JMatPro, superimposed with the experimental conditions.

stand the kinetics of the precipitation processes that produce the observed hardening behaviour, JMatPro was used to calculate the critical time and temperature for 1 and 3 weight percent of GP zones, η' and η precipitation. The time-temperature-transformation (TTT) diagram is shown in figure 5.12(b). Superimposed on this diagram are the experimental conditions used for pre-ageing. Consistent with the microstructural analysis via TEM, it is predicted that in all cases the pre-ageing treatments should produce a microstructure consisting of GP zones. Only for the 100°C pre-treatment is significant transformation to η' expected to have begun. The pre-treatments all correspond to a temperature range below the “nose” of the C-curve, so that an increase in temperature is associated with faster precipitation kinetics. This is consistent with the hardness evolution and SAXS results. The selected pre-heat treatment (8h at 80°C) is predicted to produce a microstructural state in which the transformation to η' has almost begun. This is a promising state after pre-ageing since the GP-zones will be large enough to avoid reversion during the heat-up to the paint bake, but significant strengthening attributed to η' precipitation will not have occurred.

Another important role of the pre-ageing temper is to stabilize the material against natural ageing, which is of great value in industrial applications where there may be significant delay between the pre-temper performed at the alloy supplier and the paint bake process performed after forming and assembly at the vehicle manufacturer. This was demonstrated in the present work to be effective, up to a time of

at least 7 months, with evidence from microhardness and SAXS. This is consistent but more attractive than previous studies which confirmed the stabilization effect up to 3 weeks in 7075 [31]. Both previous studies and the present work demonstrate that the pre-aged microstructure contains GP zones, which reduce the solute supersaturation sufficiently to greatly retard the natural ageing process, whilst providing a reasonable formability. However, it is worth noting the sufficiency of formability depends on the specific requirement of each application. Furthermore, the complex interactions between deformation and precipitation may impact the precipitation kinetics and mechanical properties. Future studies are needed to assess the mechanical behavior of this pre-aged temper condition in various industrial applications.

For the first time we demonstrated the effect of heating rate to the paint baking temperature revealed a similar compensation effect to the effect of changing pre-ageing conditions. The specimens heated at the slowest rate underwent significant precipitation and hardening during the heating ramp. This reduces the supersaturation and slows subsequent precipitate evolution during the paint baking process. For the rapidly heated specimen, less precipitate evolution and hardening occurred during the heating ramp, and the greater remaining supersaturation enabled faster kinetics during the paint bake hold. As a result, the precipitate size, volume fraction, and related hardness increase caught up with those from the slow ramp. Interestingly, the time to reach peak hardness was insensitive to the large change in heating rate due to this compensation effect. This is industrially useful because it suggests that the strength change during paint-baking is insensitive to heating rate once the baking time exceeds around 20 minutes. This is important because measurements of heating rates for body-in-white automotive structures show that heating rates can vary strongly depending on location, from 20 °C/min for the roof to 4 °C/min for a location inside the B-pillar [45].

The TEM and DSC results support the conclusions from the SAXS and microhardness measurement and reveal further details of the microstructure. TEM reveals the microstructure after pre-ageing at 80 °C is dominated by a homogeneous distribution of GP zones, consistent with previous observations [32]. The similarity of the precipitate size derived from the Guinier radius measured with SAXS and measured by TEM confirms that SAXS is a useful technique to track the evolution

of these precipitates during the ageing process. The SAXS results show that after only 1h of pre-ageing at 80 °C, the GP zones are well-established. Extending the pre-ageing time does not increase the number density of the GP zones, which confirms the volume fraction increase is the result of the growth of the existing GP zones. This is in consistent with the previous findings [32, 51].

DSC is a complementary technique to SAXS to understand the evolution of the precipitate fraction. It is shown that both the area under the precipitate curve in SAXS and the integrated peak area evolution from isothermal DSC demonstrate a similar rate of evolution of precipitate fraction during the paint bake cycle. Both techniques suggest that for the investigated pre-ageing treatment of 8h at 80 °C, the maximum precipitate fraction saturates after approximately 30 minutes, which is the duration of the standard paint bake process. This demonstrates that the optimised pre-ageing practice is sufficient to enable the maximum precipitation (and hence hardening potential) to be realized during the paint bake, whilst avoiding excessive over-ageing.

5.5 Conclusions

The effect of a two step pre-ageing and final ageing (paint bake) practice on the microstructure and properties of AA7075 has been investigated. The following conclusions have been drawn from this work:

1. The pre-ageing treatment at 80 °C for 8 hr produced mechanical properties that show a good balance between formability over the T6 temper, but allowed 94% of the T6 strength to be achieved during a second ageing step simulating a paint-bake practice (20 minutes at 185 °C).
2. For all pre-ageing practices investigated in this study, there is convergence of hardness values after the simulated paint-bake. This is because a low amount of precipitation in the first step is compensated by a greater amount of precipitation in the paint-bake step, and vice versa.
3. Pre-ageing leads to formation of a large number of nano-sized GP zones. During the paint bake, transformation to η' occurs, leading to an increase in mean

precipitate size and volume fraction, but no increase in number density.

4. The pre-aged microstructure (80 °C for 8 hr) is stable against natural ageing for times up to at least 7 months, with negligible change in hardness or precipitate characteristics.
5. Providing the paint-bake time exceeds 20 minutes, the final hardness and precipitate size and fraction are insensitive to the heating rate. This is because slow heating leads to a greater increase in precipitate size and fraction during the heating ramp, removing solute and slowing the subsequent evolution during the isothermal hold compared to the fast heating rate.
6. The observation that the final hardness and precipitate distribution are not highly sensitive to either the precise pre-ageing practice or heat up to the paint-bake suggest the two step route proposed here is likely to be robust for industrial application.

Acknowledgements

The authors acknowledge the funding from the EPSRC programme grant (EP/R001715/1) LightForm for supporting this research. Dr O. Shebanova and Dr A. J. Smith are thanked for their assistance with the SAXS experiment (SM27903-1) at the I22 beamline, Diamond Light Source (UK).

Z. Ma would like to thank the financial support from Constellium and EPSRC grant Centre for Doctoral Training in Advanced Metallic Systems (EP/S022635/1) for his PhD research. The support of the EPSRC grant Henry Royce Institute (EP/R00661X/1) for Z. Ma through the Royce PhD Equipment Access Scheme is also appreciated.

Data presented in this paper may be obtained from the LightForm data repository at: <https://zenodo.org/communities/lightform/>.

Bibliography

- [1] A. Deschamps, F. Livet, Y. Brechet, Influence of predeformation on ageing in an al–zn–mg alloy—i. microstructure evolution and mechanical properties, *Acta materialia* 47 (1) (1998) 281–292.
- [2] M. Starink, S. Wang, A model for the yield strength of overaged Al–Zn–Mg–Cu alloys, *Acta Materialia* 51 (17) (2003) 5131–5150.
- [3] J. Nie, Physical Metallurgy of Light Alloys, in: D. E. Laughlin, K. Hono (Eds.), *Physical Metallurgy*, 5th Edition, Elsevier, Oxford, 2014, pp. 2009–2156.
- [4] H. Hunsicker, Development of Al–Zn–Mg–Cu alloys for aircraft, *Philosophical Transactions for the Royal Society of London. Series A, Mathematical and Physical Sciences* (1976) 359–376.
- [5] P. Dai, X. Luo, Y. Yang, Z. Kou, B. Huang, J. Zang, J. Ru, Thermal stability analysis of a lightweight al–zn–mg–cu alloy by tem and tensile tests, *Materials Characterization* 153 (2019) 271–283.
- [6] W. Huo, L. Hou, Y. Zhang, J. Zhang, Warm formability and post-forming microstructure/property of high-strength AA 7075-T6 Al alloy, *Materials Science and Engineering: A* 675 (2016) 44–54.
- [7] S. Knight, N. Birbilis, B. Muddle, A. Trueman, S. Lynch, Correlations between intergranular stress corrosion cracking, grain-boundary microchemistry, and grain-boundary electrochemistry for Al–Zn–Mg–Cu alloys, *Corrosion Science* 52 (12) (2010) 4073–4080.
- [8] X. Sun, B. Zhang, H. Lin, Y. Zhou, L. Sun, J. Wang, E.-H. Han, W. Ke, Correlations between stress corrosion cracking susceptibility and grain boundary microstructures for an Al–Zn–Mg alloy, *Corrosion science* 77 (2013) 103–112.
- [9] A. Azarniya, A. K. Taheri, K. K. Taheri, Recent advances in ageing of 7xxx series aluminum alloys: a physical metallurgy perspective, *Journal of Alloys and Compounds* 781 (2019) 945–983.

- [10] J. C. Williams, E. A. Starke Jr, Progress in structural materials for aerospace systems, *Acta materialia* 51 (19) (2003) 5775–5799.
- [11] T. Dursun, C. Soutis, Recent developments in advanced aircraft aluminium alloys, *Materials & Design* (1980-2015) 56 (2014) 862–871.
- [12] W. Hui, Y.-b. LUO, P. Friedman, M.-h. CHEN, G. Lin, Warm forming behavior of high strength aluminum alloy AA7075, *Transactions of Nonferrous Metals Society of China* 22 (1) (2012) 1–7.
- [13] M. Tajally, E. Emadoddin, Mechanical and anisotropic behaviors of 7075 aluminum alloy sheets, *Materials & Design* 32 (3) (2011) 1594–1599.
- [14] P. A. Schuster, J. A. Österreichischer, G. Kirov, C. Sommitsch, O. Kessler, E. Mukeli, Characterisation and comparison of process chains for producing automotive structural parts from 7xxx aluminium sheets, *Metals* 9 (3) (2019) 305.
- [15] J. Lin, T. Dean, R. Garrett, et al., A process in forming high strength and complex-shaped Al-alloy sheet components, UK Patent WO2008059242 (2008).
- [16] O. El Fakir, L. Wang, D. Balint, J. P. Dear, J. Lin, T. A. Dean, Numerical study of the solution heat treatment, forming, and in-die quenching (HFQ) process on AA5754, *International Journal of Machine Tools and Manufacture* 87 (2014) 39–48.
- [17] K. Zheng, Y. Dong, J.-H. Zheng, A. Foster, J. Lin, H. Dong, T. A. Dean, The effect of hot form quench (HFQ[®]) conditions on precipitation and mechanical properties of aluminium alloys, *Materials Science and Engineering: A* 761 (2019) 138017.
- [18] K. Zheng, Y. Dong, D. Zheng, J. Lin, T. A. Dean, An experimental investigation on the deformation and post-formed strength of heat-treatable aluminium alloys using different elevated temperature forming processes, *Journal of Materials Processing Technology* 268 (2019) 87–96.

- [19] A. G. Leacock, C. Howe, D. Brown, O.-G. Lademo, A. Deering, Evolution of mechanical properties in a 7075 Al-alloy subject to natural ageing, *Materials & Design* 49 (2013) 160–167.
- [20] J. A. Österreicher, M. A. Tunes, F. Grabner, A. Arnoldt, T. Kremmer, S. Pogatscher, C. M. Schlögl, Warm-forming of pre-aged Al-Zn-Mg-Cu alloy sheet, *Materials & Design* 193 (2020) 108837.
- [21] J. Robson, O. Engler, C. Sigli, A. Deschamps, W. Poole, Advances in microstructural understanding of wrought aluminum alloys, *Metallurgical and Materials Transactions A* 51 (9) (2020) 4377–4389.
- [22] M. Murayama, K. Hono, M. Saga, M. Kikuchi, Atom probe studies on the early stages of precipitation in Al–Mg–Si alloys, *Materials Science and Engineering: A* 250 (1) (1998) 127–132.
- [23] S. Pogatscher, H. Antrekowitsch, H. Leitner, T. Ebner, P. J. Uggowitzer, Mechanisms controlling the artificial aging of Al–Mg–Si Alloys, *Acta Materialia* 59 (9) (2011) 3352–3363.
- [24] O. Engler, C. Marioara, Y. Aruga, M. Kozuka, O. Myhr, Effect of natural ageing or pre-ageing on the evolution of precipitate structure and strength during age hardening of Al–Mg–Si alloy AA 6016, *Materials Science and Engineering: A* 759 (2019) 520–529.
- [25] T. Abid, A. Boubertakh, S. Hamamda, Effect of pre-aging and maturing on the precipitation hardening of an Al–Mg–Si alloy, *Journal of alloys and compounds* 490 (1-2) (2010) 166–169.
- [26] H. Zhong, P. A. Rometsch, X. Wu, L. Cao, Y. Estrin, Influence of pre-ageing on the stretch formability of Al-Mg-Si automotive sheet alloys, *Materials Science and Engineering: A* 697 (2017) 79–85.
- [27] L. Ding, Y. He, Z. Wen, P. Zhao, Z. Jia, Q. Liu, Optimization of the pre-aging treatment for an AA6022 alloy at various temperatures and holding times, *Journal of Alloys and Compounds* 647 (2015) 238–244.

- [28] Y. Birol, Pre-aging to improve bake hardening in a twin-roll cast Al–Mg–Si alloy, *Materials Science and Engineering: A* 391 (1-2) (2005) 175–180.
- [29] L. Cao, P. A. Rometsch, M. J. Couper, Effect of pre-ageing and natural ageing on the paint bake response of alloy AA6181A, *Materials Science and Engineering: A* 571 (2013) 77–82.
- [30] M. Kumar, N. Ross, Influence of temper on the performance of a high-strength Al–Zn–Mg alloy sheet in the warm forming processing chain, *Journal of materials processing technology* 231 (2016) 189–198.
- [31] J. A. Österreicher, G. Kirov, S. S. Gerstl, E. Mukeli, F. Grabner, M. Kumar, Stabilization of 7xxx aluminium alloys, *Journal of alloys and compounds* 740 (2018) 167–173.
- [32] Y.-S. Lee, D.-H. Koh, H.-W. Kim, Y.-S. Ahn, Improved bake-hardening response of Al–Zn–Mg–Cu alloy through pre-aging treatment, *Scripta Materialia* 147 (2018) 45–49.
- [33] J. A. Österreicher, F. Grabner, M. A. Tunes, D. S. Coradini, S. Pogatscher, C. M. Schlögl, Two step-ageing of 7xxx series alloys with an intermediate warm-forming step, *Journal of Materials Research and Technology* 12 (2021) 1508–1515.
- [34] A. Smith, S. Alcock, L. Davidson, J. Emmins, J. Hiller Bardsley, P. Holloway, M. Malfois, A. Marshall, C. Pizzey, S. Rogers, et al., I22: SAXS/WAXS beamline at diamond light source—an overview of 10 years operation, *Journal of Synchrotron Radiation* 28 (3) (2021).
- [35] A. Deschamps, F. De Geuser, On the validity of simple precipitate size measurements by small-angle scattering in metallic systems, *Journal of Applied Crystallography* 44 (2) (2011) 343–352.
- [36] A. Deschamps, F. De Geuser, Quantitative characterization of precipitate microstructures in metallic alloys using small-angle scattering, *Metallurgical and Materials Transactions A* 44 (1) (2013) 77–86.

- [37] F. De Geuser, A. Deschamps, Precipitate characterisation in metallic systems by small-angle x-ray or neutron scattering, *Comptes Rendus Physique* 13 (3) (2012) 246–256.
- [38] S. Esmaeili, X. Wang, D. Lloyd, W. Poole, On the precipitation-hardening behavior of the Al- Mg- Si- Cu alloy AA6111, *Metallurgical and Materials Transactions A* 34 (13) (2003) 751–763.
- [39] S. Esmaeili, D. J. Lloyd, Characterization of the evolution of the volume fraction of precipitates in aged AlMgSiCu alloys using DSC technique, *Materials characterization* 55 (4-5) (2005) 307–319.
- [40] P. Sepehrband, S. Esmaeili, Application of recently developed approaches to microstructural characterization and yield strength modeling of aluminum alloy AA7030, *Materials Science and Engineering: A* 487 (1-2) (2008) 309–315.
- [41] DaVis 10, <http://www.lavision.de/en/products/davis-software/index.php> (2020).
- [42] R. Schneider, B. Heine, R. J. Grant, Z. Zouaoui, Mechanical behaviour of aircraft relevant aluminium wrought alloys at low temperatures, *Proceedings of the Institution of Mechanical Engineers, Part L: Journal of Materials: Design and Applications* 229 (2) (2015) 126–136.
- [43] Y. An, H. Vegter, S. Melzer, P. R. Triguero, Evolution of the plastic anisotropy with straining and its implication on formability for sheet metals, *Journal of Materials Processing Technology* 213 (8) (2013) 1419–1425.
- [44] Y. H. Wu, S. Surapaneni, K. Srinivasan, P. Stibich, Automotive vehicle body temperature prediction in a paint oven, *Tech. rep.*, SAE Technical Paper (2014).
- [45] P. Rao, S. Teeparthi, A semi-computational method to predict body temperatures in an automotive paint bake oven, in: *ASME International Mechanical Engineering Congress and Exposition*, Vol. 54891, 2011, pp. 85–95.
- [46] N. K. Akafuah, S. Poozesh, A. Salaimah, G. Patrick, K. Lawler, K. Saito, Evolution of the automotive body coating process—a review, *Coatings* 6 (2) (2016) 24.

- [47] W. Yang, S. Ji, M. Wang, Z. Li, Precipitation behaviour of Al–Zn–Mg–Cu alloy and diffraction analysis from η' precipitates in four variants, *Journal of alloys and compounds* 610 (2014) 623–629.
- [48] A. Deschamps, Analytical Techniques for Aluminium, in: G. E. Totten, D. S. MacKenzie (Eds.), *Handbook of Aluminum: Volume 2: Alloy Production and Materials Manufacturing*, 1st Edition, CRC Press, 2003, pp. 155–192.
- [49] O. Kratky, P. Laggner, X-Ray Small-Angle Scattering, in: R. A. Meyers (Ed.), *Encyclopedia of Physical Science and Technology*, 3rd Edition, Academic Press, New York, 2003, pp. 939–988.
- [50] N. Saunders, U. Guo, X. Li, A. Miodownik, J.-P. Schillé, Using JMatPro to model materials properties and behavior, *Jom* 55 (12) (2003) 60–65.
- [51] J. Luo, H. Luo, S. Li, R. Wang, Y. Ma, Effect of pre-ageing treatment on second nucleating of GPII zones and precipitation kinetics in an ultrafine grained 7075 aluminum alloy, *Materials & Design* 187 (2020) 108402.

Chapter 6

Understanding the Effect of Deformation Combined with Heat Treatment on Age Hardening of Al-Zn-Mg-Cu Alloy AA7075

Z. Ma¹, J. D. Robson¹

1 – Department of Materials, The University of Manchester, Manchester, M13 9PL, UK

Published at Materials Science and Engineering: A, 2023. Z.Ma: Conceptualization, Methodology, Investigation, Formal analysis, Writing - Original Draft. J.D.Robson: Conceptualization, Writing - Review & Editing, Funding acquisition and Supervision.

Abstract

Al-Zn-Mg-Cu alloys obtain their exceptional high strength predominately relying on precipitation. Deformation can influence the evolution of precipitation and may potentially provide additional strength through work hardening. In this study, the coupling of dislocation and precipitation strengthening to achieve unique property combinations with strengths greater than those due to heat treatment alone was investigated on pre-aged AA7075 subject to a pre-age, deform, post-age cycle. The evolution of precipitates and mechanical properties were characterised to understand the contribution of each mechanism to the final strength. Small angle X-ray scattering (SAXS) was used to monitor the precipitate evolution during post-ageing, with the support from transmission electron microscopy (TEM) and isothermal calorimetry. The results revealed that uni-axial deformation to 10% strain had negligible effects on pre-existing precipitates but introduced sufficient dislocations to enable significant work hardening, which resulted in strengths greater than those obtained with a T6 heat treatment but with a sacrifice in further strain to failure. Post-ageing at 120°C was found being effective on partially recovering dislocations and promoting precipitation strengthening. A simple model was applied to demonstrate that the time required to reach peak strength is determined by the competing effects of the enhanced kinetics of precipitation and dislocation recovery. The acceleration effect of prior deformation on the growth of precipitation during post-ageing is consistent with the expected effect of dislocations acting as the fast diffusion paths.

6.1 Introduction

Aluminium alloys strengthened by precipitation are extensively used as structural components in the aerospace and automotive industries owing to their excellent strength to weight ratio [1, 2]. The exceptional strength is obtained by forming nano-sized particles which precipitate out from the supersaturated matrix during artificial ageing treatments [3]. 7xxx series aluminium alloys (Al-Zn-Mg and Al-Zn-Mg-Cu systems) are particular of interest since they exhibit the highest possible strength among the family of aluminium alloys, offering the possibility for maximum weight reduction.

For conventionally processed 7xxx alloys, the majority of strength in the strongest state (T6 temper) is provided by nanoscale η' precipitates with diameters of less than 5 nm [4]. A microstructure with precipitates having a size larger than this usually corresponds to an over-aged state showing reduced strength. Apart from strength, ductility is also an important consideration in mechanical properties. Many studies have been focused on achieving simultaneously high strength and high ductility for deformed 7xxx aluminium alloys [5, 6, 7]. Another challenge in using 7xxx in high volume production applications such as automotive is the long cycle time associated with the traditional tempering treatments. For example, a classic T6 temper involves heating at 120°C for 24 h after solution treatment and quenching.

One potential method to achieve even greater strength whilst simultaneously reducing cycle times is to combine ageing and deformation. In addition to providing both precipitation strengthening and work hardening contributions to boost final strength, this combination also has the potential to unlock useful synergies. For example, deformation can accelerate ageing, and precipitates may help to retain more work hardening by retarding dislocation recovery [8]. Attempts to combine these approaches in 7xxx alloys include work on cryo-rolling and low temperature ageing [5, 6]. When used in conjunction with an optimized two-step ageing practice, such an approach has produced AA7075 with 615 MPa yield strength, whilst maintaining an acceptable uniform elongation of 7.4%, representing a useful improvement over a standard T6 temper that produces a yield strength of approximately 500 MPa. However, cryogenic rolling can be impractical and adds cost, whilst complex and low

temperature ageing treatments add process time.

Pre-ageing (prior to deformation) to an underaged state can be an effective way to resolve these difficulties. Firstly, pre-existing precipitates can impede the recovery of dislocations in the following deformation process resulting in high dislocation density. Secondly, recent studies [9, 10] reported pre-ageing can stabilize natural ageing extending the shelf life. Finally, an accelerated precipitation kinetics during the second ageing can shorten the total ageing time. However, a complete understanding of how the pre-ageing treatment influences the subsequent deformation behaviour and ageing response remains lacking. Therefore, it is difficult to determine how to optimize the overall process to give the best property balance.

The objective of this study is to investigate the coupling of dislocation and precipitation strengthening to achieve novel property combinations using pre-aged AA7075 as the initial temper condition. Characterization of the precipitate evolution and dislocation density changes have been used to understand the contribution each mechanism makes to the final strength and explain how property combinations can be tailored. This provides a useful guide to developing combined heat-treatment and deformation ageing practices.

6.2 Methodology

7075 aluminium alloy sheets of 1.5 mm thickness were used in this study. The raw materials were produced from commercially direct-chill cast and rolled plate, supplied in the F temper (as fabricated) by Constellium C-TEC (France). The nominal composition is shown in table 6.1.

Table 6.1: Nominal composition of AA7075 in wt.%								
	Zn	Mg	Cu	Si	Fe	Mn	Cr	Al
AA7075	5.6	2.5	1.6	0.2	0.25	0.15	0.23	Bal

Tensile specimens were prepared with 10 mm width and 50 mm gauge length along the rolling direction. Samples were first subjected to a solution heat treatment at 480°C in an air recirculating furnace for 1.5 h, followed by water quenching to room temperature. A pre-ageing process was immediately applied isothermally at 80°C

for 8 h. The reason for this choice will be justified later. After the pre-ageing heat treatment, samples were stored in a freezer at -23°C .

Prior to the deformation process, samples were removed from the freezer. Uni-axial deformation was performed at room temperature on an Instron 5569H1549 machine with a cross-head speed of 1 mm min^{-1} , which gives a nominal average strain rate of $4 \times 10^{-4}\text{ s}^{-1}$. An extensometer was used to monitor the evolution of strain during the deformation process. Upon reaching 10% plastic strain, unloading was then applied immediately to prevent further plastic deformation. A uni-axial plastic strain of 10% corresponds to a true plastic stress of 600MPa, indicating a significant preservation of work hardening when compared to a 0.2% proof strength of 394MPa [11].

After the deformation, samples were subjected to an additional isothermal ageing treatment at 120°C in an air recirculating furnace for times ranging from 2 to 12 h. Following this, specimens of dimensions $10 \times 5 \times 1.5\text{ mm}^3$ were cut from the gauge area of pre-deformed specimens using a Struers Accutom-5 precision cut-off machine with a feed speed of 0.05 mm s^{-1} . Vickers hardness was then measured with 10 indentations taken in each case with 0.5 kgf force and a 10 s dwell, from which the mean and standard deviation were calculated. Afterwards, samples were polished using oxide particle suspension with a particle size of 0.2 microns for X-ray diffraction measurements.

A further set of pre-aged, deformed, and aged specimens was subject to tensile testing under the same conditions as used for pre-deformation, but strained to failure. Specimens were also prepared and tested from material that experienced an identical thermal pathway (pre-age, secondary ageing) but without any intermediate deformation.

Line broadening of X-ray diffraction (XRD) peaks was used to determine the evolution of dislocation density. Peaks were collected in the 2θ range of 20° to 140° with 0.02° step size and 8 s dwelling time, on a ProtoAXRD machine equipped with Cu source. Dislocation density was estimated from the X-ray line broadening using the modified Williamson-Hall method [12, 13]. After XRD tests, samples were mechanically ground to $70\mu\text{m}$ thickness for small-angle X-ray scattering (SAXS) characterisation.

To study the evolution of precipitates during the second ageing treatment at 120°C, small-angle X-ray scattering was performed on a Bruker Nanostar modified with a Genix 3D microfocus CuK α (1.54 Å, ~7.8 keV) source by Xenocs. The accessible scattering vector range in this study is [0.01, 0.6] Å⁻¹. The exposure time was set as 1500 seconds for all SAXS measurements. Scattering signals were circularly averaged at each scattering vector q to convert 2D scattering pattern to 1D graph (intensity vs q). The 1D data was then analysed using the Porod plot (Iq^4 vs q^4) to identify the background noise caused by the Laue scattering of disordered solid solution and instrument noise [14]. After subtracting this noise from the total scattering intensity, Kratky plots (Iq^2 vs q) were made to quantify the precipitates.

The Guinier radius can be calculated using $\frac{\sqrt{3}}{q_{peak}}$, where q_{peak} is the scattering vector q corresponded to the peak in the Kratky plot [14]. The relation between the Guinier radius R_g and true radius depends on the shape and dispersion of the particles. For example, a proportional factor of $\sqrt{5/3}$ can be applied onto R_g to obtain the true radius of a spherical particle. Nevertheless, it has been demonstrated elsewhere that in 7xxx alloys, R_g alone can provide a robust measurement of the average precipitate radius without this scaling [15]. The average number density is determined by dividing the volume fraction of precipitates by the average volume of an individual precipitate [14]. In the present study, assuming the precipitate composition is invariant, the change of volume fraction of precipitates can be represented by the change of the integrated peak area of the Kratky plot. The volume of an individual precipitate is proportional to R_g^3 . The relative precipitate number density can then be estimated by dividing the integrated peak area by R_g^3 .

Isothermal calorimetry was used as a complementary method to study the volume fraction evolution of the precipitates during the second ageing treatment at 120°C. Experiments were performed on a TA instrument DSC Q1000 machine using 30 °C/minute heating rate followed by an isothermal hold, with pure aluminium as the reference. Since the precipitation process is an exothermal reaction, the evolution of the heat flow can be used to study the precipitation kinetics. To determine the relative precipitate volume fraction in the sample right before the second ageing treatment, isothermal DSC was also performed at 120 °C on a specimen solutionized at 480 °C for 1.5 hour followed by water quenching. This sample was assumed to

contain no precipitates, and so provides a benchmark for full precipitation at 120 °C. Details of using this technique to study the kinetics of precipitation can be found elsewhere [16].

Transmission electron microscopy (TEM) was performed on samples cut from the same ground specimens as for SAXS. Twin jet electropolishing was performed at 15V and -40 °C in nitric acid and methanol solution (1:3 vol%) to produce electron transparent areas. Bright field TEM images were collected using a FEI Talos machine equipped with a X-FEG field emission gun operating at an accelerating voltage of 200kV. All bright field images shown in this study were taken with the beam aligned to the $\langle 110 \rangle$ zone-axis to identify the precipitate phase.

6.3 Results

The hardness values of all specimens in the present study are shown in Figure 6.1. Immediately after pre-ageing, the hardness was measured as 155 ± 1 HVN. Without any deformation, the hardness increased approximately linearly with time during the second ageing step at 120 °C in the first four hours. Afterwards, the increase slowed down and the hardness reached 185 ± 1.3 HVN after 10 h ageing. Further increase in time to 12 h did not produce a further significant increase in hardness.

The final hardness for the two step ageing without deformation plateaued at a value slightly lower than that produced by the standard T6 treatment, which was only subjected to a single ageing of 24 h at 120 °C (dashed line in Figure 6.1). The hardness evolution when the intermediate deformation step is used is completely different (Figure 6.1). Prior to the second ageing step, the hardness is already above that for a conventional T6 temper. It then falls below the T6 hardness after 2 h ageing before increasing gradually to 195.6 ± 1.3 after 10 h, significantly above that in the T6 state. Further ageing time does not lead to any significant change in hardness.

Prior to and after the second ageing step, samples were subjected to a tensile test to failure. Example stress-strain curves from these tests are selected and plotted in Figure 6.2 (a). Consistent with the hardness results, the 0.2% proof stress of the pre-aged and deformed condition (prior to the second ageing step) is above that

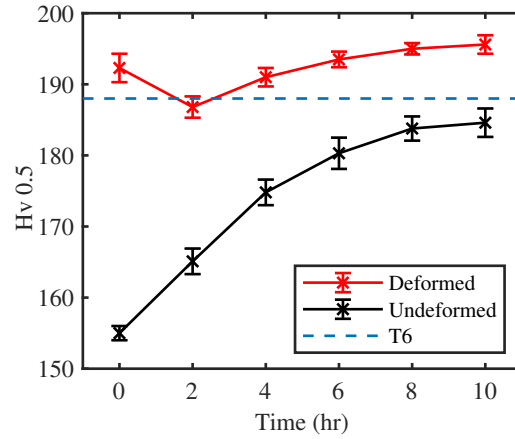


Figure 6.1: Hardness evolution at 120°C of samples with or without deformation, compared to the hardness of samples in the T6 condition (peak-aged).

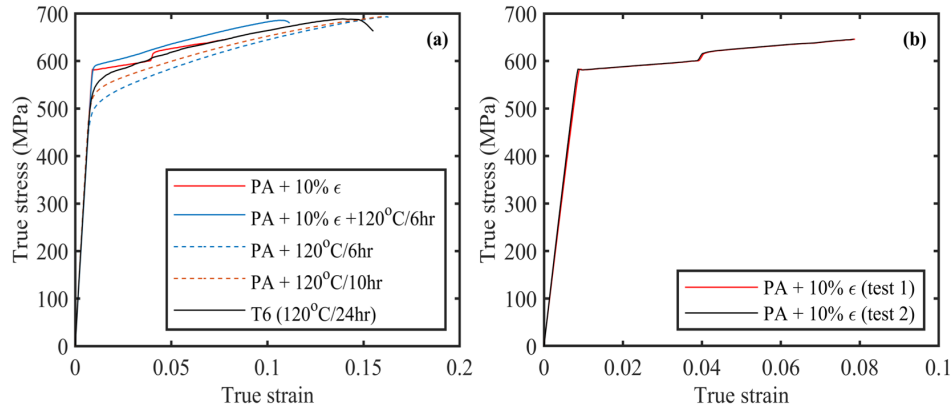


Figure 6.2: (a) True stress-strain curves of selected samples. (b) Repeated tests of deforming pre-deformed (10% strain) samples to failure. PA denotes pre-ageing 8 h at 80 °C.

obtained after a T6 temper. However, the work hardening capability is also partly exhausted, so that the additional elongation to failure is much lower (8%) than the total elongation to failure for the T6 material (16%). A elongated yield point was also observed during the second tensile deformation (up to an additional 4% plastic strain). Repeated tests were performed as shown in Figure 6.2 (b) to confirm the occurrence of this unusual behaviour. Although this behaviour is uncommon in 7xxx aluminium alloys, similar stress-strain curves were reported when reloading previously deformed underaged AA7075 [17].

Application of the second ageing step led to a small increase in 0.2% proof stress

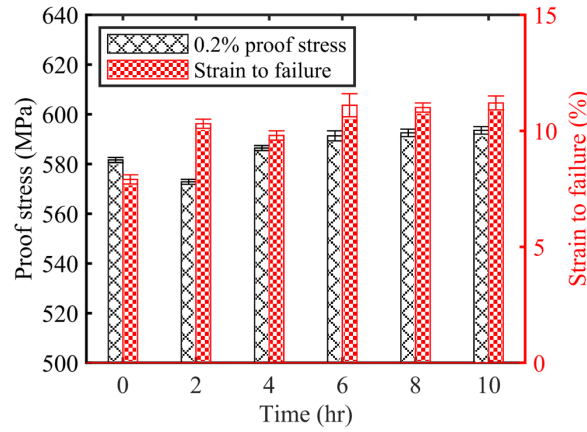


Figure 6.3: Summary of the 0.2% proof stress and strain to failure of deformed samples after the second ageing treatment at 120 °C

for ageing times in excess of 4 h, consistent with the hardness results, but had a more significant effect on the elongation to failure. For example, after 6 h of the second ageing step, the further elongation to failure was increased to 11% (compared to 8% prior to second ageing). Although this was still lower than that of the T6 sample, the 0.2% proof stress was increased to 590MPa (compared to 560MPa for the T6 temper). These results are also summarized in Figure 6.3. Figure 6.2 further demonstrates that a simple two-step ageing without any deformation in between was not enough to achieve this high strength. Pre-ageing 8 h at 80 °C followed by ageing 6 h at 120 °C resulted in a 17% total strain to failure but only 510MPa 0.2% proof stress. An additional 4 h ageing at 120 °C can increase the proof stress to 540MPa, which is then close to the T6 value, and maintain the elongation to failure at 17% but the total ageing time is now long (18 h) which may be unsuitable for high throughput production.

Figure 6.4 (a) shows the microstructure after pre-ageing and the first deformation to 10% plastic strain. Fine precipitates were observed, uniformly distributed in the matrix. Dislocations are also observed in the structure as expected. The diffraction pattern is consistent with the presence of GP-zones rather than η' or η precipitates.

After 2 h ageing at 120 °C following deformation, the microstructure is exemplified in Figure 6.4 (b). Compared to Figure 6.4 (a), precipitates in the matrix grew from 1.1 ± 0.2 nm to 1.5 ± 0.3 nm. Thin-plate shape precipitates aligned on $\{111\}$ planes can also be observed. From the diffraction pattern, they are identified as η'

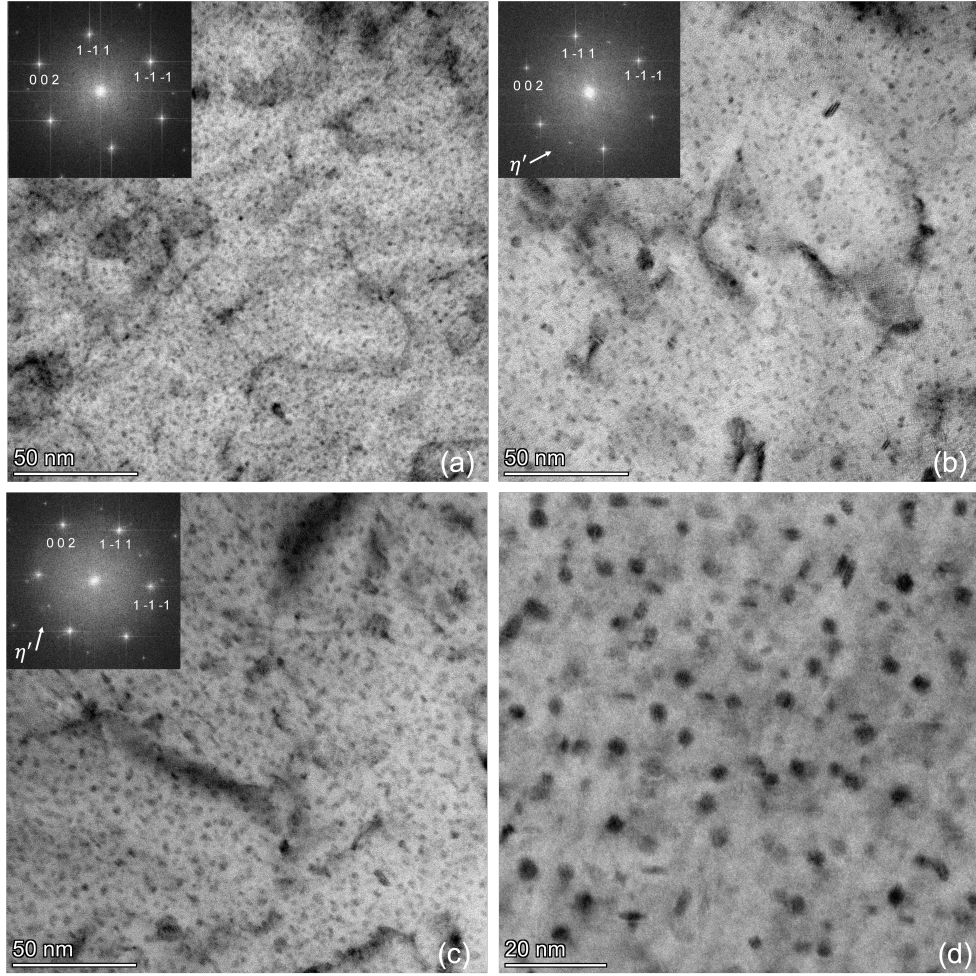


Figure 6.4: Bright field TEM images taken in $\langle 110 \rangle$ zone-axis from deformed samples (a) without any second ageing treatment, (b) after 2 h at 120 °C, (c) and (d) after 6 h at 120 °C.

precipitates [18]. Although a few large precipitates can be observed, which cause an increase of the standard deviation of the radius measurement, the distribution of precipitates was still relatively homogeneous in the matrix.

Figure 6.4 (c) and (d) were taken after 6 h ageing at 120 °C. A similar microstructure was observed to that obtained after 2 h (Figure 6.4 (b)). The mean radius of the precipitates was increased to 2.0 ± 0.3 nm. Diffraction spots corresponding to η' precipitates intensified, but there was still no evidence of transformation to η .

Small angle X-ray scattering was used to quantitatively investigate precipitate characteristics averaged over a larger volume than possible with TEM studies. The results are plotted as Iq^2 vs q in Figure 6.5 [15]. A shift in the peak in these plots towards the left (smaller q) indicates an increase in the average precipitate size. The area under the peak scales in proportion with the precipitate volume fraction,

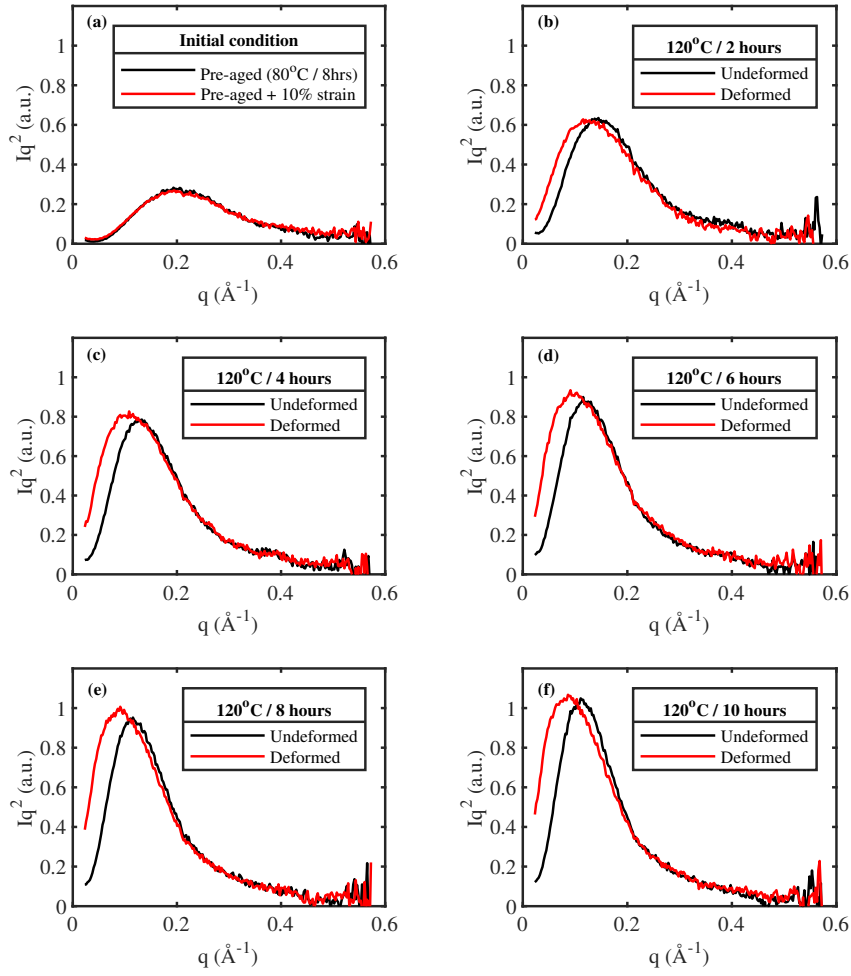


Figure 6.5: Kratky plots of SAXS results. (a) pre-aged samples before and after deformation (10% strain). (b~f) after 2~10 h ageing at 120°C from samples with or without deformation.

providing the precipitate composition and other factors are approximately invariant [14, 15].

Figure 6.5 (a) shows the SAXS results before and after the deformation step. The observation that these two curves are almost identical confirms that the deformation step itself does not modify the precipitate size distribution, as expected. Figure 6.5 (b ~ f) show the effect that deformation has on the evolution of precipitates during the subsequent ageing treatment at 120°C with increasing time. It can be seen that the curves for the deformed case deviate increasingly from those where the same heat treatment was applied without deformation. The peak of the curve in the deformation case moves up and to the left. This implies a larger average precipitate

size and greater volume fraction in the case where deformation was applied.

The Guinier radius and integrated intensity values extracted from the SAXS data are summarized in Figure 6.6. After pre-ageing, the Guinier radius is measured to be 0.9nm. Deforming the pre-aged sample to 10% strain has no significant effect on the Guinier radius. Applying a second ageing at 120 °C increased the Guinier radius for both deformed and undeformed samples as expected. The effect of deformation on accelerating the radius increase is clearly seen. For example, in the case where pre-deformation was applied, it takes only 2 h to reach the same radius as obtained after over 6 h ageing without deformation,

Figure 6.6 (b) shows the evolution of the integrated area under the Kratky plots taken as a proxy for the precipitate volume fraction. The most rapid change occurs in the first 2 h of ageing. At this time, the difference between the undeformed and pre-deformed cases is small. However, at longer times, the integrated area for the pre-deformed case continues to increase rapidly (up to 4 h) whilst in the undeformed case the increase slows. This leads to an increase in the peak intensity for the pre-deformed case that persists for subsequent ageing times.

Assuming the integrated area under the Kratky plots can be taken as proportional to the precipitate volume fraction, the relative number density can be estimated since it is determined by the mean radius and volume fraction. The result of this calculation is shown in Figure 6.6 (c). For undeformed samples, the relative number density is calculated to be approximately unchanged in the first 2 h and then decreases gradually over the next 8 h. For deformed samples, the calculation suggests that the number density is already decreasing after 2 h ageing and then continues downwards over the remaining heat treatment time. This leads to a relative number density in the pre-deformed case that is consistently below that in the undeformed case. The calculation of a stable or decreasing number density suggests that nucleation is not dominant and instead the microstructural evolution is in the regime governed by precipitate growth and coarsening.

Isothermal calorimetry provides an independent method of determining the relative precipitate volume fraction. The relative volume fraction can be determined from the area under the precipitation exotherm peaks, according to equation 6.1.

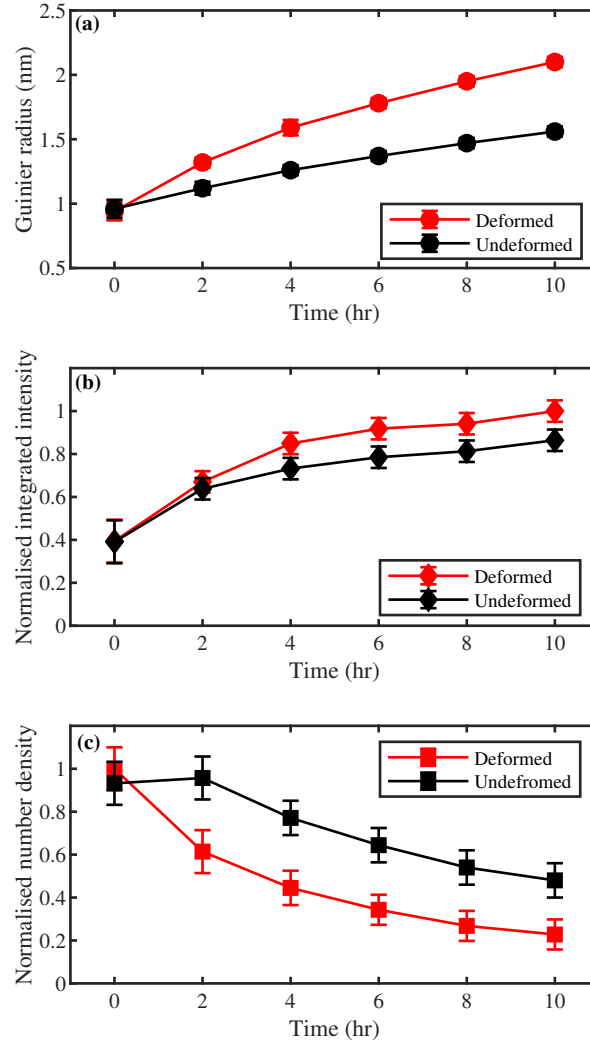


Figure 6.6: Evolution of (a) Guinier radius, (b) normalised integrated intensity and (c) normalised number density during the second ageing at 120°C for samples with or without 10% strain.

$$V_{f_{relative}}(t) = \frac{A_o - A_d + A(t)}{A_o} \quad (6.1)$$

where A_o is the integrated exothermal peak area of a sample in which the precipitate volume fraction is maximised (fully solutionised treated and aged for 24 h at 120 °C). A_d is the final total integrated exothermal peak area of the deformed sample held at 120 °C and $A(t)$ is the cumulative peak area of the deformed sample held at 120 °C as a function of hold time.

The temperature profile and the heat flow curve for the calorimetry test are

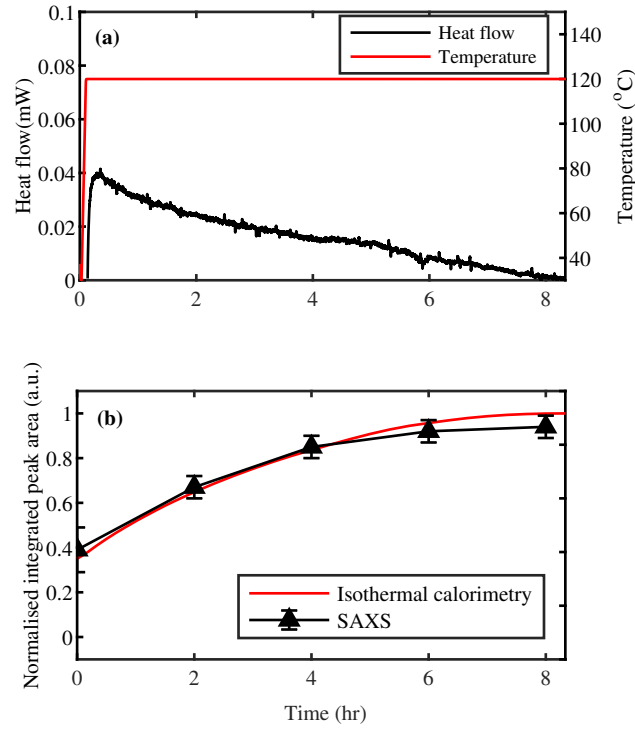


Figure 6.7: (a) Heat flow and temperature profile of the isothermal calorimetry test for the deformed sample (b) normalised integrated heat flow from isothermal calorimetry results and normalised integrated scattering intensity from SAXS results.

shown in Figure 6.7 (a). The normalized integrated peak area (equation 6.1) and the integrated scattering intensity from SAXS are compared in Figure 6.7 (b). Both methods, which independently determine the relative precipitate volume fraction, give good agreement in determining the overall precipitation kinetics.

In addition to the evolution of precipitates, the change in work-hardening contribution due to recovery of the dislocation sub-structure can also have a significant effect on the mechanical properties. To study this, X-ray line profile analysis was used to estimate the changing dislocation density during the post-deformation ageing treatment following the modified Williamson-Hall method. The theory behind the use of this method to determine dislocation densities is presented in detail elsewhere [12, 13].

Figure 6.8 (a) shows the modified Williamson-Hall plot, in which the peak broadening parameter (ΔK , the full peak width at half maximum height) is related to the dislocation density through Equation 6.2.

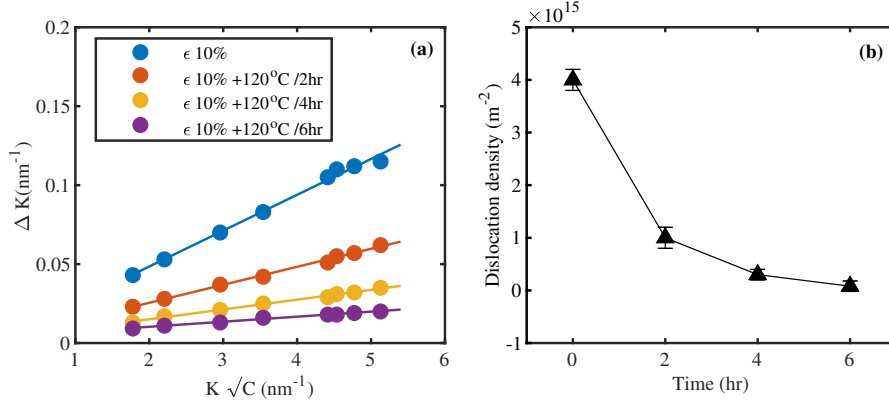


Figure 6.8: X-ray line broadening results (a)Modified Williamson-Hall plot. (b) evolution of dislocation density as a function of time at 120 °C.

$$(\Delta K)^2 = \left(\frac{0.9}{D}\right)^2 + \frac{\pi M^2 b^2}{2} \rho K^2 C_g \quad (6.2)$$

where K is the equivalent diffraction angle of each diffraction peak in the reciprocal space ($2\sin\theta/\lambda$), C_g is the contrast factor of dislocations, b is the Burgers vector, ρ is the dislocation density (to be determined), ΔK is the FWHM of each experimentally observed diffraction peak, M is a parameter describing the arrangement of dislocations that is unknown but is expected to lie between 1–2 in the present case [12]. The parameters used in producing Figure 6.8 are summarized in Table 6.2. Given the uncertainty in some of the input parameters, in particular the dislocation arrangement parameter M , the quantitative values of the dislocation density shown in Figure 6.8(b) are unlikely to be accurate. Nevertheless, the qualitative trend, which demonstrates a rapid reduction in dislocation density within the first 2 h of ageing followed by a slowed reduction for longer times, is expected to be reliable.

Table 6.2: Parameters for the modified Williamson-Hall plot

Symbol	Value
M	1 [12]
C_g	0.19 [13]
b	0.286
λ	0.154
ρ	to be determined

6.4 Discussion

The present study investigates the evolution of precipitates and mechanical properties on AA7075 subject to a pre-age/deform/post-age cycle, comparing this with the heat treated only condition. This has relevance to industrial forming operations, where a pre-age and post-age are typically used before and after the deformation step. The selection of a temperature of 80°C for 8 h is based on previous research, which has demonstrated that employing this pre-ageing strategy on AA7075 effectively stabilizes natural ageing, successfully preserves an adequate level of work hardening and provides essential precursors necessary for achieving high strength during subsequent ageing treatments [11].

Pre-ageing and 10% cold deformation leads to a synergistic strengthening effect combining both precipitation and work hardening. This results in a proof stress of 584 MPa which is considerably higher than the 560 MPa value obtained for a T6 sample. Previous studies on stretching supersaturated or naturally aged Al-Zn-Mg-Cu alloys at room temperature reported little to no direct effect on the hardness and/or yield strength [19, 20], which may be explained by the strong dynamic recovery in aluminium systems in the absence of sufficiently large precipitates. In pre-aged samples, such precipitates can be effective in accumulating dislocations by retarding dynamic recovery [8], resulting in a high working hardening contribution to the total strength. However, the increased strength due to deformation is accompanied by a significant reduction in the strain to failure from 17% to 8% due to the exhaustion of the working hardening capability. In addition, Lüders bands were observed, indicative of early strain instability and leading to elongated yield behaviour, which is an undesirable effect of the interaction of precipitates and dislocations when in the pre-aged condition. Although such behaviour is unusual in 7xxx aluminium alloys, it has been previously reported when reloading previously deformed AA7075 [17].

The post-deformation heat treatment can be used to tune the properties. This heat treatment leads to recovery of dislocations and therefore restoration of some of the work hardening capability but also increased precipitation resulting in enhanced precipitation strengthening. In the present work, a 120°C second heat treatment was used since this enables direct comparison with the classic T6 temper as well as

potentially enabling a desirable combination of both high strength and elongation to be achieved. For industrial forming, a higher temperature second step may be needed, either to reduce cycle times or to combine with some other process such as paint baking. However, when a hotter final step is used, as is typical for a paint-bake, this can lead to excess precipitate growth and an overaged microstructure [21, 22].

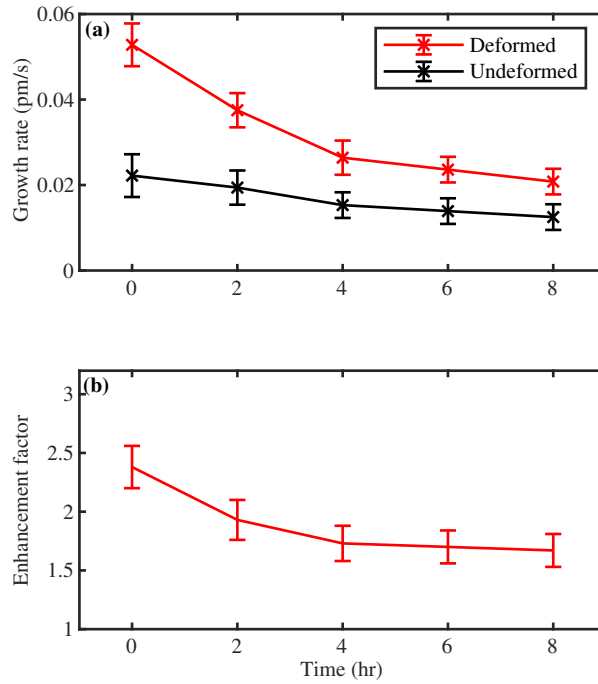


Figure 6.9: (a) The growth rate of precipitates and (b) the enhancement effect of the deformation as a function of the ageing time at 120°C.

The effect of the deformation step prior to the final ageing step is to accelerate the ageing behaviour. This accelerating effect on ageing is well known in the context of stretching of plate [20, 23]. The acceleration can be seen when comparing the evolution of precipitate size with and without deformation (Figure 6.6). Figure 6.9 (a) shows that at a given time the growth rate of precipitates in the deformed sample is much faster than the non-deformed sample. Additionally, Figure 6.9 (a) illustrates that in both cases the growth rate of precipitates continuously decreased over the ageing time at 120°C. For the non-deformed case, this phenomenon can be rationalised by the increase of size and decrease of supersaturation. For the deformed case, the evolution of the acceleration effect must also be taken into consideration.

The effect of deformation on the ageing kinetics can be expressed as an “enhance-

ment factor". The enhancement factor is calculated as the ratio of the precipitate growth rate of the deformed sample to the non-deformed sample at a given time, which reflects the acceleration effect by prior deformation. For a condition with no deformation induced acceleration, the enhancement factor is 1. In the present study, the enhancement factor was found to lie in the range of 1.5~2.5. This is in close agreement with previous studies of the effect of dislocation pipe diffusion, where an enhancement factor of 2~3 was observed by Deschamps et al. in an Al-Zn-Mg-Cu system and 2~5 was observed by Wang and Shiflet in an Al-Li system [14, 24]. In these cases, it was demonstrated using modelling that the enhanced kinetics were well explained by the effect of enhanced diffusion along the dislocation pipes.

Note that the enhancement in kinetics seen in this study is much less than that observed when deformation is applied simultaneously with precipitation during warm conditions. For example, an enhancement factor of ~ 7 was reported by Deschamps et al [14] in a warm deformed pre-aged Al-Zn-Mg-Cu system and an much higher value of ~ 50 was reported by Robson et al [25] in a supersaturated Al-Zn-Mg-Cu system. In room temperature cyclic deformation it has also shown that precipitation (natural ageing) can be accelerated by orders of magnitude due to the movement of dislocations [2]. In the case where deformation and precipitate evolution occur simultaneously, there is now strong evidence that the main effect is due to excess vacancies generated at jogs on gliding dislocations [26]. These enhance diffusion rates more powerfully than pipe diffusion along dislocations alone [27]. However, it is also predicted that once deformation stops, these excess vacancies annihilate very rapidly (typically within seconds [27]) so that they have little influence on the post-deformation ageing behaviour. Therefore an important distinction can be made between the strong effect of deformation enhanced diffusion during deformation, which is mainly due to excess vacancies, and the weaker effect of deformation enhanced diffusion post-deformation, which is mainly due to dislocations.

Although precipitation behaviour is accelerated by deformation, when considering the strength, the time to reach peak is similar in the deformed and non-deformed cases (as demonstrated by the hardness plot in Figure 6.1) at around 8 h, and this can be explained by the kinetics of not only the precipitation process but also the recovery process, that together determine the total strength in the as-deformed case.

To understand the evolution of strength during the process, and the relative contributions made by work hardening and precipitation strengthening, it is useful to use a simple model. The total strength may be broken down into the individual strengthening contributions according to [23, 28]:

$$\sigma_{tot} = \sigma_0 + \sigma_{sol} + \sigma_g + \sqrt[n]{\sigma_d^n + \sigma_{ppt}^n} \quad n \in [1, 2] \quad (6.3)$$

Parameters used in the strengthening model are summarised in Table 6.3.

Table 6.3: Parameters for the strengthening model

Symbol	Meaning	Value
σ_0	intrinsic stress of pure aluminium	10 MPa [29]
σ_g	grain boundary strengthening	19 MPa [30]
σ_d	dislocation strengthening	to be determined from Eq. 6.2
σ_{ppt}	precipitation strengthening	to be determined
n	exponent factor	1.3
c_i^0	the initial bulk concentration of solutes	from Table 6.1
c_{Mg}^{ppt}	atomic solute content of Mg in the precipitates	0.278 [31]
c_{Zn}^{ppt}	atomic solute content of Zn in the precipitates	0.389 [31]
α	dislocation strengthening constant	0.2 [31]
M	Taylor factor	3.06 [30]
G	shear modulus for aluminium	26.9 GPa [30]
β	fitting parameter	0.5 [23]
k_2	fitting parameter	0.063 [23]

In the present case, the solid solution strengthening (σ_{sol}) is considered as a linear superposition of the solid solution strengthening effects of Mg, Zn, and Cu [30]. The evolution of the solute concentration in matrix (c_i) can be calculated using Equation 6.4 [31]. In order to experimentally determine the actual volume fraction of precipitates using SAXS, it is necessary to calibrate the scattering intensity to an absolute unit and also have a comprehensive understanding of the composition of the precipitates. Unfortunately, these are not available in the current study. Therefore, the composition and maximum volume fraction of η' were predicted using Thermo-calc software with the TCAL8 database. This gave a composition of $Mg_5Zn_7Al_6$ and maximum volume fraction of 5.8%. The relative volume fraction from SAXS results can then be converted to the actual volume fraction (f_v) using this as a scaling factor.

$$c_i = \frac{c_i^0 - c_i^{ppt} f_v}{1 - f_v} \quad (6.4)$$

For the precipitation strengthening, a model that has been developed for 7xxx aluminium alloys under the Friedel statistics is adopted here [23].

$$\sigma_{ppt} = \frac{M}{bR\sqrt{2G\beta b^2}} \sqrt{\frac{3f_v}{2\pi}} F^{\frac{3}{2}} \quad (6.5)$$

The transition radius R_c determining whether the precipitate is by-passed or sheared is calculated as $2\beta b/k_2$ [23], which is close to 4.7nm. In the present study, precipitates in all experimental conditions have size smaller than the transition radius. Therefore, only the shearing mechanism is considered. The obstacle strength F is then given by:

$$F = 2\beta G b^2 \frac{R}{R_c} \quad (6.6)$$

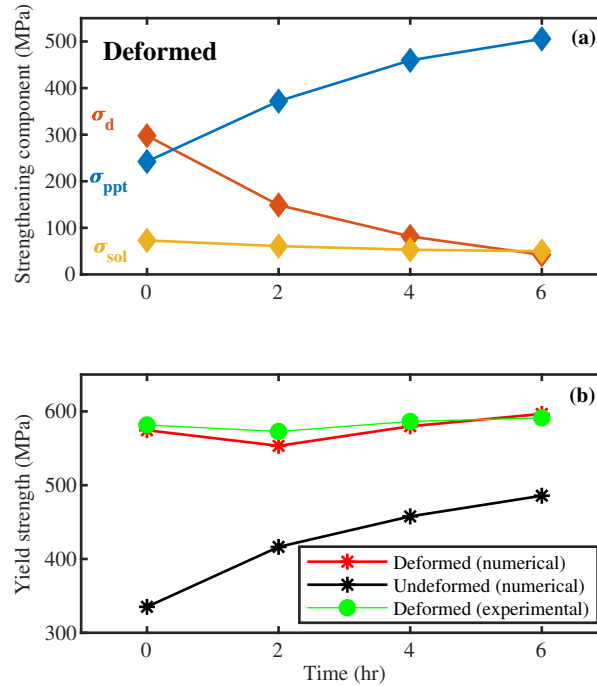


Figure 6.10: (a) Evolution of strengthening components for deformed samples at 120 °C. (b) Predicted yield strength of deformed and undeformed samples as a function of time at 120 °C.

The contribution of grain size (σ_g) to the overall strength is assumed to follow

a simple Hall-Petch relationship. In comparison to severe plastic deformation processes like equal channel angular pressing (ECAP), it is not expected that a plastic strain of 10% will lead to a significant decrease in grain size [30]. Additionally, the second ageing treatment at 120°C is well below the recrystallization temperature of AA7075 (which is usually above 300°C) [32]. Consequently, the effect of grain size is not anticipated to dominate the evolution of the overall strength. For this study, the grain size strengthening is estimated to be 19MPa, considering that the grain diameter in a typical commercial AA7075 sheet is approximately 40 μm [30].

A plot of the calculated strengthening components for deformed samples as a function of the ageing time at 120 °C is shown in Figure 6.10 (a). The solid solution strengthening effect has little contribution to the total yield strength and decreases over ageing time. Therefore, the evolution of the yield strength is mainly governed by the recovery of dislocations and growth of precipitates. Without the second heat treatment, the effect of dislocation strengthening is stronger than the precipitation strengthening resulting in the high yield strength.

A slight decrease of the yield strength is calculated after 2 h ageing at 120 °C, which is consistent with the experimental observations. This behaviour can be explained by the fast recovery of the dislocation strengthening during the first 2 h, which overcomes the strength increase due to additional precipitation in this period. Afterwards, the continued increase of precipitation strengthening overcomes the now slower recovery of dislocation strengthening, resulting in a strength increase.

Figure 6.10 (b) compares the evolution of this calculated yield strength in deformed and undeformed samples. For undeformed samples, the dislocation strengthening effect is not considered. The increase of the yield strength is simply a result of the precipitation strengthening. Overall, this figure reproduces the key features in the hardness measurement in Figure 6.1. A good fitting is obtained between the experimental and numerical yield strength in deformed samples, which verifies the applicability of this strengthening model in predicting the strength of the present Al-Zn-Mg-Cu system. Furthermore, this demonstrates that if recovery is suppressed by pre-ageing, the strength contribution due to work hardening can approach that due to precipitation, leading to a combined strength that significantly exceeds that obtained in the T6 temper. The balance of strengthening mechanisms and resultant

mechanical properties can be further tuned by varying the conditions of the second ageing step.

6.5 Conclusions

The present study investigated a strategy to obtain ultra-high strength for a Al-Zn-Mg-Cu alloy by combining working hardening and precipitation strengthening. To achieve this, experiments were performed on AA7075 following the route of solution heat treatment, pre-ageing, deformation and the second ageing. The effect of deformation on the evolution of precipitates and mechanical properties during the second heat treatment were characterised in detail. The following conclusions may be drawn from this work:

1. Stretching pre-aged (8 hours at 80 °C) AA7075 leads to strengths above T6 level prior to the final ageing step due to a high contribution of dislocation strengthening. However, the initial straining exhausts some of the work hardening capacity of the material so that a further elongation of only 8% is achieved.
2. The mechanical properties and precipitation status can be further tuned by the second heat treatment. 6 hours heat treatment at 120 °C results in a 0.2% proof stress of 590 MPa (a significant increase over the T6 level of 560 MPa) combined with a useful further 11% strain to failure.
3. SAXS reveals that room temperature deformation has a negligible effect on the precipitate size and volume fraction formed during the pre-ageing, but does accelerate precipitate growth during the final ageing step.
4. The effect of enhanced precipitate growth post-deformation is weaker than that observed in previously studies where precipitation and deformation occurs simultaneously.
5. Despite the accelerating effect of dislocations on precipitation, the time required to reach peak strength is similar with or without prior deformation. This is because the strength evolution with prior deformation is determined by the kinetics of both precipitate growth and recovery.

6. The evolution of strength during the second ageing strength can be well predicted using a simple model that considers all of the strengthening contributions. Such a model provides a useful guide in tuning the second ageing step to obtain the desired property balance for a given application.

Acknowledgements

Constellium is thanked for the provision of materials and financial support for this research. The EPSRC is thanked for financial support through the associated programme grant LightFORM (EP/R001715/1). Z.M. thanks the financial support from EPSRC grant Centre for Doctoral Training in Advanced Metallic Systems (EP/S022635/1) for his PhD research. J.D.R. acknowledges the support of the DSTL/RAEng Chair in Alloys for Extreme Environments.

The data required to reproduce these findings are available from the LightFORM Zenodo repository <https://zenodo.org/communities/lightform/>.

Bibliography

- [1] E. A. Starke Jr, J. T. Staley, Application of modern aluminum alloys to aircraft, Progress in aerospace sciences 32 (2-3) (1996) 131–172.
- [2] W. Sun, Y. Zhu, R. Marceau, L. Wang, Q. Zhang, X. Gao, C. Hutchinson, Precipitation strengthening of aluminum alloys by room-temperature cyclic plasticity, Science 363 (6430) (2019) 972–975.
- [3] T. Marlaud, A. Deschamps, F. Bley, W. Lefebvre, B. Baroux, Influence of alloy composition and heat treatment on precipitate composition in al–zn–mg–cu alloys, Acta Materialia 58 (1) (2010) 248–260.
- [4] H. Zhao, Y. Chen, B. Gault, S. K. Makineni, D. Ponge, D. Raabe, (al, zn) 3zr dispersoids assisted η precipitation in anal-zn-mg-cu-zr alloy, Materialia 10 (2020) 100641.
- [5] S. K. Panigrahi, R. Jayaganthan, Effect of ageing on microstructure and me-

- chanical properties of bulk, cryorolled, and room temperature rolled al 7075 alloy, *Journal of Alloys and Compounds* 509 (40) (2011) 9609–9616.
- [6] Y.-H. Zhao, X.-Z. Liao, S. Cheng, E. Ma, Y. T. Zhu, Simultaneously increasing the ductility and strength of nanostructured alloys, *Advanced Materials* 18 (17) (2006) 2280–2283.
- [7] W. Kim, J. Kim, H. Kim, J. Park, Y. Jeong, Effect of post equal-channel-angular-pressing aging on the modified 7075 al alloy containing sc, *Journal of alloys and Compounds* 450 (1-2) (2008) 222–228.
- [8] S. Cheng, Y. Zhao, Y. Zhu, E. Ma, Optimizing the strength and ductility of fine structured 2024 al alloy by nano-precipitation, *Acta Materialia* 55 (17) (2007) 5822–5832.
- [9] Y.-S. Lee, D.-H. Koh, H.-W. Kim, Y.-S. Ahn, Improved bake-hardening response of Al-Zn-Mg-Cu alloy through pre-aging treatment, *Scripta Materialia* 147 (2018) 45–49.
- [10] J. A. Österreicher, G. Kirov, S. S. Gerstl, E. Mukeli, F. Grabner, M. Kumar, Stabilization of 7xxx aluminium alloys, *Journal of alloys and compounds* 740 (2018) 167–173.
- [11] Z. Ma, E. Cooksey-Nash, D. Barbier, J. Robson, Microstructural stability and paint bake response of pre-aged aa7075, *Materials Characterization* 200 (2023) 112862.
- [12] G. Ribárik, T. Ungár, Characterization of the microstructure in random and textured polycrystals and single crystals by diffraction line profile analysis, *Materials Science and Engineering: A* 528 (1) (2010) 112–121.
- [13] T. Ungár, I. Dragomir, Á. Révész, A. Borbély, The contrast factors of dislocations in cubic crystals: the dislocation model of strain anisotropy in practice, *Journal of applied crystallography* 32 (5) (1999) 992–1002.
- [14] F. De Geuser, A. Deschamps, Precipitate characterisation in metallic systems by small-angle x-ray or neutron scattering, *Comptes Rendus Physique* 13 (3) (2012) 246–256.

- [15] A. Deschamps, F. De Geuser, Quantitative characterization of precipitate microstructures in metallic alloys using small-angle scattering, *Metallurgical and Materials Transactions A* 44 (1) (2013) 77–86.
- [16] S. Esmaili, D. J. Lloyd, Characterization of the evolution of the volume fraction of precipitates in aged AlMgSiCu alloys using DSC technique, *Materials characterization* 55 (4-5) (2005) 307–319.
- [17] H. Choi, H. Kim, H.-J. Jeong, E. Shin, W. Woo, S.-T. Hong, M.-G. Lee, H. N. Han, Investigation of the unloading yield effect in 7075 al alloys based on microstructural and digital image correlation analysis, *Materials Characterization* 173 (2021) 110963.
- [18] W. Yang, S. Ji, M. Wang, Z. Li, Precipitation behaviour of Al–Zn–Mg–Cu alloy and diffraction analysis from η' precipitates in four variants, *Journal of alloys and compounds* 610 (2014) 623–629.
- [19] W. Poole, H. Shercliff, T. Castillo, Process model for two step age hardening of 7475 aluminium alloy, *Materials science and technology* 13 (11) (1997) 897–904.
- [20] V. Hansen, J. Gjønnnes, S. Skjervold, Effect of predeformation and preaging at room temperature in al–zn–mg–(cu, zr) alloys, *Materials Science and Engineering: A* 303 (1-2) (2001) 226–233.
- [21] Y. Fan, X. Tang, S. Wang, B. Chen, Comparisons of age hardening and precipitation behavior in 7075 alloy under single and double-stage aging treatments, *Metals and Materials International* 27 (10) (2021) 4204–4215.
- [22] W. Huo, L. Hou, Y. Zhang, J. Zhang, Warm formability and post-forming microstructure/property of high-strength AA 7075-T6 Al alloy, *Materials Science and Engineering: A* 675 (2016) 44–54.
- [23] A. Deschamps, F. Livet, Y. Brechet, Influence of predeformation on ageing in an al–zn–mg alloy—i. microstructure evolution and mechanical properties, *Acta materialia* 47 (1) (1998) 281–292.
- [24] Z. Wang, G. Shiflet, Growth of δ on dislocations in a dilute al–li alloy, *Metallurgical and Materials Transactions A* 29 (8) (1998) 2073–2085.

- [25] J. Robson, P. Jessner, M. Taylor, Z. Ma, Dynamic precipitation in supersaturated al–zn–mg–cu alloy during warm stretching, *Metallurgical and Materials Transactions* (2023) 1–11.
- [26] M. Bignon, Z. Ma, J. D. Robson, P. Shanthraj, Interactions between plastic deformation and precipitation in aluminium alloys: A crystal plasticity model, *Acta Materialia* 247 (2023) 118735.
- [27] J. Robson, Deformation enhanced diffusion in aluminium alloys, *Metallurgical and Materials Transactions A* 51 (10) (2020) 5401–5413.
- [28] S.-H. Lee, J.-G. Jung, S.-I. Baik, D. N. Seidman, M.-S. Kim, Y.-K. Lee, K. Euh, Precipitation strengthening in naturally aged al–zn–mg–cu alloy, *Materials Science and Engineering: A* 803 (2021) 140719.
- [29] M. Starink, A. Deschamps, S. Wang, The strength of friction stir welded and friction stir processed aluminium alloys, *Scripta materialia* 58 (5) (2008) 377–382.
- [30] K. Ma, H. Wen, T. Hu, T. D. Topping, D. Isheim, D. N. Seidman, E. J. Lavernia, J. M. Schoenung, Mechanical behavior and strengthening mechanisms in ultrafine grain precipitation-strengthened aluminum alloy, *Acta Materialia* 62 (2014) 141–155.
- [31] M. Bignon, P. Shanthraj, J. D. Robson, Modelling dynamic precipitation in pre-aged aluminium alloys under warm forming conditions, *Acta Materialia* (2022) 118036.
- [32] W. Xiao, B. Wang, Y. Wu, X. Yang, Constitutive modeling of flow behavior and microstructure evolution of aa7075 in hot tensile deformation, *Materials Science and Engineering: A* 712 (2018) 704–713.

Chapter 7

In-situ Investigation of Dynamic Precipitation in Pre-aged Al-Zn-Mg-Cu Alloy AA7075

Z. Ma¹, M. Bignon¹, F. Gao¹, S. Michalik², J. D. Robson¹

1 – Department of Materials, The University of Manchester, Manchester, M13 9PL, UK

2 – Diamond Light Source, Didcot, OX11 0DE, UK

Z.Ma: Conceptualization, Methodology, Investigation, Formal analysis, Writing - Original Draft, Writing - Review & Editing. M.Bignon: Investigation. F.Gao: Investigation. S.Michalik: Investigation. J.D.Robson: Conceptualization, Writing - Review & Editing and Supervision.

Abstract

High strength Al-Zn-Mg-Cu alloys rely for their properties on nano-scaled precipitates formed during artificial ageing. The evolution of these precipitates can be profoundly affected by deformation. This study investigates in-situ the effect of warm deformation on precipitation in a pre-aged 7075 aluminium alloy. Warm deformation was performed on an electro-thermo-mechanical testing machine allowing rapid resistance heating to the target temperature. Transmission electron microscopy demonstrated the precipitates in the warm deformed sample were slightly larger than in a condition subject to the same thermal treatment without deformation, but still homogeneously distributed. Synchrotron small angle X-ray scattering revealed the growth rate of precipitates was strongly accelerated by deformation. In the range of low plastic strains, the precipitate growth rate linearly increased with the applied strain. In the range of high plastic strains, the relation between the precipitate growth rate and the applied strain slightly deviated from the linear behaviour. The temperature and strain rate effects were also studied, with a stronger enhancement effect at a low temperature and a fast strain rate for a given strain. Upon finishing plastic deformation, the deformation enhancement effect was rapidly lost (within 400s for the condition studied). The evolution of the enhanced growth rate during and after deformation can be reasonably fitted to predictions of the excess vacancy concentration, which is consistent with the idea that the enhanced precipitate growth rate during warm deformation is mainly attributed to the effect of strain-induced excess vacancies. However, the simple excess vacancy model used does not correctly capture the observed strain rate effect, and possible explanations for this discrepancy are discussed.

7.1 Introduction

Al-Zn-Mg-Cu alloys obtain their high strength by forming nano-scale precipitates from the supersaturated solid solution. Extensive studies have demonstrated deformation can strongly affect the thermodynamics and kinetics of the precipitation process [1, 2, 3]. The instantaneous effect of deformation on precipitation is particularly of interest since it is the most relevant case to the industrial warm forming process.

Previous studies have shown the dynamic interactions between deformation and precipitation at warm temperature is mainly governed by the excess vacancies produced during plastic straining by the non-conservative motion of dislocation jogs [2, 4, 5, 6]. The concentration of excess vacancies can profoundly influence the diffusion of solutes. In a pre-aged microstructure, the effect of excess vacancies has been observed on accelerating the growth and coarsening of pre-existing precipitates at warm temperature [2, 4, 5]. In a supersaturated microstructure, it has been reported excess vacancies can promote the nucleation of new clusters during cyclic loading at room temperature [7, 8].

Apart from the initial temper condition, the dynamic interactions between deformation and precipitation are also strongly affected by the parameters of the deformation process, such as strains, strain rates and temperatures, which controls the vacancy production and annihilation [9, 10]. Previous studies on pre-aged microstructures under uni-axial tensile strains have observed an enhanced growth rate with a strain dependency [2, 4]. In these cases, vacancy production dominates the overall evolution with negligible effect from vacancy annihilation at the vacancy sinks. When dislocations are the primary vacancy sinks, a low dislocation density is usually necessary to ensure that the spacing of dislocations is smaller than the distance of vacancy diffusion. However, in cases where dislocations can accumulate to a high density, the impact of vacancy annihilation on dislocations must be taken into consideration.

Another limitation of previous studies is that most experimental investigations of the dynamic precipitation in 7xxx aluminium alloys are limited to one deformation temperature for a given microstructure (temper condition) [2, 4, 5, 6, 7]. Since

vacancy annihilation is a diffusion-controlled process, the temperature is expected to play an important role on controlling the overall vacancy evolution.

The key objective of the present study is to investigate dynamic precipitation in a pre-tempered microstructure that shows a significant work hardening capability. The vacancy annihilation and its effect on the precipitate growth rate during and after deformation are investigated at different temperatures.

7.2 Methodology

7075 aluminium alloy sheets of 1.5 mm thickness with the nominal composition shown in table 7.1 produced from commercially direct-chill cast and rolled plates were supplied by Constellium C-TEC (France) in the as-fabricated condition (F temper).

Table 7.1: Nominal composition of AA7075 in wt.%

	Zn	Mg	Cu	Si	Fe	Mn	Cr	Al
AA7075	5.6	2.5	1.6	0.2	0.25	0.15	0.23	Bal

Uni-axial deformation at warm temperature was performed on an Instron electro-thermo-mechanical testing machine (ETMT), which was integrated on the I12 beam-line of Diamond Light Source enabling in-situ microstructural characterisation. This instrument (ETMT) allows rapid specimen heating up to $200^{\circ}\text{C s}^{-1}$ using resistance heating with direct current (DC), and fast cooling up to $100^{\circ}\text{C s}^{-1}$ by water cooling the holding grips.

Tensile specimens of 3.5 mm width and 15 mm gauge length were prepared using electrical discharge machining. To dissolve the large precipitates present in the F-temper condition and produce a fully solutionized microstructure, solution heat treatment was performed in an air recirculating furnace at 480°C for 1.5 h, followed by water quenching to room temperature. To produce a consistent pre-aged microstructure, samples were immediately subjected to an isothermal pre-ageing process at 80°C in an air recirculating furnace for 8 h. Prior to loading in the ETMT, K-type thermocouples were resistance spot welded onto the centre of the gauge area to monitor the temperature of the sample during the thermomechanical process.

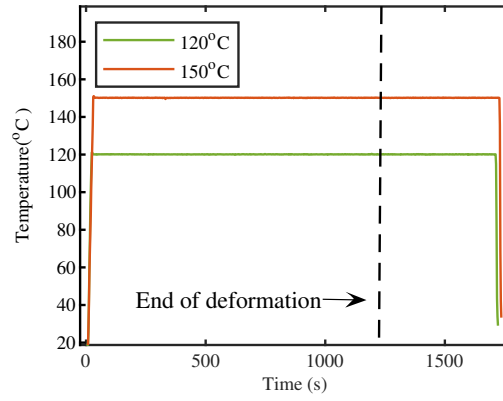


Figure 7.1: Temperature profile of samples deformed at 120°C and 150°C with the slow strain rate $1 \times 10^{-4} \text{ s}^{-1}$. Upon reaching the target strain, load was immediately reduced to 0 N. The sample was maintained at the target temperature for additional 400 seconds.

Uni-axial tensile tests were performed individually at 120°C and 150°C with a heating rate of 10°C s^{-1} . Upon reaching the target temperature, an additional 5 seconds of holding was applied to stabilise the temperature before any deformation. Average strain rates for plastic deformations were calculated by fitting a linear function on the strain-time plot. Nominal average strain rates of $1 \times 10^{-4} \text{ s}^{-1}$, $2 \times 10^{-4} \text{ s}^{-1}$ and $2 \times 10^{-3} \text{ s}^{-1}$ were measured for slow, intermediate and fast deformation. Upon reaching the target strain, samples were immediately unloaded to prevent further plastic deformation. The temperature was then maintained for additional 400 seconds with measurements continued to study the decay in the deformation enhancement effect. An example thermal history for samples deformed at 120 and 150°C with an average strain rate of $1 \times 10^{-4} \text{ s}^{-1}$ is shown in Figure 7.1.

Reference samples that underwent exactly the same thermal history but without any deformation were also prepared using the ETMT. For reference samples, the load was maintained at zero throughout the thermomechanical process to avoid plastic deformation due to thermal expansion or contraction.

In-situ small angle X-ray scattering (SAXS) experiments were performed at I12 beamline, Diamond Light Source, UK. X-ray energy was selected as 55keV which is capable of penetrating 1.5mm thickness aluminium alloys. A Pilatus 2M CdTe detector with 1475×1679 pixels ($172 \times 172 \mu\text{m}^2$ pixel size) was located 4.5m from the sample to collect the scattering signals. Under the present experimental config-

uration, the accessible scattering vector range is from 0.02 to 0.8 Å⁻¹. Depending on the deformation strain rate, the data acquisition rate was set as 1Hz for the fast deformation ($2 \times 10^{-3} \text{ s}^{-1}$) and 0.5Hz for the intermediate and slow deformation (2×10^{-4} and $1 \times 10^{-4} \text{ s}^{-1}$). A pure aluminium sample with the same thickness of 1.5 mm was used to identify the instrument and background noise.

2-dimensional scattering patterns were analysed using an open source software DAWN 2.23.0 [11]. The 1-dimensional graph of intensity- q was obtained by performing azimuthal integration, which is the process of circularly averaging the scattering signals at each scattering vector q . The instrument and background noise identified by the pure aluminium was subtracted from the total scattering intensity. Porod plots (Iq^4 vs q^4) were then made to further identify the background noise caused by the Laue scattering of the disordered solid solution [12]. After subtracting all these noise signals, Kratky plots (Iq^2 vs q) were made to quantify the precipitates.

By indexing the scattering vector q corresponded to the peak of the Kratky plot, the Guinier radius can be calculated as $\frac{\sqrt{3}}{q_{peak}}$ [12, 13]. Guinier radius, describing the electron density weighted root-mean-square distance from the centre of the object, is an effective measurement of the overall size of the particles [14]. For monodispersed spherical particles, the true radius can be obtained by multiplying R_g with a proportional factor of $\sqrt{5/3}$. Although precipitates in 7xxx alloys are often polydispersed, it has been previously demonstrated that R_g alone can provide a robust measurement of the average precipitate radius without a proportional factor [15].

Transmission electron microscopy (TEM) was performed on a ThermoFisher Talos F200X instrument equipped with a high-brightness field emission gun (X-FEG) operating at an accelerating voltage of 200kV. To produce electron transparent areas, twin jet electropolishing was performed at 15V and -40 °C in nitric acid and methanol solution (1:3 vol%) on samples that had been mechanical ground to 80 μm thickness. For the purpose of identifying the precipitate phase, bright field images were taken with the beam aligned to the $\langle 110 \rangle$ zone-axis.

7.3 Results

7.3.1 Effect of plastic strain and strain rate

Results collected from samples deformed at 150 °C with three different strain rates ($1 \times 10^{-4} \text{ s}^{-1}$, $2 \times 10^{-4} \text{ s}^{-1}$ and $2 \times 10^{-3} \text{ s}^{-1}$) are used to investigate the effect of strain and strain rate on the evolution of precipitation during and after warm stretching.

Figure 7.2 shows the true stress-strain response. In the range of strain rates selected in this study, no distinctive difference was observed in the yield stress between samples deformed with different strain rates. However, at a given plastic strain, the sample deformed with a faster strain rate exhibited slightly higher plastic flow stress, indicative of a higher work hardening rate. It is worth noting that these tensile tests were interrupted before the onset of necking to ensure a uniform distribution of deformation. However, due to limitations in the control system of the ETMT, the tests could not be stopped at precisely the same strain, resulting in minor variations in the end strain values. Nonetheless, these differences are not expected to have a significant impact on the overall results.

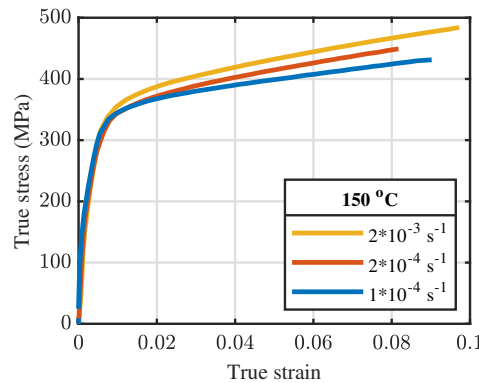


Figure 7.2: True stress-strain curves of samples deformed at 150 °C with different strain rates.

Observations of the microstructure were conducted on the sample deformed at 150 °C with the intermediate strain rate ($2 \times 10^{-4} \text{ s}^{-1}$) to 8% strain without additional 400s ageing, and the reference sample which has the same thermal history but without any deformation. Examples of the bright field TEM images are shown in figure 7.3. Slightly larger and more widely spaced precipitates are observed in the

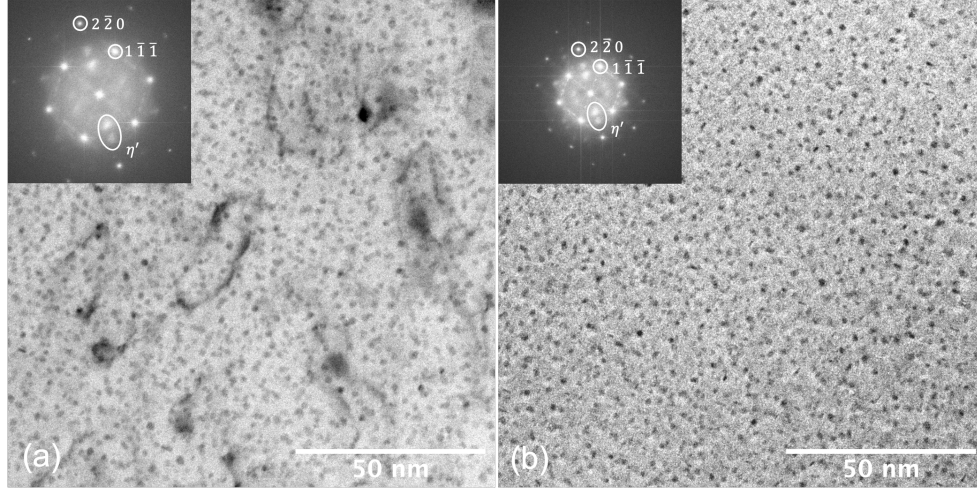


Figure 7.3: Bright field TEM images taken along $\langle 110 \rangle$ zone axis (a) from the sample deformed at 150°C with $2 \times 10^{-4} \text{ s}^{-1}$ strain rate to 8% strain. (b) from the sample having identical heat treatments but without deformation.

deformed sample than in the non-deformed sample. Dislocation structures are also found in the deformed sample (figure 7.3 (a)). It can be seen that the precipitates on and near the dislocations are not distinctively larger than those in the matrix. In both samples, the spatial distribution of precipitates is relatively homogeneous. The precipitates are identified as η' from the diffraction pattern. The average radius is measured as $1.2 \pm 0.3 \text{ nm}$ for the deformed sample and $0.9 \pm 0.2 \text{ nm}$ for the non-deformed sample.

Figure 7.3 further exemplifies that in the deformed sample, most of the precipitates have their morphology close to spherical. Whereas in the non-deformed sample, in addition to a large number of spherical precipitates, plate-shaped precipitates can also be observed. Similar diffraction patterns are obtained in both samples, indicating that the precipitate phase is the same in both deformed and non-deformed states.

In this study, the evolution of the Guinier radius during the thermomechanical process is monitored in real-time by using synchrotron small angle X-ray scattering. After the primary data cleansing as described in the previous section, the raw values of the Guinier radius from the Kratky plots were further smoothed by averaging the adjacent 10 data points. Figure 7.4 shows examples of this smoothing process on samples deformed at 150°C with the slow ($1 \times 10^{-4} \text{ s}^{-1}$) and intermediate ($2 \times 10^{-4} \text{ s}^{-1}$) strain rates. It demonstrates that the present smoothing process retains the

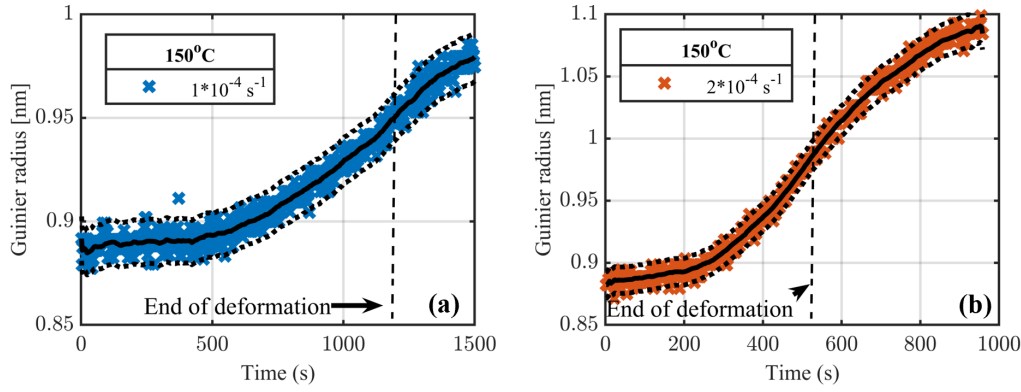


Figure 7.4: Examples of the smoothing process of the raw Guinier radius collected from samples deformed at 150 °C with (a) the slow strain rate ($1 \times 10^{-4} \text{ s}^{-1}$) and (b) the intermediate strain rate ($2 \times 10^{-4} \text{ s}^{-1}$). Raw data are marked by the scattering points. Solid lines represent the smoothed data. Dash lines, which are calculated as $\pm 2\%$ of the smoothed data, capture the upper and lower bounds of the raw data,

critical features of the raw scattering data. It further illustrates that the upper and lower bound of the raw data can be well captured by the $\pm 2\%$ of the smoothed data.

The evolution of Guinier radius during deformation, collected from samples deformed at 150 °C with different strain rates, is shown in figure 7.5, as a comparison to the change of Guinier radius in the reference sample having the same thermal history but without any deformation. It is clear that at a given time and strain rate, samples deformed at warm temperatures showed a larger Guinier radius than the sample only heated at the same temperature. Figure 7.5 further shows that at a given strain rate, the discrepancy of Guinier radius between deformed and non-deformed samples increased with time. Considering the plastic strain is proportional to the time at a given strain rate, it can be inferred that the growth of the Guinier radius accelerated with the plastic strain.

Figure 7.6 shows the change of precipitate growth rate as a function of time and strain. As expected, the growth rate of precipitates in the non-deformed sample is relatively constant and distinctly smaller than in the deformed samples. For all deformed cases, the growth rates increase with the deformation time (strain) in a close to linear manner. Figure 7.6 (b), which is a comparison at iso-strain, further illustrates the effect of strain rate on the precipitate growth rate. It can be seen that at low plastic strain, the growth rate shows little dependency on the strain rate.

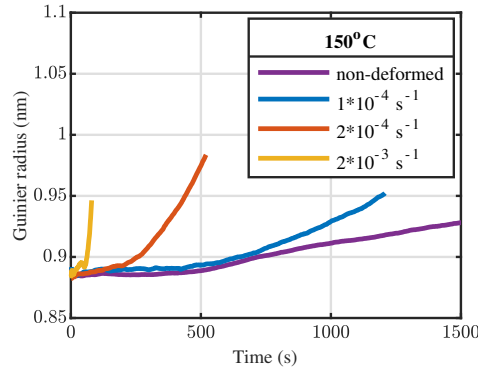


Figure 7.5: The evolution of Guinier radius during deformation at 150 °C with different strain rates, compared to the reference sample that only being heated at 150 °C without any deformation

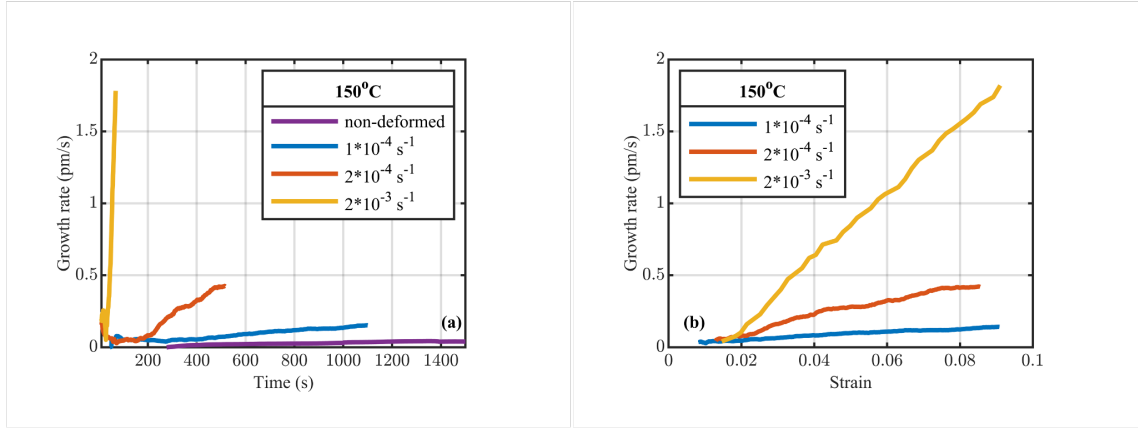


Figure 7.6: The evolution of the precipitate growth rate at 150 °C (a) as a function of time and (b) as a function of plastic strain.

With increasing the plastic strain, samples deformed with the fast strain rate show a significantly higher growth rate than samples deformed with the intermediate and slow strain rates.

7.3.2 Effect of temperature

To investigate the temperature effect on the dynamic precipitation, uni-axial warm stretching tests were performed at 120 °C and 150 °C at the slow strain rate ($1 \times 10^{-4} \text{ s}^{-1}$). The true stress-strain curves are shown in figure 7.7. As expected, the deformation temperature has a significant effect on the flow stress, with the sample deformed at 120 °C exhibited higher yield stress and plastic flow stress than the sample deformed at 150 °C. A slightly higher work hardening rate was also observed

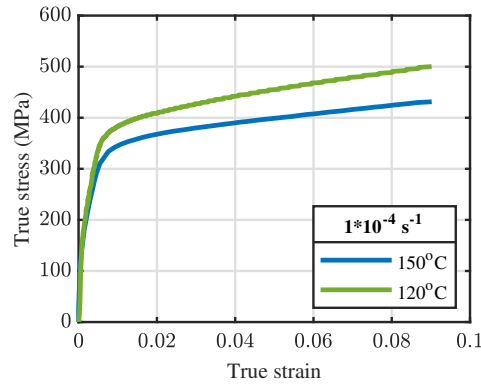


Figure 7.7: True stress-strain curves of samples deformed at 150 °C and 120 °C with the slow strain rate ($1 \times 10^{-4} \text{ s}^{-1}$).

in the sample deformed at 120 °C.

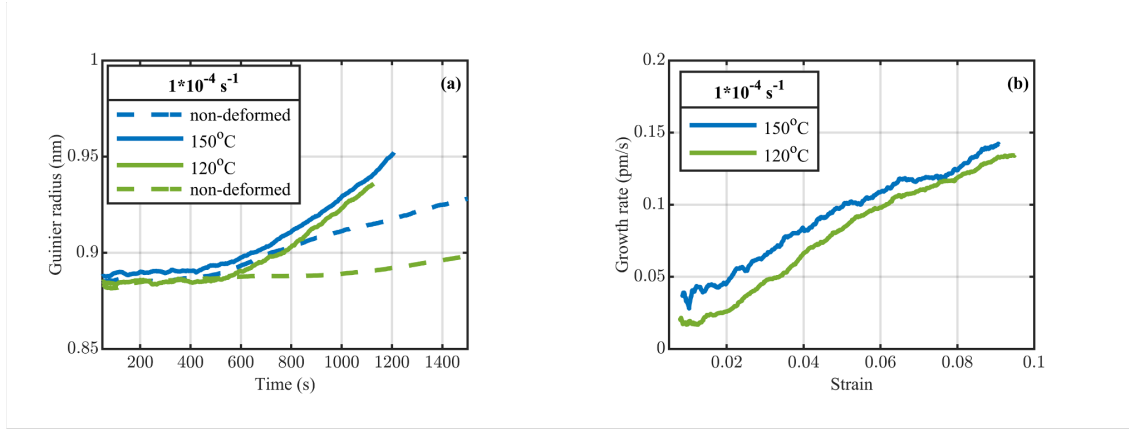


Figure 7.8: The evolution of (a) Guinier radius as a function of time (b) growth rate as a function of strain during deformation at 150 °C and 120 °C with the slow strain rate ($1 \times 10^{-4} \text{ s}^{-1}$), compared to reference samples that only being heated at 150 °C and 120 °C without any deformation

Figure 7.8 compares the evolution of Guinier radius at 120 °C and 150 °C in samples with or without deformation. As expected, due to the effect of temperature on diffusivity, in samples without any deformation, a larger Guinier radius can be found in the sample heated at 150 °C at a given time, indicating a faster precipitate growth rate than the sample heated at 120 °C. The effect of deformation on enhancing precipitation kinetics can be determined by comparing the curves for the deformed and non-deformed cases. It can be seen that even though the Guinier radius is smaller at 120 °C than at 150 °C, the difference between the deformed and non-deformed cases is much greater, indicating that the deformation enhancement

effect during plastic straining is stronger at the lower temperature.

Figure 7.9 illustrates the evolution of the growth rate during additional holding at 150°C and 120°C after removal of the plastic stress. Overall, it shows that the growth rate of precipitates in the deformed sample diminishes quickly during the isothermal holding after deformation, approaching that of the non-deformed case. Figure 7.9 also demonstrates that the decay of the precipitate growth rate is slightly faster at higher temperatures than at lower temperatures. For samples deformed at 150°C, the growth rate of precipitates decreased by 40% within 370 seconds of holding, while for the sample deformed at 120°C, it took 460 seconds to achieve the 40% reduction in the growth rate. A simple linear extrapolation suggests that the deformation enhancement effect would be lost completely after around 500s at 150°C and 1000s at 120°C, although experimental limitations preventing continued monitoring for these extended times.

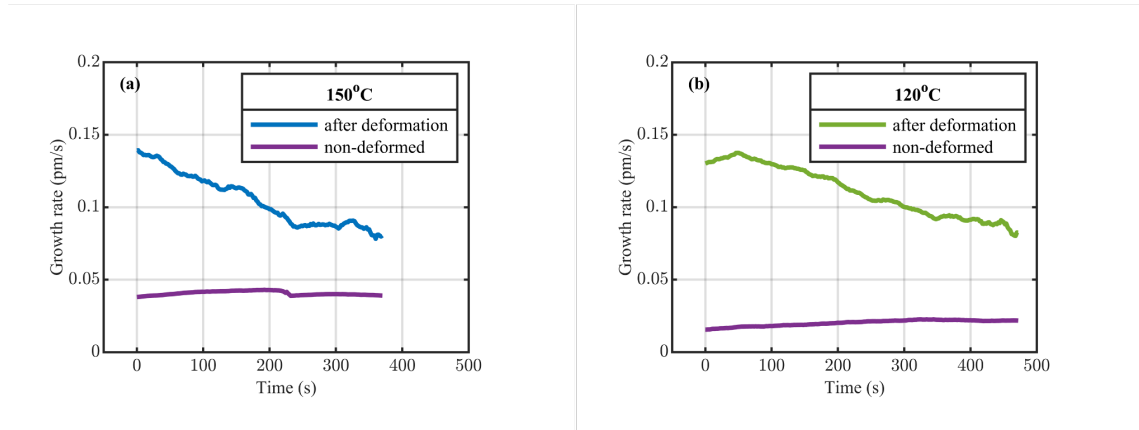


Figure 7.9: The growth rate of precipitates during additional holding at (a) 150 °C and (b) 120 °C after the deformation, compared to the reference samples without any deformation.

7.4 Discussion

The present study investigated the instantaneous effect of warm deformation on precipitation in a pre-aged Al-Zn-Mg-Cu alloy under various deformation conditions. Using the same pre-ageing process, our previous studies have demonstrated the precipitate evolution of this pre-aged microstructure at 120°C and 185°C was governed by the growth of pre-existing precipitates rather than the nucleation of new precip-

itates [16, 17]. Therefore, the discussion in this study will be limited to the effect of deformation on the evolution of precipitate size. Results from this work can then be directly compared with the previous study [2]. A key novelty of the present study is that the precipitation evolution upon removing plastic stress was tracked for additional 400 seconds at the same temperature, which can provide important information to better understand the decay of the enhanced precipitation kinetics when deformation stops.

It has been clearly demonstrated (in figure 7.5 and 7.8) deformation at warm temperatures can strongly affect the evolution of precipitate size. The effect was observed in enhancing the growth of pre-existing precipitates developed during the pre-ageing process. Previous studies have shown, in aluminium alloys, this enhancement effect of warm deformation at temperatures below 200°C is mainly controlled by the mechanically produced excess vacancies which have effects far more significant than the direct effect of dislocations acting as fast diffusion paths or as the preferred nucleation sites [2, 5, 9]. TEM images (figure 7.3) provide direct evidence of this claim. The precipitate distribution in the deformed sample is still relatively homogeneous. Despite a few precipitates being aligned along the dislocations, no distinctive difference in size can be noticed compared to the precipitates in the matrix.

In the hope to explain the observed enhancement effect caused by deformation, a phenomenological excess vacancy model (equation 7.1) is applied, which considers the total excess vacancy concentration as a result of the competing effect of production by the non-conservative motion of dislocations and annihilation by the diffusion to vacancy sinks such as dislocations and grain boundaries [9, 18]. Since the effect of dislocations on vacancy annihilation is of interest to this study, a simple empirical law (equation 7.2), describing the dislocation density increases from an initial to a saturation value, is used to estimate the evolution of dislocation density during plastic straining [9, 18]. It must be emphasised that the dislocation density values here are not expected to be accurate as the dislocation arrangement factor κ is not experimentally obtainable. Rather than over-interpreting the dislocation density, attention should be paid to the ratio of dislocation density to the square of the arrangement factor ($\frac{\rho}{\kappa^2}$) which determines the overall effect of vacancy annihilation

Table 7.2: Parameters for the excess vacancy model

Symbol	Parameters	Value
$\dot{\epsilon}$	strain rate	from experiments
σ	plastic stress	from experiments
L	grain size	$50\mu m$ [9, 10]
Ω	atomic factor	$1.66 \times 10^{-19} \text{ m}^3$ [9, 10]
b	burgers vector	0.29nm
E_j	jog formation energy	0.3eV [18]
c_j	thermal jog concentration	calculated using E_j
Q_f	vacancy formation energy	0.76eV [2]
Q_m	vacancy migration energy	0.8eV
D_v^0	pre-factor for vacancy diffusion	$1 \times 10^{-5} \text{ m}^2 \text{ s}^{-1}$ [19]
κ	dislocation arrangement factor	1 [10, 18]
χ	mechanical vacancy production term	0.1 [9, 18]
ζ	thermal jog vacancy production term	0.5 [10, 18]
D_v^{Mg}	pre-factor for solute (Mg) lattice diffusion	$1 \times 10^{-5} \text{ m}^2 \text{ s}^{-1}$ [20]
Q_{Mg}	activation energy for solute (Mg) lattice diffusion	117.71kJ mol^{-1} [20]
β_0	materials constant for dislocation model	500MPa [9]
$\rho(0)$	initial dislocation density	$1 \times 10^{10} \text{ m}^2$ [9]
ρ_s	saturated dislocation density	$1 \sim 4 \times 10^{13} \text{ m}^2$

on dislocations. All parameters used in the model are summarised in table 7.2.

$$\frac{dC_v}{dt} = \frac{dC_v^+}{dt} - \frac{dC_v^-}{dt} = \left(\chi \frac{\sigma \Omega}{Q_f} + \zeta \frac{c_j \Omega}{4b^3} \right) \dot{\epsilon} - \left(\frac{\rho}{\kappa^2} + \frac{1}{L^2} \right) D_v C_v \quad (7.1)$$

$$\rho(t) = \rho_s - (\rho_s - \rho(0)) \exp\left(-\frac{t}{\beta}\right) \quad (7.2)$$

Figure 7.10 shows the predicted vacancy production, vacancy annihilation, the overall vacancy concentration and dislocation evolution for all straining conditions investigated in this study. At a given strain rate, the vacancy production is proportional to the applied plastic strain, as expected from the first term of equation 7.1. As dislocations accumulate (equation 7.2), $\frac{\rho}{\kappa^2}$ also increases with the plastic strain, promoting the annihilation of vacancies. This eventually results in the overall vacancy concentration deviating from the vacancy production. Notably, when samples are deformed to the same plastic strain, a higher $\frac{\rho}{\kappa^2}$ is estimated in the sample deformed with a faster strain rate. However, slower vacancy annihilation is predicted, which is due to the insufficient time for diffusion at a fast strain rate.

To quantitatively investigate the contribution of deformation on the precipitate

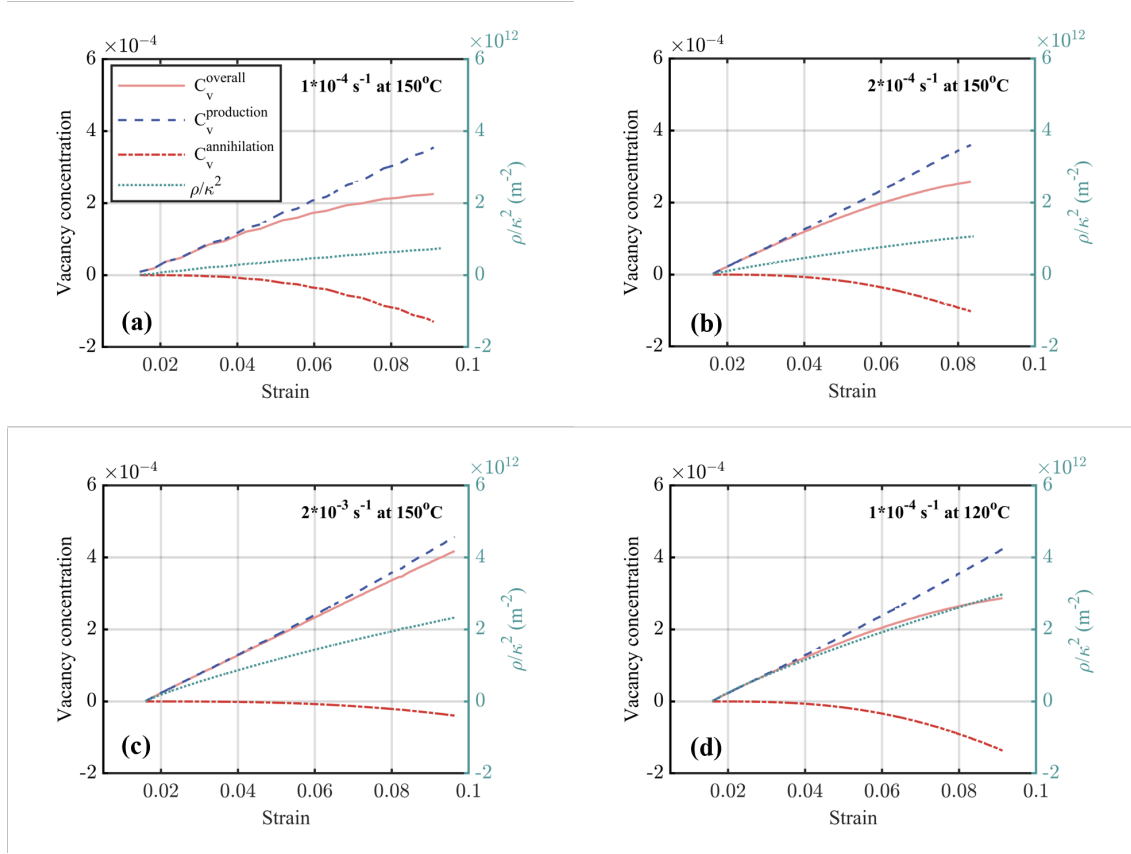


Figure 7.10: The evolution of vacancy concentration and dislocation density as a function of the plastic strain during deformation. κ is the arrangement factor in the range of 1 (homogeneous) to 10 (cellular).

growth rate, the evolution of overall vacancy concentration shown in figure 7.10 is used to fit the deformation enhanced growth rate which is calculated by subtracting the precipitate growth rate in the non-deformed sample from the deformed samples. Figure 7.11 demonstrates that for all experimental conditions in the present study, the evolution of deformation enhanced growth rate can be reasonably fitted by the change of the excess vacancy concentration.

Figure 7.11 (a, c and e) reveal the enhancement effect during straining is a function of strain and strain rate. At a given strain rate, the growth rate of precipitates increases with the plastic strain in a close to linear relationship, which is consistent with the observation by Deschamps et al.[2] in a similar 7xxx aluminium alloy in pre-aged conditions. In addition, the present results also show the relationship between plastic strain and precipitate growth rate eventually deviated from the linear behaviour, once the sample is subjected to a large plastic strain. Although this is not reported in previous experimental studies, this observation can still be rationalised

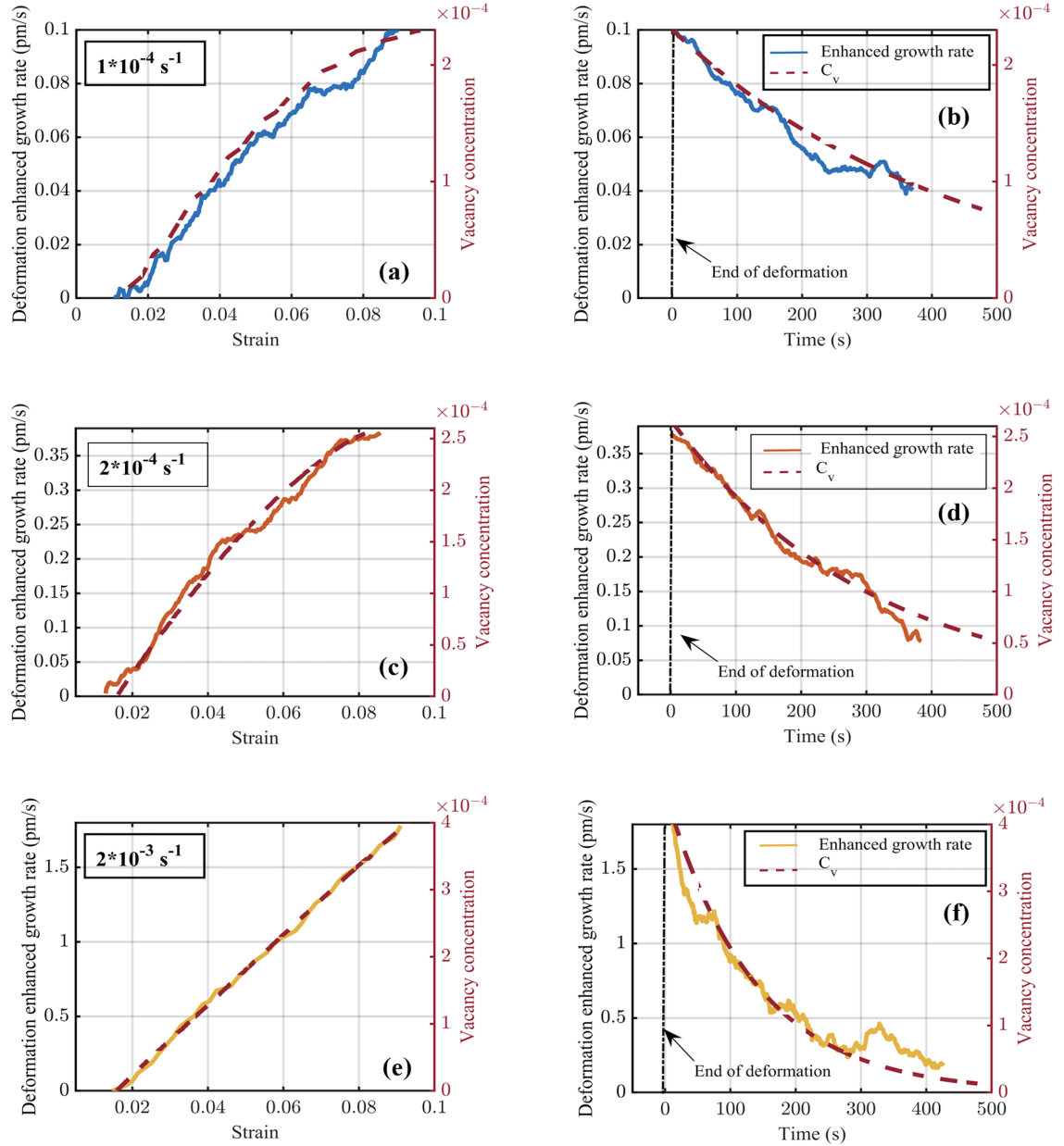


Figure 7.11: The evolution of deformation enhanced growth rate and excess vacancy concentration (a, c and e) as a function of plastic strain during deformation, (b, d and f) as a function of time during the additional 400 seconds holding at 150 °C after the deformation. (a and b) were collected from the slow strain rate test. (c and d) were collected from the intermediate strain rate test. (e and f) were collected from the fast strain rate.

by the excess vacancy model. As shown in figure 7.10, the close to linear relationship is a result of negligible vacancy annihilation compared to vacancy production. With increasing the plastic strain, the accumulation of both excess vacancies and dislocations enhances the rate of vacancy annihilation (the second term in equation 7.1) leading to the deviation from the linear behaviour.

Upon stopping the plastic deformation, the enhanced growth rates starts decreasing. Figure 7.11 (b, d and f) shows the decay of the deformation enhanced growth rate can be explained by the annihilation of vacancies on the dislocations. The excess vacancy decay rate depends on $\frac{\rho}{\kappa^2}$ and concentration of excess vacancies after deformation. Since both of these factors will be greater at a higher strain rate (figure 7.10), the decay rate is seen to be faster when the deformation step was at a higher strain rate. For the fast deformed sample, 95% the enhanced growth rate was lost during 400 seconds holding at 150 °C. Whereas samples deformed with intermediate and slow strain rates respectively lost 75% and 60% of the enhanced growth rates.

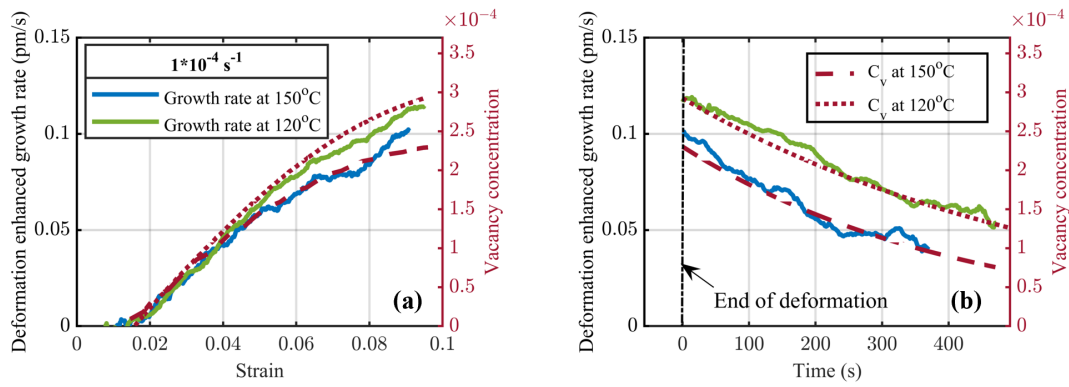


Figure 7.12: The evolution of deformation enhanced growth rate and excess vacancy concentration (a) as a function of plastic strain during deformation at 150 °C and 120 °C with the slow strain rate ($1 \times 10^{-4} \text{ s}^{-1}$), (b) as a function of time during the additional 400 seconds holding at 150 °C and 120 °C after the deformation.

The excess vacancy model is also used to explain the observed temperature dependency of the enhanced growth rate (figure 7.12). The first term in equation 7.1 demonstrates that the production of excess vacancy is sensitive to plastic stress. In the present study, the plastic stress in the sample deformed at 120°C is significantly higher than the sample deformed at 150°C, which results in a higher production rate at 120°C at a given strain. Despite a higher dislocation density estimated for the sample deformed at 120°C (figure 7.10), the vacancy annihilation is still slightly slower than the sample deformed at 150°C (figure 7.12 (b)) due to the strong temperature dependency of diffusion. Therefore, the combining effect of fast production and slow annihilation together results in the strong enhancement at 120°C during plastic straining. The temperature dependency of diffusion also governs the annihilation of

excess vacancies, hence the decay of precipitate growth rate, during the subsequent isothermal holding. As shown in Figure 7.12 (b), the deformation-enhanced growth rate decreases slightly faster at 150°C than at 120°C.

Overall, the observation of the temperature effect on deformation enhanced growth rate is consistent with the previous modelling work of excess vacancy effect on dynamic precipitation in 7xxx aluminium alloys, which predicts a stronger enhancement effect in the sample deformed at a lower temperature than at a higher temperature [9]. The fast decay of the enhanced growth rate after deformation indicates rapid annihilation of excess vacancies to sinks. This suggests compared to that after quenching [9], the excess vacancies accumulated during plastic straining are unlikely to strongly accelerate any post-deformation aging processes which may be several hours duration.

The last topic to be discussed is the strain rate dependency of the growth rate enhancement to the excess vacancy evolution. It should be noted that the fitting in figure 7.11 can only be obtained by re-scaling the maximum value of the enhanced growth rate to the maximum calculated excess vacancy concentration. The simple excess vacancy model (equation 7.1) predicts that in the low strain regime, where annihilation is negligible, the excess vacancy concentration should depend only on the plastic work and not the strain rate. Within the range of strain rates used in this study ($1 \times 10^{-4} \text{ s}^{-1}$ to $2 \times 10^{-3} \text{ s}^{-1}$), figure 7.5 (b) clearly shows a faster precipitate growth rate in the sample deformed with a faster strain rate, at a given strain and temperature. When samples were deformed to 8% strain, increasing the strain rate by a factor of 10 from $2 \times 10^{-4} \text{ s}^{-1}$ to $2 \times 10^{-3} \text{ s}^{-1}$ resulted in 3.8 times increase of the enhanced growth rate. A similar enhancement factor is reported when supersaturated AA7075 was deformed at 180°C [6]. However, this is inconsistent with the previous study reported by Deschamps et al. [2], in which strain rate independence was rationalised by the negligible annihilation of vacancies throughout the straining process.

In the present study, strain rate dependence was observed even in the regime where annihilation of excess vacancies by thermal diffusion to forest dislocation is negligible. This contradicts the simple excess vacancy model and suggests that this model is missing some potentially important physics. For example, at lower

strain rates, the possibility of excess vacancies being eliminated by diffusing to arrested glide dislocations may increase. There is also increased time for dislocation rearrangement at slower strain rates, which may sweep up excess vacancies [9]. Therefore, the simple excess vacancy model, where excess vacancies can only be annihilated by thermal diffusion to a static forest dislocation network, significantly simplifies the highly dynamic process that occurs during plastic straining. A complete understanding of these interactions will likely require more sophisticated dislocation dynamics simulations beyond the scope of the present work.

7.5 Conclusions

The present study investigated the dynamic precipitation in a pre-aged Al-Zn-Mg-Cu alloy under various deformation conditions. To understand the effect of strain, strain rate and temperature, experiments were performed at 120°C and 150°C with three different strain rates ($1 \times 10^{-4} \text{ s}^{-1}$, $2 \times 10^{-4} \text{ s}^{-1}$ and $2 \times 10^{-3} \text{ s}^{-1}$). The evolution of precipitate size was monitored during and after deformation using synchrotron small angle X-ray scattering. An excess vacancy model was used to rationalise the experimentally observed precipitation kinetics. The following conclusions may be drawn from this work:

1. The evolution of precipitate size can be significantly accelerated by applying plastic deformation at warm temperatures. The effect of deformation on precipitation is influenced by the magnitude of strains, strain rates, and temperatures. Upon removing the plastic stress, the enhancement effect quickly diminishes, suggesting the strong enhancement effect of deformation is not dominated by the enhanced diffusion along dislocation pipes, which are expected to provide a weaker enhancement.
2. TEM images reveal the precipitates after warm deformation are homogeneously distributed within the matrix with a slightly larger size than the reference condition with the same thermal history but without any deformation. This is consistent with the effect of excess vacancies enhancing the precipitate growth rate.

3. In the range of low plastic strains ($< 6\%$), the enhancement effect of deformation on the precipitate growth rate shows a close to linear relationship to the plastic strain.
4. In the range of high plastic strains ($> 6\%$), the relationship between the enhanced growth rate and the plastic strain can deviate from the linear behaviour, which is due to a strong annihilation effect of vacancies on the dislocations.
5. For a given strain and strain rate, the enhancement effect of deformation on the precipitate growth rate is stronger at a low temperature than at a high temperature, which is a result of fast vacancy production due to high plastic stress and slow vacancy annihilation due to slow diffusion.
6. A simple excess vacancy model is capable of predicting the strain and temperature dependency of the deformation-enhanced growth rate, but not the strain rate dependency observed in this study. More advanced dislocation dynamics models are likely required to predict this complicated behaviour.

Acknowledgements

Constellium is thanked for the provision of materials and financial support for this research. The EPSRC is thanked for financial support through the grant (EP/S021531/1) and the associated programme grant LightFORM (EP/R001715/1). Z.M. thanks the financial support from EPSRC grant Centre for Doctoral Training in Advanced Metallic Systems (EP/S022635/1) for his PhD research. J.D.R. acknowledges the support of the DSTL/RAEng Chair in Alloys for Extreme Environments.

The data required to reproduce these findings are available from the LightFORM Zenodo repository <https://zenodo.org/communities/lightform/>.

Bibliography

- [1] A. Deschamps, F. Livet, Y. Brechet, Influence of predeformation on ageing in an al–zn–mg alloy—i. microstructure evolution and mechanical properties, *Acta*

- materialia 47 (1) (1998) 281–292.
- [2] A. Deschamps, G. Fribourg, Y. Brechet, J. L. Chemin, C. Hutchinson, In situ evaluation of dynamic precipitation during plastic straining of an al–zn–mg–cu alloy, *Acta materialia* 60 (5) (2012) 1905–1916.
- [3] M. Kumar, C. Poletti, H. P. Degischer, Precipitation kinetics in warm forming of aw-7020 alloy, *Materials Science and Engineering: A* 561 (2013) 362–370.
- [4] L. Couturier, A. Deschamps, F. De Geuser, F. Fazeli, W. Poole, An investigation of the strain dependence of dynamic precipitation in an al–zn–mg–cu alloy, *Scripta Materialia* 136 (2017) 120–123.
- [5] W. Mirihanage, J. Robson, S. Mishra, P. Hidalgo-Manrique, J. Q. da Fonseca, C. Daniel, P. Prangnell, S. Michalik, O. Magdysyuk, T. Connolley, et al., Direct observation of the dynamic evolution of precipitates in aluminium alloy 7021 at high strain rates via high energy synchrotron x-rays, *Acta Materialia* 205 (2021) 116532.
- [6] J. Robson, P. Jessner, M. Taylor, Z. Ma, Dynamic precipitation in supersaturated al–zn–mg–cu alloy during warm stretching, *Metallurgical and Materials Transactions* (2023) 1–11.
- [7] C. Hutchinson, F. De Geuser, Y. Chen, A. Deschamps, Quantitative measurements of dynamic precipitation during fatigue of an al–zn–mg–(cu) alloy using small-angle x-ray scattering, *Acta materialia* 74 (2014) 96–109.
- [8] W. Sun, Y. Zhu, R. Marceau, L. Wang, Q. Zhang, X. Gao, C. Hutchinson, Precipitation strengthening of aluminum alloys by room-temperature cyclic plasticity, *Science* 363 (6430) (2019) 972–975.
- [9] J. Robson, Deformation enhanced diffusion in aluminium alloys, *Metallurgical and Materials Transactions A* 51 (10) (2020) 5401–5413.
- [10] M. Bignon, P. Shanthraj, J. D. Robson, Modelling dynamic precipitation in pre-aged aluminium alloys under warm forming conditions, *Acta Materialia* (2022) 118036.

- [11] M. Basham, J. Filik, M. T. Wharmby, P. C. Chang, B. El Kassaby, M. Gering, J. Aishima, K. Levik, B. C. Pulford, I. Sikharulidze, et al., Data analysis workbench (dawn), *Journal of synchrotron radiation* 22 (3) (2015) 853–858.
- [12] F. De Geuser, A. Deschamps, Precipitate characterisation in metallic systems by small-angle x-ray or neutron scattering, *Comptes Rendus Physique* 13 (3) (2012) 246–256.
- [13] A. Deschamps, F. Bley, F. Livet, D. Fabregue, L. David, In-situ small-angle x-ray scattering study of dynamic precipitation in an al-zn-mg-cu alloy, *Philosophical Magazine* 83 (6) (2003) 677–692.
- [14] H. Brumberger, D. Hagrman, J. Goodisman, K. Finkelstein, In situ anomalous small-angle x-ray scattering from metal particles in supported-metal catalysts. ii. results, *Journal of applied crystallography* 38 (2) (2005) 324–332.
- [15] A. Deschamps, F. De Geuser, Quantitative characterization of precipitate microstructures in metallic alloys using small-angle scattering, *Metallurgical and Materials Transactions A* 44 (1) (2013) 77–86.
- [16] Z. Ma, E. Cooksey-Nash, D. Barbier, J. Robson, Microstructural stability and paint bake response of pre-aged aa7075, *Materials Characterization* 200 (2023) 112862.
- [17] Z. Ma, J. Robson, Understanding the effect of deformation combined with heat treatment on age hardening of al-zn-mg-cu alloy aa7075, *Materials Science and Engineering: A* (2023) 145212.
- [18] M. Militzer, W. Sun, J. Jonas, Modelling the effect of deformation-induced vacancies on segregation and precipitation, *Acta metallurgica et materialia* 42 (1) (1994) 133–141.
- [19] J. Embury, R. Nicholson, The nucleation of precipitates: the system al-zn-mg, *Acta Metallurgica* 13 (4) (1965) 403–417.
- [20] R. Picu, D. Zhang, Atomistic study of pipe diffusion in al–mg alloys, *Acta materialia* 52 (1) (2004) 161–171.

Chapter 8

Conclusions

The main objective of this thesis is to examine the complex interactions between deformation and precipitation in a commercial 7075 aluminium alloy. Chapter 4 presents the work of investigating the immediate effect of deformation on the early stages of clustering in a supersaturated microstructure at 180°C. This was achieved by performing the solution treatment, quenching, and warm stretching sequentially using a dilatometer. Chapter 5 presents the work of optimising the pre-ageing strategy by characterising the precipitate evolution during pre-ageing, natural ageing and paint baking. Employing the pre-ageing strategy proposed in chapter 5, chapter 6 provides a comprehensive study of using dislocation hardening and precipitation strengthening together to achieve over T6 strength. And finally, chapter 7 presents an in-situ examination of the concurrent effect of precipitation and deformation in this pre-aged microstructure at warm temperatures. Detailed conclusions are presented in each chapter. The subsequent paragraphs consolidate the key conclusions may be drawn from this thesis.

1. In a supersaturated microstructure, deformation at a temperature of 180 °C has a significant impact on precipitation, which is primarily observed through enhancing the growth of small clusters/precipitates rather than increasing the nucleation of new clusters or precipitates. The enhancement effect of deformation on the growth of precipitates is consistent with the expected effect of strain-induced excess vacancies increasing the diffusion rate of solutes.
2. Pre-ageing 8 hours at 80 °C can stabilise the microstructure against natural

ageing up to at least 7 months, which still allows 94% of the T6 strength to be achieved during a short 20 minutes paint-bake treatment at 185 °C. If the paint-bake time is longer than 20 minutes, the heating rate used to reach the paint-bake temperature has no significant impact on the final hardness, the size and fraction of precipitates. This is because compared to a faster heating rate, a slower heating rate results in a greater increase in precipitate size and fraction during the heating ramp, which leads to the removal of solute and slows down subsequent evolution during the isothermal hold.

3. Pre-ageing for 8 hours at 80 ° results in a greater retained work hardening when a 10% uni-axial stretch is used after the pre-ageing step, which activates significant dislocation strengthening leading to a strength level higher than those achieved through the T6 tempering process. However, this initial straining depletes some of the work hardening capacity, allowing for only an additional 8% elongation in the subsequent straining process. The second heat treatment can further adjust the mechanical properties and precipitation state. A heat treatment of 6 hours at 120 °C can enhance precipitation and partly recover the stored dislocations. As a result, the material exhibits a 0.2% proof stress of 590 MPa higher than the T6 level of 560 MPa, and an additional 11% strain to failure higher than the 8% without the second heat treatment.
4. For this pre-aged microstructure, deformation at room temperature has a minimal impact on the size and volume fraction of precipitates formed during pre-ageing, but it does expedite precipitate growth in the final ageing step. The growth rate were found to be enhanced by 1.5-2.5 times, which is consistent with the predicted effect of increased diffusion along dislocation pipes.
5. When this pre-aged sample is deformed at warm temperatures, the precipitates evolve significantly, and the enhancement effect of deformation on the growth of precipitates during deformation is much stronger than that post-deformation. Upon removing the plastic stress, the enhancement effect diminishes rapidly. This is consistent with the hypothesis that the strong growth enhancement effect during deformation is primarily driven by strain-induced excess vacancies, rather than the enhanced diffusion along dislocation pipes.

6. The enhanced growth rate of precipitates during warm deformation is strongly influenced by factors such as the magnitude of strain, strain rate, and temperature. At low plastic strains (below 6%), the impact of deformation on precipitate growth shows a nearly linear relationship to the plastic strain. However, at high plastic strains (above 6%), the relationship between the growth rate and plastic strain can deviate from this linear behaviour due to annihilation effect of vacancies on the dislocations. Furthermore, at a given strain and strain rate, the effect of deformation on the growth rate of precipitates is more pronounced at low temperatures compared to high temperatures, primarily because of the high production of vacancies caused by the high plastic stress and the slow annihilation of vacancies due to slow diffusion.
7. The strain and temperature dependence of the deformation-enhanced growth rate observed in both pre-aged and supersaturated microstructure can be predicted by a simple excess vacancy model. However, the model cannot accurately predict the observed strain rate dependency, indicating that it is an inadequate explanation of the complex interactions between mobile dislocations and precipitation.

8.1 Future work

The present study has revealed following areas which might be of interest for future work:

1. While this study has contributed to the design of pre-ageing strategies based on precipitation behaviour for the application of 7075 aluminium alloys in the automotive industry, there are still questions that could be addressed in future work. Particularly, the formability of the proposed pre-aged microstructure under various forming conditions could be investigated in greater detail. This could involve collecting more stress-strain responses and developing forming limit diagrams.
2. Another potential avenue for future research is to validate the proposed pre-ageing strategy on other high strength 7xxx aluminium alloys and explore the

potential effect of the proposed double ageing practice (pre-ageing plus paint baking) on the behaviour of stress corrosion cracking which is a major concern for high strength Al-Zn-Mg-Cu alloys.

3. In Chapter 4, the investigation focused on the effect of warm deformation on cluster evolution in a supersaturated microstructure through an ex-situ approach. However, it is essential to acknowledge that the delay between warm deformation and the subsequent small angle X-ray scattering investigation could significantly impact the results and, consequently, the conclusions drawn. Although efforts were made to minimize this delay and reference samples were provided, which experienced the same thermal exposure but without deformation, the study could be enhanced by conducting in-situ experiments utilizing advanced tools such as synchrotron X-ray and thermomechanical machines like ETMT and dilatometer.
4. In Chapter 5, our investigation centred on the evolution of precipitation during pre-ageing and paint bake processes. While the analysis of precipitate size in the present study has focused on the Guinier radius, it is crucial to recognize that the evolution of the size distribution is another vital aspect when studying precipitation in Al-Zn-Mg-Cu systems. Consequently, it is highly beneficial to incorporate more detailed data analysis methods to obtain a comprehensive precipitate size distribution.
5. In chapter 6, we applied a cold deformation on the pre-aged microstructure and investigated its effect on the subsequent ageing process. Notably, an abnormal behaviour characterized by an elongated yield point was observed when reloading the sample after the initial 10% cold deformation. It was further demonstrated that this behaviour can be eliminated by subjecting the sample to additional ageing at 120 °C. Despite successfully addressing the issue with additional ageing, the underlying origin of this abnormal behaviour remains unknown. It is plausible that the phenomenon is associated with dynamic interactions between dislocations and precipitates during the initial 10% cold deformation. Moreover, this behaviour might also be influenced by the resting time between the 10% cold deformation and the subsequent

reloading.

6. Another promising direction for future research is to explore the deformation effect on precipitation under other stress state and strain paths. This could be accomplished by conducting warm deformation under hydrostatic stress and bi-axial or plane strain, which could provide further insights into the dynamic interactions between deformation and precipitation.
7. Finally, it may be worthwhile to design in-situ experiments combining small angle X-ray scattering and X-ray diffraction, which could help establish the relationship between the evolution of precipitates and dislocation density. This could be useful in developing more advanced dislocation dynamics models to accurately capture the strain rate dependency of the enhanced growth rate of precipitate during warm deformation.